

**Department of Chemistry**

**Better Batteries via Controlling the Properties of Electrolytic  
Manganese Dioxide**

**Jonathon Robert Morton**

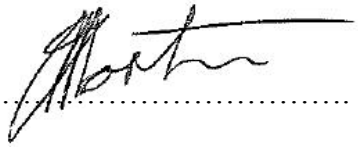
**This thesis is presented for the Degree of  
Doctor of Philosophy  
of  
Curtin University**

**November 2013**

## Declaration

To the best of my knowledge and belief this thesis contains no material previously published by any other person except where due acknowledgment has been made.

This thesis contains no material which has been accepted for the award of any other degree or diploma in any university.

Signature:  .....

Date: .....18/11/2013.....

**ABSTRACT**

Electrolytic manganese dioxide (EMD) is an essential ingredient in modern alkaline cells and other batteries. It is produced by the electrolysis of manganese sulphate solutions under rigidly controlled conditions. Over the last 60 years EMD has been extensively studied. Despite this, many fundamental aspects of EMD, such as its structure, electro-deposition mechanism, and the effect of electrolysis parameters on the properties of EMD are poorly understood. The aim of this project was to apply a multi-faceted research philosophy, which links characterization techniques such as SEM and XRD, to molecular modelling and electrochemistry, with an emphasis on the use of *in situ* experimental studies to deepen the current understanding of EMD structure and crystal growth mechanisms.

Initial characterisation and analysis of EMD was performed on powder samples and EMD chips. A wide variety of characterisation techniques were used including SEM and AFM to investigate the morphologies of EMD crystals; and XRD, SR-XRD, TEM, and Raman, to examine the crystal structure of EMD. This approach to EMD characterisation was employed to provide a wide range of complementary morphological and structural data, with the hope of developing a better understanding of the EMD crystal structure, and as a way of evaluating the suitability of various characterisation techniques for further use in this project. This work not only confirmed the highly complex nature of EMD and the need for a better structural model, but also provided valuable information on the conditions to be researched and resulted in SEM and XRD becoming the characterisation techniques of choice for this project.

EMD samples produced over the course of this study under various conditions were characterised using a combination of on-electrode SEM, and low background XRD. This work clearly showed that of the deposition condition variables studied, both current density and temperature have the largest effect on the structure of the EMD deposited, and that the results of this project were consistent with EMD crystal growth theory. This work also highlighted the need for further study of the effects of organic electrolyte bath additives on the structure and properties of EMD.

This study also conducted simultaneous electrode kinetic (EIS) and *in situ* synchrotron radiation – grazing incidence X-ray diffraction (SR-GIXRD) surface studies of the electro-deposition process of EMD, in an attempt to further elucidate the EMD deposition mechanism via a novel method; unfortunately these analyses proved problematic, although this marriage of *in situ* SR-GIXRD and EIS for use in EMD research was demonstrated to show promise.

In order to fully understand the various properties of EMD, it is necessary to develop a deep understanding of its crystal structure. However, the very nature of the EMD structure prevents us from achieving this goal through experimental methods alone. Fortunately, developments in molecular modelling techniques allow simulations of possible structures and relative energetics of a compound. Molecular modelling was employed to simulate the defects (De Wolff defects, micro-twinning, cation ordering) that occur within the EMD crystal structure. The various defect structures were modelled and optimised, and simulated XRD patterns were produced. These patterns were then compared to experimental data. This work developed a suitable potential model for the crystal structure of EMD; provided evidence that De Wolff defects, [021] and [061] twinning, and cation ordering contribute to the structure and subsequent XRD patterns of EMD; and lead to the proposal of a possible single-phase model, which challenges conventional thinking, and uses the  $\epsilon$ -MnO<sub>2</sub> structure as its starting point for EMD structures.

**TABLE OF CONTENTS**

Abstract .....	i
Table of Contents .....	iii
Acknowledgements .....	vii
1 INTRODUCTION.....	1
1.1 Manganese Oxides .....	1
1.1.1 Chain Structures .....	3
1.1.2 Spinel Structures .....	7
1.1.3 Tunnel Structures .....	8
1.1.4 Layer Structures .....	11
1.1.5 Reduced Forms of Manganese Oxides.....	11
1.2 EMD.....	12
1.2.1 Structural Defects in EMD.....	13
1.2.2 Structural Models of EMD.....	18
1.3 Literature on the Structure of EMD .....	22
1.3.1 XRD Studies.....	22
1.4 Production of EMD .....	27
1.4.1 Industrial Processes.....	28
1.4.2 Electro-deposition Conditions / Electrode Composition.....	30
1.4.3 Electrolyte Additives.....	32
1.4.4 Non-Standard Electrolytes .....	34
1.4.5 Deposition Mechanism.....	36
1.5 EMD Deposition from a Crystal Growth Perspective.....	40
1.6 EMD in Alkaline Cells.....	41
1.6.1 EMD Properties Required for Use In Alkaline Cells.....	41
1.7 Molecular Modelling of EMD .....	42
1.8 Research Plan .....	44
1.9 References .....	46
2 EXPERIMENTAL .....	56
2.1 Reagents .....	56
2.2 Electro-deposition Cell.....	57
2.3 Experimental Procedures .....	59
2.3.1 Preparation of Electrolyte Solutions .....	59
2.3.2 Preparation of EMD for SEM Analysis .....	59

---

2.3.3	Preparation of EMD Samples for XRD Analysis .....	59
2.3.4	Cyclic Voltammetry (CV).....	60
2.3.5	Electrochemical Impedance Spectroscopy (EIS).....	60
2.3.6	<i>In situ</i> Simultaneous Electrochemical Impedance Spectroscopy (EIS) and Synchrotron Radiation Grazing Incidence X-ray Diffraction (SR–XRD).....	60
2.4	Experimental Conditions Studied .....	61
2.5	Characterisation of Solids .....	63
2.5.1	Scanning Electron Microscopy (SEM) .....	63
2.5.2	X-Ray Diffraction (XRD) .....	63
2.5.3	Transmission Electron Microscopy (TEM) .....	63
2.5.4	Raman Spectroscopy .....	63
2.5.5	Infrared Spectroscopy (FT–IR).....	64
2.5.6	Atomic Force Microscopy (AFM) .....	64
2.5.7	Synchrotron Radiation X-Ray Diffraction (SR–XRD).....	64
2.6	Molecular Modelling.....	64
2.7	References .....	65
3	ANALYSIS OF EMD PRODUCED AT THE HITEC ENERGY PILOT PLANT.....	66
3.1	Analysis of EMD Powders from the HiTec Energy Pilot Plant.....	66
3.1.1	General Parameters .....	67
3.1.2	SEM.....	69
3.1.3	XRD .....	69
3.1.4	TEM .....	78
3.1.5	Raman and FT–IR Analysis.....	80
3.2	Analysis of EMD Chips from the HiTec Energy Pilot Plant .....	81
3.2.1	SEM.....	81
3.2.2	XRD .....	85
3.2.3	AFM .....	88
3.3	Conclusions .....	90
3.4	References .....	91
4	ANALYSIS OF EMD PRODUCED IN THIS STUDY .....	94
4.1	General Analysis of the EMD Deposition Process .....	95
4.2	Effect of Current Density .....	97

---

4.3	Effect of Temperature .....	103
4.4	Effect of Mn <sup>2+</sup> Concentration.....	106
4.5	Effect of H <sub>2</sub> SO <sub>4</sub> Concentration .....	109
4.6	Analytical Parameters Derived from EMDs XRD Patterns .....	112
4.7	Effect of Electrolyte .....	112
4.8	Effect of Inorganic Additives.....	114
4.9	Effect of Organic Additives .....	118
4.10	Conclusions .....	128
4.11	References .....	129
5	SIMULTANEOUS <i>IN SITU</i> SR-GIXRD AND EIS STUDIES OF THE EMD DEPOSITION PROCESS .....	133
5.1	Cell Design: Part I.....	133
5.2	Experimental .....	135
5.3	Simultaneous <i>in situ</i> SR-GIXRD and EIS – Results and Discussion: Part I .....	137
5.4	Simultaneous <i>in situ</i> SR-GIXRD and EIS – Conclusions and Recommendations: Part I .....	140
5.5	Cell Design: Part II.....	141
5.6	Simultaneous <i>in situ</i> SR-GIXRD and EIS – Results and Discussion: Part II .....	142
5.7	Simultaneous <i>in situ</i> SR-GIXRD and EIS – Conclusions and Recommendations: Part II.....	145
5.8	References .....	146
6	MODELLING THE CRYSTAL STRUCTURE OF EMD – Part I: Introduction, Determination of the Phases, and Potential Testing.....	147
6.1	Introduction to Molecular Modelling of the Crystal Structure of EMD .....	147
6.2	Determination of MnO <sub>2</sub> Phases/Mixtures present in EMD.....	148
6.3	Modelling the Crystal Structure of EMD.....	152
6.3.1	Theory .....	153
6.3.2	Potential Fitting.....	154
6.4	Testing Potentials .....	156
6.4.1	2x2 Tunnels Structures.....	156
6.4.2	2x3 Tunnel Structures .....	159
6.4.3	3x3 Tunnel Structures .....	160

---

6.4.4	Spinel Structures .....	160
6.4.5	Stability of Polymorphs.....	161
6.4.6	Conclusions Drawn from Potential Testing.....	163
6.5	References .....	164
7	MODELLING THE CRYSTAL STRUCTURE OF EMD – Part II:	
	Modelling Defects in EMD, and Determination of a Structural Model.....	168
7.1	Foundation Work For This Project .....	168
7.2	Modelling De Wolff Defects.....	169
7.2.1	The Slab Method .....	170
7.2.2	The Layer Method.....	176
7.3	Modelling Micro-twinning.....	180
7.3.1	Micro-twinning on the 021 Lattice Plane.....	181
7.3.2	Micro-twinning on the 061 Lattice Plane.....	185
7.3.3	Conclusions Drawn by Modelling Microtwinning via the Cation Translation Method.....	190
7.4	Combining Defects.....	191
7.5	$\epsilon$ -MnO <sub>2</sub> .....	193
7.5.1	Cation/Vacancy Ordering in $\epsilon$ -MnO <sub>2</sub> .....	195
7.6	Determination of a structural model for EMD .....	203
7.6.1	A Mixed-Phase Model .....	203
7.6.2	A Single-Phase Model.....	205
7.7	Conclusions .....	205
7.8	References .....	208
8	FUTURE WORK.....	211
8.1	Future Experimental Work.....	211
8.1.1	Characterisation Techniques .....	211
8.1.2	Organic Additives .....	211
8.1.3	<i>In-situ</i> Work .....	212
8.2	Future Modelling Work.....	212
8.3	References .....	214
	Appendix I - ELECTROCHEMICAL STUDIES OF EMD .....	I
	Electrochemical Impedance Spectroscopy (EIS).....	II
	Cyclic Voltammetry (CV).....	II
	References .....	VI

## **ACKNOWLEDGEMENTS**

Firstly I would like to thank my supervisors Mark Ogden, Andrew Rohl, and Chris Ward, for their help, support and patience throughout the duration of this project.

Thank you to APA(I) and HiTec Energy Ltd. for my scholarship and the ABNF for funding my work at the Photon Factory, Tsukuba, Japan.

I would also like to thank the many staff from the Curtin Chemistry, and Physics Departments who helped me with the characterisation work for this project, your assistance and patience was very much appreciated.

Finally I would like to thank my friends and family for their love, patience and support throughout this project (it took a while but we got there in the end!).

And a special thanks to Jade and Jordan for getting me over the line, love you both!

## 1 INTRODUCTION

Electrolytic manganese dioxide (EMD) is an essential ingredient in modern alkaline cells and other batteries. It is produced by the electrolysis of manganese sulphate solutions under rigidly controlled conditions. Over the last 60 years EMD has been extensively studied. Despite this, many fundamental aspects of EMD, such as its structure, electro-deposition mechanism, and the effect of electrolysis parameters on the properties of EMD are poorly understood.

### 1.1 Manganese Oxides

Making up 0.08% of the Earth's crust, manganese (Mn) is the 10<sup>th</sup> most abundant crustal element [1-3]. Mn is widely distributed and commonly replaces iron, aluminium, and the alkaline earth metals within minerals[4]. Mn oxides are by far the most common Mn minerals, although Mn is also found as carbonates (rhodochrosite, dialogite,  $\text{MnCO}_3$ ), silicates (rhodonite,  $\text{MnSiCO}_3$ ) and sulphides (alabandite,  $\text{MnS}$ ) [2].

More than 30 Mn oxides exist in various geological settings including, the ocean floor, the bottom of many fresh-water lakes as well as sediments and soils. There are also many synthetic Mn oxides such as EMD. Mn oxides have many uses, in ancient times as pigments and to clarify glass [1]; in more recent times Mn oxides have generated interest because of their commercial applications in the manufacture of steel, paints, glass, catalysts, water-purifying agents, fertilizers, livestock feed additives, colorants and the battery industry [1, 2]. Mn occurs naturally in three oxidation states +2, +3 and +4 (although usually in the +4 state), resulting in a range of multivalent phases, this contributes (along with a wide range of formation conditions, and diverse array of atomic structures, many of which can accommodate metal cations, and water), to the complexity and large variety of structures found in Mn oxide minerals [1].

There have been many attempts to classify the various forms of Mn oxides, and conflicts regarding structure and groupings within literature are common. Original

classifications of Mn oxides were very broad, with minerals being split into two groups ([5] along with, Read [4] and Turner and Buseck [6] in Williams [2]):

- Wad (soft oxide minerals).
- Psilomelane (hard and botryoidal).

Classification of Mn oxide minerals is difficult for several reasons [2]:

- Mn oxides are usually non-stoichiometric materials, that contain interstitial water, cations and cation vacancies.
- Mn oxides have very small crystallite sizes, which results in XRD patterns that are almost amorphous, ie. broad peaks.
- Mn oxides usually occur as intimate mixtures, solid solutions or structural intergrowths.

Of the Mn oxides, MnO<sub>2</sub> is the most important and contains the largest structural complexity. Polymorphism is very common in MnO<sub>2</sub> minerals, in fact no less than 14 modifications have been mentioned in literature [7, 8], although many of these modifications were later shown to be members of the same structural families. The complexity of MnO<sub>2</sub> structures is thought to be a result of the small ionic radius of Mn<sup>4+</sup> ( $r = 0.53\text{\AA}$ ), which puts MnO<sub>2</sub> at the lower limit of stability for the rutile structure. Although this small radius could be thought to favour tetrahedral coordination, the 3d<sup>3</sup> electron configuration of Mn<sup>4+</sup> actually favours octahedral coordination [7]. As a result, the fundamental building block for MnO<sub>2</sub> structures is the [MnO<sub>6</sub>] octahedron, which shares edges and/or corners to produce a large array of chain, tunnel, layer, and spinel structures, as well as intergrowths of these structures [1, 2, 7, 9, 10]. A more elegant way to express this concept is to explain it in terms of differing cation decorations. Basically, all MnO<sub>2</sub> structures have an approximately close packed oxygen sub-lattice, with Mn<sup>4+</sup> cations distributed over the octahedral sites; the large degree of complexity found in MnO<sub>2</sub> structures arises from the fact that there are many different cation decoration/ordering schemes possible within the octahedral sites of the oxygen sub-lattice. The redox chemistry of manganese also contributes to the structural complexity of MnO<sub>2</sub>, as the multiple valence states of manganese, can produce an array of closely related structures, containing differing amounts of Mn<sup>4+</sup>, Mn<sup>3+</sup>, and Mn<sup>2+</sup> [7].

There have been many systems proposed by various authors to classify the large number of both natural and synthetic MnO<sub>2</sub> polymorphs that are known to occur. Generally conflicts between classification systems for MnO<sub>2</sub> arise from disagreements relating to the true structure of some MnO<sub>2</sub> polymorphs, and whether various polymorphs have unique structures, or belong to a larger family of related structures. The classification system used in this study is based on that of Williams [2], and classifies MnO<sub>2</sub> polymorphs into four major groups:

- Chain structures
- Spinel structures
- Tunnel structures
- Layer structures

This classification system represents a summary of a large body of literature, not the work of a single author.

### 1.1.1 Chain Structures

There are two stable and ordered chain structure polymorphs of MnO<sub>2</sub>, pyrolucite ( $\beta$ -MnO<sub>2</sub>), and ramsdellite. Chain structures also exist as intergrowths ( $\gamma$ -MnO<sub>2</sub>) and disordered ( $\epsilon$ -MnO<sub>2</sub>) polymorphs. All these structures consist of a slightly distorted hexagonally close packed array of oxygen ions, and it is their differing cation decorations that give these polymorphs their unique structures.

#### 1.1.1.1 Pyrolucite ( $\beta$ -MnO<sub>2</sub>)

Pyrolucite is the most stable and dense MnO<sub>2</sub> and has the structure of rutile [2, 7, 11]. In pyrolucite (Figure 1.1), every second row of octahedral sites in the  $[ab]$  plane is occupied by Mn<sup>4+</sup> ions, leading to the appearance of 1x1 tunnels in the  $c$  direction [12]. These tunnels are too small to accommodate other chemical species within them [1]. Early literature states that all octahedra are equivalent and the average Mn — O distance is 1.88 Å [7], although a more recent powder neutron diffraction study found that the octahedra are actually elongated, with two Mn — O distances of 1.894 Å, and four Mn — O distances of 1.882 Å (Bolzan *et al.* [13] in Williams [2]). Pyrolucite has tetragonal symmetry, with cell dimensions  $a$ ,  $b= 4.3980$ ,  $c=2.8730\text{Å}$

and space group  $P4_2/mnm$  [11, 14], and typically has an acicular crystal morphology [1].

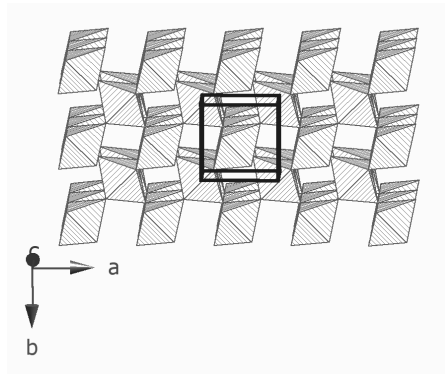


**Figure 1.1:** The crystal structure of pyrolucite, viewed along the  $c$  axis.

### 1.1.1.2 Ramsdellite

Ramsdellite is a rare mineral that has a diaspore type structure [2, 15]. Ramsdellite (Figure 1.2) has a similar structure to pyrolucite, except that pairs of rows are occupied by  $Mn^{4+}$  ions along the  $c$  axis, leading to  $2 \times 1$  tunnels [7]. The location of cations within the ramsdellite structure results in two different kinds of oxygen atoms [7]:

- $O_{\text{planar}}$ ; which are located at the centre of an almost equilateral triangle of  $Mn^{4+}$  ions, resulting in  $sp^2$  hybridization of the O atom, giving Mn—O distances of 1.86 Å (twice) and 1.89 Å.
- $O_{\text{pyramidal}}$ ; which are located at the apex of a trigonal pyramid of  $Mn^{4+}$  ions, resulting in  $sp^3$  hybridization, and giving Mn—O distances of 1.92 Å (twice) and 1.89 Å. It is this oxygen that is hydroxylated when ramsdellite is reduced to  $\alpha$ - $MnOOH$ .

The ramsdellite lattice occurs in the  $Pnma$  space group, although the non-standard settings  $Pnam$  or  $Pbnm$  are often used in the literature. When modeling or comparing unit cells in this study the space group was matched with the literature being referenced to avoid unnecessary complications. Ramsdellite only occurs as a mineral, and is often mixed with pyrolucite. Pure ramsdellite has never been synthesized, and even highly crystalline samples still contain a significant amount of

structural defects [7]. The tunnels in the ramsdellite structure are generally empty, although chemical analysis has found minor amounts of water, Na and Ca, that are thought to be located in the tunnels. The water in the structure is thought to be present in the form of acid—OH groups associated with  $\text{Mn}^{3+}$  ions in the lattice [1]. Ramsdellite has an orthorhombic symmetry, with cell dimensions  $a= 9.3329$ ,  $b= 4.4533$ , and  $c= 2.8482 \text{ \AA}$  [16].

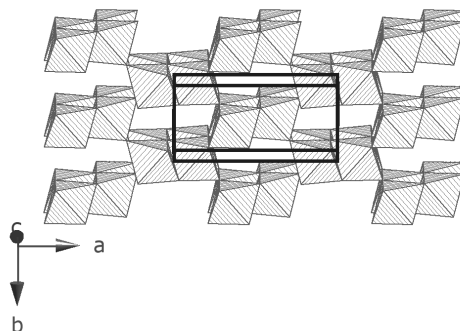


**Figure 1.2:** The ramsdellite crystal structure in the  $Pnam$  setting, viewed along the  $c$  axis.

### 1.1.1.3 $\gamma\text{-MnO}_2$

$\gamma\text{-MnO}_2$  occurs naturally as the mineral nsutite (Natural Manganese Dioxide - NMD), along with CMD (Chemical Manganese Dioxide), and EMD, which is a battery active form of  $\text{MnO}_2$ .  $\gamma\text{-MnO}_2$  is described as an irregular intergrowth of ramsdellite and pyrolucite phases (Figure 1.3). The crystal lattice appears to have no regular periodicity or superstructure. Because of this random structure, the term  $\gamma\text{-MnO}_2$  refers to a family of crystal structures characterised as differing ramsdellite and pyrolucite concentrations, not a single structure [2].  $\gamma\text{-MnO}_2$  is a non-stoichiometric material that contains structural defects, cation vacancies,  $\text{Mn}^{3+}$  and structural water [17]. High-resolution transmission electron microscopy (HRTEM) studies on  $\gamma\text{-MnO}_2$  by Turner and Buseck [18] revealed that larger tunnels such as  $1 \times 3$ ,  $2 \times 2$ ,  $2 \times 3$  and todorokite-like  $3 \times 3$  and  $3 \times 4$  can occur in  $\gamma\text{-MnO}_2$  as well as much larger irregular tunnels, which may affect the battery activity of the material.

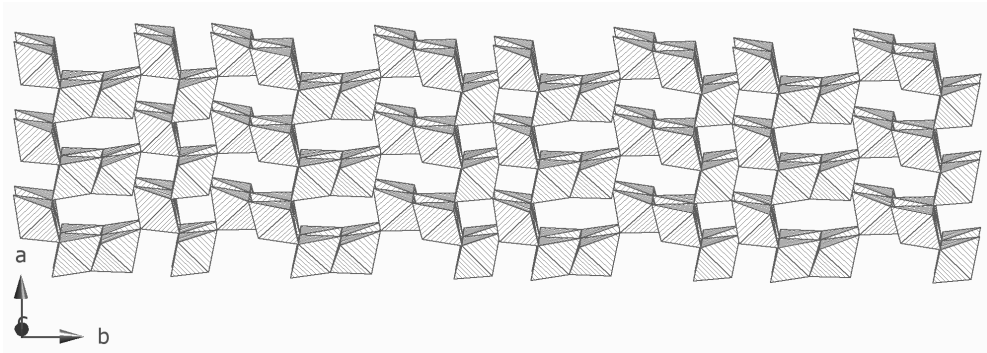


**Figure 1.3:** A representation of the crystal structure of  $\gamma$ - $\text{MnO}_2$ .

#### 1.1.1.4 $\epsilon$ - $\text{MnO}_2$

$\epsilon$ - $\text{MnO}_2$  is thought to occur naturally as the mineral akhtenskite, however there has been much debate over the legitimacy of  $\epsilon$ - $\text{MnO}_2$  as a unique  $\text{MnO}_2$  phase. Crystallographically,  $\epsilon$ - $\text{MnO}_2$  can be described as a defective NiAs type structure. This results in a hexagonal dense packed array of  $\text{O}^{2-}$  ions, with a purely statistical distribution of  $\text{Mn}^{4+}$  ions which are randomly distributed over 50% of the available octahedral sites, see Figure 1.4. The random distribution of  $\text{Mn}^{4+}$  has resulted in  $\epsilon$ - $\text{MnO}_2$  being described as totally disordered [14, 19]. Like  $\gamma$ - $\text{MnO}_2$ ,  $\epsilon$ - $\text{MnO}_2$  contains structural water, cation vacancies,  $\text{Mn}^{3+}$  ions, and structural defects, which is unsurprising as some authors have described  $\gamma$ - $\text{MnO}_2$  and  $\epsilon$ - $\text{MnO}_2$  as end members of a single structural family [7]. Formation of  $\epsilon$ - $\text{MnO}_2$  via electrolytic means is usually favoured by high current densities, and the presence of  $\text{Cl}^-$ ,  $\text{NO}_3^-$  or  $\text{ClO}_4^-$  in the electrolyte solution during electro-deposition.

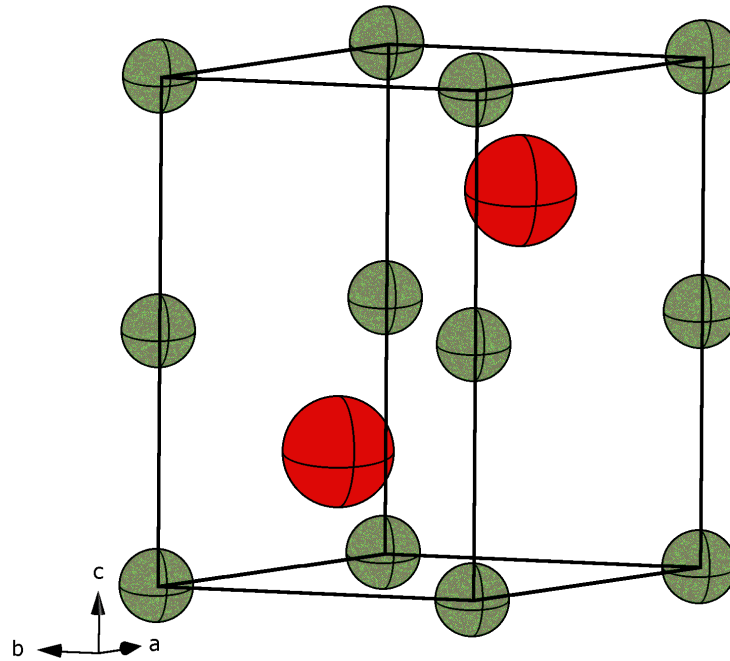


**Figure 1.4:** The NiAs structure of  $\epsilon$ -MnO<sub>2</sub>, the green spheres represent Mn atoms with 50% occupancy, the red spheres represent O atoms.

### 1.1.2 Spinel Structures

Spinel MnO<sub>2</sub> ( $\lambda$ -MnO<sub>2</sub>) structures (Figure 1.5) have a cubic closed packed oxygen substructure, where the manganese cations occupy the spinel octahedral sites [20]. These compounds are prepared by removing Li<sup>+</sup> from LiMn<sub>2</sub>O<sub>4</sub> [21], and have applications as lithium battery materials as they can reversibly intercalate Li<sup>+</sup> ions (Thackeray *et al.* [22], in Chabre and Pannetier [7]).

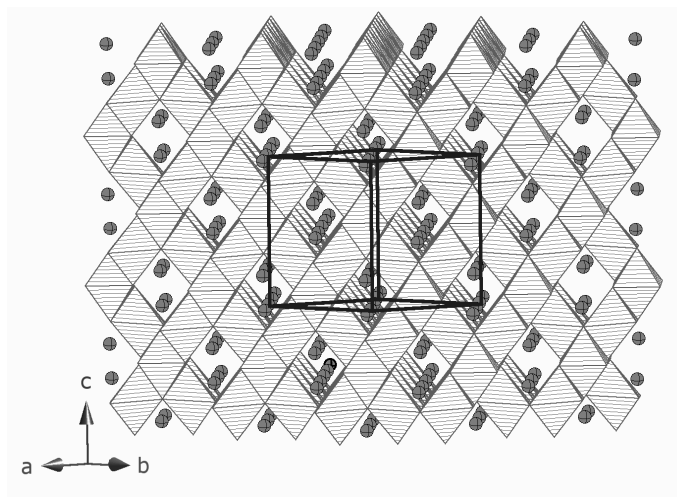


**Figure 1.5:** The crystal structure of  $\text{LiMn}_2\text{O}_4$  viewed along the  $ab$  axis, as an example of the structure of  $\lambda\text{-MnO}_2$ .

### 1.1.3 Tunnel Structures

$\text{MnO}_2$  tunnel structures are based on the structure of ramsdellite and related to the  $\alpha\text{-MnO}_2$  (the hollandite group) modification of  $\text{MnO}_2$  [2, 7, 9]. These compounds are found in Nature [5], but can also be produced via both electrochemical [23] and chemical [24] means. In these structures, even more rows of adjacent octahedral sites are occupied, which in turn leads to larger 3D-tunnels (Figure 1.6-Figure 1.8). In natural specimens, some of the  $\text{Mn}^{4+}$  is replaced by  $\text{Mn}^{3+}$ . This charge is balanced by cations such as  $\text{Ba}^{2+}$ ,  $\text{Pb}^{2+}$ ,  $\text{Li}^+$ ,  $\text{Na}^+$ ,  $\text{K}^+$ , and  $\text{NH}_4^+$ , which are located in the cavities/tunnels within these structures along with water molecules [2]. This leads to a variety of mineral species [5], dictated by the type of cation found in the cavities/tunnels [2]. For example hollandite, corondite, and cryptomelane all possess  $2 \times 2$  tunnel structures, but are characterised by their tunnels containing mainly  $\text{Ba}^{2+}$ ,  $\text{Pb}^{2+}$  and  $\text{K}^+$  respectively [25-27].

Turner and Buseck [28] developed a nomenclature that describes the tunnel structures of manganese dioxides. This system was based on the formula  $\mathbf{T}(\mathbf{m}, \mathbf{n})$ , where  $\mathbf{T}$  denotes a tunnel structure, and  $\mathbf{m}$  and  $\mathbf{n}$  denote the dimensions of the tunnels,  $\mathbf{m}$  is also the dimension that is the basis for the intergrowth. Table 1.1 shows various  $\text{MnO}_2$  structures described using this nomenclature.

**Table 1.1:** Various  $\text{MnO}_2$  structures described using the nomenclature developed by Turner and Buseck [28].

$\text{MnO}_2$ Structure	T(m,n) nomenclature
Pyrolucite	T(1,1)
Ramsdellite	T(1,2)
Hollandite	T(2,2)
Romanechite	T(2,3)
Hollandite – Romanechite family	T(2,n)
Todorokite	T(3,3)
Todorokite family	T(3,n)

This system can also be used to describe intergrowth structures such as  $\gamma\text{-MnO}_2$  and EMD, which are generally characterised as T(1,1)-T(1,2) intergrowths that may also contain T(1,3), T(1,4), T(2,1) and T(2,2) tunnel structures (Turner and Buseck [6], in Williams [2]).

As  $n$  increases these tunnel structures approach layer structures [28].

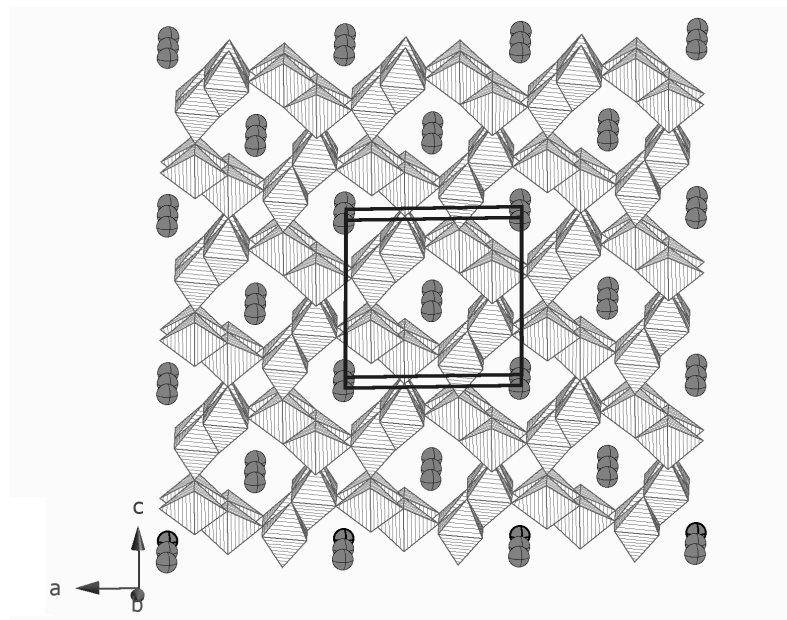


**Figure 1.6:** The typical crystal structure of 2x2 tunnel structures (hollandite, coronadite, cryptomelane, etc.) viewed along the  $b$  axis.

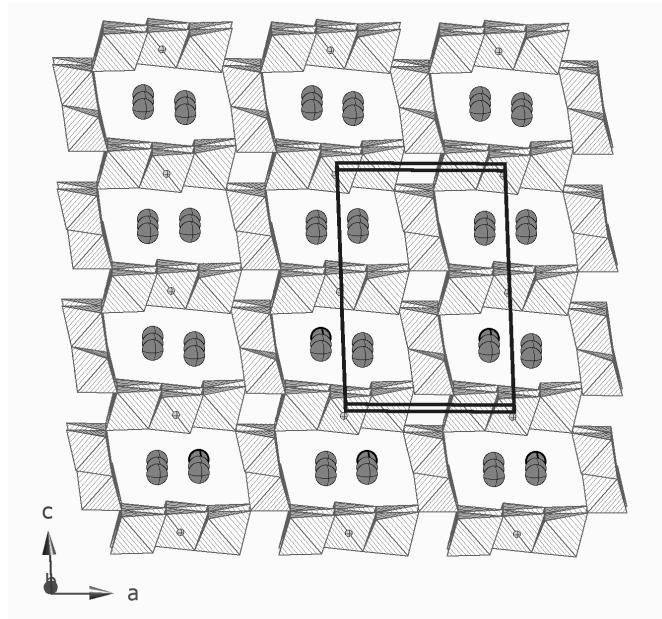


**Figure 1.7:** The typical crystal structure of 2x3 tunnel structures (romanechite) viewed along the  $b$  axis.

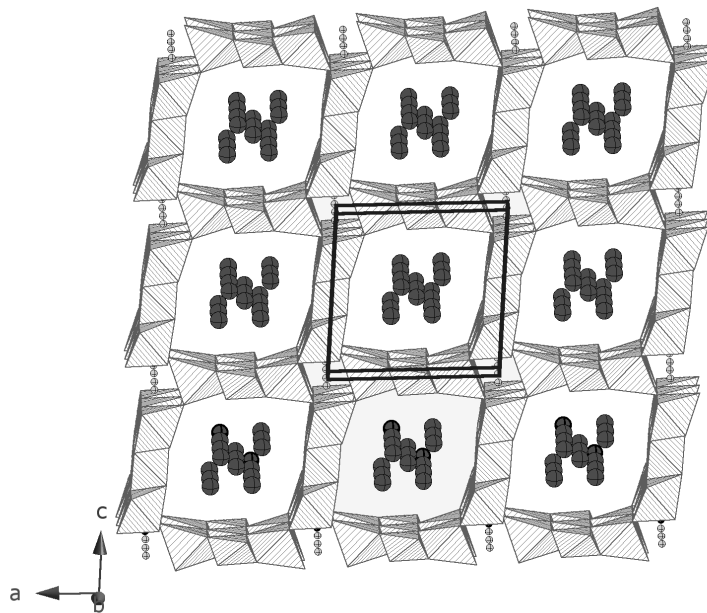


**Figure 1.8:** The typical crystal structure of 3x3 tunnel structures (todorokite) viewed along the  $b$  axis.

### 1.1.4 Layer Structures

In general, layer structured manganese dioxides consist of single layers of water and/or cations sandwiched between layers of edge shared Mn octahedra [9]. As a result structural strength is maintained by coordination and hydrogen bonding. Layered structure manganese oxides are known as manganese manganates, and can be split into two sub-groups; birnessites (the 7Å phyllo-manganates) and busserites (the 10Å phyllo-manganates) [2].

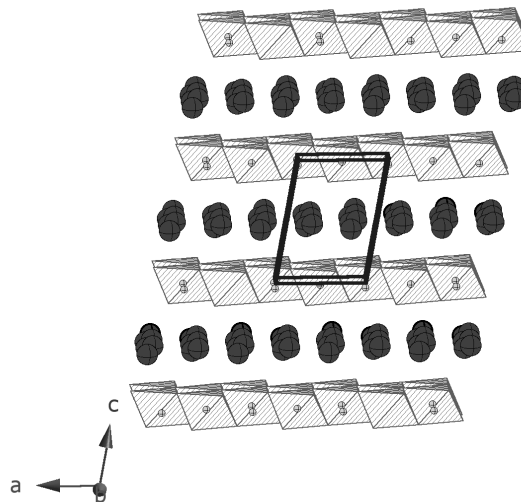


**Figure 1.9:** The typical crystal structure of layered  $\text{MnO}_2$  structures (birnessite) viewed along the  $b$  axis.

### 1.1.5 Reduced Forms of Manganese Oxides

This project has focused mainly on EMD and its defective structure, however for the sake of completeness this section will briefly describe some reduced forms of  $\text{MnO}_2$ . Although many manganese oxyhydroxides occur naturally, some also may form as the discharge products of EMD [7]. Table 1.2 shows the characteristics of some important manganese oxyhydroxides.

**Table 1.2:** The characteristics of some important manganese oxyhydroxides [2, 5, 7, 9, 10].

Name	Formula	Symmetry	
		(Space Group)	Comments
Manganite	$\gamma$ -MnOOH	Monoclinic (B2 <sub>1</sub> /d)	Formed by the reduction of pyrolucite.
Groutite	$\alpha$ -MnOOH	Orthorhombic (Pbnm)	Formed by the reduction of ramsdellite, and the dominant product of the reduction of $\gamma$ -MnO <sub>2</sub> .
—	$\delta$ -MnOOH	—	Believed to be an intergrowth of manganite and groutite lattices, and a product of the reduction of $\gamma$ -MnO <sub>2</sub> .
Feitknechte	$\beta$ -MnOOH	Hexagonal (P3m1)	—
Groutellite	Mn <sub>2</sub> O <sub>3</sub> OH	Orthorhombic (Pbnm)	Believed to be an intermediate phase between ramsdellite and groutite.
Pyrochroite	Mn(OH) <sub>2</sub>	Hexagonal (P3m1)	—

## 1.2 EMD

EMD is an industrially important form of manganese dioxide as it is an essential ingredient in modern alkaline cells and other batteries. The reasons for its popularity include (i) its low cost, (ii) its long shelf life and (iii) its stable performance over a wide temperature range [29]. In 2011 the world EMD market exceeded 349,000 mt and demand is projected to rise to nearly 608,000 mt in 2021. Future growth in the EMD market is expected to increase after 2015 due to the increased market penetration of electric vehicles [30].

Along with NMD (natural manganese dioxide) and CMD (chemical manganese dioxide), EMD is a member of the electrochemically active  $\gamma$ -MnO<sub>2</sub> family. Unlike the naturally occurring NMD and the chemically produced CMD, EMD is produced

via the high temperature electrolysis of aqueous  $\text{Mn}^{2+}$  solutions (see Equations 1.1-1.3 [31]). Due to its electrochemical superiority to other forms of  $\gamma\text{-MnO}_2$ , EMD is used as the primary constituent of cathodes in primary alkaline and button cell batteries [32-37].



EMD is a much-studied system, but despite this the structure of EMD is not well characterised and is thought to be highly disordered. The  $\gamma\text{-MnO}_2$  family is described as a continuum of structures, and there is no single compound, formula, structure or model that completely defines EMD. Its structure and properties vary with the electro-deposition conditions it was produced under, meaning that no two EMD samples produced at different times are identical. The structural complexity of EMD arises from the existence of a large number of defects in the crystal structure, and is further complicated by its extremely small crystallite size. While defects in the structure add a degree of difficulty to the production and study of EMD, they are the very essence of the material, and are responsible for the battery activity that sets EMD apart from other metallurgical and chemical grades of  $\text{MnO}_2$  [37].

### 1.2.1 Structural Defects in EMD

The EMD crystal structure is thought to be based on the ramsdellite structure and contain at least three types of defects:

- De Wolff defects
- Micro-twinning defects
- and, Point defects

It is the high concentration of defects in EMD that make structural characterisation so difficult.

### 1.2.1.1 De Wolff Defects

De Wolff defects are a stacking disorder, which occurs at the interface between ramsdellite and pyrolucite regions. De Wolff defects occur as a result of the replacement of some of the ramsdellite double chains of octahedra in the lattice by single octahedral, rutile-like chains. This type of defect was first postulated by Byström and Byström in 1950, but was further explained in 1959 by De Wolff and hence this form of disorder is usually referred to as De Wolff defects [7].

De Wolff investigated a number of  $\gamma$ -MnO<sub>2</sub> samples via XRD to characterise their crystal structure and observed large difference in the diffraction patterns between samples. He also observed that:

- The XRD patterns contained both sharp and broad peaks.
- Some patterns contained a few peaks that correspond to some pyrolucite peaks, over a diffuse background.
- Some patterns contained many more peaks that correspond to ramsdellite peaks.

Hendricks and Teller ([38] in [7]) had previously observed that peak shifts and broadening was common in materials whose structure could be explained using a random layer model. De Wolff used this information, and suggested that the XRD patterns of  $\gamma$ -MnO<sub>2</sub> could be explained by a layer model, that is a random intergrowth of pyrolucite layers in a ramsdellite matrix [note: “layer” in reference to  $\gamma$ -MnO<sub>2</sub>, refers to a sequence of two different basis slabs, not a lamellar MnO<sub>2</sub> structure such as birnessite.]. The incorporation of pyrolucite layers into the ramsdellite lattice does not affect the  $a$  and  $c$  unit cell dimensions (in the Pbnm setting), but shortens the  $b$  unit cell dimension. The  $b$  unit cell dimension can be calculated using Equation 1.4.

$$b' = 3/4b_r + 1/2c_r$$

**Equation 1.4**

Where  $b'$  is the  $b$  unit cell dimension for  $\gamma$ -MnO<sub>2</sub> and  $b_r$  and  $c_r$  are the corresponding unit cell dimensions for ramsdellite.

De Wolff was able to use the above model to describe the structure of three  $\gamma$ - $\text{MnO}_2$  materials from their XRD patterns. The presence of De Wolff defects however does not fully account for the features observed in XRD patterns of EMD [2, 7].

For clarity this study will define De Wolff defects as simply the interfaces between pyrolucite and ramsdellite domains within the EMD structure. Figure 1.10 shows a diagrammatic representation of De Wolff defects.

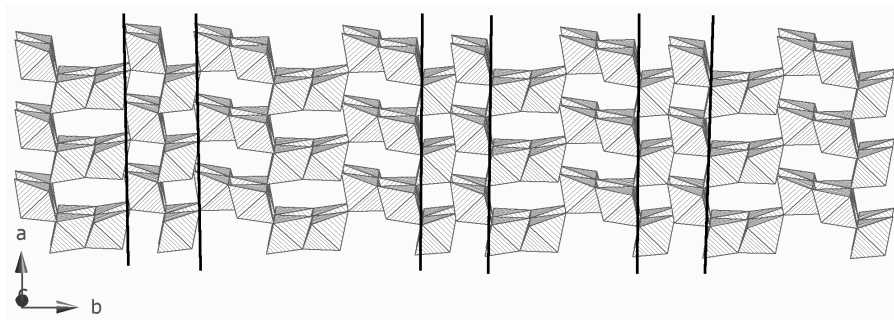


**Figure 1.10:** A diagrammatic representation of a De Wolff defect, approximate defect boundaries marked in black.

### 1.2.1.2 Micro-twinning

Micro-twinning corresponds to structural twinning which occurs on the (021) and (061) lattice planes of the ramsdellite structure [39, 40]. Micro-twinning has no effect on the anionic lattice of ramsdellite, but changes the cationic decoration within the octahedral voids of the anionic lattice, without changing the immediate octahedrally coordinated environment of a Mn atom. More simply, micro-twinning does not modify the oxygen sub-lattice, but corresponds to a change in distribution of  $\text{Mn}^{4+}$  vacancies within the anionic network. This change in distribution results in a rotation of the structure around the  $a$ -axis (depending on how the structure is indexed) by either  $\pm 60^\circ$  or  $\pm 120^\circ$ , resulting in 2D “kinking” of the structure, sometimes referred to as “geniculated or knee-shaped twins”. As the presence of De Wolff defects alone do not fully account for the observed XRD pattern of EMD, another kind of structural defect must be present. This is confirmed by the following observations:

- The merging of the h21/h40 peaks.

- The 110 peak is shifted to higher  $2\theta$  values by De Wolff defects, however many EMD samples exhibit a strong broad peak at lower  $2\theta$  values than those expected.
- Cell parameters obtained from peaks with even  $k/2+1$  values, depart from expected values, as the amount of De Wolff defects increases the  $b/2c$  ratio should decrease, yet experimental results give evidence that the  $b/2c$  ratio actually increases [2, 7].

Chabre and Pannetier [7] provided evidence of twinning in EMD by two independent observations:

- Firstly that the same “knee-shaped” twinning occurs in natural samples of rutile ( $\text{TiO}_2$ ) and cassiterite ( $\text{SnO}_2$ ), along the 011 and 031 lattice planes.
- And secondly that EMD often exhibits a fibrous texture; examination of the XRD of these samples showed that the axis of the fibres correspond to the 021 or 061 lattice planes.

This latter observation indicates that EMD crystallites grow perpendicular to these faces, and therefore that extended structural defects, if they exist, are likely to be located in these planes.

Bowden and co-workers provide further proof of the existence micro-twinning via electron diffraction, and TEM investigations of EMD samples [33, 34]. It should be noted however, that the existence of micro-twinning is disputed by some authors [41]. Figure 1.11 shows a diagrammatic representation of micro-twinning defects.

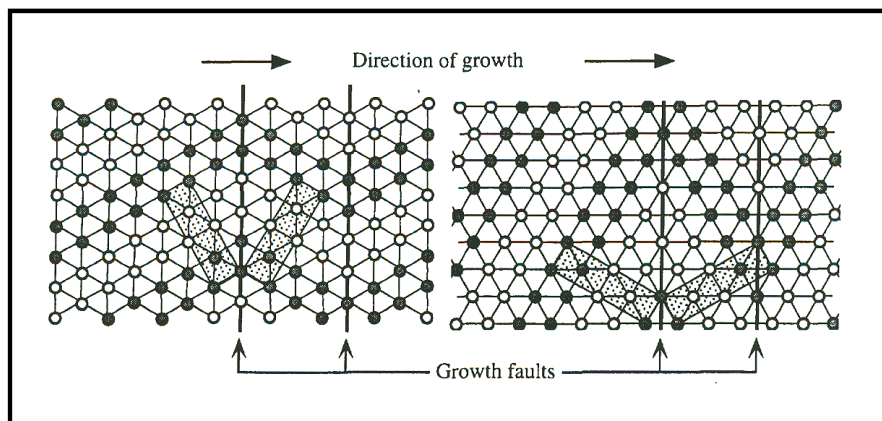
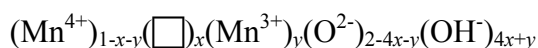


**Figure 1.11:** A diagrammatic representation of micro-twinning defects: micro-twinning on the 021 lattice plane (left), micro-twinning on the 061 lattice plane (right). Only Mn atoms are shown, full circles:  $\text{Mn}^{4+}$  at  $x=1/2$ , open circles  $\text{Mn}^{4+}$  at  $x=0$ , twin planes in bold, ramsdellite unit cell (**b**, **c**) shaded reproduced from [7].

### 1.2.1.3 Point Defects

Chemically, EMD is non-stoichiometric, and contains point defects such as cation vacancies and  $\text{Mn}^{3+}$ , as well as structural  $\text{H}_2\text{O}$  in its crystal lattice [2, 17, 42]. A large number of point defects are known to occur in EMD; these are important to the electrochemistry, but they are of lesser importance to structural characterisation [12]. Ruetschi developed a model for point defects in 1984; according to this model the crystal structure is composed of closely packed  $\text{O}^{2-}$  ions that form octahedra about  $\text{Mn}^{4+}$  ions, these  $[\text{MnO}_6]$  octahedra share edges and corners and contain Mn vacancies. These vacancies are coordinated to and electrostatically compensated by protons in the lattice that are present in the lattice in the form of  $\text{OH}^-$  ions which replace  $\text{O}^{2-}$  in the lattice, with no noticeable change in lattice parameters. This model helps explain many previously unexplained experimental observations, such as density, chemical composition (ie. water content), conductivity, electrochemical capacity, proton transfer rates, and electrode potential. Furthermore the electrochemical reactivity of EMD is shown to be a result of these cation vacancies [17]. The chemical composition of EMD is described in terms of the  $\gamma\text{-MnO}_2$  chemical formula is shown in Equation 1.5.



**Equation 1.5**

Where  $\square$  represents a cation vacancy, and  $x$  and  $y$  represent the mole fractions of cation vacancies and  $\text{Mn}^{3+}$  ions. Structural  $\text{H}_2\text{O}$  is present as the protons associated with the  $\text{O}^{2-}$  ions [7, 17, 42]. For typical EMD samples  $x$  values of 0.06-0.08, and  $y$  values of 0.04-0.12 are expected [2]. Figure 1.12 shows a diagrammatic representation of point defects.

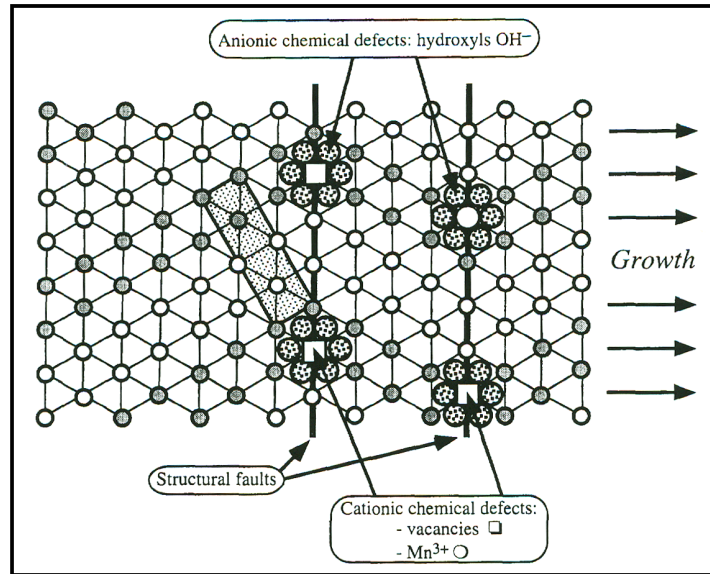


**Figure 1.12:** A diagrammatic representation of point defects in EMD. Only Mn atoms are shown, full circles:  $\text{Mn}^{4+}$  at  $x=1/2$ , open circles  $\text{Mn}^{4+}$  at  $x=0$ , twin planes in bold, ramsdellite unit cell (**b**, **c**) shaded reproduced from [7].

## 1.2.2 Structural Models of EMD

There has been much debate over the structure of EMD. Generally the EMD structure is thought to be either a single phase with a high degree of disorder [7, 34] or a mixture of multiple phases, that may contain a degree of disorder [41, 43].

### 1.2.2.1 Single Phase Models

Single phase models suggest that EMD consists of predominantly ramsdellite, with randomly dispersed regions of pyrolucite [44]. These models generally describe EMD as an ideal ramsdellite lattice containing two kinds of defects, De Wolff defects, and also micro-twinning defects, on the 021 and 061 lattice planes. Because

of the high concentration of defects in EMD, authors who believe EMD is a single phase have classified the structure as a disordered, random intergrowth of ramsdellite and pyrolucite, which contains extensive twinning. Hence EMD has been quantitatively characterised in the literature by defect concentrations, most importantly the pyrolucite concentration and the degree of micro-twinning that occurs within the ramsdellite matrix [7].

Chabre and Pannetier used the XRD simulation package DIFFaX and statistics to develop their defect model, which is an extension of De Wolff's original model. This model characterises  $\gamma$ -MnO<sub>2</sub> by the pyrolucite concentration ( $P_r$ ) and the percentage of twinning ( $T_w$ ) present in the structure. These values are derived from the peak positions of the sample. The Pannetier model relies on good quality experimental data, and a series of approximations and assumptions. These are as follows:

- That De Wolff disorder and micro-twinning are not correlated and their effects on the powder XRD pattern are additive.
- That the stacking of pyrolucite and ramsdellite layers is more or less random.
- That the cell parameters and atomic co-ordinates described by Byström in 1949 are an accurate representation of non-faulted ramsdellite, as all numerical calculations used by this model rely on these measurements.
- That the effect of various point defects and other additional effects such as the possible sample inhomogeneity are neglected.

The Pannetier model provides equations to calculate  $P_r$  and  $T_w$  values for four types of  $\gamma$ -MnO<sub>2</sub> materials (see [7] for more detail). Pannetier and co-workers classified EMD as a Type III material; that is, it contains a very large concentration of defects (greater than 60% micro-twinning), which reduces the XRD pattern to a few broad peaks due to the broadening and merging of peaks.  $P_r$  and  $T_w$  values for EMD can be calculated using Equations 1.6–1.9 [7].

Using CuK $\alpha$  radiation:

$$P_r = 0.602 \delta(\text{DW}) - 0.198 \delta^2(\text{DW}) + 0.026 \delta^3(\text{DW}) \quad \text{Equation 1.6}$$

where,

$$\delta(\text{DW}) = 2\theta(110)_{\text{exp}} - \delta(\text{Tw}) - 21.808 \text{ (in degrees } 2\theta) \quad \text{Equation 1.7}$$

where,

$$\delta(\text{Tw}) = -0.56^\circ \text{ as } Tw \geq 55\% \quad \text{Equation 1.8}$$

$$Tw(\%) = 100 - 25.20 \Delta 2\theta \quad \text{Equation 1.9}$$

Where  $\Delta 2\theta$  is the degree of splitting between the 002 and 061 peaks.

The Pannetier model predicts that EMD will have  $P_r$  values of  $\sim 0.45$  (which means  $\sim 30\%$  of manganese atoms will be located in pyrolucite positions) and  $Tw$  values of between 0 and 100% [2, 7].

In more recent EMD literature some authors [45-50] have chosen to represent micro-twinning via the term Mt, which is crudely  $Tw/2$ . The new model was conceived because it appears that a  $Tw$  value of 100% does not actually correspond to the maximum amount of twinning possible in a structure, however even though the Mt model is different to the  $Tw$  model it leads to similar simulations [45]. In the light of this and for the sake of continuity this study elected to use the more classical  $Tw$  term and calculation for micro-twinning.

Bowden and co-workers [34] performed convergent beam electron diffraction on EMD powders, their results showed parallel sheets of reciprocal lattice intensity (perpendicular to the  $c$ -axis in the 001 direction). These results were interpreted in terms of Guiniers 'linear disorder' model [51]. 'Linear disorder' can be described as a displacement of atomic positions from a periodic structure in all but one dimension, or aperiodic, one dimension defects in the atomic packing order [34, 52]. Bowden and co-workers used this approach to develop a model that can reproduce the XRD patterns of numerous EMD samples. Similar to the Pannetier model, the

Bowden *et al.* model considered EMD to consist of randomly oriented homogeneous ramsdellite crystallites, that are distorted by one-dimensional (chain or ribbon) pyrolucite defects, and are heavily twinned on multiple habit planes. An earlier study by Bowden and Hackney [33] interpreted the structure of EMD as a heterogeneous material, composed of a disordered ramsdellite component and a more highly twinned ramsdellite component, but this was reconsidered in their later structural model [34] as additional CBED and TEM investigation revealed that the apparent heterogeneity of the material was a result of random crystallite orientation. This model uses four input parameters to simulate XRD patterns of EMD [34]:

- Crystallite size (nm)
- Micro-twin spacing (nm)
- Fraction of linear pyrolucite defects
- and, Linear distortion ( $\text{\AA}$ )

The simulated XRD patterns produced by this model showed good fits to experimental EMD XRD patterns, and the results suggested that commercial EMD consists of ~85% ramsdellite (with extensive twinning), and ~15% pyrolucite. The Bowden *et al.*, model however, does not perform well for commercial CMD or HEMD (Heat-treated EMD) samples, as these samples are thought to contain discrete pyrolucite domains which are not accounted for by this model.

### 1.2.2.2 Multi-phase Models

Multi-phase models suggest EMD is a heterogenous mixture of  $\text{MnO}_2$  phases, usually ramsdellite,  $\gamma\text{-MnO}_2$ , pyrolucite and  $\varepsilon\text{-MnO}_2$ .

Simon and co-workers [43] used Rietveld refinement to explain the characteristics of a wide variety of EMD samples. The model postulates that EMD consists of a binary mixture of 40%  $\gamma\text{-MnO}_2$  and 60%  $\varepsilon\text{-MnO}_2$  phases (although some samples were also found to contain  $\beta\text{-MnO}_2$ ). These phases are said to occur with two different crystallite sizes, 18 - 50  $\text{\AA}$  for the  $\gamma\text{-MnO}_2$  phase and 50 - 85  $\text{\AA}$  for the  $\varepsilon\text{-MnO}_2$  phase, these crystallite sizes vary with the samples surface area. This model also calculated the  $Pr$  and  $Tw$  of the  $\gamma\text{-MnO}_2$  phase using Chabre and Pannetiers [7] equations, the results of which were consistent with past studies. In 2001, Simon and

co-workers revisited their work and concluded that  $\epsilon$ -MnO<sub>2</sub> was probably not a discrete phase in EMD, however in 2004 Simon, Morton, and Gislason revisited this work again and proposed that the  $\epsilon$ -MnO<sub>2</sub> structure seen in the EMD XRD patterns is not a discrete phase, but rather a result of long range structural disorder, and that EMD must be composed of either short range ordered  $\gamma$ -MnO<sub>2</sub> or long range disordered  $\epsilon$ -MnO<sub>2</sub> depending on your point of view [53].

Heuer and co-workers [41] used TEM and electron diffraction to study the structure of EMD. They reported structure at two length scales;  $\sim$ 10 nm single phase crystallites, and 0.1 – 0.3  $\mu$ m grained, most of which were multiphase. This study postulated that EMD consisted of  $\sim$ 50% ramsdellite, 30%  $\epsilon$ -MnO<sub>2</sub>, and 15% pyrolucite, they also found no evidence of microtwinning, and that ordering was prevalent in either the ramsdellite or  $\epsilon$ -MnO<sub>2</sub> phase, and suggested a model for a fully ordered form of  $\epsilon$ -MnO<sub>2</sub>. A study by Chang-hoon Kim and co-workers [54] confirms the multi-phase model of Heuer *et al.* [41], but also states that EMDs can be single-phase ordered  $\epsilon$ -MnO<sub>2</sub>, and questions the model of Chabre and Pannetier [7] and also the use of the term  $\gamma$ -MnO<sub>2</sub> for some EMD samples.

### 1.3 Literature on the Structure of EMD

EMD has been characterised by many techniques. The following overview covers the literature that reports on those characterisation techniques that relate to this study.

#### 1.3.1 XRD Studies

X-ray diffraction (XRD) and in particular powder XRD has generally been the technique of choice to characterise the crystal structure of EMD, because of its speed, convenience, and the quantities of sample required for analysis. Battery manufacturers and mine operators use XRD for quality control purposes, and the technique has and continues to perform an important role in fundamental studies of EMD [55].

EMDs are generally poor scatterers of X-ray energy, and are known to be highly defective/disordered structures that have no apparent periodicity or superstructure.

These factors, coupled with small crystallite size, result in a continuum of structure giving an infinite number of XRD patterns, and reduce the quality of EMD XRD patterns, which in turn complicates analysis [7, 9]. De Wolff defects and microtwinning also displace and broaden peaks by a magnitude which is dependent on the values of %Pr and %Tw. This means that peak positions cannot be used to directly calculate the average unit-cell size [40]. This also applies to average crystallite size calculations [7].

Figure 1.13 shows a typical EMD powder XRD pattern. EMD produced for use in batteries usually exhibits a pattern consisting of five major peaks: a broad peak at  $\sim 22.2^\circ$   $2\theta$ ; three sharper major peaks at  $\sim 37.2^\circ$ ,  $42.5^\circ$ , and  $56.2^\circ$ ; and a minor peak at  $\sim 40.5^\circ$   $2\theta$ ; all over a diffuse background, also see Table 1.3 for peak positions [2, 55].

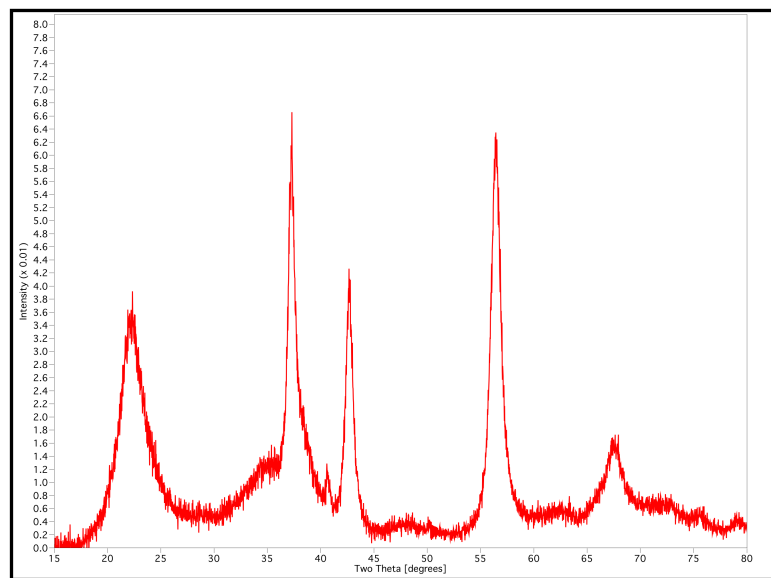


**Figure 1.13:** A Typical EMD powder XRD pattern (IBA 30).

**Table 1.3:** The approximate positions of the XRD peaks of EMD.

[hkl]	2 $\theta$ (Cu K $\alpha$ )	D-Spacing (Å)
110	22.0	4.00
021	37.2	2.42
121	42.5	2.12
221	56.3	1.63
061	67.3	1.38

**Note:** [hkl] values above are based on the ramsdellite structure in the *Pbnm* setting, EMD samples are often indexed using this system.

The XRD pattern produced by the continuum of EMD structures can be categorised according to several different criteria, but three that are most useful are:

- Structural order.
- Composition.
- Defect concentration.

Structural order is interpreted using the intensity and sharpness of the XRD peaks, generally sharper, more defined peaks indicate increased structural order. Figure 1.14 shows a comparison of lower and higher order EMD samples. Higher order samples show increased structure at 22.2, 34.6, 38.6, 47.8, 62.8, 65.5, 68.6, and 70.3° 2 $\theta$ , which roughly corresponds to peaks found in the ramsdellite pattern. Lower order samples show much more diffuse peaks in these regions, in fact several of the above mentioned peaks are almost totally absent in lower order samples [55].

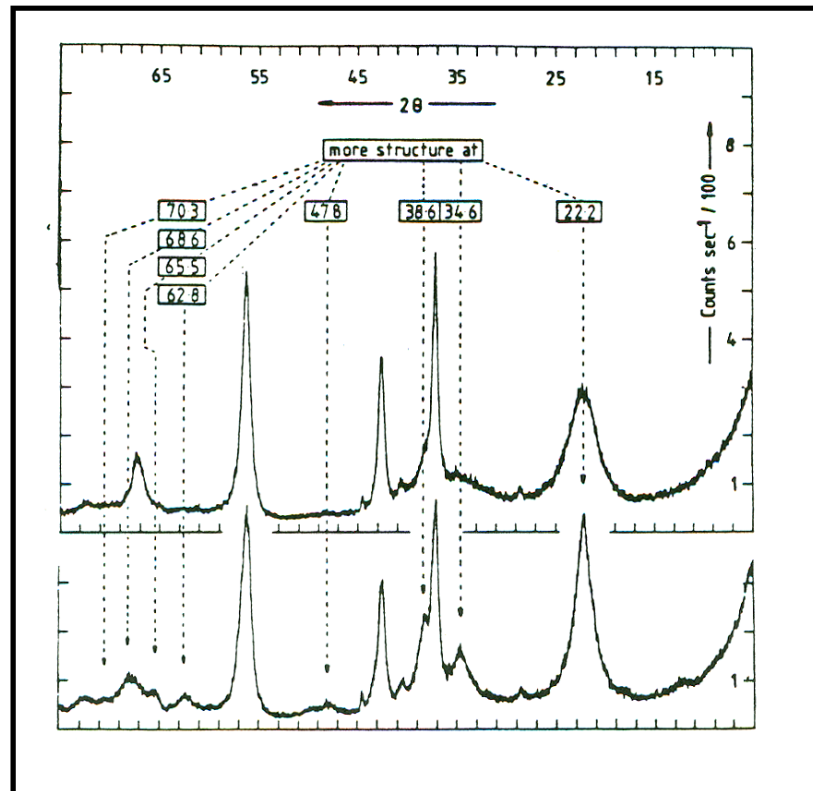


**Figure 1.14:** A comparison of lower (top pattern) and higher (bottom pattern) order EMD samples XRD patterns reproduced from [55].

In terms of composition, EMD samples are usually categorised via the phases present in the sample. Generally the phases of most interest are pyrolucite, ramsdellite, and impurities such as graphite. A high pyrolucite content is indicated by the presence of peaks in the region of  $28^\circ$   $2\theta$ , a sharp peak at  $28.7^\circ$   $2\theta$  indicates the presence of crystalline pyrolucite which is said to reduce the performance of EMD in batteries, although information on the effect of pyrolucite is scarce [55].

Correctly indexing EMD XRD patterns is a difficult task, and there is some ambiguity in the literature as to whether the patterns should be indexed according to an orthorhombic unit cell or a hexagonal unit [2]. Higher order EMD tends to exhibit patterns that have similarities to ramsdellite XRD patterns and hence have been indexed using the orthorhombic system. Whereas lower order, highly disordered / highly twinned EMD indexes well to the hexagonal system (with the exception of the peak at  $\sim 4.0$  Å, which is thought to be due to the avoidance of face sharing  $[\text{MnO}_6]$  octahedra, creating ordering within the lattice) [2]. Ripert *et al.* postulate that this

apparent hexagonal symmetry is a result of the orthorhombic peaks smearing and merging together to form a pattern that does not differ significantly to a hexagonal pattern [40]. This project will investigate both indexing systems, however for clarity EMD XRD patterns will generally be indexed according to an orthorhombic unit cell, using [hkl] coordinates based on the ramsdellite unit cell in a *Pbnm* setting.

### 1.3.1.1 Analytical Parameters of EMD Calculated from XRD Data

Over the years many authors have attempted to derive meaningful analytical parameters from XRD data with varying degrees of success. The five most accepted analytical parameters derived from XRD patterns of EMD are briefly described below:

#### – The Preisler Q-value:

The Preisler Q-value is the ratio of baseline corrected peak heights of the peaks at approximately  $22^\circ 2\theta$  and  $37.2^\circ 2\theta$  respectively. Q-values can vary between 1.5 for  $\gamma$ -MnO<sub>2</sub> and 0.35 for  $\epsilon$ -MnO<sub>2</sub>, generally higher Q-values are associated with materials that are predominately  $\gamma$ -MnO<sub>2</sub>, while lower Q-values are associated with materials that are predominately  $\epsilon$ -MnO<sub>2</sub> [2]. Q-values have been observed to increase with increasing bath temperature and Mn<sup>2+</sup> concentration [37], and decrease with increases in current density and BET surface area [2].

#### – The IPM Number:

The IPM number (named after its founder I. Paul Mail), is the ratio of the baseline corrected peak heights of the peaks at  $2\theta = 37.2^\circ$  and  $42.5^\circ$  respectively, and has been used by both the Eveready battery company and Energiser to characterise EMD quality from XRD patterns. Due to a lack of any strong correlation between the IPM number and EMD properties, the IPM number has been given little attention in literature [2, 37].

#### – The H<sub>1</sub>/H<sub>2</sub> Ratio:

The H<sub>1</sub>/H<sub>2</sub> ratio is the ratio of the baseline corrected peak heights of the peaks at  $2\theta = 22.0^\circ$  and  $42.5^\circ$  respectively. This ratio is used by the Mitsui EMD Company to

characterise the EMD they produce. There has been little discussion of this ratio in literature, although EMD quality is considered to improve as this ratio increases [2].

– **Position of the 110 XRD Peak:**

The position of the 110 EMD XRD peak, gives an estimate of the degree of De Wolff disorder and microtwinning in the EMD crystal structure [37]. These values can be calculated using equations postulated by Chabre and Pannetier [7].

– **Peak Width at Half Height and Average Crystallite Size:**

Several authors (Anderson [56] in Williams [2], Preisler [57]) have observed that the intensity and sharpness of the 110 peak in the EMD XRD pattern changes with deposition conditions. Broadening of this peak gives a quantitative estimate of increasing structural disorder as a result of decreasing crystal size. The average crystallite size can be calculated using the Scherrer equation, see Equation 1.10.

$$t = 0.9\lambda / \Delta\theta\cos\theta$$

**Equation 1.10**

The average crystallite size is important as it influences conductivity, proton diffusion and other important factors in optimising battery performance. Increases in average crystallite size have been related to increases in discharge capacity [2, 37, 58].

#### **1.4 Production of EMD**

As previously mentioned, EMD is essentially  $\gamma$ -MnO<sub>2</sub>, produced via the electrolysis of hot acidic (H<sub>2</sub>SO<sub>4</sub>) MnSO<sub>4</sub> solutions. Using this method EMD can be produced from a wide range of electro-deposition conditions (see Table 1.4). Despite this the conditions required to produce EMD with optimum electrochemical performance are very specific [42].

**Table 1.4:** The ranges of electro-deposition conditions that produce EMD [42].

<b>Variable</b>	<b>Range</b>
Temperature (°C)	85-99
Anodic Current Density (A/m <sup>2</sup> )	10-100
[MnSO <sub>4</sub> ]	Very dilute up to saturated
[H <sub>2</sub> SO <sub>4</sub> ]	Very dilute up to ~5M

This has resulted in numerous investigations into the effects of various electro-deposition conditions, including the effect of electrode composition, additives, and non-standard electrolytes. This section provides a brief overview of these studies, as well as a description of how EMD is produced in an industrial setting.

#### 1.4.1 Industrial Processes

The EMD production process from ore to final product is briefly described below [59] and shown in Figure 1.15:

1. MnSO<sub>4</sub> (aq) solution is prepared by either dissolving MnO (obtained by the thermal decomposition of natural Mn ores at 1000°C in the presence of a reducing agent), or rhodocrosite (MnCO<sub>3</sub>) in H<sub>2</sub>SO<sub>4</sub>, or performing a reduction leach on the Mn ore using SO<sub>2</sub> [60].
2. The solution is then separated from insolubles.
3. Heavy metals are then precipitated as sulfides, which are allowed to settle out.
4. The solution is then further purified by increasing the pH and air oxidization. This removes iron and other metallic impurities (converts them to insoluble hydroxides), which are removed by filtration.
5. The purified solution is then electrolysed; the EMD collects at the anode as a hard lava-like layer (greyish black in colour).
6. The raw EMD is then removed from the electrode, air dried, and ground in a stone mill (metal cannot be used in the milling stage because of the H<sub>2</sub>SO<sub>4</sub> retained in the EMD).
7. The ground EMD is then subject to 10 washing operations, with the 9<sup>th</sup> wash containing BaCl<sub>2</sub> to precipitate any remaining sulphate, and the 10<sup>th</sup> wash

containing a neutralizing agent (usually ZnO, but Na<sub>2</sub>CO<sub>3</sub> and ammonia are also used), to neutralize any remaining acid.

8. The EMD is then dried, graded and packaged for distribution.

Step 5 is the key step in producing battery grade EMD, as in order to produce high quality EMD, the composition of the electrolyte and the electroplating conditions must be carefully controlled [59, 61]. Typically the EMD is deposited onto titanium anodes at current densities of between 55 and 75 A/m<sup>2</sup>, using graphite cathodes. The solution electrolysed is purified acidic MnSO<sub>4</sub> (with a Mn/acid ratio of approximately 2) at a temperature in excess of 95 °C. The duration of the deposition process is ~2 weeks, during which time a ~10 mm thick layer of EMD is deposited onto the titanium anodes. These conditions produce EMD with a crystal structure that provides the best compromise between electrochemical and physical properties of the product [61]. For commercial reasons, producers of EMD usually keep information about their exact processes, and optimal deposition conditions, well guarded.

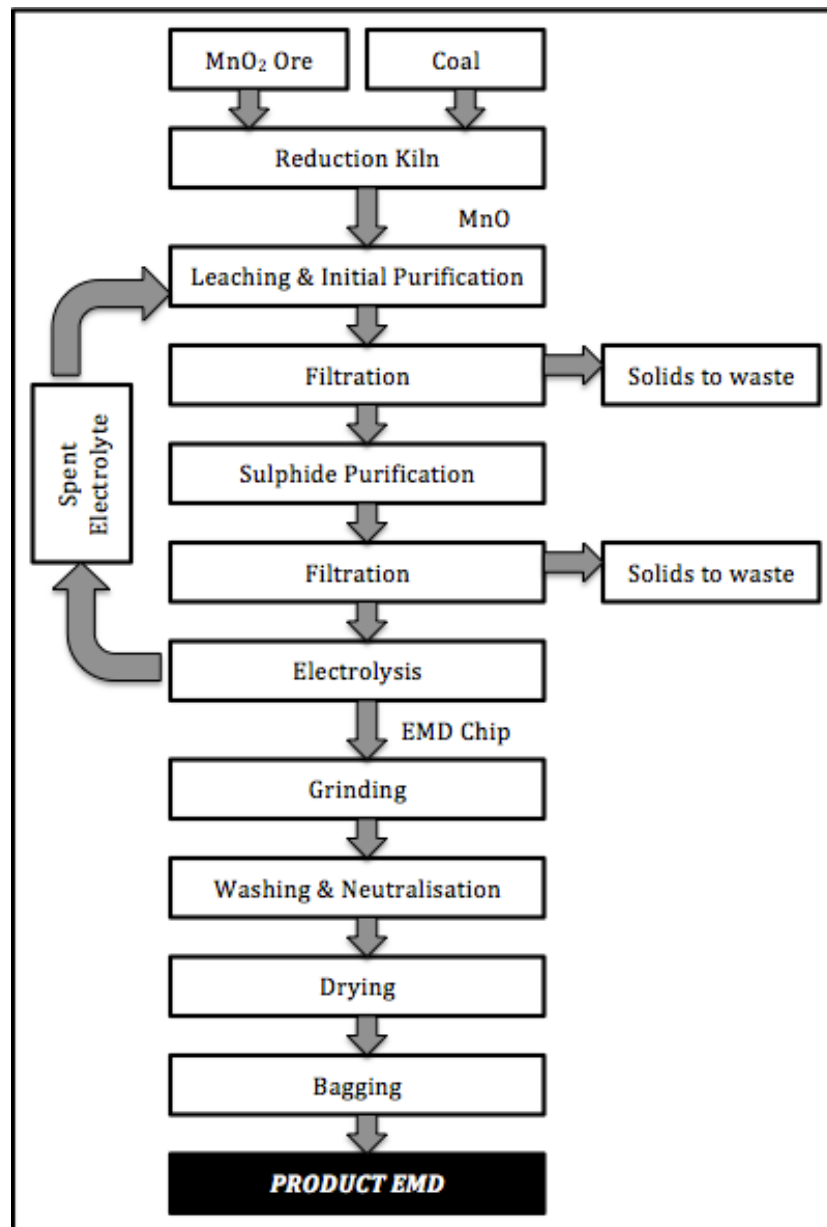


**Figure 1.15:** Basic process flow chart for the production of EMD. Redrawn from [61].

#### 1.4.2 Electro-deposition Conditions / Electrode Composition

Although the actual conditions for the production are closely guarded Table 1.5 shows the general conditions and electrodes used for the industrial production of EMD [62]

**Table 1.5:** Electro-deposition conditions and electrode compositions used in the production of EMD. Adapted from [62].

<b>Anodes</b>	Pure lead, Antimonial lead	Graphite	Titanium
<b>Cathodes</b>	Antimonial lead	Graphite, Copper, Steel	Graphite, Lead, Copper, Steel
<b>Anodic Current (A dm<sup>-2</sup>)</b>	0.5 – 1.2	0.7 – 1.0	0.7 – 1.0
<b>Electrolyte</b>			
<b>MnSO<sub>4</sub> (mol L<sup>-1</sup>)</b>	0.5 – 1.0	0.5 – 1.0	0.1 – 0.4
<b>H<sub>2</sub>SO<sub>4</sub> (mol L<sup>-1</sup>)</b>	0.5 – 1.0	0.5 – 1.0	0.1 – 0.4
<b>Temperature (°C)</b>	90 - 95	90 - 95	90 - 95

Literature regarding the various effects of EMD deposition conditions will be discussed in Chapter 4.

Electrodes for use in the industrial production of EMD should have the following properties [62]:

1. Low corrosion rates (even at high temperatures).
2. Low deposition potential.
3. No passivation.
4. Good mechanical strength.
5. Will not contaminate the EMD.
6. Allow repeated use.
7. Good deposit adherence.
8. Ease of deposit recovery.
9. Low costs.

Typical materials used in industry are titanium anodes, and graphite cathodes [2, 61]. For this study, however, to limit any deposit interaction with the electrodes, platinum electrodes were used.

### 1.4.3 Electrolyte Additives

Over the years there have been many studies that have investigated the effect of electrolyte bath additives on the structure of EMD and its electrochemistry, in order to improve the performance of the finished product, reduce production costs or increase production efficiency. In general, previously studied electrolyte additives can be categorized into two broad groups, soluble (quaternary amines,  $\text{H}_3\text{PO}_4$ ,  $\text{K}^+$  and other cations), and insoluble ( $\beta\text{-MnO}_2$ ,  $\alpha\text{-Mn}_2\text{O}_3$ ,  $\text{Al}_2\text{O}_3$  and acetylene black).

#### 1.4.3.1 Soluble

Yamaguchi found that EMD deposited in the presence of  $\text{H}_3\text{PO}_4$  ( $< 0.1$  M), showed an increase in BET surface area and  $\text{H}_2\text{O}$  content. It was also reported that the  $\text{PO}_4^{3-}$  was preferentially incorporated over  $\text{SO}_4^{2-}$ , with the suggestion that the EMD (named P - EMD) produced was superior to conventional EMD for use in Li –  $\text{MnO}_2$  primary cells [2].

Kao *et al.*, studied the influence of potassium ( $\text{K}^+$ ) ions on the electro-deposition and electrochemistry of EMD in conventional sulphate solutions. This study found that  $\text{K}^+$  was incorporated in the lattice structure. This incorporation was increased with increased  $\text{K}^+$  concentration at constant  $\text{H}_2\text{SO}_4$  concentrations, and decreased with higher  $\text{H}_2\text{SO}_4$  concentration and higher current densities. XRD analysis of these samples showed that increasing the  $\text{K}^+$  concentration in the EMD resulted in the formation of  $\alpha\text{-MnO}_2$ , which was shown to be detrimental to battery activity [23].

Studies have also been conducted on the influence of sodium, ammonium, calcium, vanadium, bismuth, lead and titanium, by mixing the EMD with suitable oxides, by co-precipitation or by impregnation / precipitation using aqueous solution of the ions [63, 64]. Machefaux *et al.* have also investigated the effect of various metal ions (Al, Co, Ni and Li) in the preparation of nanowires of metal substituted manganese dioxides [49].

Probably of most interest to this study was the work of Biswal *et al.* on the effect of quaternary amines on the electrodeposition of manganese dioxide, which showed that the presence of quaternary amine salts during the deposition process may have potential for battery applications. They reported that the presence of these additives during deposition resulted in; increased current efficiency; decreased energy consumption during the deposition process; and enhanced the electrochemical properties of EMD produced [65].

#### 1.4.3.2 Insoluble

Several studies such as those of Preisler [57], Matsuki *et al.* ([66] in [2]), have investigated the influence of insoluble additives in suspension on EMD deposition and performance.

Preisler investigated EMD,  $\beta$ -MnO<sub>2</sub>,  $\alpha$ -Mn<sub>2</sub>O<sub>3</sub>, Al<sub>2</sub>O<sub>3</sub> and MnO<sub>1.7</sub>.xH<sub>2</sub>O suspensions. The EMD produced via the suspension method was termed REMD and was appear to have a roughened surface that contained no visible cracks, unlike regular EMD, however the REMD did contain macropores in the range of hundreds of micrometers. All the insoluble additives tested except for Al<sub>2</sub>O<sub>3</sub> produced REMD, which had a much lower surface area and combined water content than conventional EMD with XRD patterns similar to those of conventional EMD deposited at a low current density [2]

Matsuki *et al.*, investigated EMD deposited from solutions containing dispersions of acetylene black. The material deposited was shown to have increased crystallinity and decreased BET surface area. The product was also said to be easier to grind and give excellent discharge performance, while not passivating the electrode during deposition [2].

There have been many studies using suspensions of manganese oxide, multivalent solids, or neutral particles, that have produced good quality EMD, however this technique has not been adopted commercially as yet [63].

#### 1.4.4 Non-Standard Electrolytes

Commercially EMD is generally only produced using sulfate electrolytes, however there have been several studies that have investigated effects on EMD electrolysed from nitrate and chloride electrolyte baths [67].

##### 1.4.4.1 NO<sub>3</sub><sup>-</sup> Electrolytes

It has been shown by various authors that EMD can be obtained from nitrate solutions. The reported advantages and disadvantages of an NO<sub>3</sub><sup>-</sup> electrolyte are listed below [67]:

- **Advantages:**

1. The electrolyte is highly conductive.
2. High solubility (>1000 gL<sup>-1</sup>).
3. A reduction in electrical energy consumption.

- **Disadvantages:**

1. High cost.
2. The NO<sub>3</sub><sup>-</sup> ion is reduced at the cathode to form nitrogen oxides (NO<sub>x</sub>), this makes the process noncyclic, unless the oxides formed are totally converted back to acid.

EMD deposition from NO<sub>3</sub><sup>-</sup> electrolyte baths results in a high anode current efficiency being achieved with a very low cell voltage, it was also reported that orientation of crystal growth of the EMD deposited differs from that of conventional EMD ([68] in [63])

EMD deposited at -30 °C from 3 - 3.3 M Mn(NO<sub>3</sub>)<sub>2</sub> solutions onto Pt plated, Ti anodes using current densities of 10 - 20 A/m<sup>2</sup> was found to have better rechargeability than ICS 2 ([69] in [2]). It should be noted, however, that these conditions are far removed from industrial standards.

#### 1.4.4.2 Cl<sup>-</sup> Electrolytes

Chloride electrolytes were reported by Prabhakar and Visvanathan to be the next best alternative to SO<sub>4</sub><sup>2-</sup> electrolytes because of numerous advantages [63].

- **Advantages:**

1. High conductivity.
2. High solubility.
3. Utilization of a cheaper by-product ie. HCl from chlor-alkali/PVC industries (probably not applicable in Australia)
4. Produces a superior quality, more active EMD, with better chemical, physical, catalytic and electrochemical properties.
5. Higher leaching efficiency
6. Less salt crystallization during deposition.
7. Easier washing of the EMD, due to the absence of entrapped SO<sub>4</sub><sup>2-</sup>.
8. Consumption of graphite anodes is reduced, resulting in higher purity and longer anode life.

Studies have shown that solutions of 1 M MnCl<sub>2</sub> and 0.35 - 0.75M HCl produces  $\gamma$ -EMD when electrolysed using graphite or Ti anodes at temperatures of either 80 or 96 °C. The optimum current densities were determined to be 10 - 18 A/dm<sup>2</sup> depending on the anode used ([70, 71] in [63]). Lab-scale experiments using Cl<sup>-</sup> electrolytes produced fibrous EMD or FEMD. FEMD was found to have improved physical properties, and superior discharge characteristics [72]. It was also reported that EMD produced with higher concentrations of HCl exhibit superior electrochemical activity ([71, 73] in [63]).

According to Rethinajar, many of the relationships between deposition conditions and EMD properties observed in the SO<sub>4</sub><sup>2-</sup> system, also exist in the Cl<sup>-</sup> system. The exception to this observation was that an increase in HCl concentration resulted in a decrease in surface area, whereas an increase in H<sub>2</sub>SO<sub>4</sub> resulted in an increase in BET surface area ([74] in [2]).

#### 1.4.4.3 Effect of Anion Charge

Preisler noted that electrolytes containing singly charged anions produced EMD with a significantly preferred orientation (FEMD). This material was designated  $\gamma$ -EMD via XRD ([75] in [2]). Preisler also observed that  $\text{SO}_4^{2-}$  was more significantly incorporated into the EMD structure during electrolysis than singly charged anions. From this he postulated that  $\text{X}^{2-}$  anions are more strongly bound to EMD than  $\text{X}^-$  anions, and therefore the resulting adsorption of  $\text{X}^{2-}$  anions onto the fastest growing crystal faces effectively stops crystal growth. As  $\text{X}^-$  anions are less strongly adsorbed they do not significantly inhibit crystal growth, resulting in the formation of FEMD ([76] in [2]).

#### 1.4.5 Deposition Mechanism

The overall reaction for the electro-deposition of EMD can be simply described by equations 1.1 – 1.3, however these equations do not reflect the complexity of the actual EMD deposition mechanism [42]. Over the years there have been many studies conducted to elucidate the true deposition mechanism of EMD, unfortunately the distinguishing feature of research on the EMD deposition mechanism is the contradictory nature of the results obtained by various authors. Below are brief descriptions of possible deposition mechanisms proposed by various authors.

During the 1950s the electrochemical oxidation of  $\text{Mn}^{2+}$ , in dilute  $\text{H}_2\text{SO}_4$ , to EMD was thought to occur via a mediated oxidation process, involving hydroxyl and persulphate ions. The mediated oxidation mechanism was later dismissed, because the thermodynamic potentials required for the formation of the mediator ions were greater than that of  $\text{Mn}^{2+}$  oxidation to  $\text{MnO}_2$  [77]. However, in 1954 Zaretskii *et al.* proposed a direct oxidation of  $\text{Mn}^{2+}$  to  $\text{Mn}^{3+}$  or  $\text{Mn}^{4+}$ . The  $\text{Mn}^{3+}$  then underwent a disproportionation reaction to produce  $\text{Mn}^{2+}$  and  $\text{Mn}^{4+}$ , which was then hydrolysed to form  $\text{MnO}_2$  ([78] in [77]).

Fleischmann [79] studied EMD deposition, using a constant potential method, depositing EMD from  $\text{MnSO}_4/\text{H}_2\text{SO}_4$  solutions onto platinum electrodes. Fleischmann observed that the EMD is deposited at discrete growth centres and oxide nuclei grow in three dimensions, and postulated a deposition mechanism that

firstly sees surface absorbed Mn(II) oxidised to either  $[\text{Mn}(\text{H}_2\text{O})_n]^{3+}$  or  $[\text{Mn}(\text{H}_2\text{O})_n]^{4+}$  species, these can be considered as intermediates. A multi-step dissociation of the absorbed Mn(IV) hydroxide species was then suggested to occur, followed by the dehydration of adsorbed  $\text{Mn}^{4+}$  ion to  $\text{MnO}_2$ . This dehydration reaction was found to be the rate-determining step of the mechanism.

During the 1980's Cartwright and Paul [80-82] published a series of papers that investigated the EMD deposition mechanism. Using a constant potential method, EMD was deposited onto a rotating vitreous-carbon electrode, and the deposition mechanism probed via current vs time transient analysis, electrode impedance studies, rotating ring-disc studies, and examination of the effect of the ferrous – ferric redox couple. As a result of these studies Cartwright and Paul proposed two possible mechanisms, (shown in Equations 1.11 – 1.18 below).

#### Mechanism A:



#### Mechanism B:



In the mid 1980s Preisler ([76] in [2]) proposed an electro-deposition mechanism based on the mechanism proposed by Fleischmann *et al.* [79]. This mechanism allowed for the possibility of both the incorporation of Mn(III) into the lattice and cation vacancies. This mechanism postulated that there are a number of species that can be incorporated into the EMD lattice as it grows, such as  $\text{MnO}_2$ ,  $\text{MnOOH}$ , as well as other species such as  $\text{MnO}(\text{OH})_2$  and  $\text{H}_2\text{O}$  that create cation vacancies in the

lattice. This mechanism takes into account the non-stoichiometric nature of EMD deposits.

Cyclic voltammetry (CV), in conjunction with other electrochemical techniques, has been used extensively to study the electro-deposition mechanism of EMD. In 1992, Kao and Weibel [77] studied the electrochemical oxidation of  $\text{Mn}^{2+}$  to  $\text{MnO}_2$  in  $\text{H}_2\text{SO}_4$  onto stationary and rotating platinum/platinum ring-disc electrodes using a combination of CV and chronoamperometry. They concluded that EMD deposition is initiated by the oxidation of  $\text{Mn}^{2+}$  to  $\text{Mn}^{3+}$  followed by the disproportionation of  $\text{Mn}^{3+}$  to form  $\text{MnO}_2$  nuclei, however they did not confirm the identity of the  $\text{Mn}^{3+}$  intermediate formed. They also concluded that growth of EMD occurs via a *ce* mechanism where  $\text{Mn}^{2+}$  in solution reduces surface  $\text{MnO}_2$  to form  $\text{MnOOH}$  intermediates which are then oxidised to  $\text{MnO}_2$  by releasing a  $\text{H}^+$  ion. When the concentration of  $\text{Mn}^{2+}$  in solution is adequate, a layer of  $\text{MnOOH}$  is built up and the rate-determining step is the in-solid diffusion of  $\text{H}^+$  ions, while at low concentrations of  $\text{Mn}^{2+}$ , the factor controlling crystal growth is the diffusion of  $\text{Mn}^{2+}$  from the bulk electrolyte to the  $\text{MnO}_2$ /electrolyte interface.

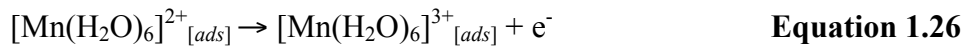
In 1998 Rodrigues and co-workers [36] studied the kinetics and mechanism of the electro-deposition of EMD from sulphate solutions onto platinum electrodes at  $80^\circ\text{C}$ , using CV. They postulated that the deposition of EMD involved the diffusion of  $\text{Mn}^{2+}$  ions to the electrode surface, then the oxidation of  $\text{Mn}^{2+}_{[\text{surface}]}$  to  $\text{Mn}^{3+}_{[\text{ads}]}$  along with  $\text{H}_2\text{O}$  to  $\text{OH}_{[\text{ads}]}$ . The adsorbed  $\text{Mn}^{3+}$  then undergo a disproportionation reaction at the electrode surface to  $\text{Mn}^{2+}_{[\text{ads}]}$  and  $\text{Mn}^{4+}_{[\text{ads}]}$ . These ions then react with  $\text{OH}_{[\text{ads}]}$  and  $\text{H}_2\text{O}$  respectively to form  $\text{MnO}_2$  (see Equations 1.19 – 1.24).



Nijjer and co-workers [83] investigated the electro-deposition of MnO<sub>2</sub> in sulphate solution onto platinum electrode using CV, as a function of Mn<sup>2+</sup> concentration, H<sub>2</sub>SO<sub>4</sub> concentration, scan rate, temperature, and convection. Similarly to Petitpierre *et al.* [84], they postulated that the EMD deposition mechanism from Mn<sup>2+</sup> to MnO<sub>2</sub> was an ECE sequence with the formation of an insulating intermediate (MnOOH).

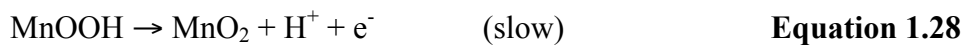
Clarke *et al.*[42] used a combination of rotating disk electrode (RDE) and rotating ring-disk electrode (RRDE) voltammetry to examine the EMD electrodeposition mechanism. They concluded that the deposition process revolves around the formation of a Mn(III) intermediate and its stability under different concentrations of acid. This led to the development of different deposition mechanisms for dilute acid (<1.0M) systems and concentrated acid (>1.0M) systems. These mechanisms are shown in Equations 1.25 - 1.33 below.

**Dilute acid (<1.0M) mechanism:**

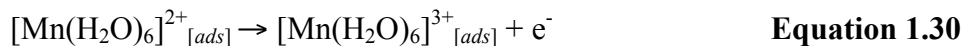


↓

↓ (fast)



**Concentrated acid (>1.0M) mechanism:**



There have been many studies of the EMD deposition mechanism, yet there is still disagreement and debate as to what the true EMD electrodeposition mechanism is. Although there is conflict in the literature, the steps in each different mechanism

typically involve the oxidation of aqueous Mn(II), followed by the precipitation of a solid phase, which then dehydrates to form EMD. The main areas of debate seem to concern the Mn(II) oxidation product and the solid phase dehydration mechanism [2, 42].

### **1.5 EMD Deposition from a Crystal Growth Perspective**

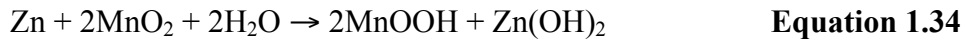
Swinkels and Williams [85] were the first to apply a general electro-deposition model to EMD production. They used classical electro-crystallisation theory to relate the properties of EMD to deposition conditions. Similar to standard crystallisation models, the electro-deposition process can be thought of in terms of crystal nucleation (the creation of new EMD crystals), and crystal growth (the growth of existing EMD crystals), with the driving force of deposition being the voltage or current applied to the solution, which is represented by the deposition voltage. Generally conditions that favour nucleation over crystal growth produce deposits that are fine grained with small crystallite size, while larger crystallites are deposited when crystal growth is favoured. Nucleation has a higher activation energy than crystal growth [86], so in general a higher driving force is required to favour nucleation. For example, increasing the deposition rate via increasing the current density, which in turn increases the deposition voltage, should favour nucleation over crystal growth, as the activation and concentration overpotentials are increased, which will lead to finer grained less crystalline deposits [37, 85].

Deposition voltages (polarization) are assumed by Swinkels and Williams [85] to increase with increasing current density, decreasing temperature, increasing acid concentrations, and decreasing manganese concentration.

It is proposed that both nucleation and growth contribute significantly to the overall rate. According to Swinkels and Williams [85], nucleation must occur when first depositing EMD onto a clean electrode. However, it can also occur on an existing EMD deposit resulting in the loss of the underlying crystal pattern, which may lead to an accumulation of defects in the growing deposits [37, 85].

## 1.6 EMD in Alkaline Cells

The cathode in alkaline cells is a blend of EMD and graphite, where EMD is the active component. Alkaline cells generally use a steel can as a cathode current collector, a potassium hydroxide electrolyte, an anode of powdered zinc, and usually a brass nail as an anode current collector. The basic chemical reaction that allows alkaline batteries to produce charge is shown below in Equation 1.34 [55].



EMD is also used as the cathode material in other battery systems, such as lithium, aluminium, magnesium, and Leclanche cells, as well as some secondary systems [55].

### 1.6.1 EMD Properties Required for Use In Alkaline Cells

EMD for use in alkaline cells requires a number of physical, chemical, and electrical properties. There are some twenty key analytical parameters that control the performance of EMD in alkaline cells (Table 1.6 shows the thirteen parameters used by this study), although EMD quality can generally be defined by five characteristics [2, 37]:

- Crystal structure – disorder, hydrated, non-stoichiometric
- Chemical purity – low impurity levels (single ppm level or lower)
- High MnO<sub>2</sub> content – 92% minimum with the remainder essentially water.
- High density – batteries are fixed volume devices
- Specific discharge capacity – a high battery activity, measured in mAh/g MnO<sub>2</sub>

**Table 1.6:** Key analytical parameters used in this study that control EMD performance, their importance, and typical values [37].

Analytical Parameter	Typical Value	Importance
<i>Total Manganese</i>	61 %	Required by battery customers.
<i>Peroxidation (x in MnO<sub>x</sub>)</i>	1.97	Required by battery customers, and a fundamental feature of EMD structure.
<i>Combined Water</i>	3-3.5 %	Required by battery customers, and a fundamental feature of EMD structure.
<i>Preisler Q-value</i>	0.7	Used as an indication of EMD quality, and estimates structural order.
<i>IPM Number</i>	1.24	Used by some battery companies to characterise EMD quality.
<i>H<sub>1</sub>/H<sub>2</sub> Ratio</i>	0.864	Used by some EMD producers to characterise their EMD. EMD quality is considered to increase with increases in the ratio.
<i>Position of the 110 XRD Peak</i>	4.04 Å	Used to estimate the contributions of De Wolff defects and micro-twinning to the structure.
<i>PWHPH of the 110 XRD Peak</i>	0.3-0.6 Å	Gives an estimate on increased structural disorder due to decreased crystallite size.
<i>Average Crystallite Size</i>	50-100 Å	Influences factors important to optimising high and low rate discharge performance such as conductivity and proton diffusion.
<i>BET Surface Area</i>	28-35 m <sup>2</sup> /g	Required by most battery customers.
<i>True Density</i>	4.4-4.5 g/cm <sup>3</sup>	Required by most battery customers, its optimum value is a compromise depending on the intended application.
<i>Open Circuit Voltage (OCV)</i>	1.56-1.61 V	Required by most battery customers, optimum value is a compromise (high but not too high).

## 1.7 Molecular Modelling of EMD

To date there have been few true molecular modelling studies of EMD, as most modelling studies such as those from Chabre and Pannetier [7], and Schilling and Dahn [87] have been empirical in nature and did not involve the optimisation and relaxation of the structures studied using a suitable potential model. However, in the last ten years there have been several significant modelling studies that have attempted to rationalise the structures of EMD.

Balachandran and co-workers [32, 52, 88] used DFT to successfully study various proposed small unit representations of EMD. The main findings from these studies were that:

- Pyrolucite is the ground state of stoichiometric  $\text{MnO}_2$ , however a structure with a perfect alternation of Mn atoms and vacancies along the  $c$ -axis has an energy close to that of pyrolucite.
- Ruetschi defects stabilise ramsdellite and twinning over pyrolucite, and introduce disorder in  $\text{MnO}_2$ . This could be responsible for the structural complexity of EMD.

Hill *et al.* [35] used interatomic potentials and the CVFF forcefield to directly examine De Wolff defects, micro-twinning and point defects. They concluded that:

- Point defects have little impact on the XRD patterns of EMD.
- De Wolff disorder is the major structural feature of EMD.
- Micro-twinning occurs to a higher extent in EMD.
- De Wolff defects and micro-twinning do not fully account for the structure of EMD, and that another defect or combination of defects may be responsible for some of the structural features in EMD.

Maphanga, Parker, and Ngoepe [89] used atomistic simulation methods to study the surface structures and stabilities of ramsdellite and pyrolucite, using the Born model of solids to describe the interaction of the atoms in the structure, and concluded that the pyrolucite  $\{1\ 0\ 0\}$  and the ramsdellite  $\{1\ 0\ 0\}_b$  surfaces have equivalent energies and therefore intergrowths are likely between these surfaces.

Sayle *et al.* [90, 91] have also used modelling techniques to investigate the structure of  $\text{MnO}_2$  using a technique known as amorphisation and recrystallization (A&R). Basically the A&R procedure starts with an amorphous configuration, and then the structure is allowed to recrystallize to structures that may occur experimentally. The technique uses the Born model of ionic solids, in which the Mn and O ions react via short-range parameterised interactions and long-range Coulombic interactions. The result was structures that conform to the pyrolucite polymorph, containing intergrowths, micro-twinning, point defects, dislocations and stacking faults. It should be noted that ramsdellite, suggested to be present in the structure predicted in

the 2005 paper [90], is absent in the 2006 paper. This is thought to be a result of the lack of Ruetschi defects in the updated model [91].

## 1.8 Research Plan

The aim of this project was to underpin the development of better batteries by controlling the properties of EMD, with a focus on EMD from a crystal growth perspective. A combined experimental and computational approach was used, with the aim of overcoming some of the difficulties encountered in earlier investigations.

The main characterization methods used in this study of EMD were SEM, and powder XRD. SEM analysis gave information about the surface topography of as-deposited EMD, crystallite size and shape (to sub-micron resolution), as well as chemical composition, *e.g.* of impurities (to a lower limit of *ca* 1 wt%) by energy dispersive spectroscopy (EDS). Powder XRD (both standard and low background) gave information about crystal structure, phase purity, as well estimates of crystallite size and strain information (through line broadening analysis). AFM analysis was also attempted to gain higher resolution surface, topographical, and morphological information crystal structure of EMD. TEM, synchrotron radiation – XRD (SR-XRD), and Raman spectroscopy were also used as complementary characterization techniques.

To further understand the structure and properties of EMD, molecular modeling was employed to simulate the defects (De Wolff defects, micro-twinning, and point defects) that occur within the EMD crystal structure. The various structures of EMD are modeled using a variable charge model (Qeq), using potentials adapted from previously published TiO<sub>2</sub> potentials, **GDIS** [92] and **CrystalMaker** [93] were used as a graphical interfaces, and **GULP** [94] was used to perform minimization calculations. XRD patterns were then simulated using **CrystalDiffract** [95]. These patterns were then compared to experimental data, with the goal of producing a suitable structural model for the EMD system.

For the sake of completeness, in conjunction with characterization experiments and molecular modeling, the electrochemistry of EMD was briefly investigated using

electrochemical impedance spectroscopy (EIS) and cyclic-voltammetry (CV). The results of these experiments can be found in Appendix I. EIS is an electrode kinetic technique that provides information about resistive-capacitive (RC) elements of differing time constants corresponding to non-porous and porous electrode surface films, along with the effects of kinetically and diffusion controlled electrochemical processes at the electrode/electrolyte interface. A marriage of EIS and various characterization techniques can provide a powerful research tool for elucidation of the mechanistic chemistry of electrochemical systems, and this approach was explored in this project. CV provides redox and mechanistic information about electrochemical systems. Therefore a combination of EIS and CV experiments was conducted with the goal of deciphering the EMD electro-deposition mechanism, and clearing up discrepancies in literature on the EMD deposition mechanism.

Novel simultaneous electrode kinetic and *in situ* synchrotron radiation – grazing incidence X-ray diffraction (SR-GIXRD) surface studies of the electro-deposition process of EMD were also performed at the Photon Factory, Tsukuba, Japan. As the exact chemical and structural nature of EMD films formed on the electrodes under operating conditions are still unknown, this study endeavoured to characterise these films *in situ*, thus avoiding the atmospheric degradation of electrode reaction products and the interference with crystal growth that normally occurs during *ex situ* surface analyses. It was necessary to conduct these experiments using synchrotron radiation GIXRD (SR-GIXRD) techniques as; 1) the very high mass absorption of X-rays by aqueous  $\text{Mn}^{2+}$  solutions obviates the use of a laboratory-based X-ray source as it does not permit sensitive *in situ* monitoring of electrochemical reaction products; 2) the poor signal-to-noise ratio of laboratory-based GIXRD, even in air, leads to a small number of diffraction peaks in *ex situ* analyses, preventing the unequivocal identification of electrochemical reaction products. Obviously, the true surface structure of the deposited EMD and its electrode kinetic properties must be known if a full understanding of its electrochemistry is to be obtained. This necessitated the use of a combination of *in situ* SR-GIXRD and EIS in this investigation.

## 1.9 References

1. Post, J.E., *Manganese oxide minerals: Crystal structures and economic and environmental significance*. Proc. Natl. Acad. Sci. U. S. A., 1999. **96**(7): p. 3447-3454.
2. Williams, R.P., *Characterisation and Production of High Performance Electrolytic Manganese Dioxide for use in Primary Alkaline Cells.*, in *Department of Chemistry*, 1995, The University of Newcastle: Newcastle, Australia.
3. Heslop, R.B. and P.L. Robinson, *Inorganic Chemistry*, 1960, Amsterdam: Elsevier.
4. Read, H.H. and F. Rutley, *[Frank] Rutley's [Begr.] Elements of Mineralogy*. 26 ed, 1974, London: Murby.
5. Burns, V.M., R.G. Burns, and W.K. Zwicker. *Classification of Natural Manganese Dioxide Materials*. in *Manganese Dioxide Symposium*. 1975. Cleveland: The Electrochemical Society, Inc.
6. Turner, S. and P.R. Buseck, *Manganese Oxide Tunnel Structures and Their Intergrowths*. Science, 1979. **203**(4379): p. 456-458.
7. Chabre, Y. and J. Pannetier, *Structural and Electrochemical Properties of the Proton / gamma MnO<sub>2</sub> System*. Prog. Solid State Chem., 1995. **23**: p. 1-130.
8. Ruetschi, P., R. Giovanoli, and P. Burki. *The Electrochemistry of MnO<sub>2</sub>*. in *Manganese Dioxide Symposium*. 1975. Cleveland: The Electrochemical Society, Inc.
9. Burns, R.G. and V.M. Burns. *Structural Relationships between the Manganese (IV) Oxides* in *Manganese Dioxide Symposium*. 1975. Cleveland: The Electrochemical Society, Inc.

10. Burns, R.G. and V.M. Burns. *Recent Structural Data for Manganese (IV) Oxides*. in *Manganese Dioxide Symposium*. 1980. Tokyo: The Electrochemical Society, Inc.
11. Baur, W.H., *Rutile-type compounds. V, Refinements of MnO<sub>2</sub> and MgF<sub>2</sub>*. Acta Crystallogr., 1976. **B32**: p. 2200-2204.
12. Donne, S.W., *Alkaline manganese dioxide electrochemistry*. ITE Lett. Batteries, New Technol. Med., 2000. **1**: p. 915-925.
13. Bolzan, A.A., C. Fong, B.J. Kennedy, and C.J. Howard, *Powder Neutron Diffraction Study of Pyrolusite,  $\beta$ -MnO<sub>2</sub>*. Aust. J. Chem., 1993. **46**(6): p. 939-944.
14. Chichagov, A.V., A.B. Belonozhko, A.L. Lopatin, T.N. Dokina, O.L. Samokhvalova, T.V. Ushakovskaya, and Z.V. Shilova, *Information-Calculating System on the Crystal Structure Data of Minerals (MINCRYST)*. Kristallografiya, 1990. **35**(3): p. 610-616.
15. Ohzuku, T. and T. Hirai, *Heat-treated Electrolytic Manganese Dioxide - Its Structure, Physicochemical Properties, and Electrochemical Reactivity*. Prog. Batteries Sol. Cells, 1988. **7**: p. 31-37.
16. Fong, C., B.J. Kennedy, and M.M. Elcombe, *A powder neutron diffraction study of lambda and gamma manganese dioxide and of LiMn<sub>2</sub>O<sub>4</sub>*. Z. Kristallogr., 1994. **209**(12): p. 941-945.
17. Ruetschi, P., *Cation-Vacancy Model for MnO<sub>2</sub>*. J. Electrochem. Soc., 1984. **131**(12): p. 2737-2744.
18. Turner, S. and P.R. Buseck, *Defects in nsutite (gamma-MnO<sub>2</sub>) and dry-cell efficiency*. Nature, 1983. **304**: p. 143-146.

19. Giovanoli, R. *A Review on Structural Data of Electrolytical and chemical MnO<sub>2</sub> (EMD and CMD)*. in *Manganese Dioxide Symposium*. 1980. Tokyo: The Electrochemical Society, Inc.
20. Mosbah, A., A. Verbaere, and M. Tournoux, *Lithium manganate (Li<sub>x</sub>MnO<sub>2</sub>lamda) phases intercalated in the spinel type*. Mater. Res. Bull., 1983. **18**(11): p. 1375-1381.
21. Hunter, J.C., *Preparation of a new crystal form of manganese dioxide lamda-MnO<sub>2</sub>*. J. Solid State Chem., 1981. **39**(2): p. 142-147.
22. Thackeray, M.M., M.H. Rossouw, R.J. Gummow, D.C. Liles, K. Pearce, A. De Kock, W.I.F. David, and S. Hull, *Ramsdellite-MnO<sub>2</sub> for lithium batteries: the ramsdellite to spinel transformation*. Electrochim. Acta, 1993. **38**(9): p. 1259-1267.
23. Kao, W.-H., V.J. Weibel, and M.J. Root, *The Influence of Potassium Ion on the Electrodeposition and Electrochemistry of Electrochemistry of Electrolytic Manganese Dioxide*. J. Electrochem. Soc., 1992. **139**(5): p. 1223-1226.
24. Cai, J., J. Liu, W.S. Willis, and S.L. Suib, *Framework Doping of Iron in Tunnel Structure Cryptomelane*. Chem. Mater., 2001. **13**: p. 2413-2422.
25. Post, J.E., R.B. Von Dreele, and P.R. Buseck, *Symmetry and cation displacement in hollandites: structure refinements of hollandite, cryptomelane and priderite*. Acta Crystallogr., 1982. **B38**: p. 1056-1065.
26. Post, J.E. and D.L. Bish, *Rietveld refinement of the coronadite structure*. Am. Mineral., 1989. **74**(7-8): p. 913-917.
27. Miura, H., *The crystal structure hollandite*. Mineral. J., 1986. **13**: p. 119-129.
28. Turner, S. and P.R. Buseck, *Todorokites: A New Family of Naturally Occuring Manganese Oxides*. Science, 1981. **212**(4498): p. 1024-1027.

- 
29. Yao, Y.F., N. Gupta, and H.S. Wrobelowa, *Rechargeable manganese oxide electrodes: Part I. Chemically modified materials*. J. Electroanal. Chem., 1987. **223**(1-2): p. 107-117.
  30. Virga, C., D. Horn, J. Hornath, and M. Li, *Manganese Market Outlook*, 2012, CPM Group.
  31. Ghaemi, M. and L. Binder, *Effects of direct and pulse current on electrodeposition of manganese dioxide*. J. Power Sources, 2002. **111**: p. 248-254.
  32. Balachandran, D., D. Morgan, G. Ceder, and A. van de Walle, *First-principles study of the structure of stoichiometric and Mn-deficient MnO<sub>2</sub>*. J. Solid State Chem., 2003. **173**: p. 462-475.
  33. Bowden, W., R. Sirotina, and S. Hackney, *Manganese Dioxide for Alkaline Zinc Batteries: Why Electrolytic MnO<sub>2</sub>*. ITE Lett. Batteries, New Technol. Med., 2000. **1**(6): p. 53-64.
  34. Bowden, W., R. Sirotina, and S. Hackney, *Manganese Dioxide for Alkaline Zinc Batteries: A single-phase model*. ITE Lett. Batteries, New Technol. Med., 2003. **4**(1): p. 26-37.
  35. Hill, J.-R., C.M. Freeman, and M.H. Rossouw, *Understanding gamma-MnO<sub>2</sub> by molecular modeling*. J. Solid State Chem., 2004. **177**: p. 165-175.
  36. Rodrigues, S., N. Munichandraiah, and A.K. Shukla, *A cyclic voltametric study of the kinetics and mechanism of electrodeposition of manganese dioxide*. J. Appl. Electrochem., 1998. **28**: p. 1235-1241.
  37. Ward, C., *Notes on the Production and Analysis of EMD*, 2001, HiTec Energy.
  38. Hendricks, T. and E. Teller, *X-Ray Interference in Partially Ordered Layer Lattices*. J. Chem. Phys., 1942. **10**(3): p. 147-167.

39. Pannetier, J., *Characterization of Manganese Dioxides by X-ray Diffraction*. Prog. Batteries Battery Mater., 1994. **13**: p. 132-135.
40. Ripert, M., C. Poinsignon, Y. Chabre, and J. Pannetier, *Structural study of proton electrochemical intercalation in manganese dioxide*. Phase Transitions, 1991. **32**: p. 205-209.
41. Heuer, A.H., A.Q. He, P.J. Hughes, and F.H. Feddrix, *Microstructure of Electrolytic MnO<sub>2</sub>: A Transmission Electron Microscopy Study of Bulk Material*. ITE Lett. Batteries, New Technol. Med., 2000. **1**(6): p. 76-80.
42. Clarke, C.J., G.J. Browning, and S.W. Donne, *An RDE and RRDE study into the electrodeposition of manganese dioxide*. Electrochim. Acta, 2006. **51**(26): p. 5773-5784.
43. Simon, D.E., T.N. Andersen, and C.D. Elliott, *A Rietveld Refinement Model of EMD Powder Patterns*. ITE Lett. Batteries, New Technol. Med., 2000. **1**(3): p. 10-19.
44. Wyckoff, R.W.G., *Crystal Structures*, 1963, New York: Wiley.
45. Sarciaux, S., A. Le Gal La Salle, A. Verbaere, Y. Piffard, and D. Guyomard, *gamma-MnO<sub>2</sub> for Li batteries Part 1. gamma-MnO<sub>2</sub>: Relationships between synthesis conditions, material characteristics and performance in lithium batteries*. J. Power Sources, 1999. **81-82**: p. 656-660.
46. Sarciaux, S., A. Le Gal La Salle, A. Verbaere, Y. Piffard, and D. Guyomard, *gamma-MnO<sub>2</sub> for Li batteries Part 2. Some aspects of the lithium insertion process into gamma-MnO<sub>2</sub> and electrochemically lithiated gamma-LixMnO<sub>2</sub> compounds*. J. Power Sources, 1999. **81-82**: p. 661-665.
47. Hill, L.I., H. Arrive, D. Guyomard, and H. Arrivé, *Effect of synthesis conditions on the morphology of MnO<sub>2</sub> ( $\alpha$ -,  $\beta$ -,  $\gamma$ -) synthesized by the hydrothermal-electrochemical method*. Ionics, 2002. **8**(3-4): p. 161-171.

48. Hill, L.I., A. Verbaere, and D. Guyomard, *Synthesis of alpha-, beta-, and low defect gamma-manganese dioxides using the electrochemical-hydrothermal method and study of their Li insertion behavior*. J. New Mater. Electrochem. Syst., 2002. **5**(2): p. 129-133.
49. Machefaux, E., A. Verbaere, and D. Guyomard, *Preparation of nanowires of M substituted manganese dioxides (M=Al, Co, Ni) by the electrochemical-hydrothermal method*. J. Phys. Chem. Solids, 2006. **67**(5-6): p. 1315-1319.
50. Pitteloud, C., M. Nagao, K. Itoh, and R. Kanno, *The structure of manganese dioxide and the position of proton studied by neutron diffraction with isotopic substitution*. J. Solid State Chem., 2008. **181**: p. 467-472.
51. Guinier, A., *X-Ray Diffraction*, 1963, San Francisco: W. H. Freeman and Co.
52. Balachandran, D., *First Principles Study of Structure, Defects and Proton Insertion in MnO<sub>2</sub>*, in *Department of Materials Science and Engineering*, 2001.
53. Simon, D.E., R.W. Morton, and J.J. Gislason, *A CLOSE LOOK AT ELECTROLYTIC MANGANESE DIOXIDE (EMD) AND THE gamma-MnO<sub>2</sub> & epsilon-MnO<sub>2</sub> PHASE USING RIETVELD MODELING*. Adv. X-Ray Anal., 2004. **47**: p. 267-280.
54. Kim, C.-H., Z. Akase, L. Zhang, A. Heuer, A. Newman, and P. Hughes, *The structure and ordering of ε-MnO<sub>2</sub>*. J. Solid State Chem., 2006. **179**(3): p. 753-774.
55. *Handbook of Manganese Dioxides Battery Grade*, ed. D. Glover, B.S. Jr, and A. Kozawa 1989: The International Battery Association (IBA, Inc.).
56. Andersen, T.N., *Effect of Some EMD Structural Features on Alkaline Discharge Capacity*. Prog. Batteries Battery Mater., 1992. **11**: p. 105-129.

- 
57. Preisler, E., *Growth of electrodeposited  $\gamma$ -manganese dioxide from a suspension bath*. J. Appl. Electrochem., 1989. **19**: p. 540-546.
  58. Andersen, T.N. and J.M. Derby, *Electrochemistry in Transition*, ed. O.J. Murphy, S. Srinivasan, and B.E. Conway, 1992, New York: Plenum Press. 655-678.
  59. *Batteries*, ed. K.V. Kordesch, 1974, New York: Marcel Dekker, Inc.
  60. HiTec-Energy, *The Electrofuel Process*, 2002.
  61. Ward, C.B., A.I. Walker, and A.R. Taylor, *The Production of Alkaline Grade EMD at Australian Manganese Company Limited*. Prog. Batteries Battery Mater., 1992. **11**: p. 40-46.
  62. Preisler, E., *Material problems encountered in anodic  $MnO_2$  deposition* \*. J. Appl. Electrochem., 1989. **19**: p. 559-565.
  63. Rethinaraj, J.P. and S. Visvanathan, *Preparation and properties of electrolytic manganese dioxide*. J. Power Sources, 1993. **42**: p. 335-343.
  64. Binder, L., W. Jantscher, F. Hofer, and G. Kothleitner, *Production and characterisation of electrolytically doped manganese dioxide*. J. Power Sources, 1998. **70**: p. 1-7.
  65. Biswal, A., B.C. Tripathy, T. Subbaiah, D. Meyrick, and M. Minakshi, *Electrodeposition of manganese dioxide: effect of quaternary amines*. J. Solid State Electrochem., 2013. **17**(5): p. 1349-1356.
  66. Matsuki, K., M. Sugawar, and A. Kozawa, *Codeposition of carbon materials in electrolytic manganese dioxide*. Prog. Batteries Battery Mater., 1992. **11**: p. 25-33.

- 
67. Prabhakar, J., J.P. Rethinaraj, and S. Visvanathan, *Preparation and properties of electrolytic manganese dioxide*. *J. Power Sources*, 1993. **42**: p. 335-343.
68. Preisler, E., *Anfangsstadien der elektrokristallisation von braunstein*. *Electrochim. Acta*, 1981. **26**: p. 1389-1395.
69. Ouboumour, H., C. Cachet, M. Bode, J. Ginoux, M. Laborde, C. Levy-Clement, and L.T. Yu, *Prog. Batteries Battery Mater.*, 1994. **13**: p. 170-187.
70. Aravamuthan, R., S. Srinivasan, S.C. Chockalingam, S. Kulandaisamy, C.C. Gopalakrishnan, J.P. Rethinaraj, S. Visvanathan, and H.V.K. Udupa. in *2nd Int. Symp. Industrial Oriented Basic Electrochemistry*. 1980. Karaikudi.
71. Aravamuthan, R., S. Srinivasan, S.C. Chockalingam, S. Kulandaisamy, C.C. Gopalakrishnan, J.P. Rethinaraj, S. Visvanathan, and H.V.K. Udupa. in *2nd Int. Symp. Industrial Oriented Basic Electrochemistry*. 1980. Karaikudi.
72. Chang, C., C. Zhao, A. Chen, Z. Zhu, W. Lin, and Y. Zhu. *A Study of Some Characteristic Properties of FEMD and Simultaneous Electrodeposition of FEMD on Anode and Metallic Mn on Cathode*. in *Manganese Dioxide Symposium*. 1980. Tokyo: I.C. MnO<sub>2</sub> Sample Office.
73. Jinming, L., *Fujian Shifan Daxue Xuebao, Ziran Kexueban*. *Fujian Shifan Daxue Xuebao, Ziran Kexueban*, 1989. **5**: p. 57-60.
74. Rethinaraj, J.P., S.C. Chockalingam, S. Kulandaisamy, and S. Visvanathan, *Electrolytic manganese dioxide from chloride electrolyte*. *Hydrometallurgy*, 1993. **34**(1): p. 119-133.
75. Preisler, E., *Electrodeposited manganese dioxide with preferred crystal growth*. *J. Appl. Electrochem.*, 1976. **6**(4): p. 301-310.
76. Preisler, E. in *Proceedings of the Second Battery Materials Symposium*. 1985. Graz.

- 
77. Kao, W.-H. and V.J. Weibel, *Electrochemical oxidation of manganese (II) at a platinum electrode*. J. Appl. Electrochem., 1992. **22**(1): p. 21-27.
78. Zaretskii, S.A. and E.I. Antonovskaya, *Elektrokhimiya Margansta*, Akad, Nauk Gruz. SSR, 1957. **3**: p. 232.
79. Fleischmann, M., H.R. Thirsk, and I.M. Tordesillas, *Kinetics of Electrodeposition of  $\gamma$ -Manganese Dioxide*. Trans. Faraday Soc., 1962. **58**: p. 1865-1877.
80. Paul, R.L. and A. Cartwright, *The Mechanism of the Deposition of Manganese Dioxide Part III. Rotating Ring-Disc Studies*. J. Electroanal. Chem., 1986. **201**: p. 123-131.
81. Paul, R.L. and A. Cartwright, *The Mechanism of the Deposition of Manganese Dioxide Part II. Electrode Impedance Studies*. J. Electroanal. Chem., 1986. **201**: p. 113-122.
82. Cartwright, A. and R.L. Paul. *A Study of the Mechanism of Manganese Dioxide Deposition*. in *Manganese Dioxide Symposium*. 1980. Tokyo.
83. Nijjer, S., J. Thonstad, and G.M. Haarberg, *Oxidation of manganese(II) and reduction of manganese dioxide in sulphuric acid*. Electrochim. Acta, 2000. **46**: p. 395-399.
84. Petitpierre, J.-P., C. Comninellis, and E. Plattner, *Oxydation du  $MnSO_4$  en Dioxyde de Manganese dans  $H_2SO_4$  30%*. Electrochim. Acta, 1990. **35**(1): p. 281-287.
85. Swinkels, D.A.J. and R.P. Williams, *A Model for EMD Production and Properties*. Prog. Batteries Battery Mater., 1996. **15**: p. 1-7.
86. Mullin, J.W., *Crystallisation*. 3rd ed, 1961, Oxford: Butterworth-Heinemann.

87. Schilling, O. and J.R. Dahn, *Fits of the gamma-MnO<sub>2</sub> Structure Model to Disordered Manganese Dioxides*. J. Appl. Cryst., 1998(31): p. 396-406.
88. Morgan, D., D. Balachandran, G. Ceder, and A. van de Walle. *A Drastic Influence of Point Defects on Phase Stability in MnO<sub>2</sub>*. in *Mat. Res. Symp. Proc.* 2003. Materials Research Society.
89. Maphanga, R.R., S.C. Parker, and P.E. Ngoepe, *Atomistic simulation of the surface structure of electrolytic manganese dioxide*. Surf. Sci., 2009. **603**(21): p. 3184-3190.
90. Sayle, T.X.T., C.R.A. Catlow, R.R. Maphanga, P. Ngoepe, and D. Sayle, *Generating MnO<sub>2</sub> nanoparticles using simulated amorphization and recrystallization*. J. Am. Chem. Soc., 2005. **127**(37): p. 12828-12837.
91. Sayle, T.X.T., R.R. Maphanga, P. Ngoepe, and D. Sayle, *Evolving microstructure in MnO<sub>2</sub> using amorphisation and recrystallisation*. J. Cryst. Growth, 2006. **294**(1): p. 118-129.
92. Fleming, S. and A. Rohl, *GDIS: A visualization program for molecular and periodic systems*. Z. Kristallogr., 2005. **220**: p. 580-584.
93. Palmer, D. and M. Conley, *CrystalMaker for Mac OS X*, 2004.
94. Gale, J.D. and A.L. Rohl, *The General Utility Lattice Program (GULP)*. Mol. Simul., 2003. **29**(5): p. 291-341.
95. Palmer, D., *CrystalDiffra for Mac OS X*, 2005.

*Every reasonable effort has been made to acknowledge the owners of copyright material. I would be pleased to hear from any copyright owner who has been omitted or incorrectly acknowledged.*

## 2 EXPERIMENTAL

### 2.1 Reagents

The reagents used in this project are outlined in Table 2.1.

**Table 2.1:** Reagents used in this project.

Reagent	Quality	Manufacturer
Manganese Sulfate Monohydrate	Analytical Grade	UNIVAR
Manganese Sulfate Pentahydrate	Analytical Grade	—
Manganese Chloride Tetrahydrate	Analytical Grade	UNIVAR
Manganese Nitrate Tetrahydrate	—	SIGMA
Conc. Sulfuric Acid	Analytical Grade	LAB-SCAN
Conc. Hydrochloric Acid	Analytical Grade	UNIVAR
Conc. Nitric Acid	Analytical Grade	LAB-SCAN
Conc. Orthophosphoric Acid	Analytical Grade	UNIVAR
Potassium Sulfate	Analytical Grade	UNIVAR
Calcium Flouride	Extra Pure	BDH
Nitrilotriacetic Acid (NTA)	Minimum 99%	SIGMA
1-Hydroxyethane-1,1,-Diphosphonic Acid (HEDP)	Photographic (60%) Grade	SIGMA
Ethylenediamine Tetra-Acetic Acid (EDTA)	Minimum 99%	BDH
Nitrilotris(methylenephosphonic Acid) (NTMP)	50 wt%	Aldrich Chemical Company
Sulfonated calix-4-erene	—	Made in-house
Ethylenediamine Tetra-Methylenephosponic Acid (EDTP)	—	Made in-house
Propylenediamine Tetra-Methylenephosponic Acid (PDTP)	—	Made in-house
Nitrilo(bis)methylenephosonic Acetic Acid (NADP)	—	Made in-house
Nitrilo(mono)methylenephosponic Di-Acetic Acid (NMPDA)	—	Made in-house

## 2.2 Electro-deposition Cell

A schematic diagram and photographs of the electro-deposition cell used to produce EMD in the study are shown in Diagram 2.1 and Figure 2.1 respectively. The cell is 500 mL - 1L in capacity, and utilizes interchangeable 1x1 cm flag and 1 cm diameter rotating disc [RDE] platinum working electrodes (Figure 2.2), a platinum mesh counter electrode, and a Ag/AgCl double junction reference electrode. Platinum working electrodes were used instead of the industry standard titanium electrodes to avoid any complicating effects associated with passivation, and the substrate-deposit interface [1]. Current was supplied by an EG&G Princeton Applied Research PARSTAT 2263 portable potentiostat using *Powersuite* [2] software, this instrument was also used to perform CV and EIS experiments. Temperature was controlled using an ACTIVON 720-Series digital hotplate/stirrer fitted with a temperature probe. The bath was agitated via a magnetic stirrer rotating at 150-250 rpm, insuring thorough mixing of the bath solution, preventing layering of the EMD deposit due to concentration gradients within the solution caused by poor mixing. During electrochemical impedance spectroscopy, and cyclic voltammetry experiments the RDEs were rotated using a Pine Instrument Company MSRX speed controlled rotator.

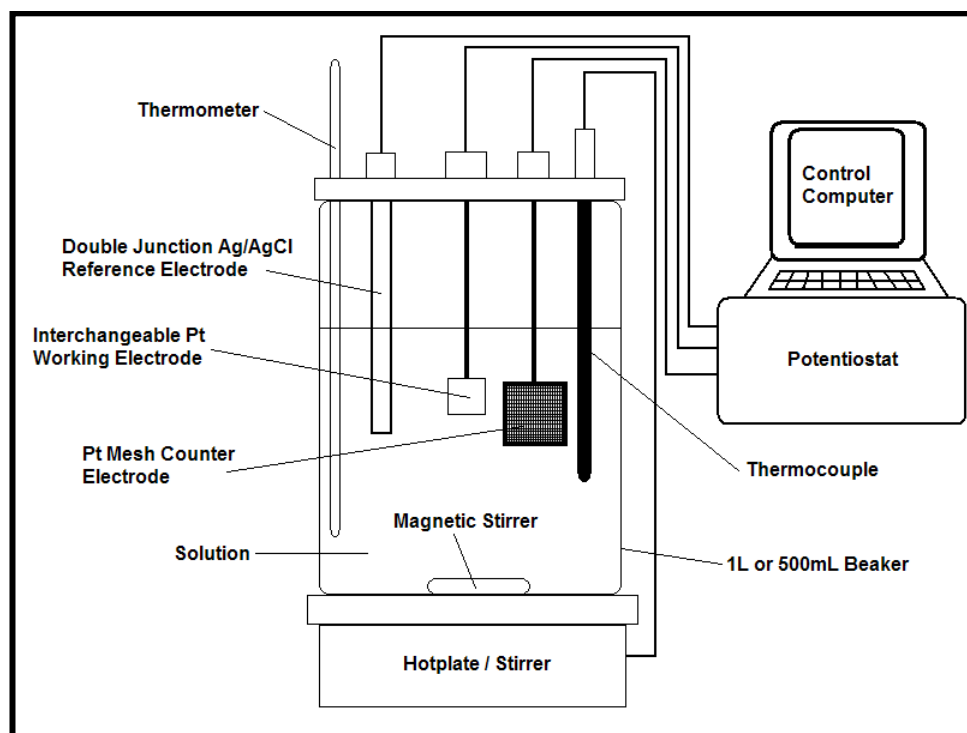


**Diagram 2.1:** A schematic of the EMD electro-deposition cell used in this project.

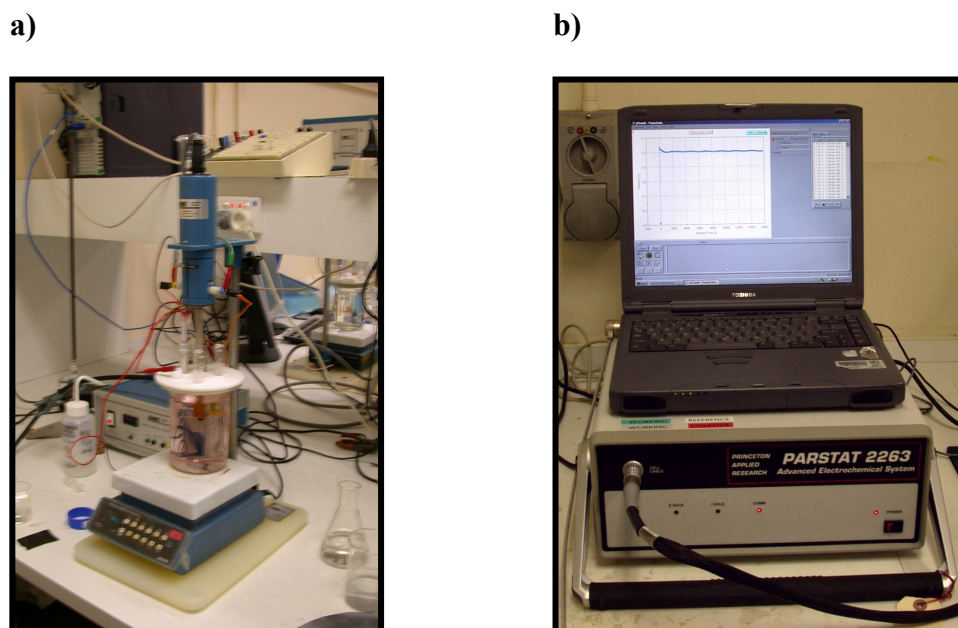


**Figure 2.1:** Photographs of a) the EMD electro-deposition cell used in this project, b) the computer and potentiostat used to applied current and perform electrochemical experiments.

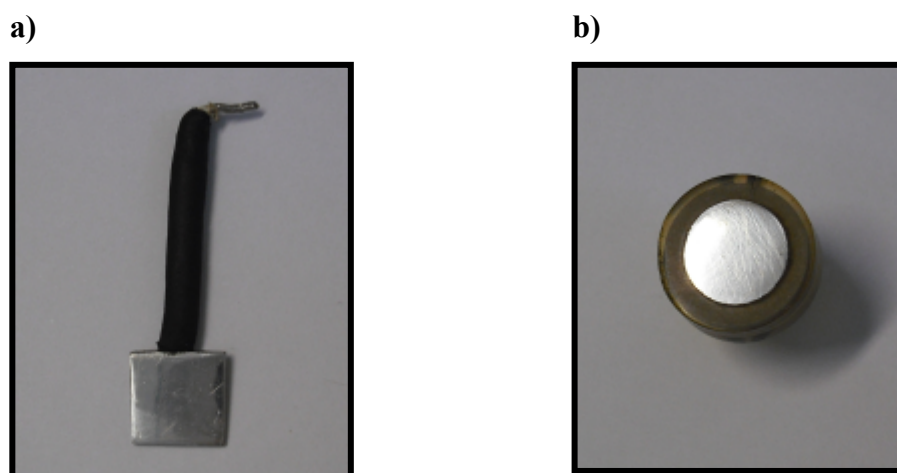


**Figure 2.2:** Photographs of the interchangeable platinum working electrodes used in this project, a) a 1x1 cm flag electrode, b) a 1 cm diameter rotating disc electrode [RDE].

## **2.3 Experimental Procedures**

### **2.3.1 Preparation of Electrolyte Solutions**

Electrolytes used in this project were prepared in volumetric flasks, from the highest quality chemicals available (generally analytical grade) using Milli-Q water.

### **2.3.2 Preparation of EMD for SEM Analysis**

1x1 cm platinum flag electrodes were polished using 4000 grit SiC abrasive paper, and then washed twice with Milli Q water and ethanol. The clean electrodes were connected to the electro-deposition rig described in Section 2.2, which contained the appropriate solution (500 mL - 1 L) at the required temperature. The desired constant current was then applied for 600 s. The electrode was removed from the rig and washed twice with Milli Q water and ethanol and dried at 55 °C overnight. The electrodes were then mounted on SEM stubs and the EMD produced analysed as-deposited via SEM.

### **2.3.3 Preparation of EMD Samples for XRD Analysis**

The procedure was as described in the previous section, except the desired constant current was then applied for 1800 s. The electrodes were then removed from the rig and washed twice with Milli Q water and ethanol and dried at 55 °C overnight. The deposited EMD was mechanically removed from the electrodes. The samples were then lightly ground, dispersed in acetone (~0.5 mL) and sonicated for 1800 s, then drop-cast onto low-background XRD sample holders.

EMD samples supplied by HiTec Energy, were ground by hand using a mortar and pestle, and then packed into powder XRD sample holders. If there was insufficient sample for powder XRD analysis, the ground sample was dispersed in acetone and sonicated for 1800 s, then drop-cast onto low-background XRD sample holders.

EMD samples prepared for XRD analysis were first analysed without an internal standard to allow analysis of peak shape. The samples were then re-analysed using CaF<sub>2</sub> as an internal standard to allow accurate analysis of peak positions and shifts.

For powder XRD samples 10% w/w CaF<sub>2</sub> was added to the EMD sample and mixed in thoroughly by gentle grinding in a mortar and pestle. For low-background XRD samples, CaF<sub>2</sub> was dispersed in acetone and sonicated for 1800 s, then drop-cast onto low-background XRD sample holders containing the EMD sample.

#### 2.3.4 Cyclic Voltammetry (CV)

1 cm diameter platinum RDEs were polished using 4000 grit SiC abrasive paper, and then washed twice with Milli Q water and ethanol. The clean electrodes were connected to the electro-deposition rig described in Section 2.2, which contained the appropriate solution (500 mL -1 L) at the target temperature. The RDE was held at 0.5 V for an equilibration period of 15 s, then swept from 0.2 to 1.4 V (starting and finishing at 0.5 V) at various scan rates (1 – 50 mV/s), and rotation speeds (50 – 2000rpm).

#### 2.3.5 Electrochemical Impedance Spectroscopy (EIS)

The procedure was as described in the previous section, except the RDE was rotated at 1000 rpm and plated with EMD using a current density of 40 A/m<sup>2</sup>, applied for 600 s. EIS was then performed on the freshly plated electrode. EIS spectra were collected at open circuit potential using an A.C. amplitude of ±5 mV rms, and measured using thirty data points over a frequency range of 100 kHz to 10 MHz with a data quality of four. The plated RDE was then removed from the rig and washed twice with Milli Q water and ethanol, then dried at 55 °C overnight. The electrodes were then analysed as-deposited via SEM.

#### 2.3.6 *In situ* Simultaneous Electrochemical Impedance Spectroscopy (EIS) and Synchrotron Radiation Grazing Incidence X-ray Diffraction (SR-XRD)

These experiments were performed on Beamline 20B at the Photon Factory in Tsukuba, Japan using the “BIGDIFF” diffractometer, an EG&G Princeton Applied Research PARSTAT 2263 portable potentiostat, and two custom designed *in situ*

electro-deposition cells. For more detailed *in situ* EIS / SR-GIXRD experimental procedures, see section 6.1 and 6.5.

## 2.4 Experimental Conditions Studied

This study investigated a wide range of deposition variables, and the effect they had on the structure, morphology, and the electro-deposition chemistry of EMD. For simplicity these variables were split into three categories:

1. **General deposition parameters;** current density, temperature, sulfuric acid concentration, and manganese concentration. The ranges for these variables are shown in Table 2.2.
2. **Deposition electrolyte;** chloride and nitrate baths were used as alternatives to the standard sulfate deposition electrolyte.
3. **Electrolyte additives;** various organic/inorganic compounds that are known crystal growth modifiers were added to the deposition electrolyte. See Table 2.3 for a comprehensive list of electrolyte additives and their concentrations in the electrolyte bath.

**Table 2.2:** General deposition parameters and the ranges investigated by this project.

<b>General Deposition Parameter</b>	<b>Range</b>
Current Density	20 – 80 A/m <sup>2</sup>
Temperature	30 – 93 °C
Sulfuric Acid Concentration [H <sub>2</sub> SO <sub>4</sub> ]	5 – 50 g/L
Manganese Concentration [Mn]	10 – 85 g/L

**Table 2.3:** Electrolyte additives used in this project and their approximate concentrations in the electrolyte bath.

Electrolyte Additive	Concentration [ppm]
<i>Inorganic</i>	
$K^+$	3000
$H_3PO_4$	106
<i>Organic</i>	
<i>p</i> -Sulfonatocalix[4]arene, HEDP, NTMP, EDTP, PDTP, NADP	100

Figure 2.3 shows the structures of the organic additives used in this study.

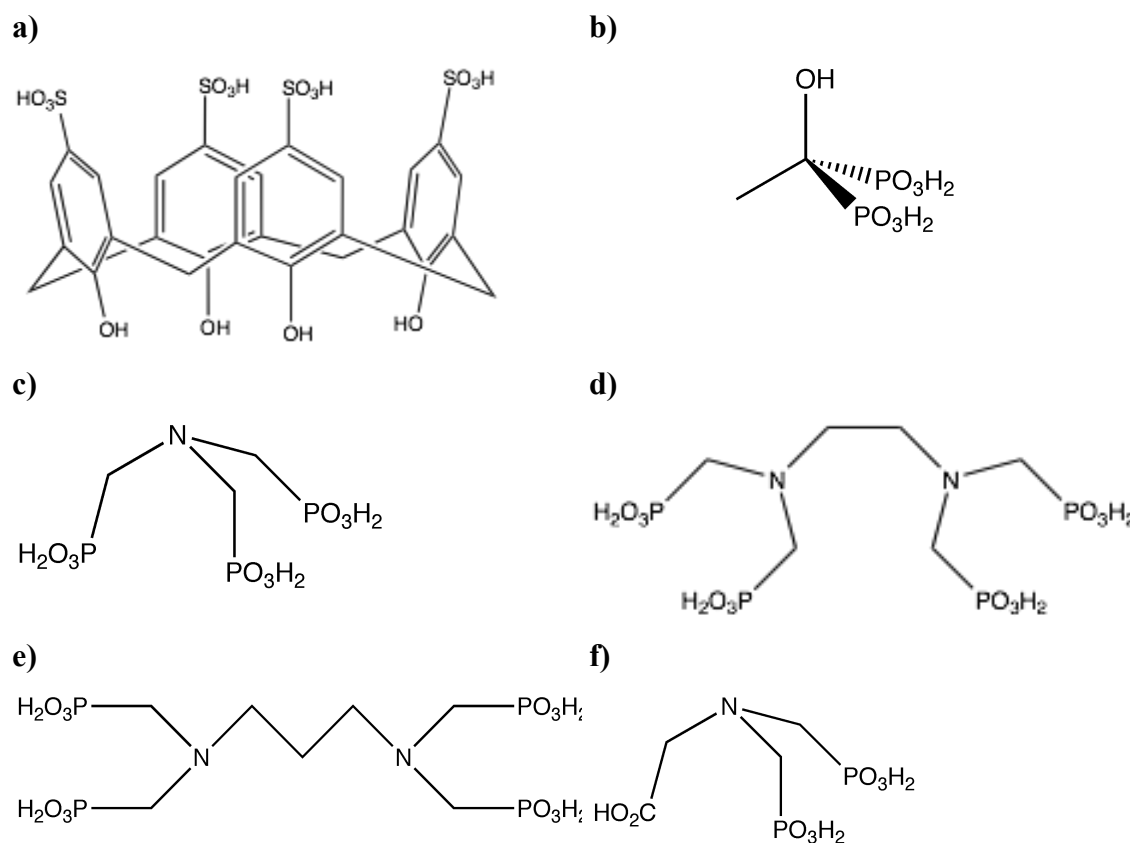


**Figure 2.3:** Molecular structure of the organic additives used in this study **a)** *p*-sulfonatocalix[4]arene, **b)** HEDP, **c)** NTMP, **d)** EDTP, **e)** PDTP, and **f)** NADP.

## 2.5 Characterisation of Solids

### 2.5.1 Scanning Electron Microscopy (SEM)

SEM images were recorded on a Phillips XL30 scanning electron microscope. Energy dispersive spectroscopy (EDS) was performed using an Oxford Instruments, Model 6650 EDS analyser. Samples for SEM analysis were mounted on stubs using carbon tape and analysed without any further treatment.

### 2.5.2 X-Ray Diffraction (XRD)

X-ray diffraction was performed using a D500 Siemens Kristalloflex diffractometer, using a copper tube ( $\lambda = 1.541\text{\AA}$ ), operating at 40kV and 30mA. Diffraction data were collected between 3 and  $80^\circ 2\theta$ , at  $0.4^\circ/\text{min}$ , using a step size of  $0.02^\circ$ .

In some cases, samples were also sent to the commercial laboratory Ultratrace to enable higher quality XRD analysis. These samples were analysed using a PANalytical X'pert PRO X-ray diffractometer, using a copper tube ( $\lambda = 1.541\text{\AA}$ ), operating at 40kV and 50mA. Diffraction data was collected between 3 and  $80^\circ 2\theta$ , with a continuous scan, using a step size of  $0.0167^\circ$ .

### 2.5.3 Transmission Electron Microscopy (TEM)

TEM images were recorded on a JEOL 3000 Field Emission Gun Transmission Electron Microscope (FEG-TEM) operating at 300 kV. Samples ground and dispersed in acetone, then drop-cast onto 200-mesh copper grids coated with holey carbon film.

### 2.5.4 Raman Spectroscopy

Dispersive Raman analysis was performed using an Olympus BX40 instrument, using a 633 nm HeNe laser, at 100x magnification, using an 1800 grating, and 2 micron spot size.

### 2.5.5 Infrared Spectroscopy (FT-IR)

Fourier Transform Infrared analysis was performed using a Bruker Vector22 FT-IR spectrometer. Spectra were collected in the region of 4000 – 400  $\text{cm}^{-1}$ , at a resolution of 4  $\text{cm}^{-1}$ , with an interval of 2  $\text{cm}^{-1}$ , using 4 scans. Samples were ground and then dispersed in KBr, and pressed into discs under vacuum.

### 2.5.6 Atomic Force Microscopy (AFM)

AFM was performed using a Digital Instruments Dimension 3000 AFM.  $\text{SiN}_3$  cantilevers with spring constants of 0.06 N/m were in contact mode, while TESP nanoprobe SPM tips of length 125  $\mu\text{m}$  were used in tapping mode.

### 2.5.7 Synchrotron Radiation X-Ray Diffraction (SR-XRD)

SR-XRD was performed on Beamline 20B at the Photon Factory in Tsukuba, Japan using the “BIGDIFF” diffractometer. Capillary SR-XRD was performed on EMD powder samples, using a wavelength of 0.75049 Å. SR-GIXRD was performed, using a wavelength of 1.000 Å, at incidence angles of  $\alpha = 5^\circ - 0.5^\circ$  using two custom designed *in situ* electro-deposition cells (see sections 6.2.1.1 and 6.3.1.1) and a “dummy cell” for powdered analysis, patterns were recorded using Fuji imaging plates for data collection times of 10 - 20 mins.

## 2.6 Molecular Modelling

Molecular modeling was performed using the computational facilities of Curtin University and iVEC. EMD crystal structures were modeled using a variable charge model (Qeq), using potentials adapted from previously published  $\text{TiO}_2$  potentials, **GDIS** [3] and **CrystalMaker** [4] were used as a graphical interfaces, and **GULP** [5] using a Newton-Raphson optimizer and a combination of BFGS and RFO minimization algorithms was used to perform optimisation calculations. XRD patterns were then simulated using **CrystalDiffract** [6]. Molecular modeling procedures will be explained in more detail in chapters 7 and 8.

## 2.7 References

1. Clarke, C.J., G.J. Browning, and S.W. Donne, *An RDE and RRDE study into the electrodeposition of manganese dioxide*. *Electrochim. Acta*, 2006. **51**(26): p. 5773-5784.
2. Research, P.A., *PowerSuite-2.33.0*, 2000, PerkinElmer Instruments Inc.
3. Fleming, S. and A. Rohl, *GDIS: A visualization program for molecular and periodic systems*. *Z. Kristallogr.*, 2005. **220**: p. 580-584.
4. Palmer, D. and M. Conley, *CrystalMaker for Mac OS X*, 2004.
5. Gale, J.D. and A.L. Rohl, *The General Utility Lattice Program (GULP)*. *Mol. Simul.*, 2003. **29**(5): p. 291-341.
6. Palmer, D., *CrystalDiffract for Mac OS X*, 2005.

*Every reasonable effort has been made to acknowledge the owners of copyright material. I would be pleased to hear from any copyright owner who has been omitted or incorrectly acknowledged.*

### **3 ANALYSIS OF EMD PRODUCED AT THE HITEC ENERGY PILOT PLANT**

Initial characterisation and analysis of EMD was performed on powder samples and EMD chips produced at the HiTec Energy Ltd pilot plant, and the international EMD standards, IBA No. 30 and I.C. No. 19. To complement the analyses performed by HiTec Energy, these samples were further characterised using: SEM and AFM, to investigate the morphologies of EMD crystals; and XRD, SR-XRD, TEM, and Raman, to examine the crystal structure of EMD. This multi-faceted approach to EMD characterisation was employed to provide a wide range a complementary morphological and structural data, with the hope of developing a better understanding of the EMD crystal structure, and as a way of evaluating the suitability of various characterisation techniques for further use in this project.

Where possible, sample preparation was kept to a minimum and samples were generally analysed as-received. This approach reduced the likelihood of damage to the crystal structure and morphology, as well as limiting possible structural transformations due to over zealous sample preparation.

#### **3.1 Analysis of EMD Powders from the HiTec Energy Pilot Plant**

HiTec Energy provided a number of powdered EMD samples for analysis. These samples were produced at the HiTec Energy EMD pilot plant located at Murdoch University. All of these samples were deposited onto titanium electrodes at 98 °C; Table 3.1 shows the bath conditions that were used to deposit these samples. After electrolysis the EMD was removed from the electrodes, crushed, milled, and washed. The EMD was then dried overnight at 105 – 110 °C. The resulting EMD powders were then analysed.

**Table 3.1:** The bath conditions used to deposit EMD samples for analysis, at the HiTec Energy pilot plant.

Sample	Bath Conditions		
	Current Density ( $A/m^2$ )	[Mn] (g/L)	[H <sub>2</sub> SO <sub>4</sub> ] (g/L)
<i>Run 2</i>	55	45	35
<i>Run 4</i>	65	45	35
<i>Run 5</i>	60	45	35
<i>Run 6</i>	65	60	35
<i>Run 10A</i>	60	60	35

### 3.1.1 General Parameters

HiTec Energy performed a series of tests on the EMD produced at their pilot plant; these tests analysed impurities and composition, the surface area, density, pore size and electrochemical properties. The results of these tests are shown in Table 3.2.

**Table 3.2:** The results of various tests performed by HiTec Energy on EMD samples produced at the HiTec Energy pilot plant.

Analytical Parameter	Sample						
	<i>Run 2</i>	<i>Run 4</i>	<i>Run 5</i>	<i>Run 6</i>	<i>Run 10A</i>	<i>IBA 30</i>	<i>Target Values</i>
<i>Mn (%)</i>	60.4	60.8	60.9	60.6	60.3	60.8	60 (min)
<i>MnO<sub>2</sub> (%)</i>	92.4	92.6	93.1	92.1	91.9	91.5	92 (min)
<i>MnO<sub>2</sub>/Mn Ratio</i>	1.53	1.52	1.53	1.52	1.52	1.50	1.50 (min)
<i>Peroxidation (%)</i>	96.70	96.27	96.63	96.07	96.36	95.13	95 (min)
<i>x in MnO<sub>x</sub></i>	1.97	1.96	1.97	1.96	1.96	1.95	1.97
<i>Combined H<sub>2</sub>O (%)</i>	3.44	3.44	3.30	3.28	3.35	–	3.0 – 3.5
<i>Open Circuit Voltage (V)</i>	1.62	1.64	1.61	1.62	1.62	–	1.59 – 1.65
<i>BET Surface Area (m<sup>2</sup>/g)</i>	29.3	31.8	27.6	28.8	31.1	23.4	25 – 35
<i>True Density (g/cm<sup>3</sup>)</i>	4.446	4.515	4.521	4.449	4.523	4.509	4.40 – 4.57

Table 3.2 clearly shows that the EMD samples produced at HiTec Energy have very similar chemical, physical, and electrochemical properties. The results also show the high quality of the EMD produced at the pilot plant, as almost all the parameters

examined were within the appropriate target ranges of values set by industry [1, 2], and if they were not within the ranges, only slight deviations were evident. In fact, overall the HiTec Energy samples seemed to possess slightly more favourable properties than the IBA 30 (standard) EMD sample. Unfortunately due to the similarity of the results, and the small range of samples, there were no discernable trends within the data between properties and deposition conditions. However, the above results seem to suggest that at these particular conditions, small changes in the electro-deposition conditions of EMD have little effect on its physical, chemical and electrochemical properties, and that HiTec Energy possess the knowledge and facilities to produce high quality EMD, reproducibly on the pilot plant scale.

Chemical impurities in EMD samples produced at the HiTec Energy pilot plant were generally less than a few ppm. However, some impurities such as Si, Mg, Fe, Na, K, Al, Ca, S, and Ti were present at higher levels. The elevated levels of Si (~200 ppm), Mg (~20 ppm), Fe (~45 ppm), Al (~50 ppm), and Ca (~70 ppm), are likely to be a result of the plant environment that the samples were produced in, as these elements are commonly found in industrial settings. It should also be noted that the levels of these impurities in the HiTec Energy samples are still well below typical specifications for alkaline grade EMD [2, 3]. The higher levels of Na (~1460 ppm) and K (~155 ppm) are not unexpected as they are generally ubiquitous in most water sources. However, the levels of these impurities are also below industry specifications. The higher levels of S (~3160 ppm) are also not unexpected, as the  $\text{SO}_4^{2-}$  ion is known to adsorb onto EMD crystals during deposition. The presence of Ti impurities is likely to be a result of dissolution of the Ti anodes used to deposit the sample, this is confirmed by the Ti concentration in the samples decreasing as the electrodes were reused; that is, EMD deposited onto new electrodes contained ~210 ppm Ti, which is substantially higher than the prescribed maximum concentration of 20 ppm, while EMD deposited onto electrodes that had been reused nine times contained only ~10 ppm Ti, and Ti levels of below 20ppm were achieved during the fourth reuse of the anode.

### 3.1.2 SEM

SEM analysis of the powdered EMD samples revealed little information about the morphology of EMD crystallites. This was not unexpected as the samples:

- had been uniformly ground, which tends to destroy morphological and structure features of samples, especially the fine features that maybe be present as a result of EMDs small crystallite size.
- and exhibited very similar XRD patterns to each other (see section 3.1.3).

Therefore further SEM analysis of the pilot plant EMD samples in this study concentrated on the graded EMD chips supplied to us by HiTec Energy Ltd.

### 3.1.3 XRD

The EMD samples analysed from the HiTec Energy pilot plant produced XRD patterns characteristic of EMD used in alkaline cells, that is they all exhibited a broad peak at  $\sim 22.2^\circ 2\theta$ ; three sharper major peaks at  $\sim 37.2^\circ$ ,  $42.5^\circ$ , and  $56.2^\circ$ ; and a minor peak at  $\sim 40.5^\circ 2\theta$ ; all over a diffuse background [3, 4]. There is little to distinguish separate patterns, which all closely resemble IBA 30, an international standard, generally accepted as “standard” EMD, see Figure 3.1. The XRD patterns of these samples gave relatively low counts and peaks show significant anisotropic broadening, suggesting EMD is a poorly crystalline or nano-crystalline material that has significant disorder, and a small crystallite size. The sharper peaks over an undulating background may indicate a bi-variate crystal size distribution, with peak positions suggesting a mixture of a disordered ramsdellite phase with a smaller crystallite size, and an  $\epsilon$ -MnO<sub>2</sub> phase with a larger crystallite size. This is consistent with Simon and co-workers [5] mixed phase model of EMD, although there are several theories that can also explain these characteristics of the EMD XRD pattern. The absence of a peak at  $\sim 28.7^\circ 2\theta$ , except for a very small hump, indicates that these samples contain little crystalline pyrolucite. The presence of this peak is usually associated with EMD of “poorer” quality [6].

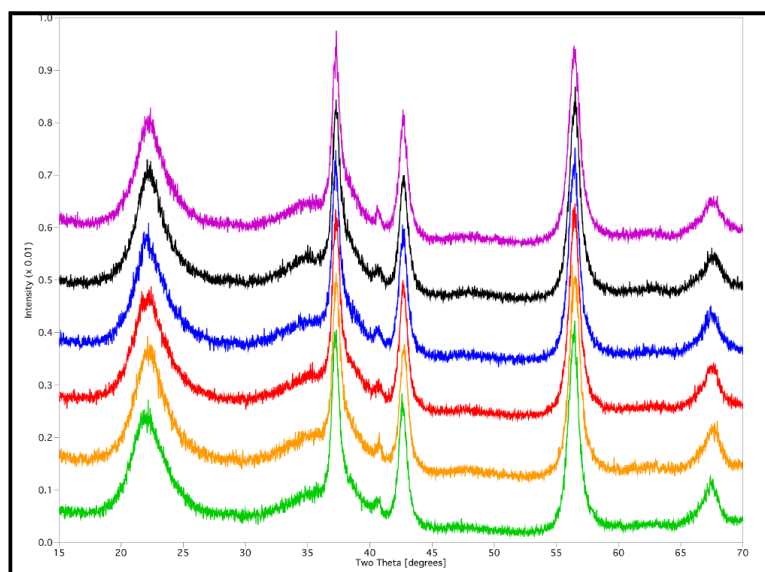


**Figure 3.1:** XRD patterns of EMD samples produced at the HiTec Energy pilot plant and IBA 30: Run 2 - 55A, 45 g/L Mn, 35 g/L H<sub>2</sub>SO<sub>4</sub> [Green]; Run 5 - 60A, 45 g/L, 35 g/L H<sub>2</sub>SO<sub>4</sub> [Orange]; Run 4 - 65A, 45 g/L Mn, 35 g/L H<sub>2</sub>SO<sub>4</sub> [Red]; Run 6 - 65A, 60 g/L Mn, 35 g/L H<sub>2</sub>SO<sub>4</sub> [Blue]; Run 10A - 60A, 60 g/L, 35 g/L H<sub>2</sub>SO<sub>4</sub> [Black]; and IBA 30 [Purple].

Table 3.3 shows that the peaks of the EMD produced at the pilot plant vary very little, in relation to the deposition conditions, with the greatest difference between peak positions of HiTec samples being  $\sim 0.4^\circ 2\theta$ , which occurs on the 061 peak. This coupled with the small sample size of deposition conditions, means that trends between peak positions and deposition conditions are difficult to correlate. There is also little difference between peak positions of the HiTec samples and IBA 30, with the greatest difference between peak position being  $\sim 0.5^\circ 2\theta$ , again occurring on the 061 peak. Note for the sake of simplicity the Miller indices shown in Table 3.3 are based on the ramsdellite unit cell, as several authors use this indexing system [7].

**Table 3.3:** Positions of major XRD peaks of EMD samples produced at the HiTec pilot plant. The Miller indices shown are based on a ramsdellite unit cell.

Sample	Peak Positions ( $^{\circ} 2\theta$ )					
	110	021	200	121	221	061
<i>Run 2</i>	21.97	37.45	40.91	42.96	56.46	67.88
<i>Run 5</i>	22.01	37.45	41.04	43.01	56.53	67.83
<i>Run 4</i>	22.01	37.45	41.02	42.96	56.53	67.83
<i>Run 6</i>	21.99	37.45	40.91	42.96	56.53	67.77
<i>Run 10A</i>	22.08	37.42	40.92	42.99	56.53	67.45
<i>IBA 30</i>	22.13	37.45	40.96	42.96	56.53	67.94

**Note:** XRD peak positions were determined manually, with a maximum error of approximately  $\pm 0.26^{\circ} 2\theta$ , for the broadest 110 peak.

Examination of the shape of various peaks and the diffuse background showed few distinguishing features between patterns, although the asymmetry of the majority of peaks suggests the presence of an extremely disordered crystal structure. There seems to be some slight broadening and differences in the shape the 061 peak, as a result of increased  $Mn^{2+}$  concentration in electrolyte bath. As  $Mn^{2+}$  concentration increases there is an apparent increase in the asymmetry of the 061 peak ( $\sim 67.5^{\circ} 2\theta$ ) to lower  $2\theta$  values; this is illustrated in Figure 3.2 and Table 3.3. The general shape of the 061 peak suggests that the peak may be a result of multiple peaks that have merged together to form a single broad peak.

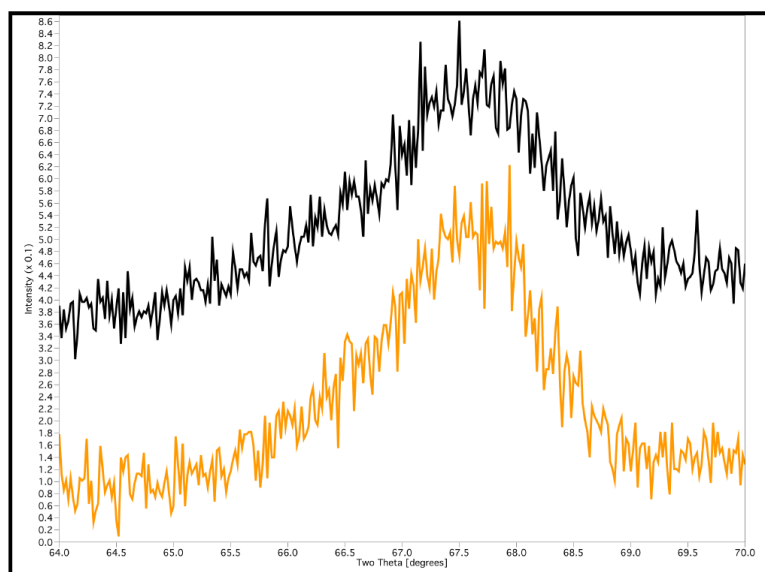


**Figure 3.2:** The effect of  $\text{Mn}^{2+}$  on the peak shape of the 061 EMD peak; Run 5 - 60A, 45 g/L, 35 g/L  $\text{H}_2\text{SO}_4$  [Orange]; Run 10A - 60A, 60 g/L, 35 g/L  $\text{H}_2\text{SO}_4$  [Black], viewed between  $64^\circ$  and  $70^\circ$   $2\theta$ .

This series of samples shows that small changes in the electro-deposition conditions have a negligible effect on the XRD patterns of the EMD produced. In light of this knowledge, selected samples were analysed using synchrotron radiation in an attempt to increase the resolution of these patterns, and a wide range of experimental conditions will be used in this study to investigate the effect of electro-deposition conditions on EMD.

### 3.1.3.1 SR-XRD

Manganese dioxides are poor X-ray scatterers [8], therefore to increase the resolution of the above XRD patterns, selected samples were re-analysed using synchrotron radiation. Patterns produced using synchrotron radiation had superior signal to noise ratios, showed slightly more defined peaks, and an increase in the asymmetry of the 110 peak. Unfortunately, however, SR-XRD analysis did not provide any new crystallographic data. This is illustrated in Figure 3.3, which shows differences between the SR-XRD patterns and the standard powder XRD patterns are slight.

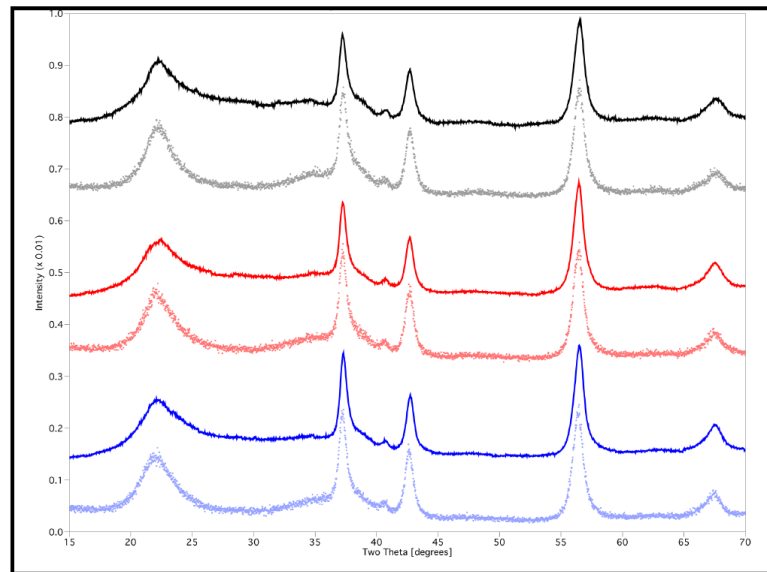


**Figure 3.3:** A comparison of SR-XRD patterns (represented by the darker, solid lines) and standard powder XRD patterns (represented by the lighter, dotted lines); Run 10A - 60A, 60 g/L, 35 g/L H<sub>2</sub>SO<sub>4</sub> [black], Run 6 - 65A, 60 g/L Mn, 35 g/L H<sub>2</sub>SO<sub>4</sub> [red], Run 2 - 55A, 45 g/L Mn, 35 g/L H<sub>2</sub>SO<sub>4</sub> [blue].

### 3.1.3.2 Analytical XRD Parameters of HiTec Energy's Powdered EMD Samples

As mentioned previously in the introduction, there are several important parameters that can be derived from the XRD pattern of EMD, these include [4]:

- The average crystallite size.
- The unit cell parameters (both orthorhombic and hexagonal).
- Pannetiers'  $P_r$  and  $T_w$  values.
- Structural parameters calculated using Bowden and co-workers EMD XRD simulation program.
- The Preisler Q – value.
- The IPM Number.
- And, the H<sub>1</sub>/H<sub>2</sub> Ratio.

All of these parameters can provide some information about the structure and quality of the EMD deposited.

The average crystallite sizes of these samples were calculated using the Scherrer equation shown in equation 3.1 [4]. As the defects in EMD tend to broaden the XRD peaks, no attempts were made to correct the data for instrumental broadening etc, therefore the results shown in Table 3.4 should be treated with caution as they are essentially only a rough estimate of the actual crystallite size.

$$\text{Crystallite Thickness } (\text{\AA}) = 0.9\lambda/\Delta\theta\cos\theta \quad \text{Equation 3.1}$$

Where  $\lambda$  is the wavelength of the X-rays,  $\Delta\theta$  is the peak width at half peak height in radians, and  $\theta$  is the angle at the peak centre.

**Table 3.4:** The estimated average crystallite sizes<sup>1</sup> of powdered EMD samples from the HiTec Energy pilot plant.

Sample	Average Crystallite Size (nm)				
	110	021	121	221	061
<i>Run 2</i>	3.09	13.32	12.20	9.80	7.43
<i>Run 4</i>	2.85	13.53	11.54	10.02	5.87
<i>Run 5</i>	2.95	13.32	10.95	9.70	6.89
<i>Run 6</i>	3.19	12.16	12.03	9.70	6.84
<i>Run 10A</i>	3.42	13.98	10.95	9.11	6.54
<i>IBA 30</i>	3.39	12.52	12.56	9.81	6.70

As expected with samples exhibiting such similar XRD patterns, there is little variation in crystallite size between these samples.

There are several different ways to calculate the unit cells of EMD structures. This, combined with confusion over the correct indexing system for use in highly defective EMD structures (such as the samples examined in this section), and the inherent inaccuracies of unit cell calculations for highly faulted structures, means that the following calculations are approximations at best. Pannetier and Chabre [8]

<sup>1</sup> Due to the defects and crystal strain in the EMD crystal structure causing peak shifts and broadening, there is some degree of error for any crystallite size analysis performed using XRD data.

have even suggested that it is impossible to calculate the true unit cell parameters for EMD. Table 3.5 shows both the orthorhombic and hexagonal unit cells, calculated using an indexing system developed by Krey. Again there is little variation within these results.

**Table 3.5:** The orthorhombic and hexagonal unit cells of powdered EMD samples from the HiTec Energy pilot plant, calculated using the Krey indexing system.

Sample	Orthorhombic Unit Cell			Hexagonal Unit Cell	
	$a$ (Å)	$b$ (Å)	$c$ (Å)	$a$ (Å)	$c$ (Å)
<i>Run 2</i>	4.373	9.452	2.777	2.777	4.373
<i>Run 4</i>	4.373	9.552	2.776	2.776	4.373
<i>Run 5</i>	4.355	9.552	2.776	2.776	4.355
<i>Run 6</i>	4.373	9.562	2.775	2.775	4.373
<i>Run 10A</i>	4.352	9.618	2.773	2.773	4.352
<i>IBA 30</i>	4.373	9.531	2.778	2.778	4.373

The Krey system was used to index these structures as it was found over the course of this project, and by several other authors [4, 8] to be superior to other methods, such as the Maskell system, which tends to overestimate the  $b$  lattice parameter.

Table 3.6 shows the concentration of pyrolocite ( $P_r$ ) and the degree of micro-twinning ( $T_w$ ) present in the HiTec Energy pilot plant samples. These values were calculated using the structural model suggested by Pannetier and Chabre [8]. These results show that according to the Pannetier model, the levels of both pyrolocite and micro-twinning vary very little between the samples, and there does not appear to be any significant trends between the results of this model and the deposition conditions. Given the samples exhibit such similar XRD patterns this is not unexpected. The HiTec Energy samples have  $P_r$  values of  $\sim 0.36$  (%pyro = 22%) which is slightly less than the  $P_r \sim 0.45$  (%pyro = 33%) reported for EMD samples by Pannetier [8], but compares well to the results of Williams [4] who reported values  $P_r$  of  $\sim 0.32$  (%pyro = 19%) for EMD samples with similar amounts of twinning. These results indicate that the concentration of pyrolocite within these samples is generally quite low, which is consistent with the literature [4, 9], and is a

good indicator that the EMD produced at the HiTec pilot plant is of fairly high quality. As there is no evidence of the 221 or 061 peaks splitting into the 221/240 or 002/061 doublets, these samples are assigned  $Tw$  values of 100%. This result was consistent with those found in literature which report high  $Tw$  values that are close to 100% [8]. However slight changes in the peak shapes of the 221 and 061 peaks may suggest that the degree of twinning is more varied in these samples than the Pannetier model predicts. With this in mind  $Tw$  was recalculated using equation 3.2 [8], and the Krey unit cell parameters (shown in Table 3.6). These results confirm that the Pannetier model breaks down for highly disordered EMD samples, such as those supplied by HiTec Energy. The inaccuracies and ambiguity of this model highlight the need for a more comprehensive model of the EMD crystal structure.

$$\%Tw = 871(b/2c) - 1409 \quad \text{Equation 3.2}$$

Where  $b$  and  $c$  are the EMD lattice parameters calculated using the Krey method.

**Table 3.6:** The concentration of pyrolucite ( $P_r$ ) and the degree of micro-twinning ( $Tw$ ) present in the HiTec Energy pilot plant samples, calculated using Pannetier and Chabres structural model and Krey lattice parameters [8].

Sample	$P_r$	$Tw$ (%)	$Tw$ (%) [Krey]
<i>Run 2</i>	0.34	100	87
<i>Run 4</i>	0.36	100	90
<i>Run 5</i>	0.36	100	90
<i>Run 6</i>	0.35	100	92
<i>Run 10A</i>	0.38	100	100
<i>IBA 30</i>	0.39	100	85
<i>Typical Values</i>	~ 0.45 – 0.50	~ 100	~ 100

These samples were also analysed using a computational model similar to that developed by Bowden and co-workers [6], the results of which are shown in Table 3.7.

**Table 3.7:** Structural parameters of powdered EMD samples from the HiTec Energy pilot plant calculated using Bowden and co-workers EMD XRD simulation program [10].

Sample	Lattice Parameters (Å)			$P_r$ And [%pyro]	Twin Spacing (nm)	[221] Crystallite Size (nm)
	<i>a</i>	<i>b</i>	<i>c</i>			
<b>Run 2</b>	4.435	9.548	2.810	0.19 [10%]	2.91	12.51
<b>Run 4</b>	4.414	9.593	2.800	0.16 [9%]	3.00	10.02
<b>Run 5</b>	4.429	9.555	2.789	0.14 [8%]	3.00	10.02
<b>Run 6</b>	4.414	9.593	2.800	0.17 [9%]	3.43	8.35
<b>Run 10A</b>	4.414	9.574	2.802	0.14 [8%]	3.32	10.02
<b>IBA 30</b>	4.432	9.636	2.791	0.20 [11%]	3.54	8.34

Although Bowden and co-workers' simulation program [10] was specifically designed for lithium EMD, it was deemed suitable for use in this study to simulate standard EMD samples, as the program produced good fits to the EMD XRD patterns it was applied to.

The simulated lattice parameters compare fairly well to those calculated using the Krey method, however all these axes are slightly expanded in all samples (except for sample Run10A, where there is a 0.044 Å decrease in the *b* axis). The simulated [221] crystallite size compared well to the XRD and TEM results obtain in this and other studies [11]. However the  $P_r$  (%pyro) values calculated using this program are much lower than those calculated using Pannetier and Chabres structural model [8] and those calculated by Williams [4]. At this point it is unclear which model is more accurate, which again highlights the contradictory nature of EMD research.

Table 3.8 shows the calculated Preisler Q-values, IPM numbers, and  $H_1/H_2$  ratios of the powdered EMD samples produced at the HiTec pilot plant. As expected these values are similar. These samples give typical Preisler Q-values of ~0.7 that are expected in the EMD industry, however there does not appear to be any strong correlation between the Q-value and the deposition conditions. The IPM number and  $H_1/H_2$  ratio also show no strong correlation to the deposition conditions, however the

H<sub>1</sub>/H<sub>2</sub> ratio does suggest that Run 10A is the best quality EMD produced at the HiTec Energy pilot plant.

**Table 3.8:** The calculated Preisler Q-values, IPM numbers, and H<sub>1</sub>/H<sub>2</sub> ratios of the powdered EMD samples produced at the HiTec pilot plant.

<b>Sample</b>	<b>Preisler Q-value</b>	<b>IPM number</b>	<b>H<sub>1</sub>/H<sub>2</sub> ratio</b>
<i>Run 2</i>	0.680	1.353	0.920
<i>Run 4</i>	0.703	1.319	0.926
<i>Run 5</i>	0.681	1.378	0.938
<i>Run 6</i>	0.721	1.314	0.947
<i>Run 10A</i>	0.726	1.450	1.052
<i>IBA 30</i>	0.699	1.326	0.927

### 3.1.4 TEM

Transmission electron microscopy was performed on; IBA 30, because of its similarity in terms of structure and performance to the previously analysed HiTec samples; and IC 19, because of its structural differences to the other EMD samples analysed, that is the presence of a small peak at  $\sim 28.7^\circ 2\theta$ , which was found by d-space analysis to be a result of the presence of pyrolucite in the sample. TEM analysis of IBA No. 30 and I.C. 19 confirmed that the crystal structure of EMD is indeed extremely disordered. There also seemed to be evidence of stacking disorders and twinning, however further d-space analysis is need to confirm this (see Figure 3.4). The TEM analysis also showed that the EMD grains consisted of many randomly orientated crystallites, the crystallites predominantly appear to be elliptical in morphology, with a characteristic dimension of  $\sim 10$  nm (see Figure 3.5). This is consistent with the XRD derived crystallite size results obtained in this work (excluding the broad 110 peak, which is thought to be broadened due to De Wolff defects), along with the results of Heuer and co-workers [11]. Only TEM images of IBA No. 30 are show in this thesis as they best illustrate the above observations.

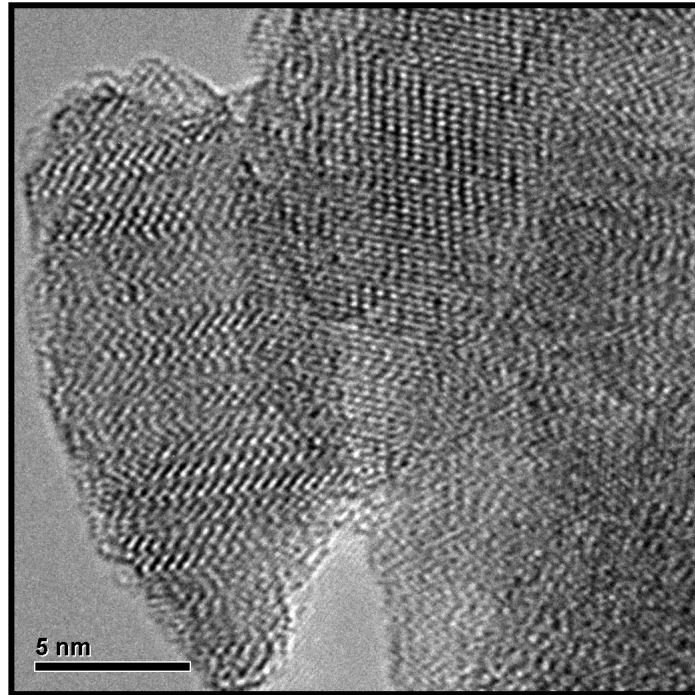


**Figure 3.4:** TEM image of IBA 30 showing a large amount of structural disorder, possible stacking faults, and twinning defects.

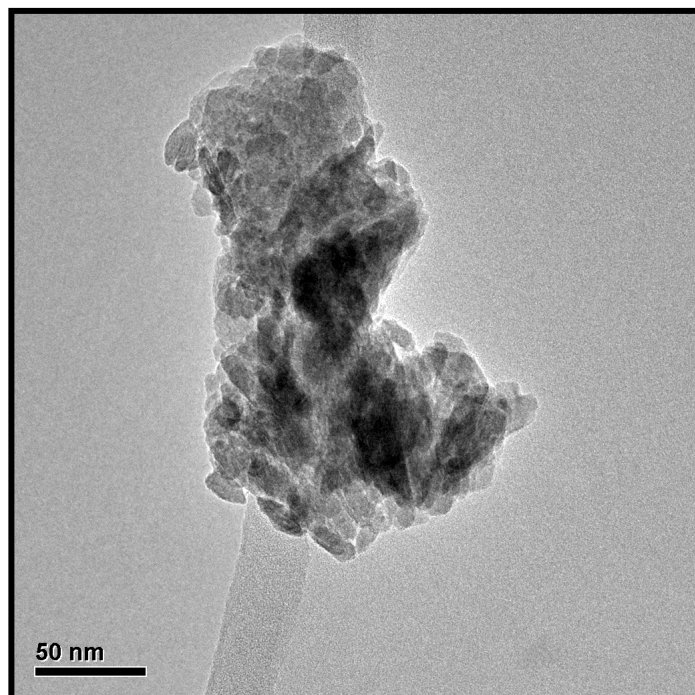


**Figure 3.5:** TEM image of IBA 30 showing, an EMD grain consisting of many randomly orientated crystallites.

### 3.1.5 Raman and FT–IR Analysis

Raman and FT–IR techniques were briefly used in this project to investigate the structure of EMD samples, as it was thought that these techniques would provide information on both the surface (Raman) and bulk (IR) aspects of the EMD crystal structure [12]. However, a combination of factors made these characterisation techniques unsuitable for use in this project. These factors are listed below:

- Raman and FT–IR are not primary structural analysis techniques hence they require calibration samples to allow meaningful analysis [13], generally these calibration samples are well-crystallised  $\text{MnO}_2$  phases with structures previously determined by XRD. This calibration method works on the assumption that the spectra of these phases can be used to determine presence of these structures in disordered  $\text{MnO}_2$  samples. Unfortunately the current lack of a suitable structural model for EMD limits the accuracy of these methods for EMD analysis, making any results obtained from attempted calibrations questionable.
- $\text{MnO}_2$  is known to be unstable and transform when exposed to laser energy. This transformation usually results in a strong Raman peak at  $\sim 650 \text{ cm}^{-1}$ , which has been attributed to the formation  $\text{Mn}_2\text{O}_3$ . As this peak was present in the majority of spectra taken, it can be assumed that significant transformation of the samples took place, thus limiting the accuracy of the analysis.
- Characteristic FT-IR  $\text{MnO}_2$  peaks are known to be located in the region of  $200 - 800 \text{ cm}^{-1}$ , unfortunately the instruments at Curtin University were unable to accurately analyse this region of the IR spectra.
- The small crystallite size of the EMD samples (calculated from XRD patterns to be on the nanometer scale) also hindered analysis of these samples via Raman. The minimum spot size available on the instrument was  $2 \mu\text{m}$ , which was far too large to accurately analyse single crystals of EMD.
- Variations in the samples surface roughness during Raman analysis made it virtually impossible to get quantitative data.

- Finally, the quality of the Raman and FT-IR spectra obtained in these preliminary analyses was relatively poor, as the spectra were quite noisy and had poor resolution.

However the preliminary analysis of these samples via Raman did provide some structural information, as differences were observed in the Raman spectra of EMD grains within a single sample, indicating possible heterogeneity within the EMD deposit.

### 3.2 Analysis of EMD Chips from the HiTec Energy Pilot Plant

Along with the powdered EMD samples, HiTec Energy also provided a series of graded EMD chips that were produced at their pilot plant. These samples were graded from “Poor” to “Very Good” based on Dr Christopher Ward’s experience in the field. The samples were analysed to allow the investigation of as-deposited EMD materials, and to determine the structural features that control EMD quality. The quality of the EMD chips and the experimental runs they were sampled from are shown in Table 3.9.

**Table 3.9:** The quality of EMD chips from the HiTec Energy pilot plant, and the experimental run they were sampled from.

Origin of Sample	Bath Conditions			Grade
	Current Density (A/m <sup>2</sup> )	[Mn] (g/L)	[H <sub>2</sub> SO <sub>4</sub> ] (g/L)	
<i>Run 10A</i>	60	60	35	Very Good
<i>Run 2</i>	55	45	35	Good
<i>Run 6</i>	65	60	35	Medium
<i>Run 4</i>	65	45	35	Poor

#### 3.2.1 SEM

SEM characterisation of EMD chips revealed that the surface topography and morphology of the EMD chips analysed can vary significantly from sample to sample (Figure 3.6), and within single samples (Figure 3.7). These variations in

morphology within single samples indicate that EMD may be a somewhat heterogeneous material, which is consistent with the results of Swinkels and Hall [14], who reported that EMD was very heterogeneous in nature. Literature also reports that EMD morphology can be independent of the structural parameters of the sample [15-18], this further complicates the characterisation of this substance. Adelkhani [15] also reported a “thistle-like” morphology which contained XRD evidence of  $\alpha$ - $\text{MnO}_2$  (a non battery active form of  $\text{MnO}_2$ ), that was similar to morphology shown in Figure 3.6c.

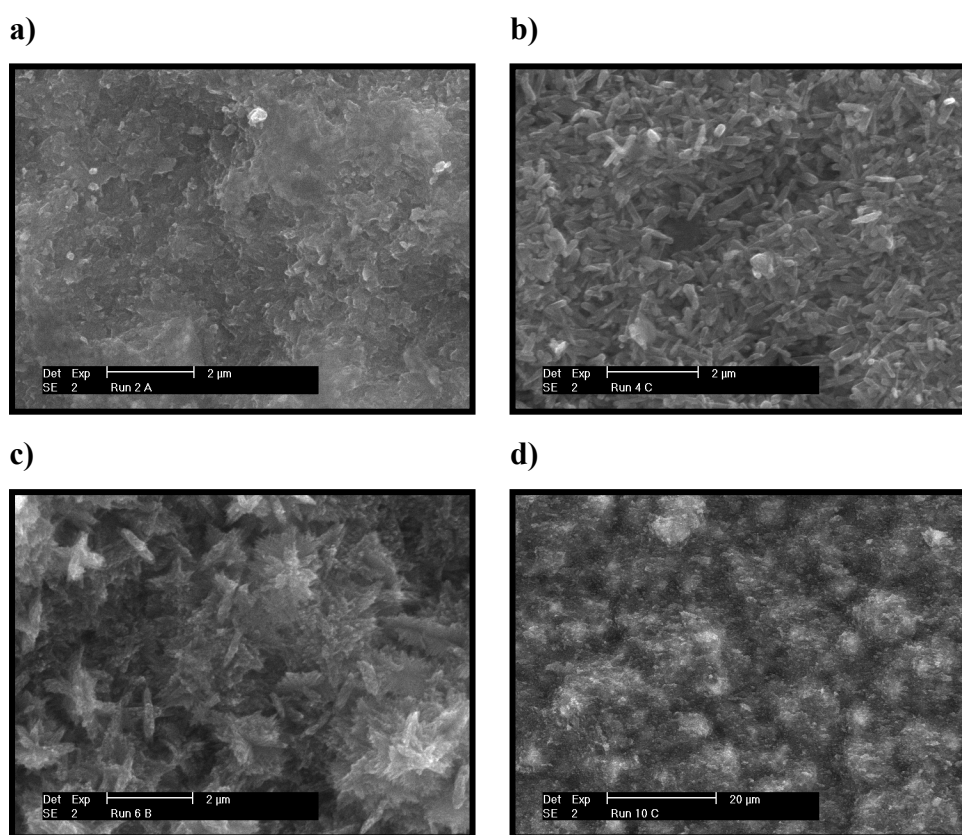


**Figure 3.6:** SEM images showing variations in morphology between EMD samples; a) Run 2, b) Run 4, c) Run 6 and, d) Run 10.

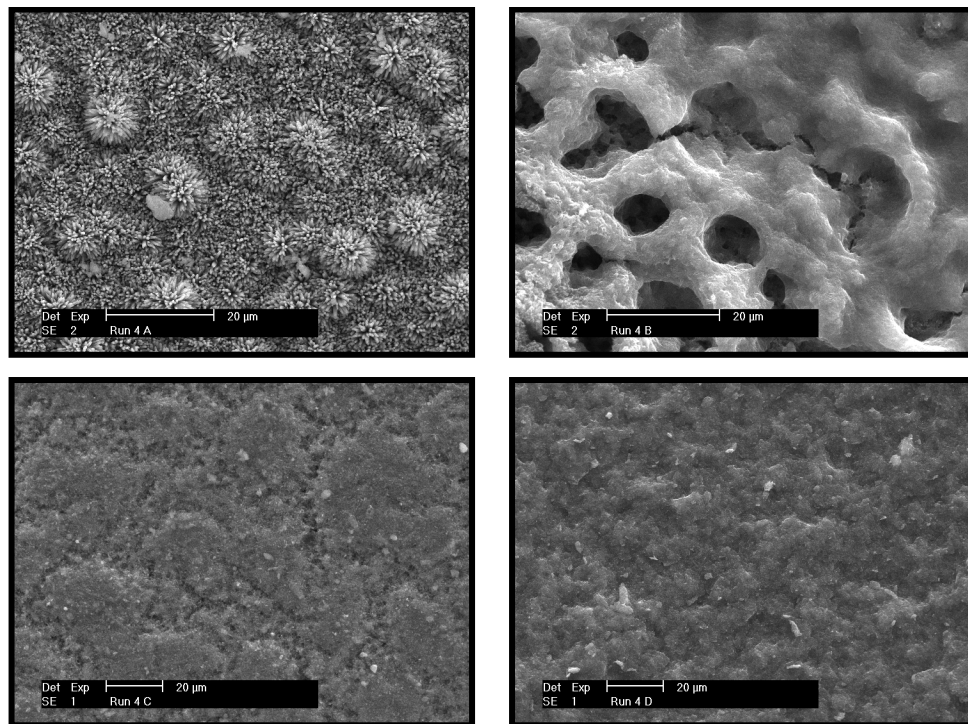


**Figure 3.7:** SEM images showing variations in morphology within a EMD single sample (Run 4).

Despite this, trends in overall morphology are evident. EMD that was classified as “Very good” and “Good” exhibited a densely packed “plate-like” crystallite morphology (Figure 3.8a), this combined with the small crystallite size, means that determination of the crystallite morphology in these samples is difficult. EMD that was classified as “Poor” exhibited areas of less densely packed “urchin-like” (that is; spheres of “needle-like” structures) and “needle-like” morphologies (Figure 3.8b). The crystallite sizes in samples classified as “Poor” were generally much larger than those in higher quality EMD samples. Samples classified as “Medium” exhibited a composite of both “urchin/needle” and “plate-like” (Figure 3.8c). It is apparent that as the quality of the EMD sample increased, the “urchin/needle” morphology seemed to become more disordered, and moved to the more “plate-like” morphology, that seems to dominate higher quality samples. It should be noted that a similar morphology has been observed by Adelkhani [15] and was found to contain the non-battery active  $\alpha$ - $\text{MnO}_2$ , this may explain the “Medium” rating however there was no evidence of  $\alpha$ - $\text{MnO}_2$  in the “Medium” samples’ XRD pattern.

The variable morphology observed in these EMD samples has also been observed in other polymorphs of manganese dioxide, such as todorokite, which exhibits a platy morphology in some samples and a fibrous morphology in others [19].

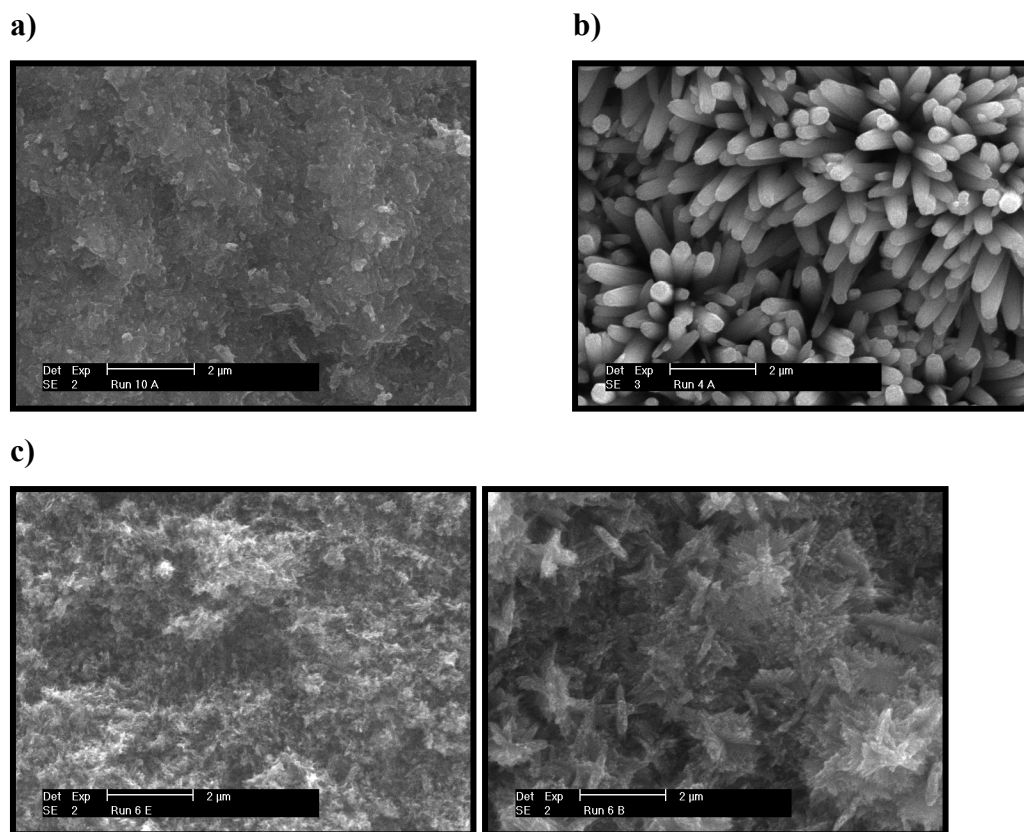


**Figure 3.8:** SEM images of EMD chips produced at the HiTec Energy pilot plant showing the different morphologies associated with **a)** Very Good and Good quality EMD, **b)** Poor quality EMD and, **c)** Medium quality EMD.

The morphologies of these samples may help explain some of their physical properties such as hardness and density. Densely packed “plate-like” morphologies, like those observed in “Good” EMD, generally result in harder/denser materials, than the less densely packed “urchin/needle-like” morphologies observed in “Poor” EMD. This corresponds well to the physical properties of these samples, and is also consistent with the literature; as batteries are fixed volume devices, higher density EMD is usually favoured [1].

Similar morphologies to those seen in the “Poor” EMD samples have been observed in both  $\alpha$  and  $\beta$ -MnO<sub>2</sub> samples prepared via a homogenous catalytic route by Li and co-workers [20]. As  $\alpha$  and  $\beta$ -MnO<sub>2</sub> are both non-battery active forms of MnO<sub>2</sub>, the presence of crystallites with similar morphologies may also in part explain the “Poor” rating of this sample. The presence of pyrolucite ( $\beta$ -MnO<sub>2</sub>) in the “Poor” EMD sample was confirmed by XRD analysis, see Figure 3.9.

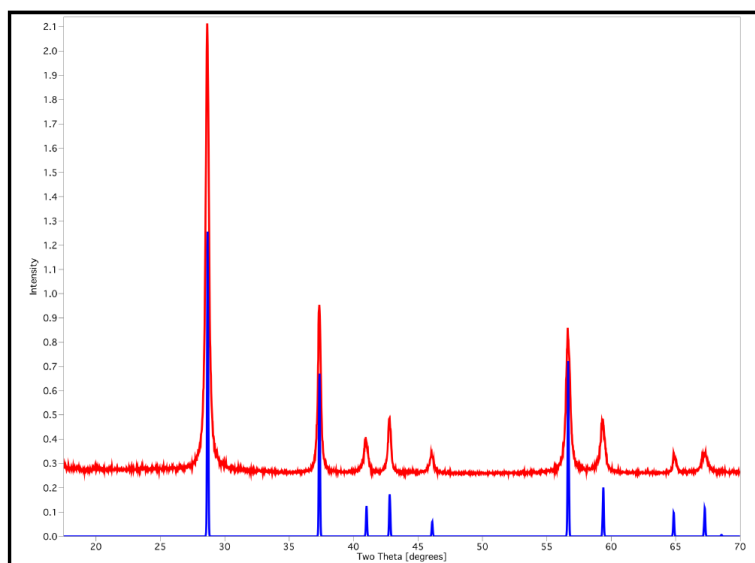


**Figure 3.9:** A comparison of the simulated XRD pattern of pyrolucite [21] [Blue] to the experimental XRD pattern of Poor quality EMD.

### 3.2.2 XRD

XRD analysis of EMD chips from the HiTec Energy pilot plant showed greater differences in structure than the bulk powder EMD samples that were previously analysed. Figure 3.10 shows the powder XRD patterns of samples classified from “poor” through to “very good”.

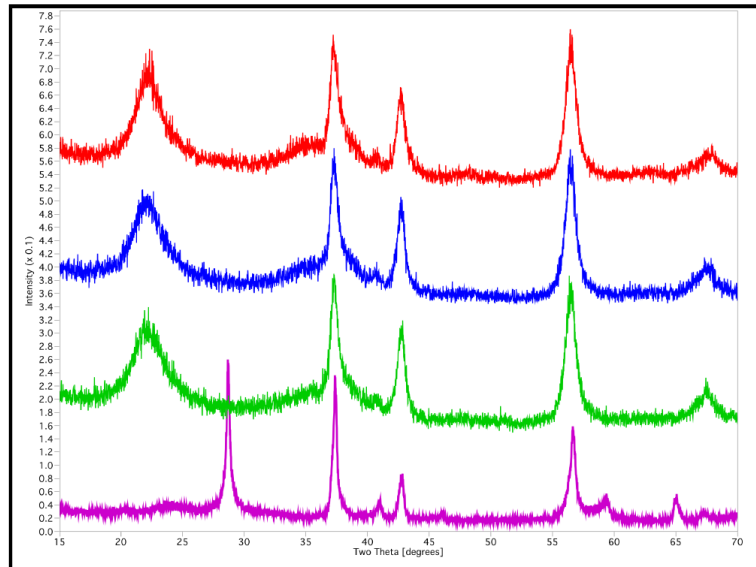


**Figure 3.10:** XRD pattern of EMD chips produced at the HiTec Energy pilot plant: Very good EMD [Red]; Good EMD [Blue]; Medium EMD [Green]; and Poor EMD [Pink].

The XRD pattern of EMD classified as “poor” shows that the sample is likely to be predominantly pyrolucite. As the quality of the EMD increased the patterns moved closer to that of IBA 30. The differences between samples classified, as “medium”, “good”, and “very good” were slight, with the “very good” sample producing a pattern with slightly more peak definition over the entire pattern, although more noticeably at  $2\theta$  values that correspond to ramsdellite peak positions.

### 3.2.2.1 Analytical XRD Parameters of HiTec Energy EMD Chips

As discussed in section 3.1.3.2 there are several important parameters that can be derived from the XRD patterns of EMD that provide information about the structure and quality of the EMD deposited. Due to the fact that the “Poor” EMD sample was found to be pyrolucite, it has been omitted from this section.

**Table 3.10:** The average crystallite sizes of EMD chips from the HiTec Energy pilot plant.

Grade	Average Crystallite Size (nm)				
	110	021	121	221	061
<i>Very Good</i>	3.09	13.32	12.20	9.80	7.43
<i>Good</i>	2.85	13.53	11.54	10.02	5.87
<i>Medium</i>	2.95	13.32	10.95	9.70	6.89

**Table 3.11:** The orthorhombic and hexagonal unit cells of EMD chips from the HiTec Energy pilot plant, calculated using the Krey indexing system.

Grade	Orthorhombic Unit Cell			Hexagonal Unit Cell	
	<i>a</i> (Å)	<i>b</i> (Å)	<i>c</i> (Å)	<i>a</i> (Å)	<i>c</i> (Å)
<i>Very Good</i>	4.367	9.468	2.786	2.786	4.367
<i>Good</i>	4.358	9.560	2.777	2.777	4.358
<i>Medium</i>	4.367	9.556	2.772	2.772	4.367

**Table 3.12:** The concentration of pyrolucite ( $P_r$ ) and the degree of micro-twinning ( $Tw$ ) present in the HiTec Energy pilot plant EMD chips, calculated using Pannetier and Chabres structural model and Krey lattice parameters [8].

Grade	$P_r$	$Tw$ (%)	$Tw$ (%) [Krey]
<i>Very Good</i>	0.39	100	71
<i>Good</i>	0.39	100	90
<i>Medium</i>	0.38	100	92

**Table 3.13:** Structural parameters of EMD chips from the HiTec Energy pilot plant calculated using Bowden and co-workers EMD XRD simulation program [10].

Grade	Lattice Parameters (Å)			$P_r$ and [%pyro]	Twin Spacing (nm)	[221] Crystallite Size (nm)
	<i>a</i>	<i>b</i>	<i>c</i>			
<i>Very Good</i>	4.418	9.561	2.813	0.12 [6%]	4.18	10.01
<i>Good</i>	4.435	9.623	2.803	0.19 [10%]	3.77	12.51
<i>Medium</i>	4.465	9.641	2.772	0.15 [8%]	3.72	10.01

**Table 3.14:** The calculated Preisler Q-values, IPM numbers, and  $H_1/H_2$  ratios of the EMD chips produced at the HiTec pilot plant.

Grade	Preisler Q-value	IPM number	$H_1/H_2$ ratio
<i>Very Good</i>	0.877	1.365	1.197
<i>Good</i>	0.741	1.295	0.959
<i>Medium</i>	0.743	1.364	1.014

The above Table 3.10 – 3.14 show that there is very little difference between “Very Good, Good, and Medium” grade EMD when analysed by XRD, however “Very Good” EMD does seem to exhibit less twinning than the other grades of EMD. The calculated Q-values suggest that all the samples contain similar amounts of  $\gamma$ -MnO<sub>2</sub> and  $\epsilon$ -MnO<sub>2</sub>, however the “Very Good” EMD also exhibits a higher Q-value than the other grades suggesting it contains more  $\gamma$ -MnO<sub>2</sub> than the other samples. The “Very Good” sample also has a higher  $H_1/H_2$  ratio, which adds some weight to the assertion that higher  $H_1/H_2$  ratios indicate a high quality of EMD.

### 3.2.3 AFM

Atomic force microscopy was performed on several EMD samples from the HiTec Energy pilot plant, unfortunately the majority of the samples exhibited surface and bulk structures that produced cantilever artefacts, indicating the samples were too rough for meaningful analysis. Examination of SEM images of the sample showed that the most suitable sample for AFM analysis was a chip from RUN 6, which was

classified as a medium class EMD, produced at  $65 \text{ A/m}^2$ , from an electrolyte containing  $60 \text{ g/L Mn}^{2+}$  and  $35 \text{ g/L H}_2\text{SO}_4$ . Although the quality of the AFM scan was slightly improved using this sample, the surface still appeared to be too rough. To combat this the AFM was switched from contact mode to tapping mode, as tapping mode uses a cantilever with a sharper tip, which allows for imaging of samples with fine/rough structures. Switching to tapping mode produced significantly improved image, but unfortunately due to sample roughness high-resolution images could not be obtained. The lower resolution images did not contain any meaningful structural data. An AFM image of the RUN 6 chip, is shown below in Figure 3.11.

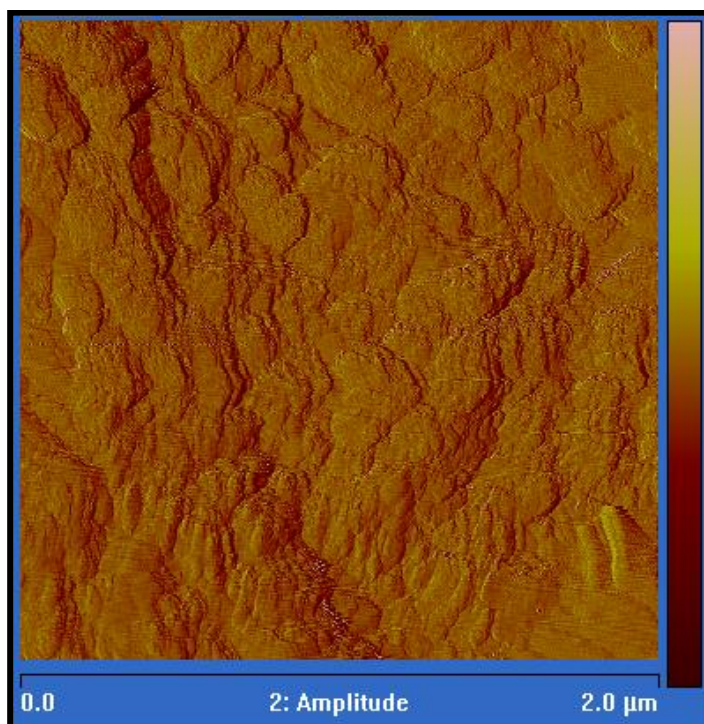


**Figure 3.11:** An AFM image (max amplitude 215.2 mV) of a chip from RUN 6, a medium class EMD, produced at  $65 \text{ A/m}^2$ , from an electrolyte containing  $60 \text{ g/L Mn}^{2+}$  and  $35 \text{ g/L H}_2\text{SO}_4$ , from the HiTec Energy pilot plant

Note: Attempts were made to construct a custom AFM electro-deposition rig, using a platinum coated mica disc as the working electrode, unfortunately these attempts were unsuccessful and therefore abandoned.

### 3.3 Conclusions

Analysis of the HiTec samples confirms that EMD is a disordered material, with very small crystallite sizes (~10 nm) in an apparent random orientation; the material also exhibits both homogeneous and heterogeneous traits. Small changes in the deposition conditions of EMD have little effect on the structural characteristics of EMD, therefore this study will use a wide range of deposition conditions to investigate the effect of deposition conditions on the structural characteristics of EMD.

There were very few discernable differences between the EMD samples analysed in this section, (this may have been a function of the small number of samples analysed), and highlights the possible need for chemometric treatment of EMD XRD patterns as described by Swinkels [22]. Analysis of EMD chips, however, shows when grading EMD the most obvious indicator of poor quality is the physical properties of the sample. That is, high quality EMD is generally harder and denser than lower quality samples and possesses a “plate-like” morphology. The presence of discrete crystalline pyrolycrite within the sample is also a key indicator of lower quality EMD, the pyrolycrite can be detected via XRD, or SEM via the differing morphologies (pyrolycrite has a distinctive “urchin” morphology). With this knowledge in hand, SEM and XRD could be used as basic quality control methods. The relative consistency and robustness of SEM and XRD, along with the large amount of information that can be gleaned from the use of these techniques, make SEM and XRD analysis the most appropriate characterisation techniques for use in this study.

The above analyses also show the contradictory nature of models used to characterise EMD, and highlights the need for a better EMD model.

### 3.4 References

1. Ward, C., *Notes on the Production and Analysis of EMD*, 2001, HiTec Energy.
2. Ward, C.B., A.I. Walker, and A.R. Taylor, *The Production of Alkaline Grade EMD at Australian Manganese Company Limited*. Prog. Batteries Battery Mater., 1992. **11**: p. 40-46.
3. *Handbook of Manganese Dioxides Battery Grade*, ed. D. Glover, B.S. Jr, and A. Kozawa, 1989: The International Battery Association (IBA, Inc.).
4. Williams, R.P., *Characterisation and Production of High Performance Electrolytic Manganese Dioxide for use in Primary Alkaline Cells.*, in *Department of Chemistry*, 1995, The University of Newcastle: Newcastle, Australia.
5. Simon, D.E., T.N. Andersen, and C.D. Elliott, *A Rietveld Refinement Model of EMD Powder Patterns*. ITE Lett. Batteries, New Technol. Med., 2000. **1**(3): p. 10-19.
6. Bowden, W., R. Sirotina, and S. Hackney, *Manganese Dioxide for Alkaline Zinc Batteries: A single-phase model*. ITE Lett. Batteries, New Technol. Med., 2003. **4**(1): p. 26-37.
7. Ghaemi, M., Z. Biglari, and L. Binder, *Effect of bath temperature on electrochemical properties of the anodically deposited manganese dioxide*. J. Electroanal. Chem., 2001. **102**(1-2): p. 29-34.
8. Chabre, Y. and J. Pannetier, *Structural and Electrochemical Properties of the Proton / gamma MnO<sub>2</sub> System*. Prog. Solid State Chem., 1995. **23**: p. 1-130.
9. Pannetier, J., *Characterization of Manganese Dioxides by X-ray Diffraction*. Prog. Batteries Battery Mater., 1994. **13**: p. 132-135.

10. Hackney, S., *EMDXRDSIMBeta2*, 2002.
11. Heuer, A.H., A.Q. He, P.J. Hughes, and F.H. Feddrix, *Microstructure of Electrolytic MnO<sub>2</sub>: A Transmission Electron Microscopy Study of Bulk Material*. ITE Lett. Batteries, New Technol. Med., 2000. **1**(6): p. 76-80.
12. Mermoux, M., C. Poinignon, and P.-O. Robert, *Structural-Chemical Disorder of Manganese Dioxides: Influence on the Infrared and Raman Spectra*. ITE Lett. Batteries, New Technol. Med., 2001. **2**(1): p. 59-68.
13. Potter, R.M. and G.R. Rossman, *The tetravalent manganese oxides: identification, hydration, and structural relationships by infrared spectroscopy*. Am. Mineral., 1979. **64**: p. 1199-1218.
14. Swinkels, D.A.J. and K.N. Hall, *Some Physical Properties of EMD*. Prog. Batteries Battery Mater., 1992. **11**: p. 16-21.
15. Adelkhani, H., *The effect of acidity of electrolyte on the porosity and nanostructure morphology of electrolytic manganese dioxide*. Appl. Surf. Sci., 2012. **258**: p. 6232-6238.
16. Adelkhani, H. and M. Ghaemi, *Influence of the solution pH on the nanostructural, and electrochemical performance of electrolytic manganese dioxide*. J. Alloys Compd., 2009. **481**(1-2): p. 446-449.
17. Hill, L.I., H. Arrive, D. Guyomard, and H. Arrivé, *Effect of synthesis conditions on the morphology of MnO<sub>2</sub> ( $\alpha$ -,  $\beta$ -,  $\gamma$ -) synthesized by the hydrothermal-electrochemical method*. Ionics, 2002. **8**(3-4): p. 161-171.
18. Machefaux, E., A. Verbaere, and D. Guyomard, *Preparation of nanowires of M substituted manganese dioxides (M=Al, Co, Ni) by the electrochemical-hydrothermal method*. J. Phys. Chem. Solids, 2006. **67**(5-6): p. 1315-1319.
19. Turner, S. and P.R. Buseck, *Todorokites: A New Family of Naturally Occuring Manganese Oxides*. Science, 1981. **212**(4498): p. 1024-1027.

20. Li, Z., Y. Ding, Y. Xiong, and Y. Xie, *Rational Growth of Various of  $\alpha$ -MnO<sub>2</sub> Hierarchical Structures and  $\beta$ -MnO<sub>2</sub> Nanorods via a Homogeneous Catalytic Route*. *Cryst. Growth Des.*, 2005. **5**: p. 1953-1958.
21. Baur, W.H., *Rutile-type compounds. V, Refinements of MnO<sub>2</sub> and MgF<sub>2</sub>*. *Acta Crystallogr.*, 1976. **B32**: p. 2200-2204.
22. Swinkels, D.A.J., *Chemometric Treatments of XRD Patterns*. *Prog. Batteries Sol. Cells*, 1990. **9**: p. 9-18.

*Every reasonable effort has been made to acknowledge the owners of copyright material. I would be pleased to hear from any copyright owner who has been omitted or incorrectly acknowledged.*

#### 4 ANALYSIS OF EMD PRODUCED IN THIS STUDY

EMD samples produced over the course of this study were characterised using a combination of on-electrode SEM, and low background XRD. SEM analysis was used to examine the surface topography of as-deposited EMD, crystallite size and morphology (to sub-micron resolution), as well as chemical composition including impurities (to a lower limit of approximately 1 wt%) via energy dispersive spectroscopy (EDS). Platinum electrodes were used as they are inert, and thought to have a negligible effect on the deposition process and provide good performance [1, 2]. SEM analysis was performed on-electrode to preserve the surface features of the deposited EMD and avoid any artefacts that may arise from sample preparation. Electro-deposition times of 10 minutes were used to allow total electrode coverage, while keeping the surface:bulk ratio high. Low background XRD was used to provide information about the crystal structure, phase purity, as well as crystallite size and strain information. Similarly to the SEM samples, electro-deposition times of 30 minutes were used to produce enough sample for analysis, while still maintaining a high surface:bulk ratio. On-electrode XRD analysis was not performed on the EMD samples, due to potential interferences arising from the platinum substrate, and difficulties correctly mounting the electrodes for accurate analysis. Since the quantities of EMD produced by this study were insufficient to be analysed using traditional powder XRD techniques, it was necessary to use low background XRD sample holders for accurate XRD analysis. Samples for low background XRD analysis were lightly ground, and then sonicated, so as to reduce any preferred orientation effects that may result as a consequence of using low background XRD sample holders, while limiting the damage to the crystal structure that may result from over zealous sample preparation.

Unlike the majority of previous EMD studies, which have focused on the analysis of bulk samples of EMD, the aim here was to focus on the surface of the deposit, ie. the solid/solution interface. This approach was taken for several reasons:

- Bulk EMD samples have been extensively studied, and evidence from Chapter 3 suggests that further bulk studies would not have revealed any new information on the structure of EMD.

- Surface studies should provide information on the true morphology of EMD crystallites, and the EMD growth process, which may help in the elucidation of the EMD deposition mechanism. However due to the complexity of this material, experimental investigations of EMD surfaces is extremely difficult and has not been documented [3].
- Surface studies allow the small-scale production of EMD samples, which helps to keep deposition conditions constant, allowing for more robust analysis.

#### **4.1 General Analysis of the EMD Deposition Process**

SEM analysis of the deposition of EMD samples provided valuable information about several aspects of the EMD deposition process. The true crystallite morphology of EMD could not be determined via SEM as EMD crystallites are far too small. Nevertheless, a disordered “urchin-like” morphology (Figure 4.1a) was observed in samples produced throughout this study. This morphology seems to be a result of much smaller needles, or dendrites, randomly growing from a single point. The EMD seems to be deposited at discrete growth centres with the above-mentioned morphology. Once the surface is covered with these growth centres, an intergrowth phenomenon seems to occur. This was evident when the edge of the EMD deposit was examined (Figure 4.1b). No evidence of the “plate-like” morphology mentioned in chapter 3 was found, however this was observed in the bulk of the material and may be a result of a denser intergrowth phenomenon.

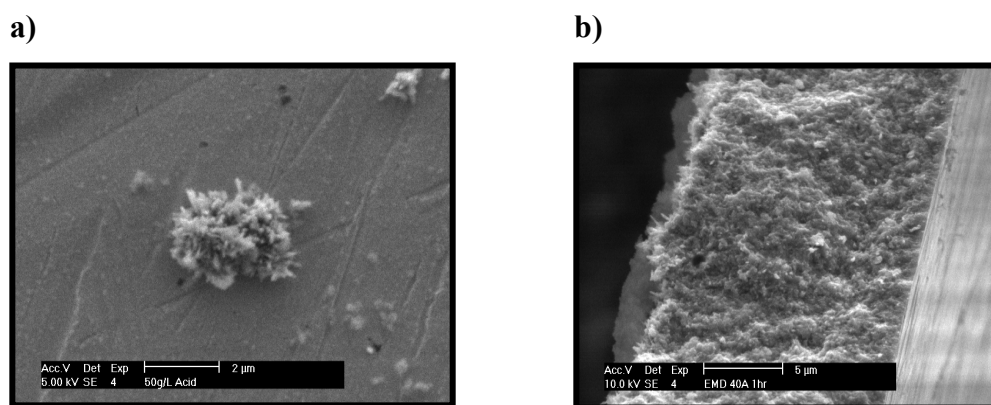


**Figure 4.1:** SEM images of EMD produced by this study, **a)** shows the disordered urchin-like morphology, **b)** shows an intergrowth of the urchin-like morphology.

During some deposition experiments a substance that did not appear to be EMD was observed on the working electrode. The appearance of additional products during deposition of EMD has been observed by several authors [4]. There are several possible explanations for this phenomenon, although it is most likely to be a result of either, an intermediate, an EMD dissolution product, or a product of a side reaction. As the origin of this substance is unknown it shall be referred to as deposition “by-product”. Only extremely small quantities of this by-product were produced, making isolation and analysis of the substance difficult. SEM analysis of what was assumed to be this by-product (Figure 4.2a) showed a much “fluffier” morphology that had far less structure than the bulk of the EMD deposited on the electrode. Analysis of the by-product using back-scattered electrons (BSE) (Figure 4.2b) revealed that the by-product and EMD have similar average atomic weights, as there was little contrast between the by-product and EMD in the BSE image. This result was confirmed by EDS analysis of the by-product, as the spectra showed that the by-product had a similar chemical composition to the EMD deposited on the electrode. This suggests that the by-product is likely to be a form of  $\text{MnO}_2$ , or a poorly crystalline manganese hydroxide or oxyhydroxide (such as  $\text{Mn}(\text{OH})_2$  or  $\text{MnOOH}$ ), as they have similar molecular weights and chemical compositions to EMD [Note: EDS is insensitive to hydrogen, so classification of hydroxides and oxyhydroxide was impossible]. Unfortunately, XRD analysis could not be performed on the by-product, due to the small quantity of sample, and thus a more accurate identification of the by-product could not be obtained. Some authors [5, 6] believe that the stability of intermediate

$\text{Mn}^{3+}$  species (for example  $\text{MnOOH}$ ,  $\text{Mn}_2\text{O}_3$  and  $[\text{Mn}(\text{H}_2\text{O})_6]^{3+}$ ) effects the morphology of EMD during the deposition process. These species are thought to form passive layers that cause inhibition of growth mechanisms and therefore have an effect on the morphology of EMD at various deposition conditions. The observation of this “by-product” adds some supporting evidence to this argument.

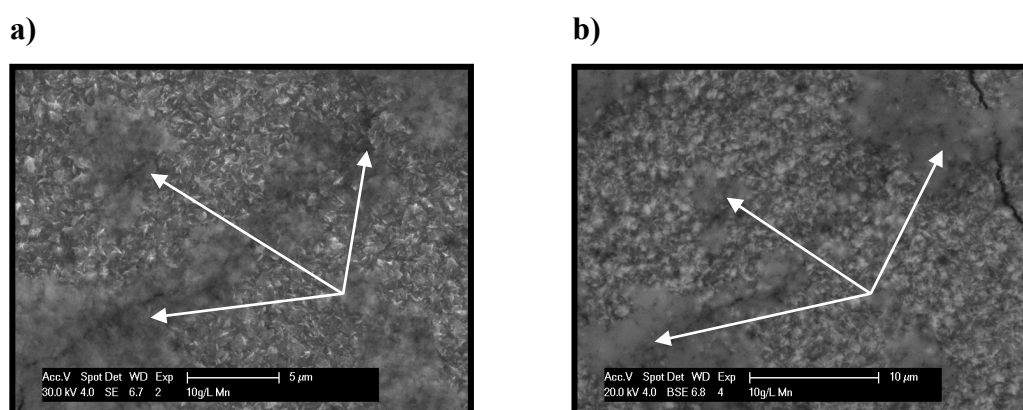


**Figure 4.2:** SEM images of EMD deposited from an electrolyte containing 10 g/L  $\text{Mn}^{2+}$  and 35 g/L  $\text{H}_2\text{SO}_4$  at 93 °C using a current density of 40  $\text{A}/\text{m}^2$ . **a)** A SEM image of EMD and the deposition by-product (indicated by arrows) on its surface. **b)** A BSE image of EMD and the deposition by-product (indicated by arrows).

## 4.2 Effect of Current Density

EMD was deposited onto a platinum working electrode from an electrolyte containing 60 g/L  $\text{Mn}^{2+}$  and 35 g/L  $\text{H}_2\text{SO}_4$  at 93 °C using current densities of 20, 40, 60, and 80  $\text{A}/\text{m}^2$ . The samples produced were then characterised using a combination of on-electrode SEM and low background XRD.

SEM analysis showed that the surface topography of EMD deposits is strongly influenced by the current density at which it is deposited. As expected, EMD produced at a low current density (20  $\text{A}/\text{m}^2$ ) has a slightly more defined crystal structure. A surface morphology is hard to determine (Figure 4.3a), but it could be tentatively described as an intergrowth of the urchin type morphology described in section 4.1 in appearance, although the structure of the dendrites seems to be broader. As the current density was increased to 40  $\text{A}/\text{m}^2$ , the morphology moved to a more disordered urchin shape (Figure 4.3b). EMD produced at 60  $\text{A}/\text{m}^2$ , however,

exhibited two distinct surface morphologies; firstly an urchin morphology similar to that of EMD produced at lower current densities (Figure 4.3c); and secondly a “cauliflower-like” surface morphology (Figure 4.3d). The locations of these different morphologies on the electrode are shown in Diagram 4.1. This suggests that EMD deposition process may proceed according to more than one mechanism (this is supported by the many and varied deposition mechanisms reported in literature), which produces dramatically different crystal morphologies. This variation in morphology could also be a result of varied intermediate thickness across the electrode surface. Therefore the  $60 \text{ A/m}^2$  sample can be viewed as a crossover point for these mechanisms, where both deposition processes are likely to occur. This shows that at certain conditions the structure (or more accurately the morphology) of EMD can be dramatically influenced by even slight changes in the deposition conditions, such as imperfections in the electrode substrate. The electrode deposited with EMD at  $80 \text{ A/m}^2$  showed a cauliflower morphology (Figure 4.3e), although unlike the EMD deposited at  $60 \text{ A/m}^2$ , this morphology was uniform over the entire electrode. It is thought that the “cauliflower” morphology maybe a smaller extremely disordered and less crystalline modification of the typical “urchin” morphology seen at lower current densities. The cauliflower also appears to have a hexagonal symmetry.

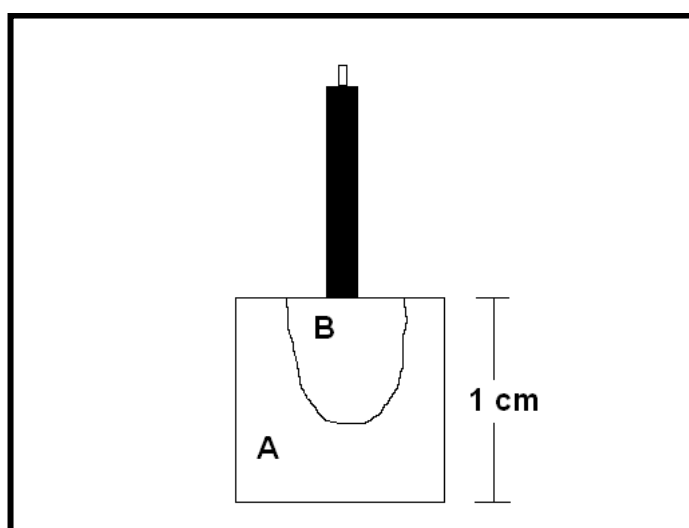


**Diagram 4.1:** The location of area of differing morphologies on a platinum electrode when plated at  $60 \text{ A/m}^2$ , “A” represents an area with a cauliflower morphology, while “B” represents the area with an urchin morphology.

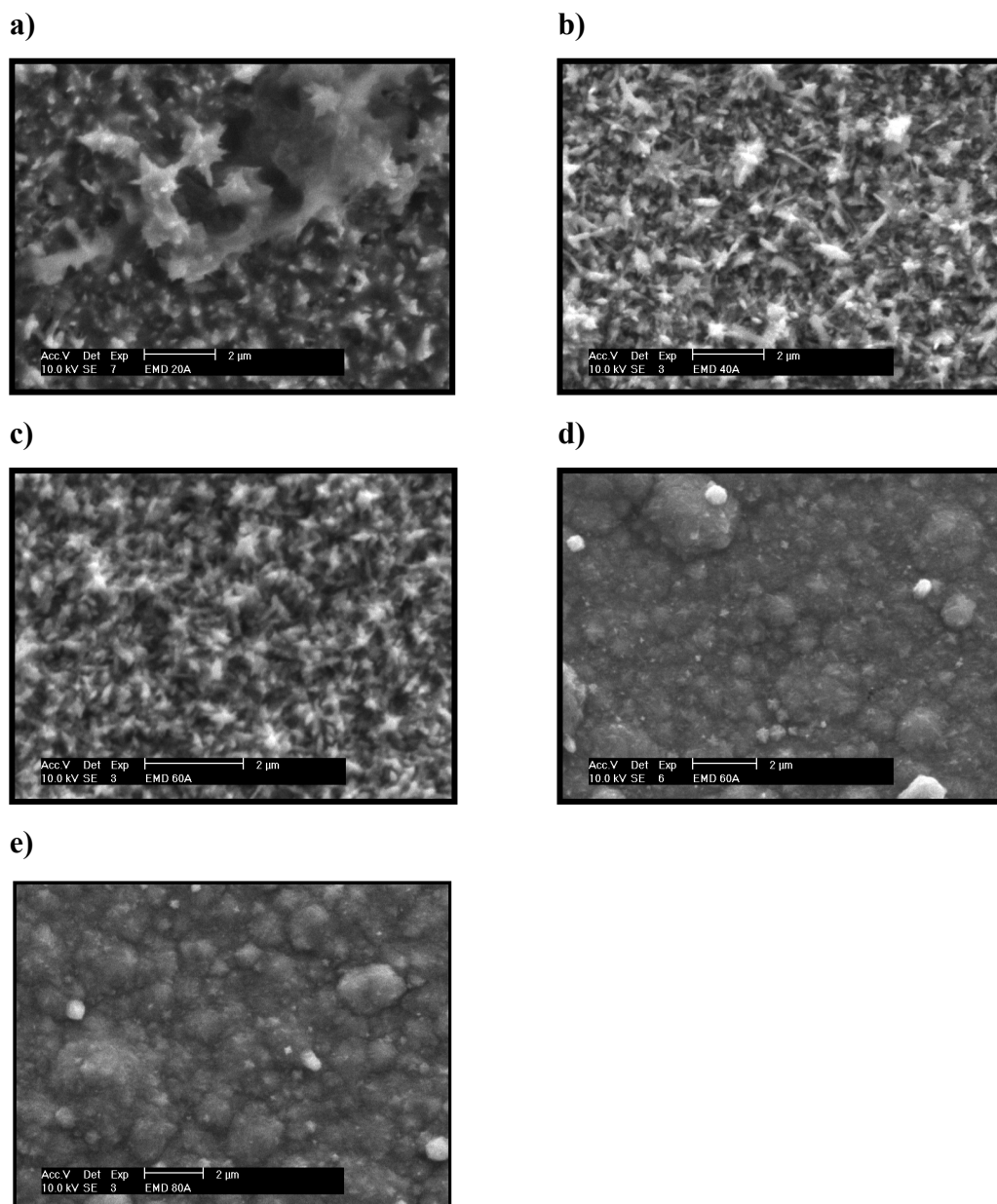


**Figure 4.3:** SEM images showing the changing surface topography at various current densities, **a)**  $20\text{A/m}^2$ , **b)**  $40\text{A/m}^2$ , **c)**  $60\text{A/m}^2$  “urchin”, **d)**  $60\text{A/m}^2$  “cauliflower”, **e)**  $80\text{A/m}^2$ .

XRD analysis of these samples (Figure 4.4), showed there was an increase in peak definition at  $\sim 21^\circ$  and from  $\sim 30^\circ$  to  $\sim 48^\circ$   $2\theta$  as a result of decreasing current density. This is likely to indicate an increase in crystallinity or order of the samples. In fact EMD samples that have more structure in these  $2\theta$  regions are referred to as “higher structure EMDs” [7]. This result is not unexpected, as increases in definition and

peak height of the 110 indicates that the sample exhibits an increased  $\gamma$ -MnO<sub>2</sub> character, which is consistent with literature [1].

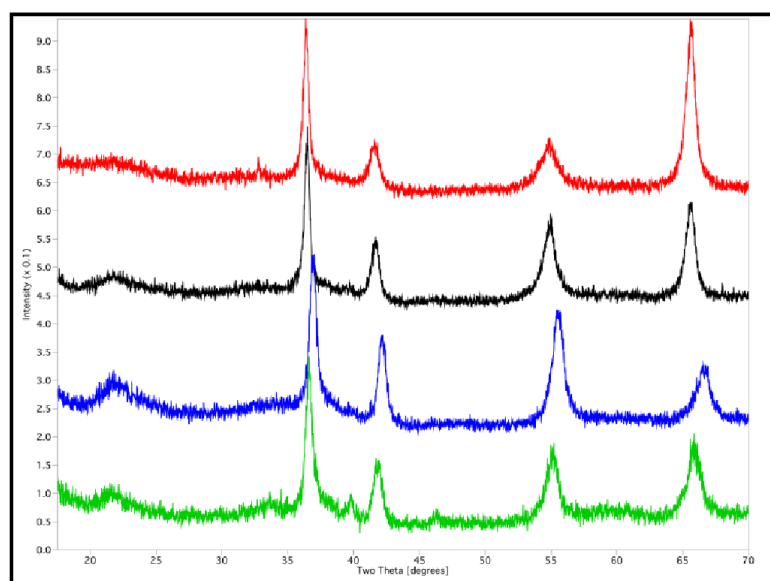


**Figure 4.4:** XRD patterns of EMD electro-deposited from electrolyte containing 60 g/L Mn<sup>2+</sup> and 35 g/L H<sub>2</sub>SO<sub>4</sub> at 93 °C at current densities of 20 [Green], 40 [Blue], 60 [Black], and 80 A/m<sup>2</sup> [Red].

As the solutions used to deposit these samples were constant, this allows the examination of the mixed potential versus time plots for these experiments (see Figure 4.5) without any artefacts created by different solution composition. Figure 4.5 shows that the electrochemical processes occurring at the working electrode differ significantly, which is consistent with the observed changes in crystallinity and morphology.

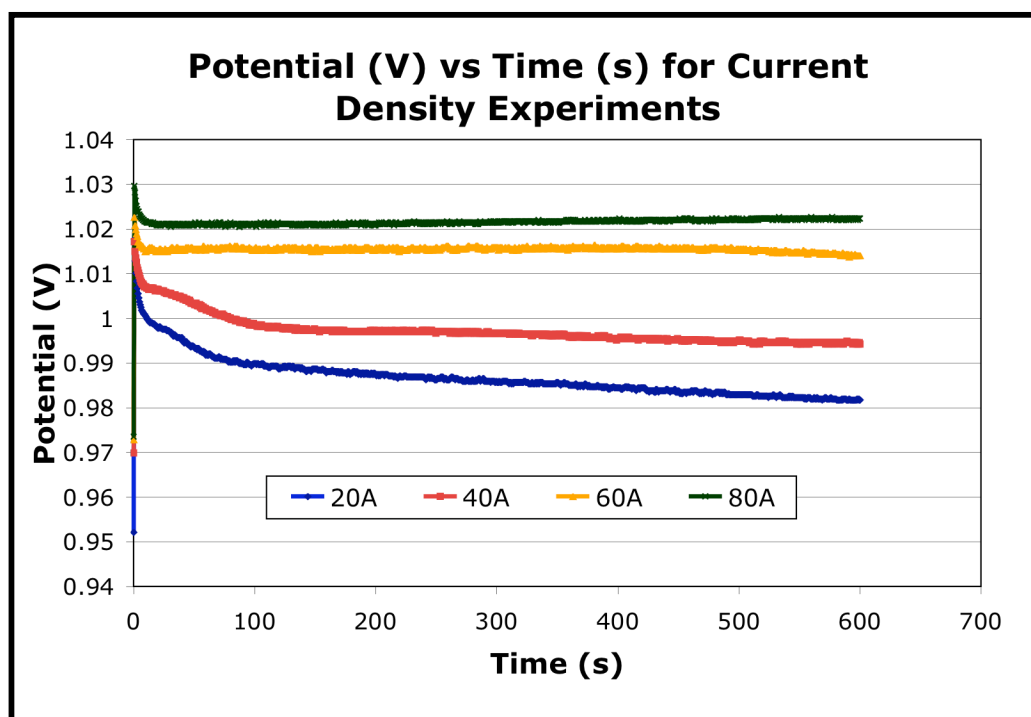


**Figure 4.5:** Mixed potential (V) versus Time (s) plot for various current densities.

The current density can be considered as the driving force of the deposition process, as the current density controls the mixed potential (deposition potential) where the higher the mixed potential the higher the driving force of deposition. In terms of a crystal growth model, higher driving forces usually favour nucleation over crystal growth, resulting in smaller crystallite sizes, a more disordered structure, and a higher concentration of defects such as lattice inclusions and vacancies (point defects). The XRDs in Figure 4.4 reflect this, exhibiting less structural order in the 22, 34 and 38 ° 2 $\theta$  peaks, and broader peaks, indicating reduced crystallite size. Unfortunately, the presence of point defects has little effect on the XRD pattern of EMD, therefore the quantity of these defects cannot be determined via XRD. However, other studies have shown that the current density controls the cell potential, oxygen generation (which creates Mn vacancies) and the amount of EMD deposited [8]. It has also been shown that increases in current density correlate to a decrease in the Mn:O ratio, and a decrease in EMD density associated with an increase in %Tw [8]. This hypothesis complements the work of Balachandran and co-workers who postulated that point defects have a stabilizing effect on twinning defects [9-11].

The XRD patterns in Figure 4.4 show evidence of preferred orientation artefacts in the spectra, as the peak height ratios change significantly in the 60 and 80A/m<sup>2</sup>. Most noticeably the height of the [061] peak is significantly increased, and the height of the [110] is significantly reduced. These preferred orientation artefacts are likely to be a result of the sample preparation, that is EMD particles which are improperly ground, or of a plate-like morphology, sit flat on the low background XRD sample holder. To test this, an 80 A/m<sup>2</sup> EMD sample was placed on to a SEM stub using the same method used for the XRD samples. The result of this analysis (see Figure 4.6) shows that preferred orientation in this type of sample would be likely to occur, as the EMD particles are laying flat. This preferred orientation affects the peak heights but does not effect the peak positions, however as the [110] peak is affected, many EMD XRD analysis methods cannot be used on these samples. These preferred orientation effects also limit the accuracy of any peak shape analysis, as it is impossible to totally differentiate real changes in peak shape and the artefacts produced by preferred orientation.

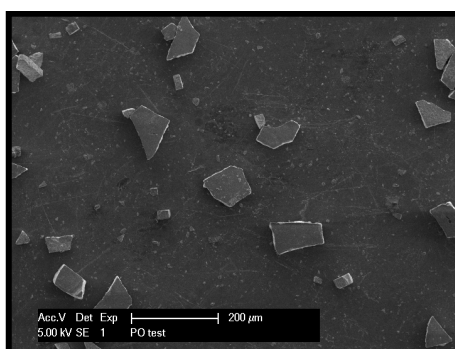


**Figure 4.6:** SEM of 80A/m<sup>2</sup> EMD prepared on an SEM stub, showing that preferred orientation of the sample is occurring, due to sample preparation.

Due to the poorer quality XRD patterns obtained from low-background XRD analysis, preferred orientation, and the nature of EMD (that is, EMD peak broadening often occurs because of defects, and peaks merging, as well as reductions in crystallite sizes) crystallite sizes were not calculated and comparisons between samples were done in a qualitative manner.

### 4.3 Effect of Temperature

EMD was deposited onto platinum working electrode at temperatures of 30, 60 and 93 °C from an electrolyte containing 60 g/L Mn<sup>2+</sup> and 35 g/L H<sub>2</sub>SO<sub>4</sub> at 40 A/m<sup>2</sup>. The samples produced were then characterised using a combination of on-electrode SEM and low background XRD.

Bath temperature had a dramatic effect on the surface topography of the EMD as well as its crystallinity. EMD deposited at 30 and 60 °C has a very smooth surface topography and does not seem to exhibit any particular morphology or crystallinity, suggesting an almost amorphous deposit (Figure 4.7a and Figure 4.7b). These samples were also more brittle than those produced at higher temperatures. EMD produced at 93 °C however exhibited a much rougher, more crystalline surface (Figure 4.7c). SEM images also suggest that the crystal size may decrease as the temperature decreases, although this observation can only be quantified by XRD analysis.

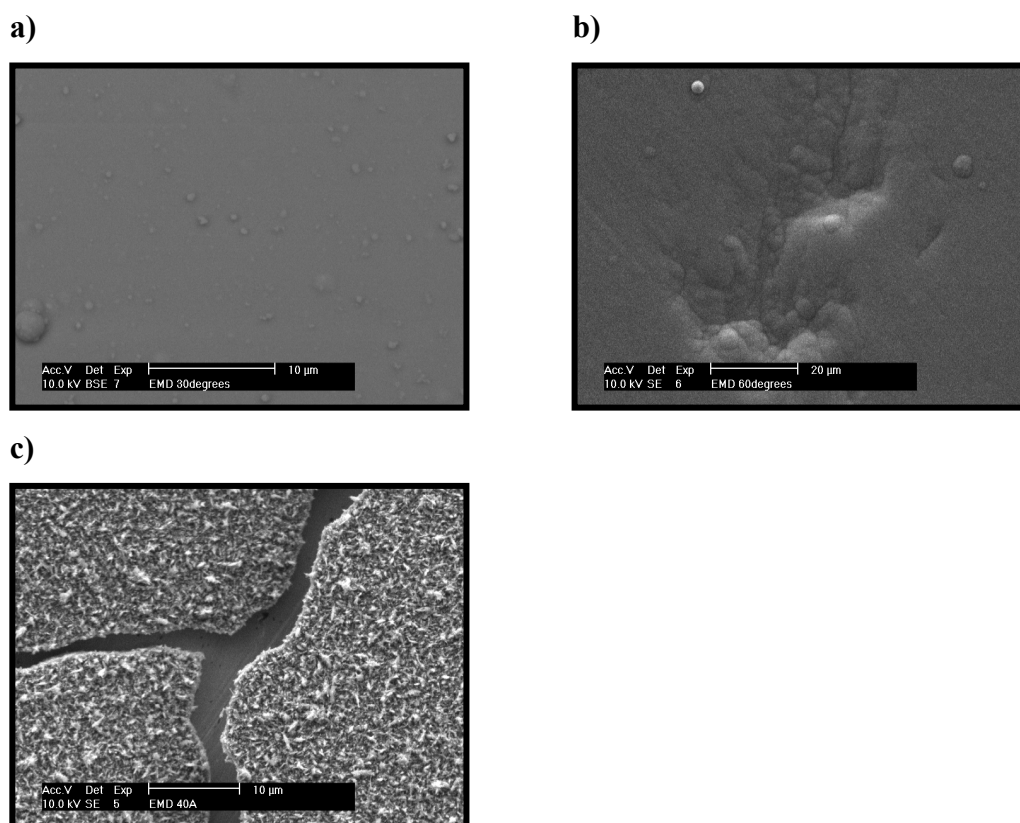


**Figure 4.7:** SEM images of the surface topographies of EMD electro-deposited at 40 A/m<sup>2</sup> from a solution containing 35 g/L H<sub>2</sub>SO<sub>4</sub>, and 60g/L Mn<sup>2+</sup> at temperatures of, a) 30 °C, b) 60 °C, c) 93 °C.

The XRD analyses of these samples are shown in Figure 4.8. These patterns confirm that, as bath temperature is decreased, both the crystallinity and crystal size of product decrease. EMD prepared at lower temperatures produces XRD patterns with amorphous characteristics, only two broad peaks that are characteristic of EMD are present at  $\sim 36^\circ$  and  $\sim 65^\circ$   $2\theta$ , other characteristic EMD peaks are only present as very broad poorly defined peaks. As the deposition temperature was increased there was an increase in definition of characteristic EMD peaks, and a decrease in peak width indicating an increase in both crystallinity and crystal size. This increase in crystallinity and crystal size occurs because as the deposition temperature increases, the deposition potential decreases (see Figure 4.9), therefore Mn species which are deposited on the growing EMD deposits surface, can move at a faster rate across the deposit surface to find a position in the crystal structure where deposition will maintain structural order. This results in crystal growth rather than nucleation and therefore larger, more ordered EMD crystals [1].

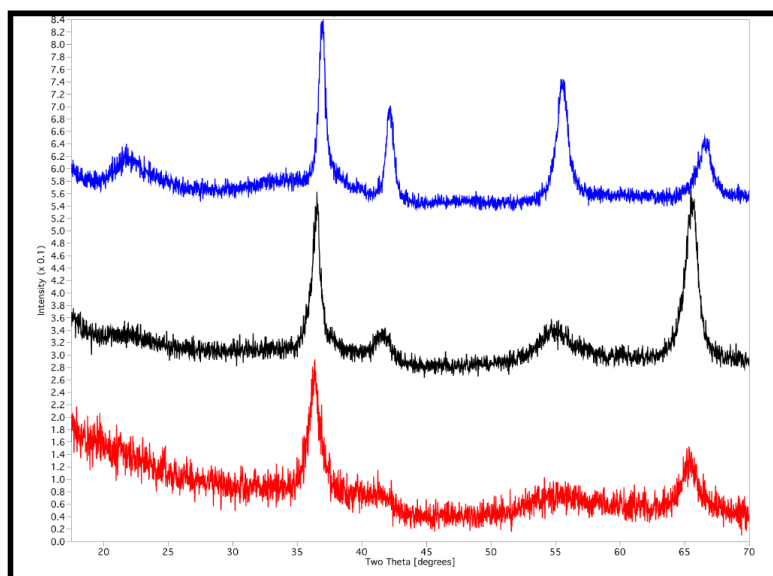


**Figure 4.8:** XRD patterns of EMD electro-deposited at  $40 \text{ A/m}^2$  from electrolyte containing  $60 \text{ g/L Mn}^{2+}$  and  $35 \text{ g/L H}_2\text{SO}_4$  at  $30 \text{ }^\circ\text{C}$  [Red],  $60 \text{ }^\circ\text{C}$  [Black], and  $93 \text{ }^\circ\text{C}$  [Blue].

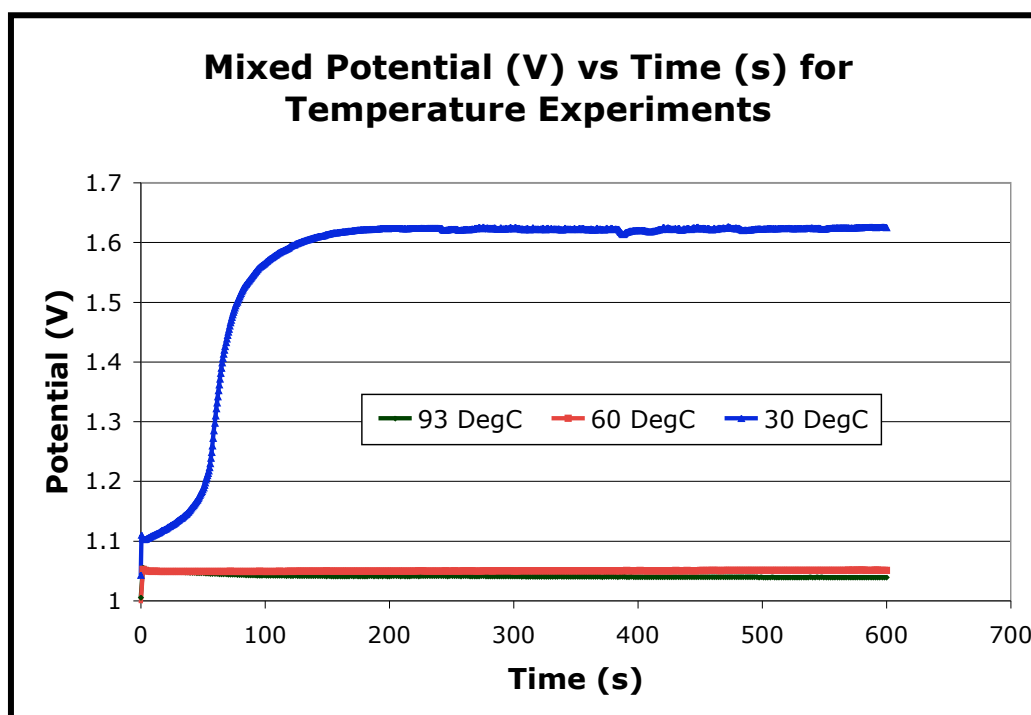


**Figure 4.9:** Mixed potential (V) versus Time (s) plot for deposition temperatures.

These results correspond well to the results of other studies, where it was observed that crystallinity increased with increased deposition temperature [12, 13]. Increasing deposition temperature is also reported to increase the amount of EMD being deposited, as higher temperatures enhance the rate of oxidation from  $\text{Mn}^{2+}$  to  $\text{MnO}_2$  [13].

#### **4.4 Effect of $\text{Mn}^{2+}$ Concentration**

EMD was deposited onto platinum working electrodes from electrolytes containing 35 g/L  $\text{H}_2\text{SO}_4$  at 40  $\text{A/m}^2$ , at 93 °C using  $\text{Mn}^{2+}$  concentrations of 10, 35, 60 and 85 g/L. The samples produced were then characterised using a combination of on-electrode SEM and low background XRD.

SEM analysis of these samples revealed that variation of the  $\text{Mn}^{2+}$  has a much smaller effect on the surface morphology of EMD deposits than temperature and current density [14]. SEM images of the surface morphologies (Figure 4.10a-d) show that the differences in morphology are slight. The most notable difference is seemingly in the 10 g/L sample, where the surface seems to be more ordered and finer in structure than those samples produced at higher  $\text{Mn}^{2+}$  concentrations.

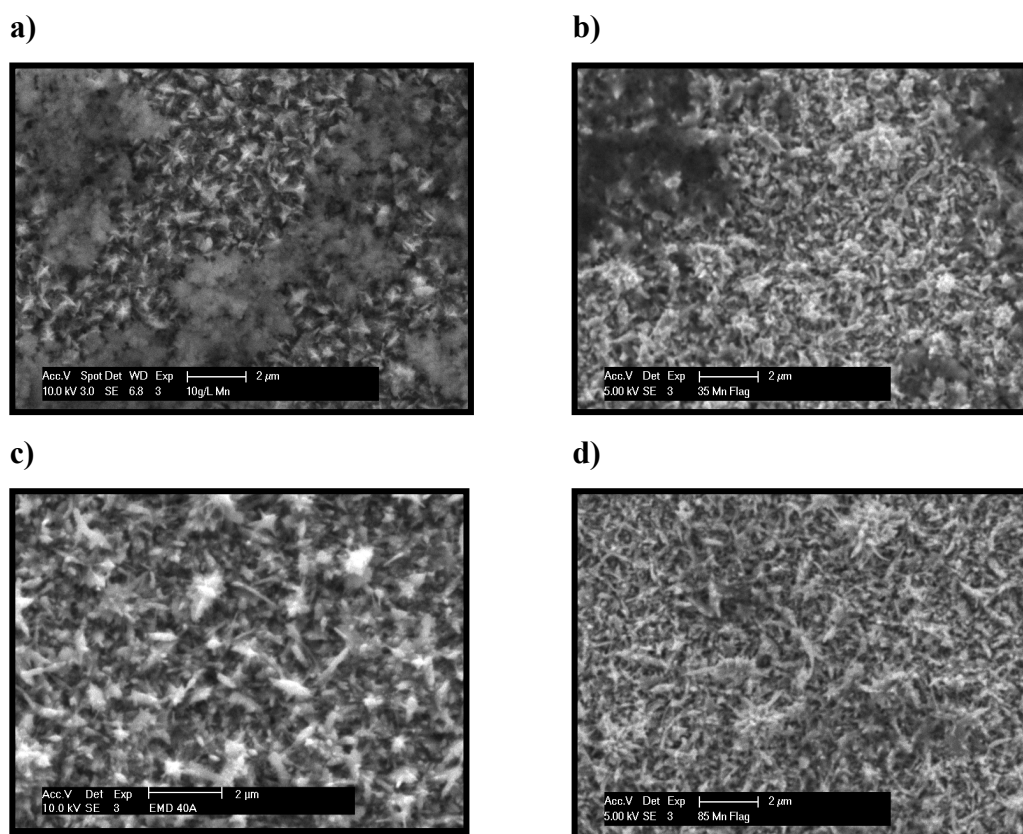


**Figure 4.10:** SEM images of the surface topographies of EMD electro-deposited at  $40 \text{ A/m}^2$  from a solution at  $93 \text{ }^\circ\text{C}$  containing  $35 \text{ g/L H}_2\text{SO}_4$  and  $\text{Mn}^{2+}$  concentrations of, **a)**  $10\text{g/L}$ , **b)**  $35 \text{ g/L}$ , **c)**  $60 \text{ g/L}$ , and **d)**  $85\text{g/L}$ .

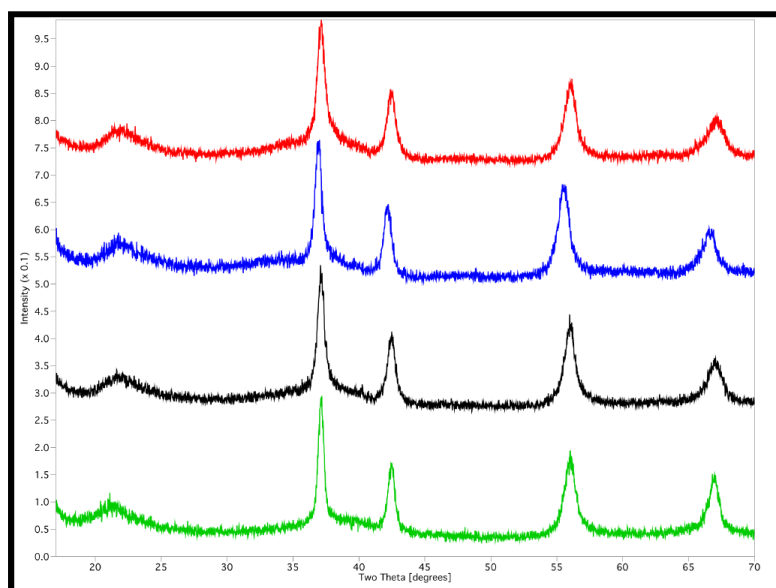


**Figure 4.11:** XRD patterns of EMD electro-deposited from electrolyte containing 35 g/L H<sub>2</sub>SO<sub>4</sub> at 93 °C, at current densities of 40 A/m<sup>2</sup>, at Mn<sup>2+</sup> concentrations of, 10 [Green], 35 [Black], 60 [Blue], and 85 g/L [Red].

The XRD patterns reveal little differences in the EMD structure at differing Mn<sup>2+</sup> concentrations. There is some evidence that there is a slight increase in structural order with increasing Mn<sup>2+</sup> concentration, however the poor quality XRD patterns make accurate analysis difficult. These results fit with crystal growth theory and the Mn<sup>2+</sup> mixed potential graphs (see Figure 4.12) and research conducted by Williams [1], [Note: although these solutions were not conductivity buffered, the effect of conductivity variations on the mixed potential was not seen to be an issue due to the high ionic strengths of the solutions]. The SEM and XRD data for the 10 g/L Mn<sup>2+</sup> sample, however, are contradictory as the SEM analysis suggests that the sample may be more ordered than the other Mn<sup>2+</sup> samples, but the XRD shows no increase in structural order, but suggests an increase in crystallite size particularly in the [061] peak. This suggests that at low Mn<sup>2+</sup> concentration, the deposition mechanism may vary from the norm.

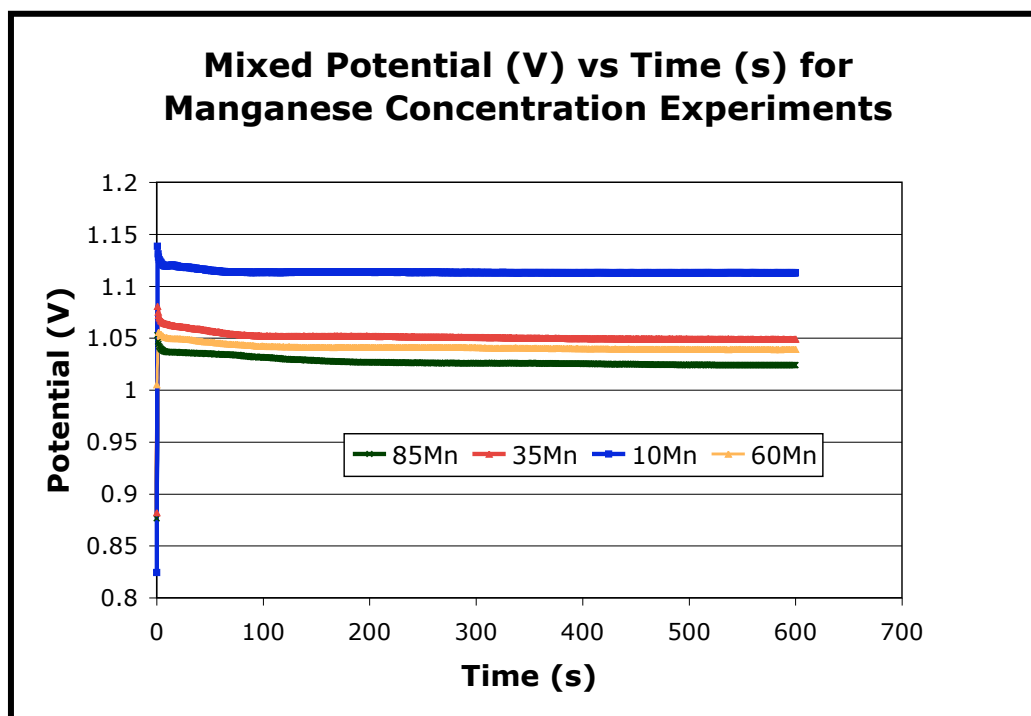


**Figure 4.12:** Mixed potential (V) versus Time (s) plot for various manganese concentrations.

#### 4.5 Effect of H<sub>2</sub>SO<sub>4</sub> Concentration

EMD was deposited onto platinum working electrodes from electrolytes containing 60 g/L Mn<sup>2+</sup> at 40 A/m<sup>2</sup>, at 93 °C using H<sub>2</sub>SO<sub>4</sub> concentration of 5, 20, 35 and 50 g/L. The samples produced were then characterised using a combination of on-electrode SEM and low background XRD.

As expected from literature studies [14], variation of the H<sub>2</sub>SO<sub>4</sub> concentration had far less of an impact on surface morphology than current density and temperature. SEM analysis clearly shows the differences in surface morphology between the 20, 35, 50 g/L are slight (see Figure 4.13a-d). The main observation that can be made about these samples, is that the 5 g/L sample seems to have a more ordered, and bulkier morphology.

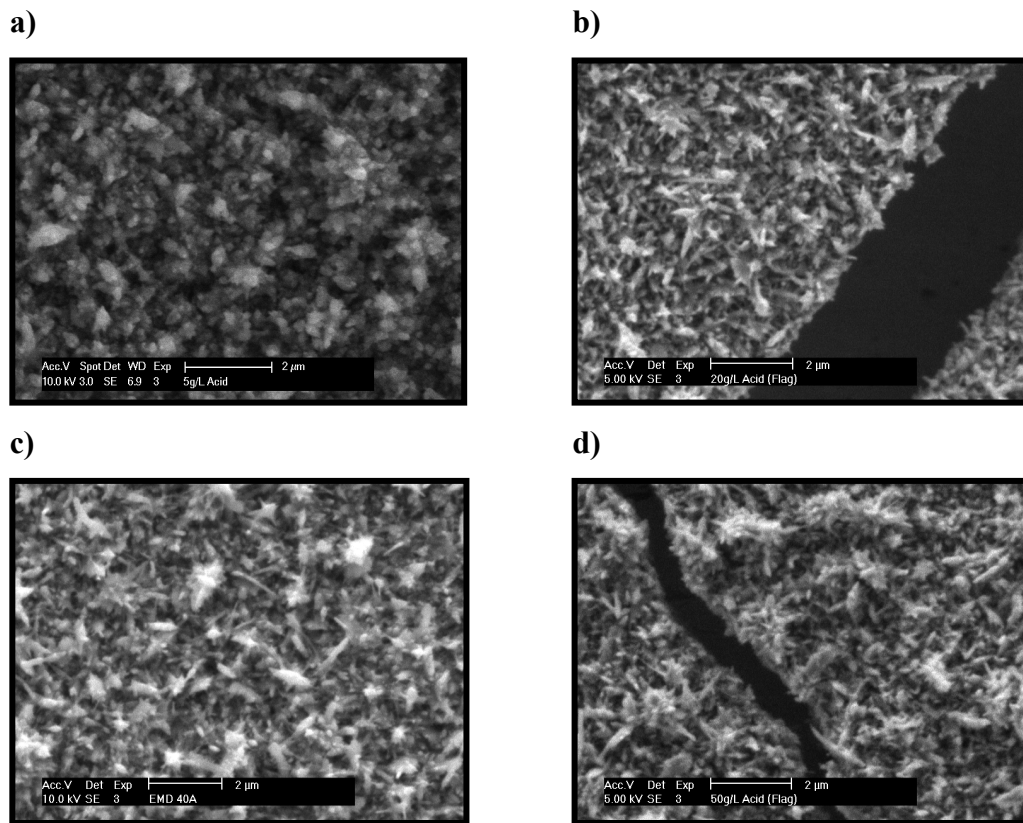


**Figure 4.13:** SEM images of surface topography at various H<sub>2</sub>SO<sub>4</sub> concentrations; **a)** 5 g/L, **b)** 20 g/L, **c)** 35 g/L, and **d)** 50 g/L.

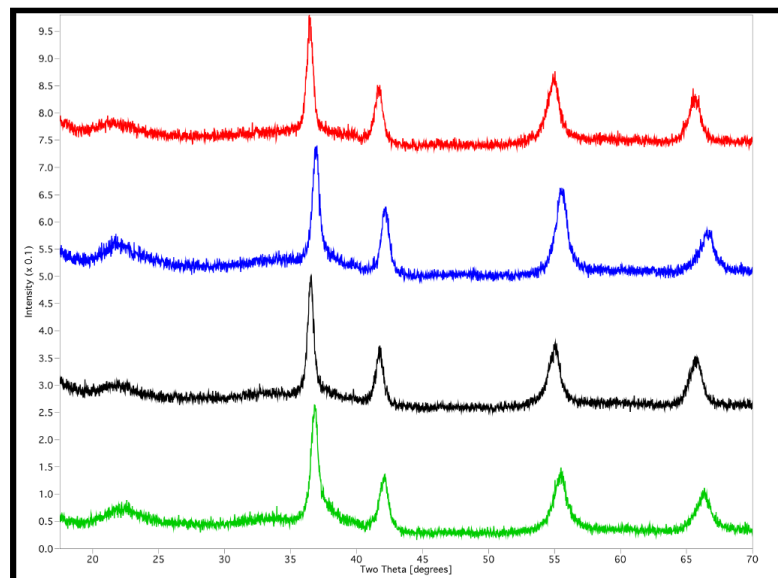


**Figure 4.14:** XRD patterns of EMD deposited onto platinum working electrode from an electrolyte containing 60 g/L Mn<sup>2+</sup> at 40 A/m<sup>2</sup>, at 93 °C using H<sub>2</sub>SO<sub>4</sub> concentration of 5 [Green], 20 [Black], 35 [Blue] and 50 [Red] g/L.

The XRD analysis shows very little difference between the samples, although there seems to be an increase in crystalline order with decrease in acid concentration. This fits with the crystal growth theory and the mixed potential versus acid concentration graphs (see **Figure 4.15**) [Note: although these solutions were not conductivity buffered, the effect of conductivity variations on the mixed potential was not seen to be an issue due to the high ionic strength of the solutions], however poor quality XRD data makes accurate data interpretation difficult.

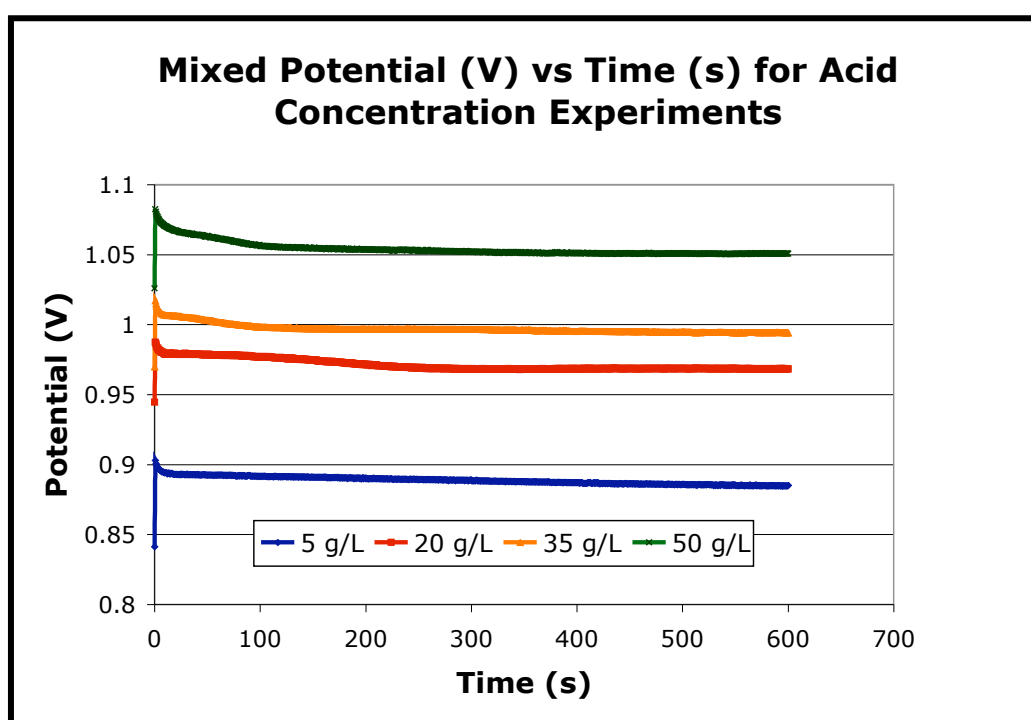


**Figure 4.15:** Mixed potential (V) versus Time (s) plot for various acid concentrations.

It is worth noting that the  $\text{SO}_4^{2-}$  ion is thought to have a detrimental effect on the EMD deposition process ([15] in [1]), and the results obtained from this work tend to support this argument as the structural order decreases as the  $\text{SO}_4^{2-}$  concentration increases. Another interesting point is that Aldenkhani and Ghaemi [5, 6], investigated the effect of deposition pH and acidity on EMD, and even though the conditions and deposition set-up was far different from those in this study similar morphologies were reported (that is “thistle-like” and “cauliflower-like”).

#### 4.6 Analytical Parameters Derived from EMDs XRD Patterns

As previously mentioned, due to the poor quality XRD patterns obtained from low-background XRD analysis, preferred orientation, and the nature of EMD (that is, EMD peak broadening often occurs because of defects, and peaks merging, as well as reductions in crystallite sizes) crystallite sizes were not calculated and comparisons between samples were done in a qualitative manner. Techniques such as the Preisler Q-value, IPM number, and  $H_1/H_2$  ratios could not be calculated due to the presence of preferred orientation in the pattern.

Lattice parameters were calculated using the Krey indexing system, however there was no correlation between lattice parameters and deposition conditions observed,

$P_r$  values of 0.40 – 0.52 and  $Tw$  (%) of 90 – 100% were calculated using Chabres structural model and Krey lattice parameters [16], which are consistent with values found in literature [16]. However no correlations were observed between these values and deposition conditions, except that  $P_r$  seems to show an increase with increased current density, this was unexpected and in disagreement with literature [1]. However, due to the poor definition of peaks used in these calculations the results should be treated with caution. The Bowden and co-workers simulation program [17] could not be used due to the poor quality of the XRD patterns.

#### 4.7 Effect of Electrolyte

Both  $Cl^-$  and  $NO_3^-$  electrolytes were tested, however the EMD could not be deposited from the  $Cl^-$  electrolyte under the conditions explored, therefore the results presented are only from EMD samples deposited using  $NO_3^-$  solutions.

SEM analysis revealed that EMD deposited from  $NO_3^-$  solutions produced a deposit with a much more defined crystal morphology (fibrous in appearance), and what appears to be larger crystallites (see Figure 4.16). This more fibrous morphology was also observed or referenced by several authors [1, 18, 19]. The larger crystallites observed here may indicate that  $SO_4^{2-}$  has a detrimental effect on crystal growth, leading to more disordered EMD crystallites when EMD is deposited from  $SO_4^{2-}$  solutions. A similar conclusion was reached by Preisler ([15] in [1]), after observing

that more  $\text{SO}_4^{2-}$  is incorporated in to EMD during deposition than singly charged species such as  $\text{NO}_3^-$ . From this he postulated that the doubly charged  $\text{SO}_4^{2-}$  ions are more strongly bound to EMD than singly charged ions, and that the resulting adsorption of  $\text{SO}_4^{2-}$  onto the fastest growing crystal faces inhibiting crystal growth, however the singly charged  $\text{NO}_3^-$  is less strongly bound, and therefore does not significantly inhibit crystal growth [1].

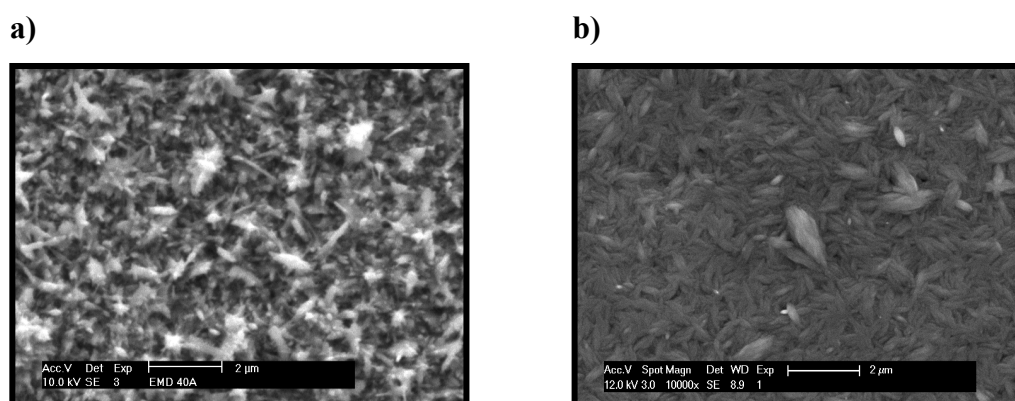


**Figure 4.16:** SEM images of EMD deposited from; **a)** sulphate, and **b)** nitrate solutions.

Figure 4.17 shows the differences between XRD patterns of EMD samples deposited in  $\text{SO}_4^{2-}$  and  $\text{NO}_3^-$  solutions. Unfortunately there seems to be preferred orientation artefacts in the  $\text{NO}_3^-$  EMD XRD pattern, so in-depth XRD analysis becomes difficult. Here, unlike the previous EMD samples discussed above, the preferred orientation effects are likely to arise from both the fibrous morphology of the EMD crystals, and the sample preparation. However the  $\text{NO}_3^-$  pattern does exhibit sharper, more defined peaks indicating an increase in crystallite size and structural order, which confirms the findings of the SEM analysis of these samples.

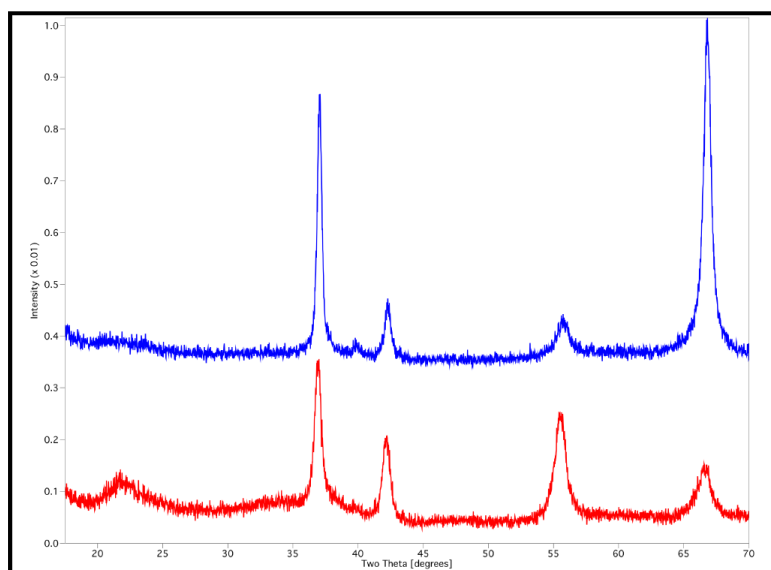


**Figure 4.17:** XRD patterns of EMD deposited from sulphate [red] and nitrate [blue] solutions.

These findings suggest that the presence of the  $\text{SO}_4^{2-}$  ion in solution actually contributes to the highly disordered nature of EMD deposited from standard sulphate solutions.

#### 4.8 Effect of Inorganic Additives

The study of inorganic electrolyte bath additives was not considered to be a core area of this study, however, the effects of  $\text{K}^+$  and  $\text{H}_3\text{PO}_4$  were briefly investigated, as  $\text{K}^+$  was to be used in later simultaneous GI-SXRD and EIS experiments to investigate the EMD deposition mechanism. And  $\text{H}_3\text{PO}_4$  is a logical starting point for organic additive experiments, as many crystal growth modifiers are organic phosphonic acids.

Experiments to determine the effect of  $\text{K}^+$  on the EMD structure were carried out at  $75^\circ\text{C}$  from a solution containing 60 g/L  $\text{Mn}^{2+}$ , 35 g/L  $\text{H}_2\text{SO}_4$  at  $5 \text{ A/m}^2$ . The effect of depositing EMD in the presence of 3000 ppm  $\text{K}^+$  is shown in Figure 4.18. Several extra peaks are evident in the XRD pattern of EMD deposited in the presence of  $\text{K}^+$  (KEMD), these peaks correspond well to those found in  $\alpha\text{-MnO}_2$  samples, particularly those of cryptomelane (a  $\text{MnO}_2$  tunnel structure containing  $\text{K}^+$ ), suggesting that  $\text{K}^+$  has been included in to the EMD structure as a cryptomelane-like

tunnel structure. This finding compares well to those of Kao and co-workers [20]. The presence of  $\alpha$ -MnO<sub>2</sub> is known to have a negative impact on EMD performance.

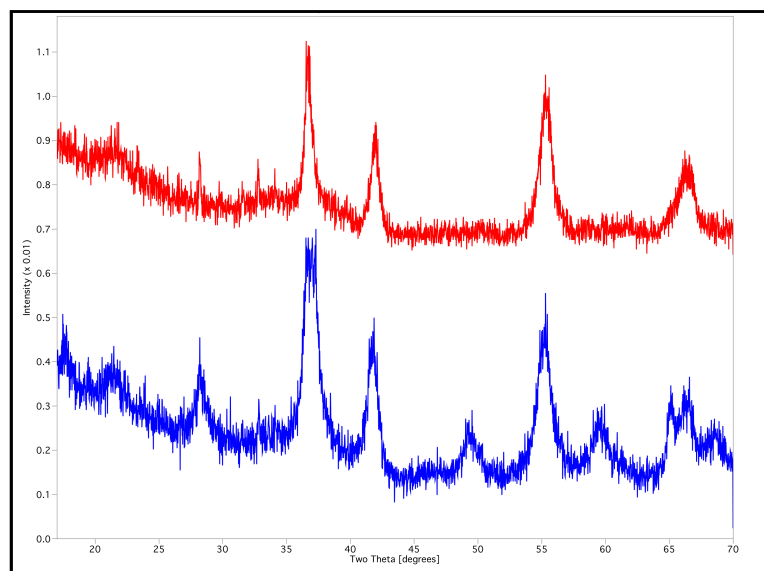


**Figure 4.18:** XRD patterns of EMD deposited at 75°C from a solution containing 60 g/L Mn<sup>2+</sup>, 35 g/L H<sub>2</sub>SO<sub>4</sub> at 5 A/m<sup>2</sup> [red] and in the presence of 3000 ppm K<sup>+</sup> [blue].

Dosing the electro-deposition electrolyte with ~100 ppm of H<sub>3</sub>PO<sub>4</sub>, also influenced the structure and morphology of the EMD produced. Figure 4.19 shows the SEM images of both normal EMD and EMD deposited in the presence of H<sub>3</sub>PO<sub>4</sub> (PEMD). The PEMD exhibits a much finer, and more defined “urchin-like” morphology than the normal EMD, with clear evidence of “needle-like” morphologies. The PEMD SEM images also show similarities to SEM images of 80 A/m<sup>2</sup> samples, although the crystal morphologies are far clearer in the PEMD sample. EDS analysis of the PEMD indicated the presence of phosphorous in the sample suggesting the PO<sub>4</sub><sup>3-</sup> maybe incorporated into the PEMD structure. SEM analysis also revealed what seemed to be a deposition by-product, that is a material with very little observable structure on the surface of the deposit. EDS and BSE analysis show that the by-product has a similar composition to the PEMD, however due to the limitations of these techniques, the exact identity of this material could not be elucidated.

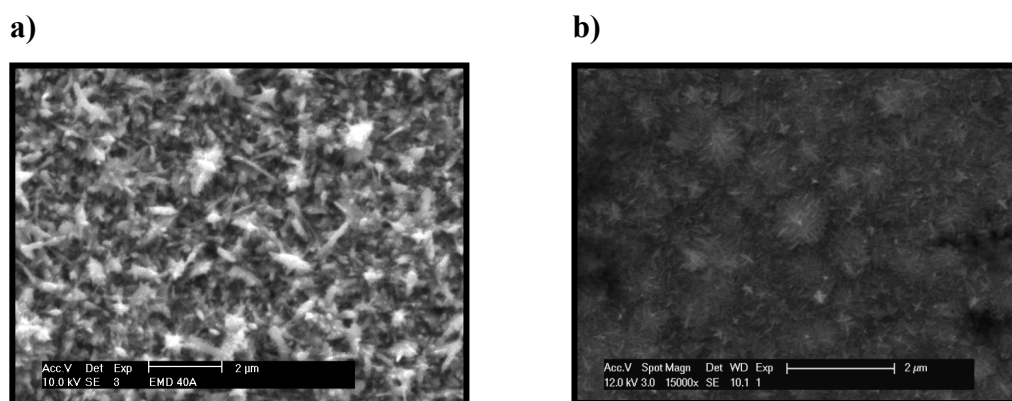


**Figure 4.19:** SEM images of a) EMD deposited at 93°C from a solution containing; a) 60 g/L Mn<sup>2+</sup>, 35 g/L H<sub>2</sub>SO<sub>4</sub> at 40 A/m<sup>2</sup> and b) in the presence of 100 ppm H<sub>3</sub>PO<sub>4</sub>.

A comparison of the EMD and PEMD XRD patterns is shown in Figure 4.20. The XRD data shows the PEMD sample exhibits a XRD pattern similar to that of the 80 A/m<sup>2</sup> sample in Figure 4.4 (which is in agreement with the above SEM data), however the preferred orientation effects observed in the PEMD may be a result of the “needle-like” crystal morphology, as well as sample preparation. Qualitatively, the PEMD seems to exhibit less structural order than EMD produced under the same conditions, although this may be an artefact of the preferred orientation in the sample. These results tends to suggest that addition of H<sub>3</sub>PO<sub>4</sub> to the electrolyte bath may reduce the effective current density required to produce EMD, as the PEMD produced at 40 A/m<sup>2</sup>, gave very similar SEM, and XRD results to EMD produced in standard electrolyte baths at 80 A/m<sup>2</sup>. However more analysis would need to be carried out to confirm this.

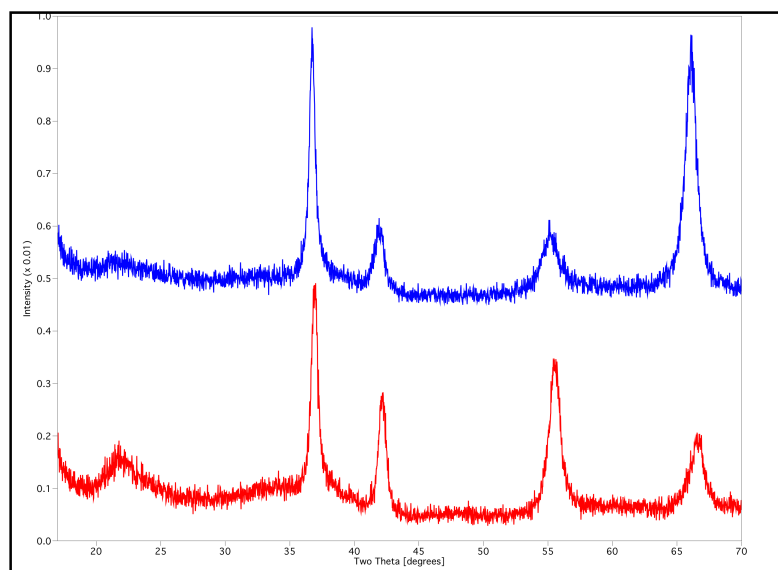


**Figure 4.20:** XRD patterns of EMD deposited at 93°C from a solution containing 60 g/L Mn<sup>2+</sup>, 35 g/L H<sub>2</sub>SO<sub>4</sub> at 40 A/m<sup>2</sup> [red] and in the presence of 100 ppm H<sub>3</sub>PO<sub>4</sub> [blue].

Yamaguchi studied the effects of H<sub>3</sub>PO<sub>4</sub>, and observed that PEMD was superior to conventional EMD for use in lithium – manganese dioxide primary cells. He observed that PO<sub>4</sub><sup>3-</sup> ions were preferentially incorporated in the deposit over SO<sub>4</sub><sup>2-</sup> ions (this is likely to be due to its higher charge), which is supported by the EDS results obtained here, and that PEMD was found to have higher BET surface areas, and combined H<sub>2</sub>O, than EMD deposited at similar conditions ([21] in [1]). This gives further weight to hypothesis that PO<sub>4</sub><sup>3-</sup> has an effect on the structure and deposition process of EMD. According to Williams and co-workers [14] increases in current density also result in increased BET surface areas, and combined H<sub>2</sub>O, providing further evidence that the addition of H<sub>3</sub>PO<sub>3</sub> may reduce the effective current density required to produce EMD.

#### 4.9 Effect of Organic Additives

A literature search revealed little information on the effect of organic bath additives on the morphology and structure of EMD. Only a single reference relating to a the effect of quaternary amine salts (QAS) was found, this research suggested that the presence QAS during the electro-deposition of EMD enhanced the end products electrochemical properties [22]. Therefore for the sake of completeness and in light of the interesting results obtained from the H<sub>3</sub>PO<sub>4</sub> dosing experiments reported in section 4.8, the effect of several organic additives on EMDs crystal morphology and structure was investigated. These additives are listed below:

- Sulfonated calix[4]arene
- HEDP
- NTMP
- EDTP
- PDTP
- NADP

Figure 4.21 shows the molecular structures of the organic additives used in this study.

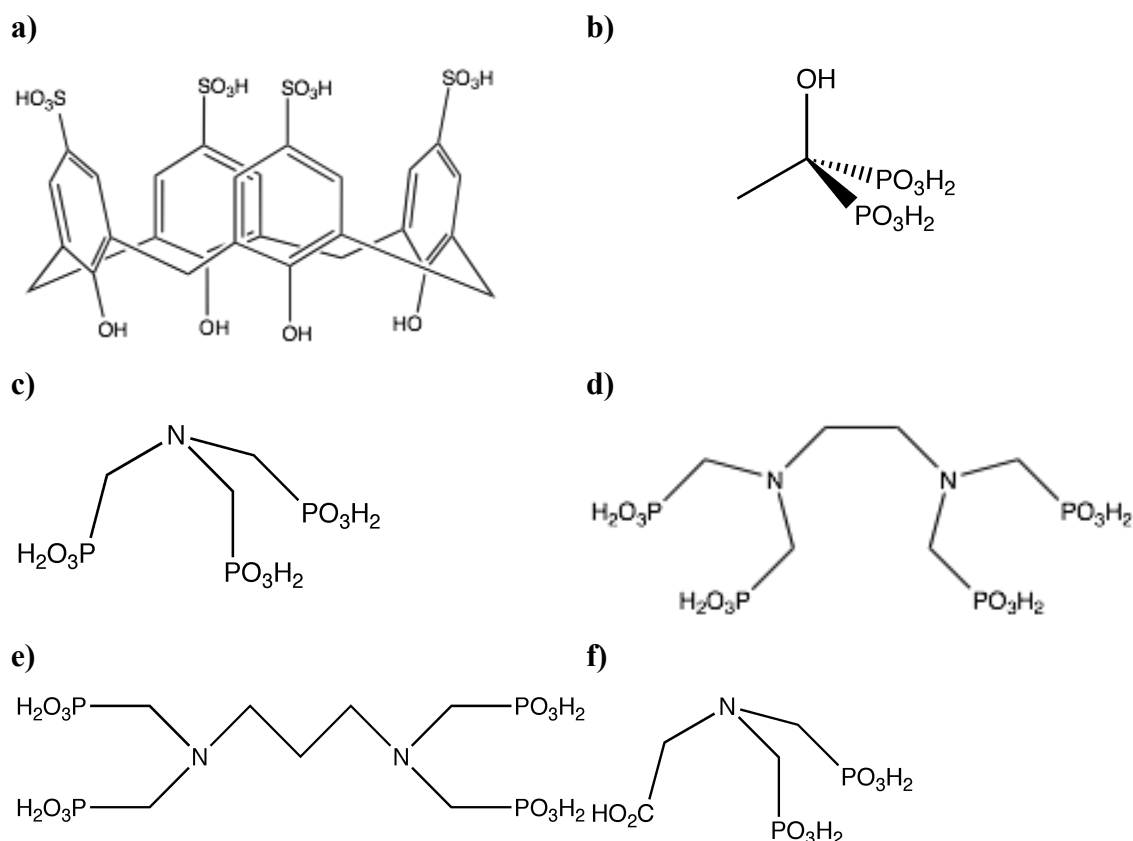


**Figure 4.21:** Molecular structure of the organic additives used in this study **a)** Sulfonated calix[4]arene, **b)** HEDP, **c)** NTMP, **d)** EDTP, **e)** PDTP, and **f)** NADP.

HEDP, PDTP, EDTP, NTMP have previously been studied as crystal growth inhibitors / modifier in  $\text{BaSO}_4$  and  $\text{CaSO}_4$  systems [23-27]

These additives were chosen from a list of known crystal growth modifiers that represented a good cross section of known phosphorus-based organic additives. The list of additive was then refined to its current state after solubility tests in the standard deposition electrolyte used in this study (60 g/L  $\text{Mn}^{2+}$  and 35 g/L  $\text{H}_2\text{SO}_4$ ). The additives were dosed at approximately 100 ppm and their effect on EMD crystal morphology and structure was characterised using SEM and XRD.

The presence of 100 ppm of sulfonated calix[4]arene did not have a great effect on the surface morphology (Figure 4.22b), in fact the surface morphology of the EMD remained relatively unaffected, except for series of circular areas (approximately 20  $\mu\text{m}$  in diameter) of distorted morphology (Figure 4.22c-d). EDS analysis of these

circular areas showed a higher sulphur content when compare to the unaffected areas, this indicates the sulfonated calix[4]arene may have been adsorbed to these areas. It was interesting to note that these circular areas were not observed on a RDE electrode, which was plated at the same conditions but rotated at 1000rpm and aligned parallel to the surface of the electrolyte. A possible explanation for these circular areas of crystal distortion maybe the limited solubility of the sulfonated calix[4]arene in the electrolyte, which may have resulted in calixarene particles or breakdown product being co-deposited with the EMD and distorting the crystal morphology. The alignment of the RDE would have limited the deposit's interaction with these particles, hence the areas of crystal distortion do not appear in the RDE deposit.

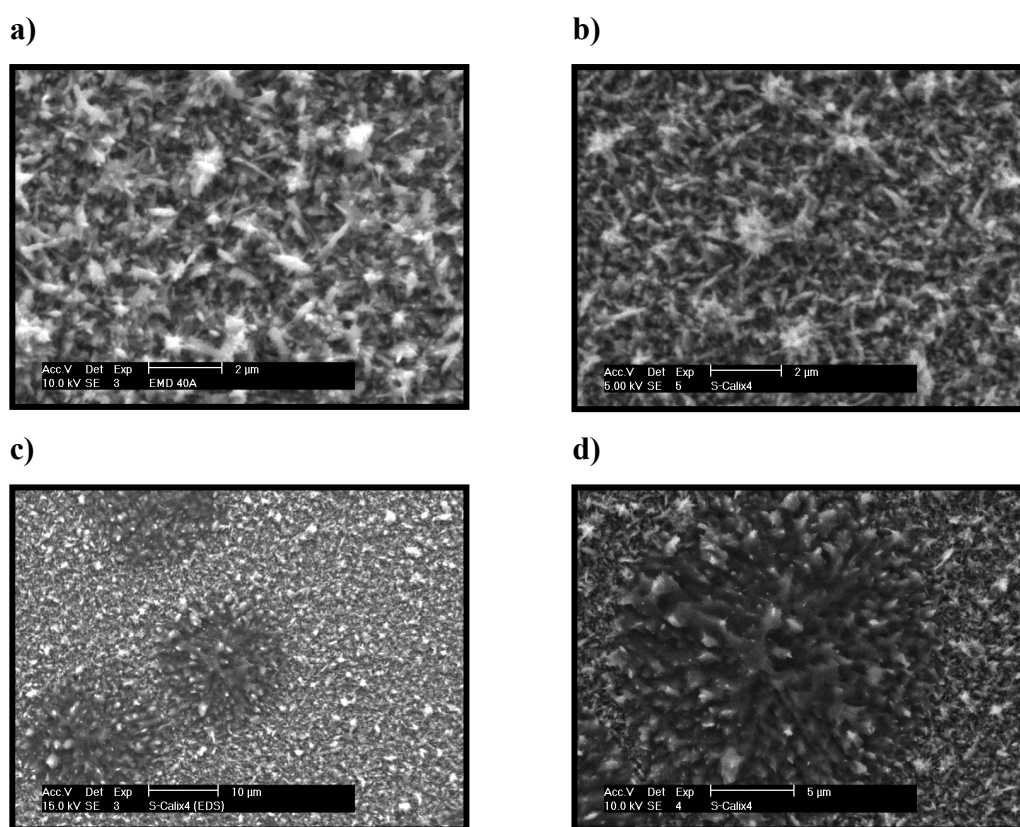


**Figure 4.22:** SEM images of a) EMD deposited from a standard solution containing no additives, b) EMD deposited from a standard solution in the presence of 100 ppm of sulfonated calix[4]arene, c) circular areas of distorted morphology in the sulfonated calix[4]arene EMD deposit, and d) a close up of a distorted area in the sulfonated calix[4]arene EMD deposit.

XRD analysis of the EMD deposited in the presence 100 ppm of sulfonated calix[4]arene (see Figure 4.23) confirmed the results of the above SEM analysis. The XRD patterns of the standard EMD and sulfonated calix[4]arene EMD show no discernable differences, indicating that sulfonated calix[4]arene as an additive has very little impact on the crystal structure and morphology of EMD at concentrations of 100 ppm.

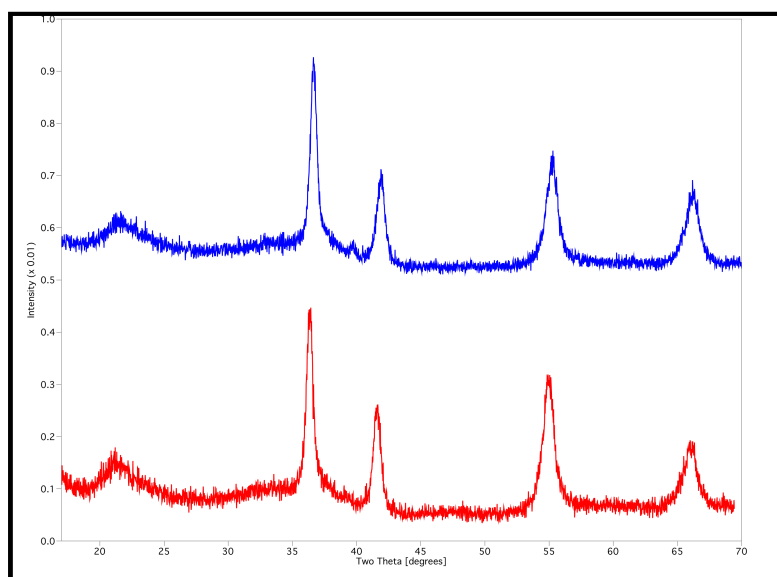


**Figure 4.23:** XRD patterns of standard EMD [red] and EMD deposited in the presence of 100 ppm sulfonated calix-4-erene [blue].

The addition of 100 ppm of HEDP to the electrolyte bath significantly impacted the surface topography of the EMD deposited. Figure 4.24 shows that the typically rough surface of the disordered “urchin-like morphology” has been smoothed to a flat, featureless, almost amorphous morphology. EDS analysis showed the presence of phosphorous. The deposit produced was also very brittle, illustrated by the cracks in the deposit shown in Figure 4.24b.

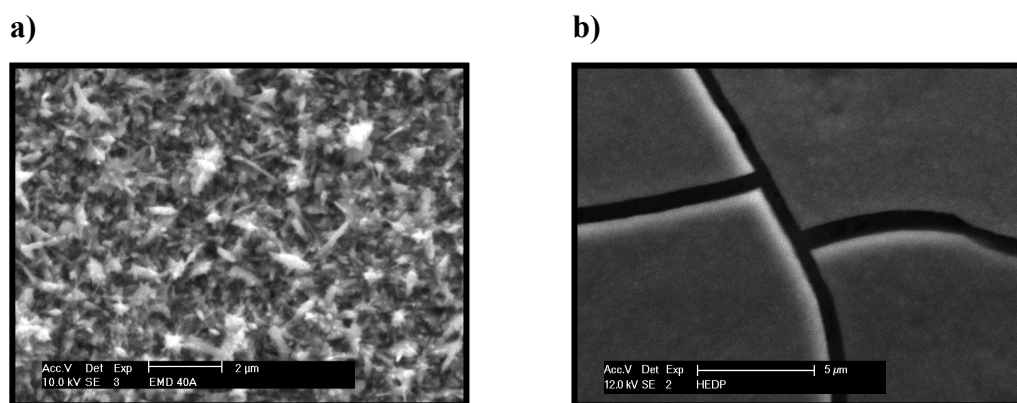


**Figure 4.24:** SEM images of **a)** EMD deposited from a standard solution containing no additives, and **b)** EMD deposited from a standard solution in the presence of 100 ppm of HEDP.

XRD analysis of the HEDP sample (see Figure 4.25) shows a more disordered crystal structure, smaller crystallite sizes, and more preferred orientation than the standard EMD. There also is an extra peak in the spectra at  $\sim 29.43^\circ 2\theta$ , the origin of which is unknown.

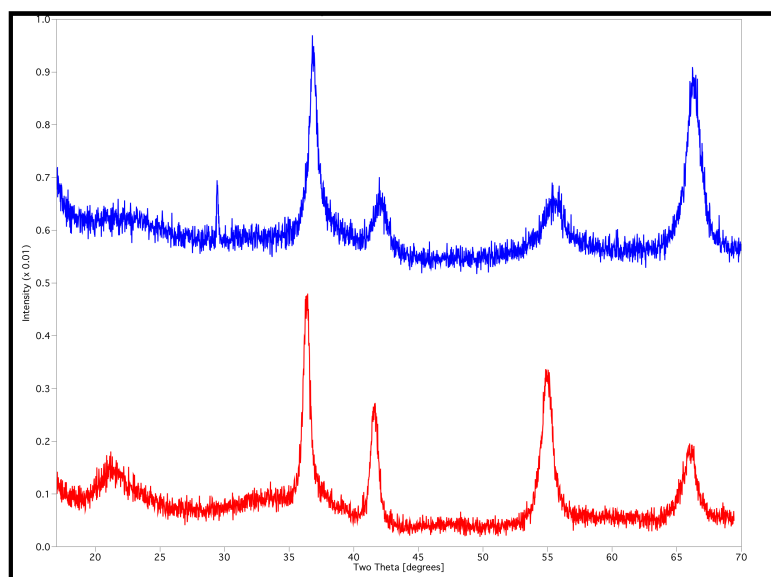


**Figure 4.25:** XRD patterns of standard EMD [red] and EMD deposited in the presence of 100 ppm HEDP [blue].

The addition of the NTMP to the bath gave similar results the HEDP additive. That is a brittle deposit, with a flat, featureless, almost amorphous topography, shown in the

SEM images in Figure 4.26. EDS analysis of the deposit again showed the presence of phosphorous. XRD analysis of the EMD deposited in the presence of NTMP, showed a more disordered crystal structure, smaller crystallite sizes, and more preferred orientation than the standard EMD (see Figure 4.27). Again, this is similar to the HEDP additive results, however the extra peak in the HEDP spectra at  $\sim 29.43^\circ 2\theta$ , is absent in the NTMP spectra.

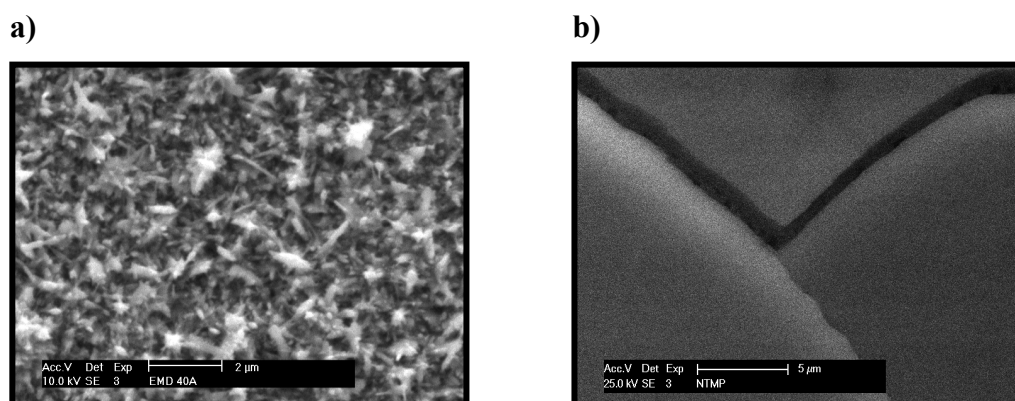


**Figure 4.26:** SEM images of **a)** EMD deposited from a standard solution containing no additives, and **b)** EMD deposited from a standard solution in the presence of 100 ppm of NTMP.

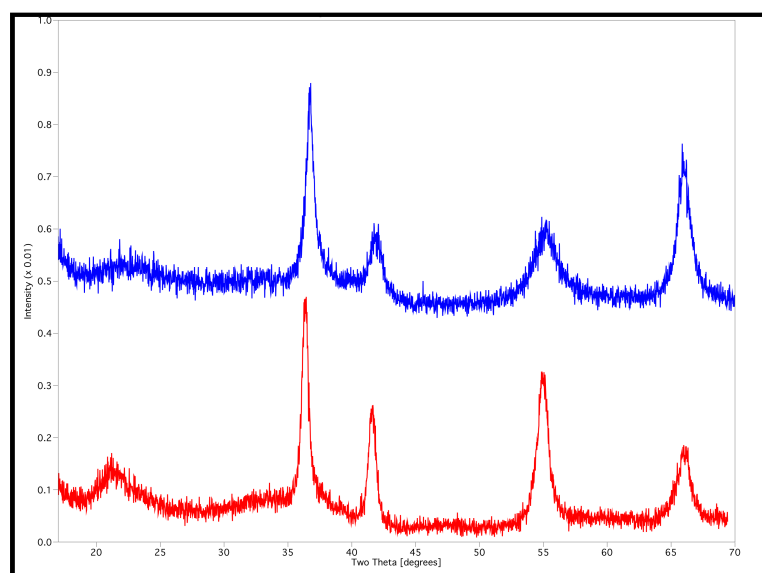


**Figure 4.27:** XRD patterns of standard EMD [red] and EMD deposited in the presence of 100 ppm NTMP [blue].

The presence of 100 ppm of EDTP again dramatically impacted the surface topography of the EMD deposited; the typical urchin morphology normally associated with these conditions was replaced by a flat featureless surface (see Figure 4.28). EDS analysis of the surface showed the presence of phosphorous, which indicates that EDTP may have adsorbed to the EMD during deposition and influenced its growth.

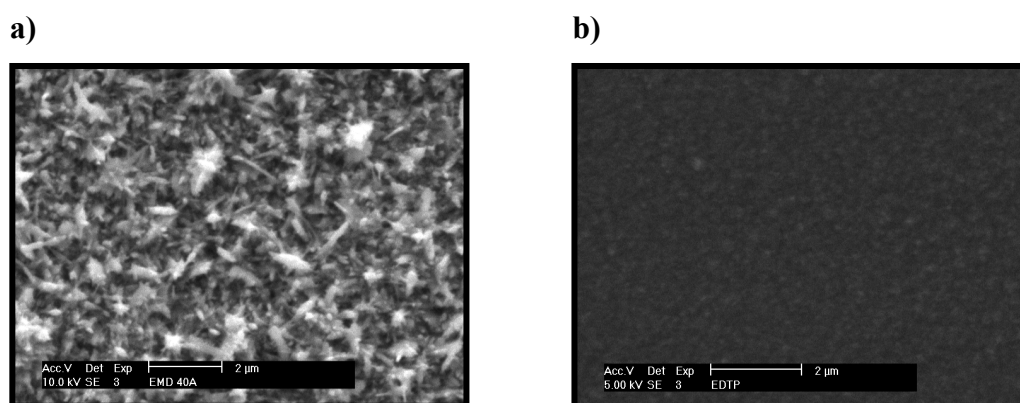


**Figure 4.28:** SEM images of **a)** EMD deposited from a standard solution containing no additives, and **b)** EMD deposited from a standard solution in the presence of 100 ppm of EDTP.

Analysis of the XRD pattern of EMD produced in the presence of EDTP (see Figure 4.29) similarly to the other additives tested, showed that the EDTP additive decreased the order in the crystal structure, decreased the crystallite size, and increased the degree of preferential orientation in the sample.

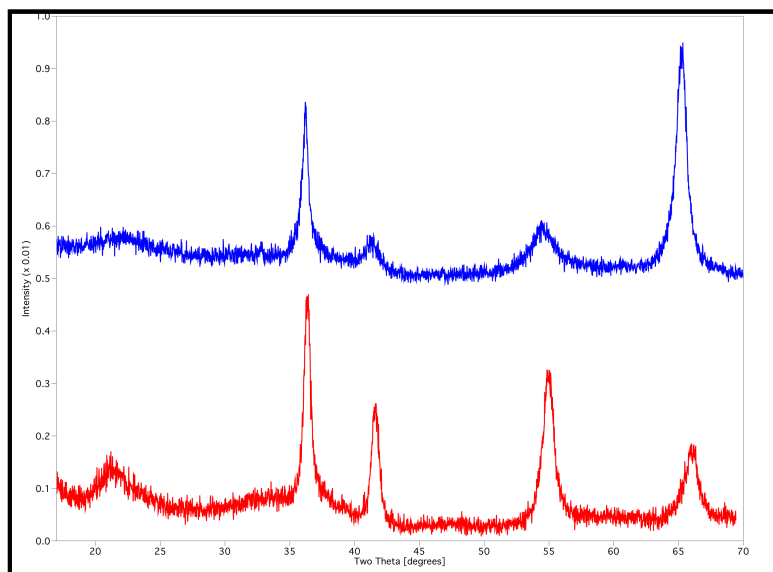


**Figure 4.29:** XRD patterns of standard EMD [red] and EMD deposited in the presence of 100 ppm EDTP [blue].

As expected the PDTP additive had a similar effect to the EDTP because of its similar molecular structure, however the effect of PDTP on the deposited EMDs structure and morphology is greater than that of the EDTP. SEM analysis of the EMD deposited in the presence of PDTP (see Figure 4.30) revealed that the surface morphology and topography of the EMD deposited using this additive was again flat featureless, and amorphous in nature. EDS analysis revealed the presence of phosphorous. The brittle nature of the deposit is also illustrated by the cracks present in the deposit (see Figure 4.30)

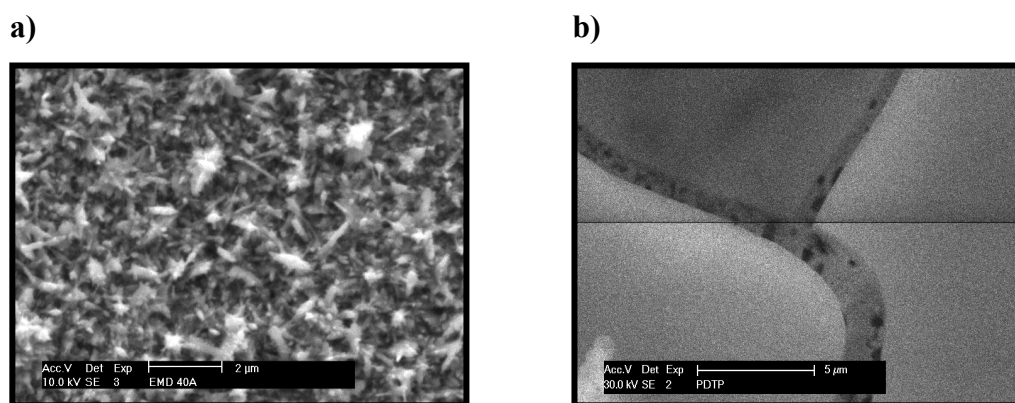


**Figure 4.30:** SEM images of a) EMD deposited from a standard solution containing no additives, and b) EMD deposited from a standard solution in the presence of 100 ppm of PDTP.

XRD analysis of EMD deposited in the presence of PDTP (see Figure 4.31) was also similar to the EDTP sample. Again, there is a decrease in structural order, and a decrease in crystal size when EMD is deposited in the presence of PDTP. The PDTP sample also appears to be less effected by preferred orientation effects.

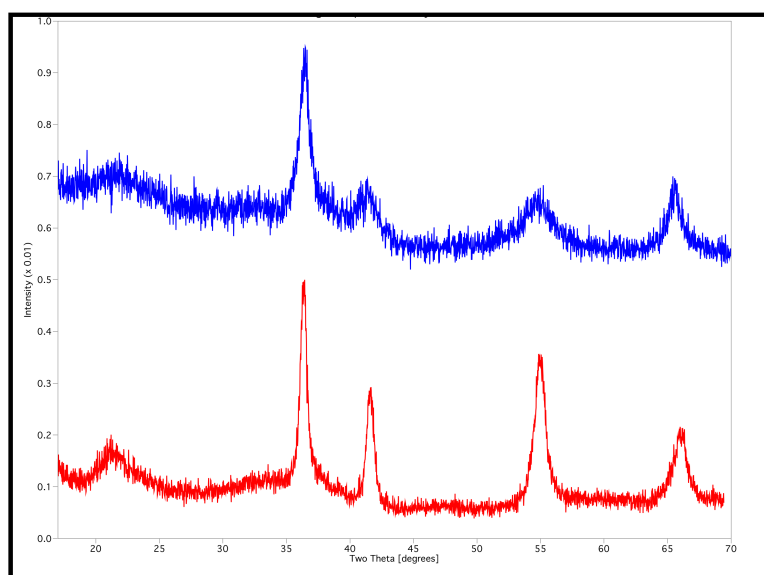


**Figure 4.31:** XRD patterns of standard EMD [red] and EMD deposited in the presence of 100 ppm PDTP [blue].

SEM and XRD analysis of EMD deposited in the presence of NADP yielded similar result to those of the other phosphonic acid based additives. SEM analysis (see

Figure 4.32) revealed that the surface morphology and topography of the EMD deposited using this additive was again flat featureless, and amorphous in nature. EDS analysis revealed the presence of phosphorous. The brittle nature of the deposit is also illustrated by the cracks present in the deposit. While XRD analysis showed the additive decreased the order in the crystal structure, decreased the crystallite size, and increased the degree of preferential orientation in the sample (see Figure 4.33).

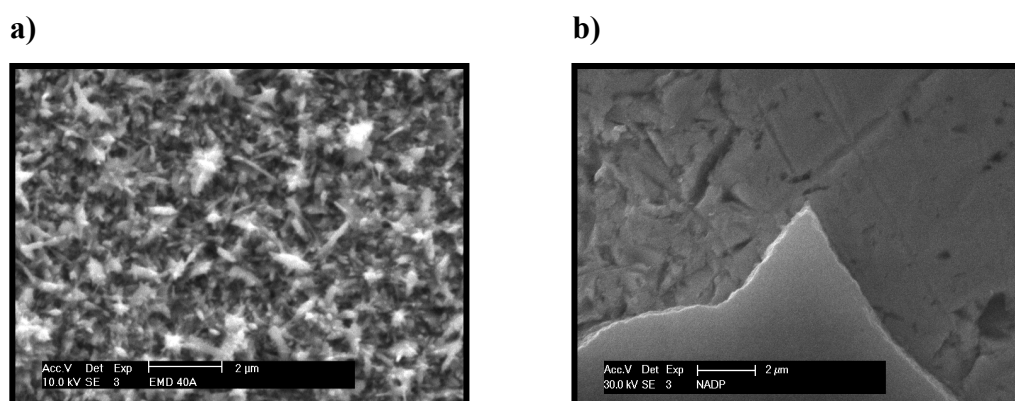


**Figure 4.32:** SEM images of a) EMD deposited from a standard solution containing no additives, and b) EMD deposited from a standard solution in the presence of 100 ppm of NADP.

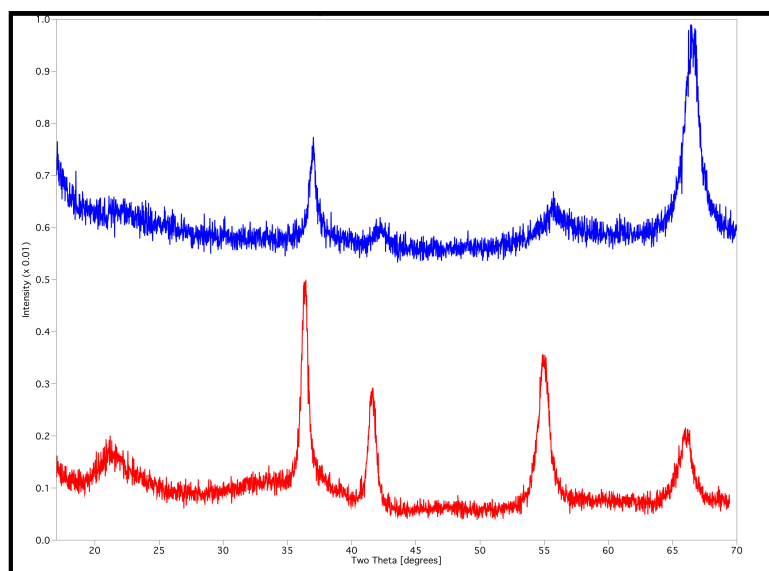


**Figure 4.33:** XRD patterns of standard EMD [red] and EMD deposited in the presence of 100 ppm NADP [blue].

With the exception of the sulfonated calix[4]arene, all the additives used had a dramatic impact on the morphology / topography of the EMD deposited; that is they produced a flat featureless deposit, amorphous in nature. This was confirmed via XRD analysis which showed a decrease in structural order and crystallite size. In fact the XRD patterns produced were reminiscent of those produce by depositing EMD at lower temperatures; that is 60 °C (see Figure 4.8). Unfortunately EMD exhibiting these characteristic often shows poorer performance in electrochemical tests, meaning that these additives will probably reduce the quality of the EMD produced, although further testing would have to be done to confirm this.

#### **4.10 Conclusions**

Unfortunately, the nature of EMD and poor quality XRD pattern hindered the analysis of the EMD samples produced in this study; despite this, a number of conclusions can still be drawn from this work.

It is clear that of the deposition condition variables studied, both current density and temperature have the largest effect on the structure of the EMD deposited. As current density increases, the structural disorder decreases and the crystallite size decreases, the opposite effect is observed when the temperature is increased. That is, the structural order increases and crystallite size increases. Increased  $\text{Mn}^{2+}$  concentrations seem to slightly increase the structural ordering of the deposit, while increased acid concentration seems to slightly decrease the structural order, however the effect of  $\text{Mn}^{2+}$  and acid concentrations are only slight when compared with current density and temperature. These results fit with EMD crystal growth theory, and the mixed (deposition) potential data, which basically means that increases in deposition potential favour nucleation and therefore disordered deposits with more defects and smaller crystallite sizes. Conversely, a decrease in deposition potential favours crystal growth and therefore more ordered deposits, with less defects and larger crystallite sizes. This hypothesis is in agreement with the deposition model put forward by Swinkels and Williams [28]. The results also show that additives, (especially organic additives) dramatically impact the deposition of EMD, and suggesting that more research is warranted in this area.

#### 4.11 References

1. Williams, R.P., *Characterisation and Production of High Performance Electrolytic Manganese Dioxide for use in Primary Alkaline Cells.*, in *Department of Chemistry*, 1995, The University of Newcastle: Newcastle, Australia.
2. Clarke, C.J., G.J. Browning, and S.W. Donne, *An RDE and RRDE study into the electrodeposition of manganese dioxide*. *Electrochim. Acta*, 2006. **51**(26): p. 5773-5784.
3. Maphanga, R.R., S.C. Parker, and P.E. Ngoepe, *Atomistic simulation of the surface structure of electrolytic manganese dioxide*. *Surf. Sci.*, 2009. **603**(21): p. 3184-3190.
4. Kao, W.-H. and V.J. Weibel, *Electrochemical oxidation of manganese (II) at a platinum electrode*. *J. Appl. Electrochem.*, 1992. **22**(1): p. 21-27.
5. Adelkhani, H., *The effect of acidity of electrolyte on the porosity and nanostructure morphology of electrolytic manganese dioxide*. *Appl. Surf. Sci.*, 2012. **258**: p. 6232-6238.
6. Adelkhani, H. and M. Ghaemi, *Influence of the solution pH on the nanostructural, and electrochemical performance of electrolytic manganese dioxide*. *J. Alloys Compd.*, 2009. **481**(1-2): p. 446-449.
7. *Handbook of Manganese Dioxides Battery Grade*, ed. D. Glover, B.S. Jr, and A. Kozawa, 1989: The International Battery Association (IBA, Inc.).
8. Prelot, B., C. Poinignon, F. Thomas, E. Schouller, and F. Villieras, *Structural-chemical disorder of manganese dioxides 1. Influence on surface properties at the solid-electrolyte interface*. *J. Colloid Interface Sci.*, 2003. **257**: p. 77-84.

9. Morgan, D., D. Balachandran, G. Ceder, and A. van de Walle. *A Drastic Influence of Point Defects on Phase Stability in MnO<sub>2</sub>*. in *Mat. Res. Symp. Proc.* 2003. Materials Research Society.
10. Balachandran, D., D. Morgan, G. Ceder, and A. van de Walle, *First-principles study of the structure of stoichiometric and Mn-deficient MnO<sub>2</sub>*. *J. Solid State Chem.*, 2003. **173**: p. 462-475.
11. Balachandran, D., *First Principles Study of Structure, Defects and Proton Insertion in MnO<sub>2</sub>*, in *Department of Materials Science and Engineering*, 2001.
12. Ghaemi, M., Z. Biglari, and L. Binder, *Effect of bath temperature on electrochemical properties of the anodically deposited manganese dioxide*. *J. Electroanal. Chem.*, 2001. **102**(1-2): p. 29-34.
13. Nijjer, S., J. Thonstad, and G.M. Haarberg, *Oxidation of manganese(II) and reduction of manganese dioxide in sulphuric acid*. *Electrochim. Acta*, 2000. **46**: p. 395-399.
14. Williams, R.P., R. Fredlein, G. Lawrance, D.A.J. Swinkels, and C. Ward, *Effect of Deposition Conditions on the Structural, Chemical, Physical and Electrochemical Properties of EMD* *Prog. Batteries Battery Mater.*, 1994. **13**: p. 102-112.
15. Preisler, E. in *Proceedings of the Second Battery Materials Symposium*. 1985. Graz.
16. Chabre, Y. and J. Pannetier, *Structural and Electrochemical Properties of the Proton / gamma MnO<sub>2</sub> System*. *Prog. Solid State Chem.*, 1995. **23**: p. 1-130.
17. Hackney, S., *EMDXRDSIMBeta2*, 2002.
18. Chi-Hsun, C., Z. Chong-Tao, C. An, Z. Ze-Shan, L. Wen-Shew, and Z. Yuo-Hua. *A Study of Some Characteristic Properties of FEMD and Simultaneous*

- Electrodeposition of FEMD on Anode and Metallic Mn on Cathode.* in *Manganese Dioxide Symposium*. 1980. Tokyo: The Electrochemical Society, Inc.
19. Freund, F., E. Konen, and E. Preisler. *Structural Data on Fibrous Electrolytic Manganese Dioxide.* in *Manganese Dioxide Symposium*. 1975. Cleveland: The Electrochemical Society, Inc
20. Kao, W.-H., V.J. Weibel, and M.J. Root, *The Influence of Potassium Ion on the Electrodeposition and Electrochemistry of Electrochemistry of Electrolytic Manganese Dioxide.* J. Electrochem. Soc., 1992. **139**(5): p. 1223-1226.
21. Yamaguchi, M., Prog. Batteries Battery Mater., 1992. **11**: p. 171-177.
22. Biswal, A., B.C. Tripathy, T. Subbaiah, D. Meyrick, and M. Minakshi, *Electrodeposition of manganese dioxide: effect of quaternary amines.* J. Solid State Electrochem., 2013. **17**(5): p. 1349-1356.
23. Uchida, M., A. Sue, T. Yoshiaki, and A. Okuwaki, *Morphology of barium sulfate synthesized with barium(II)-aminocarboxylate chelating precursors.* CrystEngComm, 2001. **5**: p. 1-6.
24. Liu, S.T. and H. Nancollas, *A Kinetic and Morphological Study of the seeded Growth of Calcium Sulfate Dihydrate in the Presence of Additives.* J. Colloid Interface Sci., 1975. **52**(3): p. 593-601.
25. Bosbach, D. and M.F.J. Hochella, *Gypsum growth in the presence of growth inhibitors: a scanning force microscopy study.* Chem. Geol., 1996. **132**: p. 227-236.
26. Bosbach, D., C. Hall, and A. Putnis, *Mineral precipitation and dissolution in aqueous solution: in-situ microscopic observations on barite (001) with atomic force microscopy.* Chem. Geol., 1998. **151**: p. 143-160.

27. Antonious, M.S., *Effect of Additives on the Crystallization of Barium Sulphate*. Phosphorus Sulfur, 1996. **112**: p. 235-245.
28. Swinkels, D.A.J. and R.P. Williams, *A Model for EMD Production and Properties*. Prog. Batteries Battery Mater., 1996. **15**: p. 1-7.

*Every reasonable effort has been made to acknowledge the owners of copyright material. I would be pleased to hear from any copyright owner who has been omitted or incorrectly acknowledged.*

## 5 SIMULTANEOUS *IN SITU* SR-GIXRD AND EIS STUDIES OF THE EMD DEPOSITION PROCESS

The objective of this study was to conduct simultaneous electrode kinetic and *in situ* synchrotron radiation – grazing incidence X-ray diffraction (SR-GIXRD) surface studies of the electro-deposition process of EMD.

The exact chemical and structural nature of the EMD films formed on the electrodes under operating conditions is unknown, and for this reason this study endeavoured to characterise these films *in situ*, thus avoiding any atmospheric degradation of electrode reaction products and the interference with crystal growth that normally occurs during *ex situ* surface analyses. It was necessary to conduct these experiments using synchrotron radiation GIXRD techniques as; 1) the very high mass absorption of X-rays by aqueous  $\text{Mn}^{2+}$  solutions obviates the use of a laboratory-based X-ray source as it does not permit sensitive *in situ* monitoring of electrochemical reaction products; 2) the poor signal-to-noise ratio of laboratory-based GIXRD, even in air, leads to a small number of diffraction peaks in *ex situ* analyses, preventing the unequivocal identification of electrochemical reaction products. Obviously, the true surface structure of the EMD deposited and its electrode kinetic properties must be known if an increased understanding of its electrochemistry is to be obtained, and the combination of *in situ* SR-GIXRD and EIS has great potential to achieve this.

Access to synchrotron radiation was provided by the ANBF and the experiments took place at the Photon Factory, Tsukuba, Japan.

### 5.1 Cell Design: Part I

A flow cell previously developed for simultaneous SR-GIXRD and electrode kinetic studies on other electrochemical systems, such as carbon dioxide corrosion on mild steel, and electrochemical oxidation of pyrite in chloride media [1] was fitted with a 2x1 cm platinum electrode and used for these experiments (see Diagram 5.1, and Figure 5.1). The flow cell was constructed of Perspex, fitted stainless steel tube fittings which doubled as the cells counter electrodes, and incorporated a replaceable 20  $\mu\text{m}$  thick window of X-ray transparent Kapton film. This original deposition cell

was then further modified in an attempt to improve the performance of the deposition cell. These modifications will be discussed further in section 5.5.

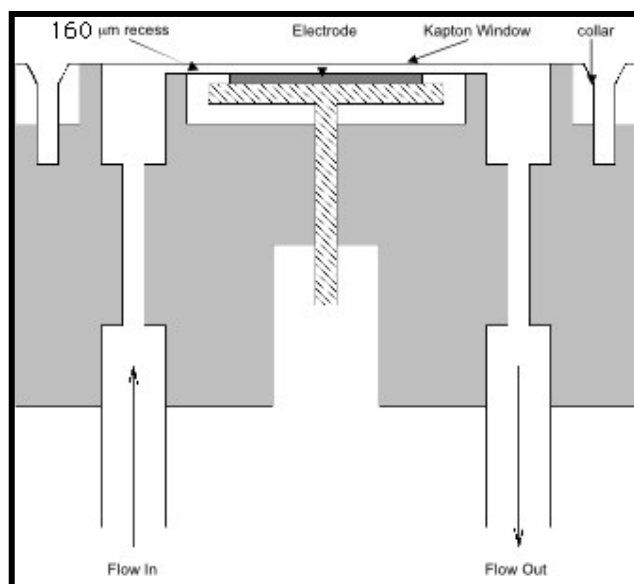


**Diagram 5.1:** A simplified schematic on the EMD deposit cell used for *in-situ* SR-GIXRD / EIS.

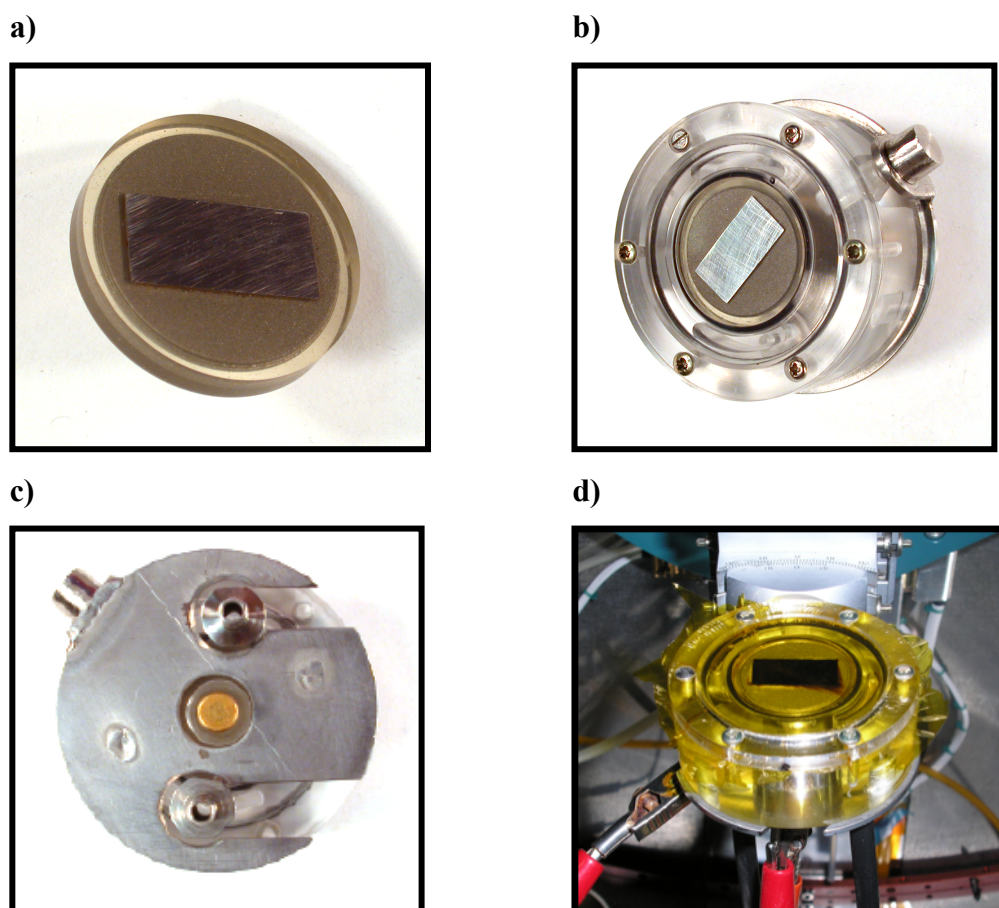


**Figure 5.1:** Photographs of **a)** the 2x1 platinum working electrode, **b)** the flow cell viewed from the top, **c)** the flow cell viewed from the bottom, and **d)** the connected flow cell inside diffractometer, with Kapton film in place, and a deposit on the electrode.

## 5.2 Experimental

The 2x1 cm platinum working electrode was polished using diamond spray and red lubricant, cleaned with 50% HNO<sub>3</sub>, ethanol and deionised H<sub>2</sub>O, and then fitted to the experimental cell. The cell was attached to the goniometer within the diffractometer at ANBF. The cell was connected to a heated, recirculating electrolyte reservoir, which also housed a double junction Ag/AgCl reference electrode, and a temperature probe. The reservoir was heated via a hotplate and the electrolyte recirculated using a peristaltic pump. The electrolyte (500 mL) used contained 60 g/L [Mn<sup>2+</sup>] and 35 g/L [H<sub>2</sub>SO<sub>4</sub>], and was prepared by dissolving MnSO<sub>4</sub>·5H<sub>2</sub>O (~131.69g) in deionised H<sub>2</sub>O, adding conc. H<sub>2</sub>SO<sub>4</sub> (~17.5g), and then made to volume in a 500 mL volumetric flask. During the second beam-line allocation, the effect of 3000 ppm of

$K^+$  was to be studied, the solutions were prepared in the same manner as the standard electro-deposition solution, except  $K_2SO_4$  (3.36g) was added to the solution. The platinum working electrode, the counter electrodes (the stainless steel inlet and outlet fittings) and reference electrode were connected to an EG&G Princeton Applied Research PARSTAT 2263 portable potentiostat. This instrument was controlled by *Powersuite* software [2], and was used to apply a constant current for EMD deposition and to monitor EIS data. EIS spectra were collected at the open circuit potential using an A.C. amplitude of  $\pm 10$  mV rms, and a frequency range of 100kHz-100mHz.

*In situ* SR-GIXRD analyses were performed on Beam-line 20B at the Photon Factory, Tsukuba, Japan, using the “BIGDIFF” diffractometer. This instrument uses a Si (111) channel cut monochromator set at 1 Å, and parallel beam optics to provide an incident beam with vertical and horizontal dimensions of 100  $\mu$ m and 2 mm respectively. SR-GIXRD patterns were recorded using Fuji imaging plates using exposure times of 10 or 20 minutes, using a wavelength of 1 Å, and an incidence angle of  $\alpha$  1° and 0.5° for the first and second series of experiments respectively. Under these conditions the technique becomes surface sensitive as total external reflection of the incident X-ray beams occurs.

It should be noted that the electrolyte solution was pumped through the cell during the electro-deposition of the EMD, and during the EIS analysis of the deposit. This was done to maximise solution thickness over the working electrode, as while pumping, the flexible Kapton film expanded allowing a thicker layer of solution to pass over the working electrode, thereby minimising solution resistance. However, during the collection of SR-GIXRD patterns the pump was switched off to minimise solution thickness over the working electrode, as cessation of pumping produced a slight suctioning effect which pulled the Kapton film closer to the working electrode. This minimised the solution thickness over the working electrode, and thereby minimised the concomitant attenuation of the X-ray beam by the electrolyte. The stainless steel inlet and outlet fittings were also used as counter electrodes, this was done to minimise the electrolyte distance between the working and counter electrodes and further minimise solution resistance.

**NB:** Due to time constraints and the complex nature of these experiments the experimental conditions were modified on an experiment-by-experiment basis. Further details about experimental conditions will be provided in the results/discussion section.

### 5.3 Simultaneous *in situ* SR-GIXRD and EIS – Results and Discussion: Part I

Initial characterisation of EMD by SR-GIXRD was carried out on the powder EMD sample “10 Thick”, which was produced at the HiTec Energy pilot plant. This initial analysis was undertaken to give an approximation of expected EMD peak positions when a wavelength of 1 Å used, and confirm the experimental set up was functioning appropriately. The sample was suspended in ethanol, and then drop-cast onto a dummy deposition cell. The sample was then analysed at incidence angles of 1, 2.5, and 5°. Of the three patterns taken, the pattern taken at 2.5° was optimal in terms of signal to noise ratio (Figure 5.2). Table 5.1 shows the approximate  $2\theta$  values of EMD when characterised using a wavelength of 1Å.

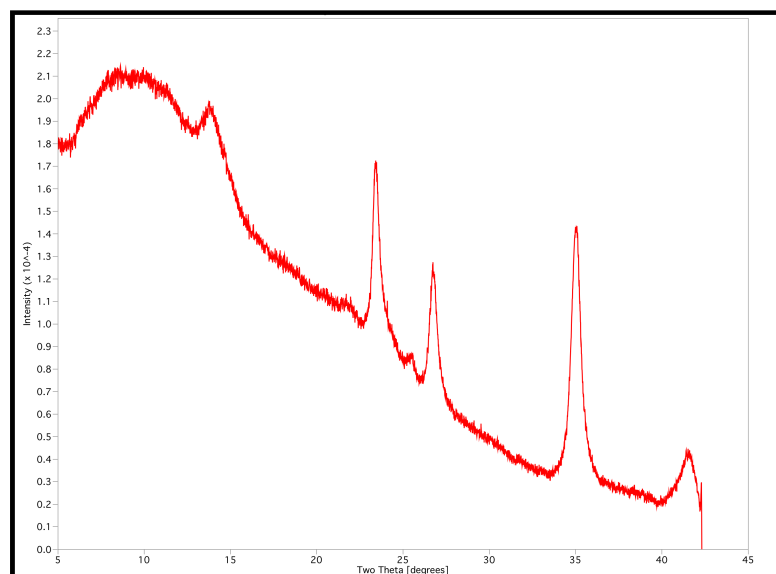


**Figure 5.2:** SR-GIXRD of the EMD sample “10 Thick” at an incidence angle of 2.5°.

**Table 5.1:** The approximate  $2\theta$  values of EMD when characterised using a wavelength of 1 Å.

<b>EMD Peaks</b>	<b><math>2\theta</math> value (<math>\lambda=1 \text{ \AA}</math>)</b>
<b>110</b>	13.8
<b>021</b>	23.4
<b>121</b>	26.7
<b>221</b>	35.0
<b>061</b>	41.4

Initial attempts at simultaneous *in situ* SR-GIXRD and EIS measurement of EMD proved problematic, and acquiring meaningful SR-GIXRD and EIS data proved extremely difficult. SR-GIXRD analysis was hindered by poor electrode coverage by the deposited EMD, the disintegration and removal of the EMD deposits from the electrode, and cell alignment problems. This resulted in SR-GIXRD spectra that contained only extremely weak, if any, EMD peaks amongst the platinum peaks of the working electrode. EIS analysis was hindered by artefacts produced by the deposition cell (that is, the spectra did not correlate well with previous lab results), significant IR losses in the system, reference electrode failures, high solution resistances created by the long length of tube needed to recirculate the electrolyte, and the presence of air bubbles that created breaks in the electrochemical circuit. These factors also influenced the electro-deposition processes of the EMD. Maintaining operating temperature was also difficult, which affects both the structure of the deposit and the electrochemistry of the system.

Through a series of adjustments made to the deposition conditions, the deposition cell, and the experimental set-up, significant improvements in the quality of the data obtained from these analyses were achieved. These adjustments included:

- All lines being primed before starting the experiments to eliminate air bubbles from the system.
- Insulating the lines and the electrolyte reservoir with aluminium foil to reduce temperature fluctuations.
- Replacing the deposition cell to address cell alignment problems.
- Overhauling the reference electrode frequently to reduce failures.

- Moving the counter electrodes closer to the working electrode to reduce IR losses, and solution resistance.
- Altering the deposition conditions, flow rates, and deposition times to produce a deposit that possessed good structural order, while giving good electrode coverage and adherence. That is, the use of low current densities, long deposition times, elevated deposition temperature and low flow rates to reduce deposit breakage.

Implementation of these adjustments improved the quality of the EIS spectra, revealing evidence of the diffusion processes observed in the spectra of previous conventional EIS experiments, however the spectra were still very noisy and suffered from poor reproducibility. Due to poor quality of the EIS spectra and lack of complementary SR-GIXRD data, modelling of the data was not deemed worthwhile.

Adjustments to the deposition condition, and the deposition cell also improved the quality of the SR-GIXRD analyses. An EMD deposit exhibiting good structural order, electrode coverage, and adherence was produced using a combination of low electrolyte flow rates and the deposit conditions described below:

- $[\text{Mn}^{2+}] = 60 \text{ gL}^{-1}$
- $[\text{H}_2\text{SO}_4] = 35 \text{ gL}^{-1}$
- Current density =  $5 \text{ A/m}^2$
- Temperature =  $\sim 75 \text{ }^\circ\text{C}$
- Plate time = 4 and 8 hours

The SR-GIXRD patterns of this deposit (see Figure 5.3) clearly show the XRD peaks from the platinum substrate being masked by an electro-deposition product after 4 hours of deposition. Peak analysis of the electro-deposition product confirmed that the product was indeed EMD, although the [110] peak has been obscured by the amorphous humps of the Kapton films SR-XRD pattern. After 8 hours of deposition the platinum peaks of the electrode substrate are almost completely masked by the deposited EMD. Unfortunately there is no complimentary EIS data available for this experiment. The EMD SR-GIXRD peaks show a slight shift to higher  $2\theta$  values with increasing deposition times, however as this shift is also observed in the platinum peaks it appears that this shift is merely an instrument artefact. As SR-GIXRD is a

surface sensitive characterisation technique, it appears that the surface of a growing EMD deposit exhibits very similar structural properties to the bulk of the material; this could indicate that any reaction intermediates that may be present on the surface of the EMD during deposition are only present in very small quantities; however it may indicate that the *in situ* SR-GIXRD characterisation technique may not be sensitive enough to differentiate between EMD and its intermediates.

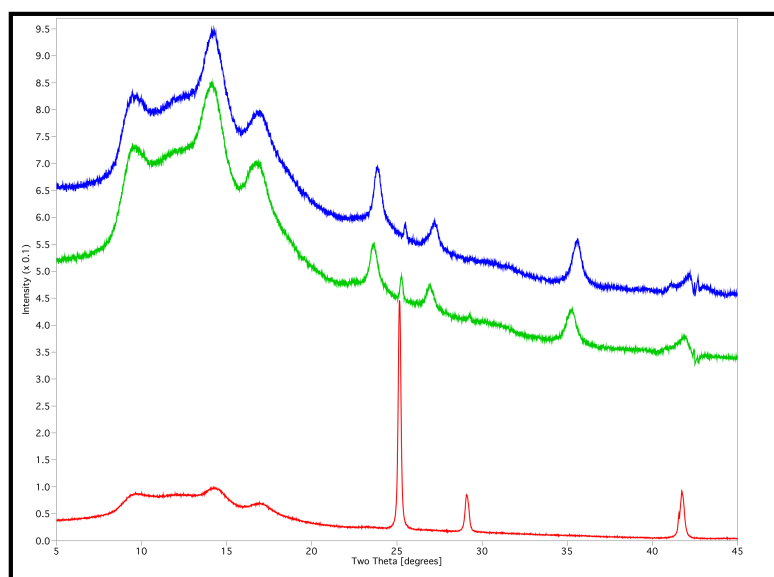


**Figure 5.3:** The SR-GIXRD patterns of the platinum substrate plus the Kapton film [red], EMD deposited at  $5\text{ A/m}^2$ , from an electrolyte containing  $60\text{ g/L Mn}^{2+}$  and  $35\text{ g/L H}_2\text{SO}_4$  at  $75\text{ }^\circ\text{C}$ , using deposition times of 4 hours [green] and 8 hours [blue].

#### 5.4 Simultaneous *in situ* SR-GIXRD and EIS – Conclusions and Recommendations: Part I

The results of the first experiment at the Photon Factory in Tsukuba, Japan, suggest that simultaneous *in situ* SR-GIXRD and EIS analysis of the deposition of EMD, although extremely difficult, is possible if the experimental set-up is suitable. Therefore to improve the quality of the analysis, the numerous problems with the experimental set-up exposed in the first round of experiments needed to be addressed. These problems are summarised below:

- Problems with cell alignment.
- The distance between the counter electrodes and the working electrode producing uneven depositions and creating IR losses.

- The inability to maintain a high enough operating temperature.
- The long lengths of tube appeared to affect the reference electrode and the electrochemistry of the system due to their high resistance.

In an attempt to alleviate the problems caused by the above issues, the deposition cell was redesigned for the second trip to the Photon Factory.

### 5.5 Cell Design: Part II

The new deposition cell was very similar to the original cell in terms of the basic design, however to reduce alignment errors the cell was machined more precisely. To promote even electrode coverage, reduce IR losses and reduce the solution resistance over the working electrode, a stainless steel counter electrode positioned concentric to the working electrode was introduced into the cell. The tubing was also shortened and insulated with aluminium foil to reduce heat losses, IR losses and the solution resistance. Photographs of the new deposition cell are shown in Figure 5.4. Due to manufacturing delays, time to test the cell was extremely limited.

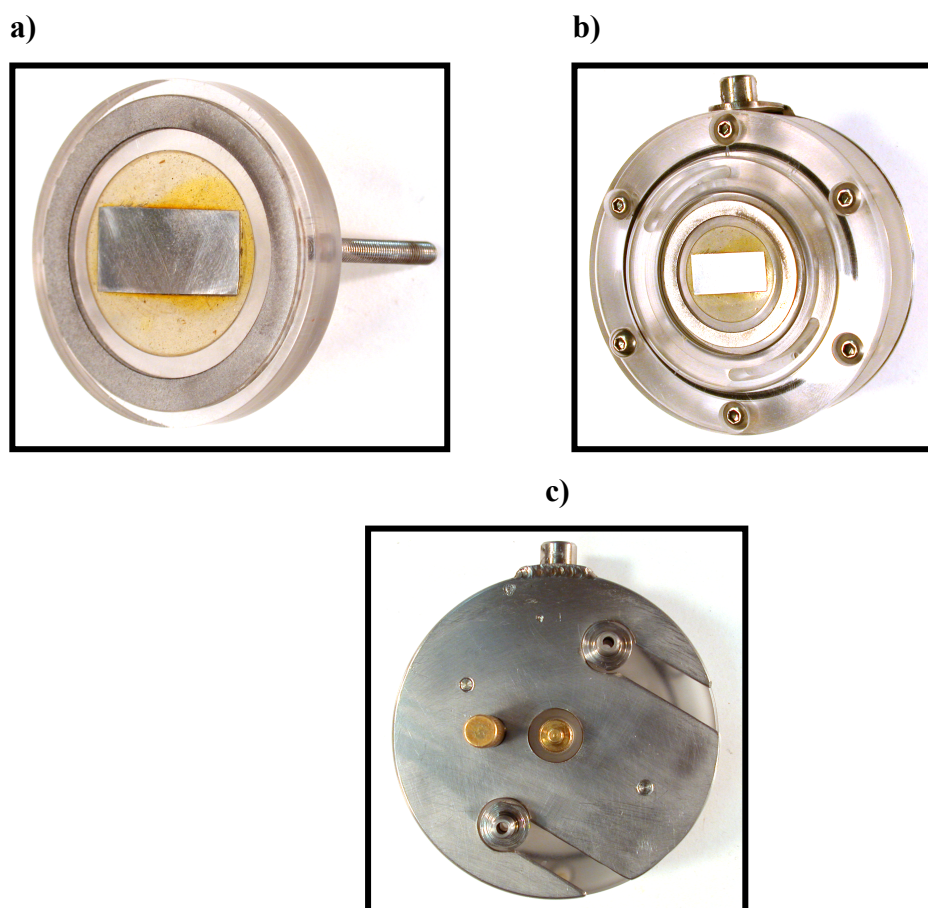


**Figure 5.4:** Photographs of **a)** the new 2x1 platinum working electrode and concentric stainless steel counter electrode, **b)** the new flow cell viewed from the top, and **c)** the new flow cell viewed from the bottom.

### 5.6 Simultaneous *in situ* SR-GIXRD and EIS – Results and Discussion: Part II

After the first round of experiments it was recognised the best results were obtained by depositing EMD at low current densities, and elevated temperature for long periods of times, as these conditions gave a well ordered deposit, which adhered well to the electrode. These deposition constraints limit the deposition conditions that can be study using this *in situ* method. Previous work in this study showed that the structure of EMD is most influenced by current density and temperature, which for these experiments must remain low and high respectively, and that variations of  $\text{Mn}^{2+}$  and acid concentrations have only a small effect on the crystal structure of EMD, which may be hard to detect using this method. Therefore it was decided that

for the second round of simultaneous *in situ* SR-GIXRD and EIS at the Photon Factory, the deposition conditions should be kept fairly constant and an additive used to alter the EMD structure, in an attempt to gain further insight into the EMD deposition process. After a literature review it was decided that the  $K^+$  ion at high concentrations should be used, as it should tend to promote the formation of  $\alpha$ - $MnO_2$  structures, which significantly alters the deposited EMDs XRD pattern [3]. This was confirmed using the standard deposition rig used in this study, and low-background XRD characterisation (results of these experiments are presented in Chapter 4, Section 4.8).

Unfortunately, as for the first round of simultaneous *in situ* SR-GIXRD and EIS experiments at the Photon Factory, the second round of experiments also proved problematic, with alignment problems (this time caused by the instrument, not the deposition cell), side reactions, bubbles causing breaks in the electrochemical circuit, possible electrode leaks causing short circuits, and deposit breakage, all hindering the analysis. Adjustments were made to the experiment set-up to try and alleviate these problems, however these efforts were fruitless. For example, to reduce interference from bubbles, all lines were primed before each experiment, flow rates were increased to prevent bubbles getting trapped in the flow cell (this increased the likelihood of deposit breakages), and the cell was orientated vertically during deposition and EIS analysis, in an attempt to trap the bubbles in a location where they could not interfere with the electrochemistry. Unfortunately these efforts proved unsuccessful.

SR-GIXRD analysis again produced very few meaningful results, in several experiments EMD failed to even deposit on the working electrode. This was attributed to possible short circuiting due to electrode leaks and possible electrode passivation. When deposits were obtained, the resulting SR-GIXRD spectra showed only extremely weak, if any, EMD /  $\alpha$ - $MnO_2$  peaks amongst the platinum peaks of the working electrode. Figure 5.5 shows the best SR-GIXRD pattern produced in this round of experiments. The spectra were obtained from an EMD /  $\alpha$ - $MnO_2$  deposit produced at  $20A/m^2$ , from an electrolyte containing 60 g/L  $Mn^{2+}$ , 35 g/L  $H_2SO_4$ , and 3000 ppm  $K^+$  at 93 °C, using a deposition time of 1 hour. Although the peaks are

small and broad, their positions correspond well to characteristic EMD /  $\alpha$ -MnO<sub>2</sub> peaks at d-spacings of approximately 2.42 Å (EMD<sub>[021]</sub>), 2.21 Å (EMD<sub>[200]</sub>), 2.12 Å (EMD<sub>[121]</sub>), 1.85 Å ( $\alpha$ -MnO<sub>2</sub>) and 1.64 Å (EMD<sub>[061]</sub>). [Note:  $\alpha$ -MnO<sub>2</sub> peaks were identified using peak positions (d-spacing) from an EMD /  $\alpha$ -MnO<sub>2</sub> sample produced at similar conditions, and that the peaks denote as EMD were also present in the EMD /  $\alpha$ -MnO<sub>2</sub>.]

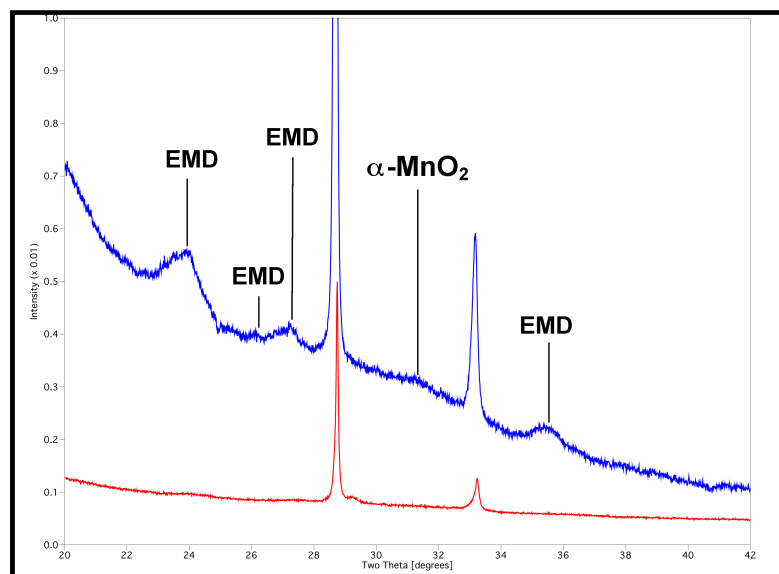


**Figure 5.5:** The SR-GIXRD patterns of the platinum substrate plus the Kapton film [red], and EMD /  $\alpha$ -MnO<sub>2</sub> deposited at 20A/m<sup>2</sup>, from an electrolyte containing 60 g/L Mn<sup>2+</sup>, 35 g/L H<sub>2</sub>SO<sub>4</sub>, and 3000 ppm K<sup>+</sup> at 93 °C, using a deposition time of 1 hour [blue]. [Note: The intensities of the EMD /  $\alpha$ -MnO<sub>2</sub> pattern have been amplified, and the amorphous humps of the Kapton film cropped, to highlight the EMD /  $\alpha$ -MnO<sub>2</sub> peaks.]

This EIS spectra collected from the EMD and EMD /  $\alpha$ -MnO<sub>2</sub> samples deposited were very noisy, of poor quality, were not reproducible and seemed to be complicated by artefacts produced by the deposition cell (that is, the counter electrode seemed to be undergoing deposition and stripping reactions of its own during the course to the experiments). The poor quality of the EIS spectra was attributed to a combination of deposit breakage, bubbles interfering with the electrochemical circuit, IR losses, high solution resistances, leaks in the electrodes, and the apparent side reactions occurring at the counter electrode.

### 5.7 Simultaneous *in situ* SR-GIXRD and EIS – Conclusions and Recommendations: Part II

The very nature of EMD and its deposition mechanism makes the simultaneous *in situ* SR-GIXRD and EIS analysis of this system extremely difficult. EMD is a poor scatterer of X-rays: it has a disordered structure; and very small crystallite sizes [4], all of which makes the conventional *ex situ* XRD structural characterisation difficult (especially when using laboratory based GI-XRD instruments which have poor signal-to-noise ratios). This situation becomes even more difficult for *in situ* characterisation, because the high mass absorption of X-rays by the electrolyte shielding the EMD deposit, which significantly reduces the X-ray beams intensity, and therefore reduces the quality spectra produced (hence the need to use synchrotron radiation). In addition, the high temperature conditions that are typically used to deposit EMD are far from the ideal conditions recommended for conventional electrochemical analysis. But as stated in Section 5.4, this research suggests, that simultaneous *in situ* SR-GIXRD and EIS analysis of the deposition of EMD, although extremely difficult, is possible if the experimental set-up is suitable. It is obvious from the results of this study that the deposition cell and experimental set-up currently used needs to be refined considerably before higher quality results can be obtained. For example, the introduction of an inert platinum counter electrode may reduce the side reactions observed in Section 5.6, and improve the quality of the EIS analysis. The usefulness of this analysis technique in future studies of EMD will be determined by surface sensitivity of the *in situ* SR-GIXRD analysis (which at present is probably too insensitive to provide critical information regarding the presence and/or identity of any intermediates that may be involved in the EMD deposition process), and the quality of the complementary EIS data obtained (which at present is quite poor, and does not appear to be representative of the processes involved in EMD deposition). In the opinion of the author, the marriage of *in situ* SR-GIXRD and EIS for use in EMD research shows promise, and once perfected it could potentially be used as a powerful research tool to gain a greater understanding of the EMD deposition mechanism and other important electrochemical processes. In fact, the marriage of any surface sensitive *in situ* structural characterisation technique (such as Raman spectroscopy) and an electrode kinetic method (such as EIS, cyclic voltammetry (CV), and amperometry etc.) has the potential to provide a great deal of insight into electrochemical systems that have solid to liquid interfaces.

## 5.8 References

1. De Marco, R., S. Bailey, Z.-T. Jiang, J. Morton, and R. Chester, *An in situ chronoamperometry/synchrotron radiation grazing incidence X-ray diffraction study of the electrochemical oxidation of pyrite in chloride media*. *Electrochem. Commun.*, 2006. **8**: p. 1661-1664.
2. Research, P.A., *PowerSuite-2.33.0*, 2000, PerkinElmer Instruments Inc.
3. Kao, W.-H., V.J. Weibel, and M.J. Root, *The Influence of Potassium Ion on the Electrodeposition and Electrochemistry of Electrochemistry of Electrolytic Manganese Dioxide*. *J. Electrochem. Soc.*, 1992. **139**(5): p. 1223-1226.
4. Chabre, Y. and J. Pannetier, *Structural and Electrochemical Properties of the Proton / gamma MnO<sub>2</sub> System*. *Prog. Solid State Chem.*, 1995. **23**: p. 1-130.

*Every reasonable effort has been made to acknowledge the owners of copyright material. I would be pleased to hear from any copyright owner who has been omitted or incorrectly acknowledged.*

## 6 MODELLING THE CRYSTAL STRUCTURE OF EMD – Part I: Introduction, Determination of the Phases, and Potential Testing

### 6.1 Introduction to Molecular Modelling of the Crystal Structure of EMD

In order to fully understand the various properties of EMD, it is necessary to develop a deep understanding of its crystal structure. However, the very nature of EMD, with its extremely small crystallite sizes and highly defective structure prevents us from achieving this goal through experimental methods alone. Fortunately, developments in molecular modelling techniques allow simulations of possible structures and relative energetics of a compound [1]. This was the approach taken in this project to further elucidate the crystal structure of EMD.

There have been many investigations into the structure of EMD and many models put forward to describe its structure, most of which (with the exception of Hill *et al.* [2], Balachandran *et al.* [3-6], Maphanga *et al.* [7] and Sayle *et al.* [8, 9]) have been empirical in nature, and did not take into account the deformations of the crystal lattice that are likely to occur as a result of the defects present in the crystal structure. The advantage of using molecular modelling to investigate the structure of EMD is that the structures are allowed to relax to a minimum lattice energy, which takes into account any lattice deformations that may occur as a result of defects. In principle, this should result in a more accurate representation of the EMD structure.

The main goals of this work were to develop a modelling workflow that could accurately reproduce the structural features of EMD, while remaining relatively simple, and computationally inexpensive. With this in mind the molecular modelling of the EMD was split into four stages:

1. The determination of the MnO<sub>2</sub> phases present in EMD.
2. The development of a suitable potential model to model the crystal structure of EMD.
3. An investigation of the various defects/structures likely to occur in EMD, and their effect on simulated XRD patterns.
4. The development of possible models for the structure of EMD, using the knowledge gained in stage 3.

The workflow used to investigate the various defects/structures that are likely to occur in EMD (i.e. 3 above) involved three steps:

1. Constructing supercells of the defects/structures, using *GDIS* [10] or *CrystalMaker* [11].
2. Minimising the supercells by employing the derived potential model, and using the *GULP* [12] computational package.
3. Simulating the XRD patterns of the minimised structures using *CrystalDiffract* [13], a commercially available XRD simulation program, and comparing the result to the experimental EMD XRD pattern of IBA 30.

The XRD patterns simulated by CrystalDiffract used the following parameters: monochromatic radiation of wavelength of 1.54050 Å (Cu anode), Lorentzian peak shape, with instrumental broadening of  $0.6^\circ$   $2\theta$  to simulate the effect of the small crystallite size of EMD, and a particle size of 1  $\mu\text{m}$ . All other settings were left at their default value. The simulated patterns were compared to IBA 30, as this is generally accepted as “standard” EMD. For the sake of simplicity, all comparisons between simulated and experimental XRD patterns were performed by eye, yielding purely qualitative results.

## 6.2 Determination of MnO<sub>2</sub> Phases/Mixtures present in EMD

Manganese oxides are known to occur as mixtures, solid solutions and intergrowths of various polymorphs: therefore to successfully model the structure of EMD, it is essential to determine the MnO<sub>2</sub> phases present. From a modelling perspective, the simplest way to achieve this is to compare the simulated XRD of various MnO<sub>2</sub> polymorphs found in the literature and modelled during this study to experimental diffraction patterns of EMD. Figure 6.1 shows that ramsdellite, pyrolucite, and akhtenskite ( $\epsilon$ -MnO<sub>2</sub>) are the most likely phases to contribute to the diffraction pattern of EMD as they share common peaks. This observation is consistent with the literature, as generally these three phases form the basis for most EMD structural models. It is also evident from the simulated XRD patterns that EMD is unlikely to contain significant quantities of 2x2 and 2x3 tunnel polymorphs of MnO<sub>2</sub>.

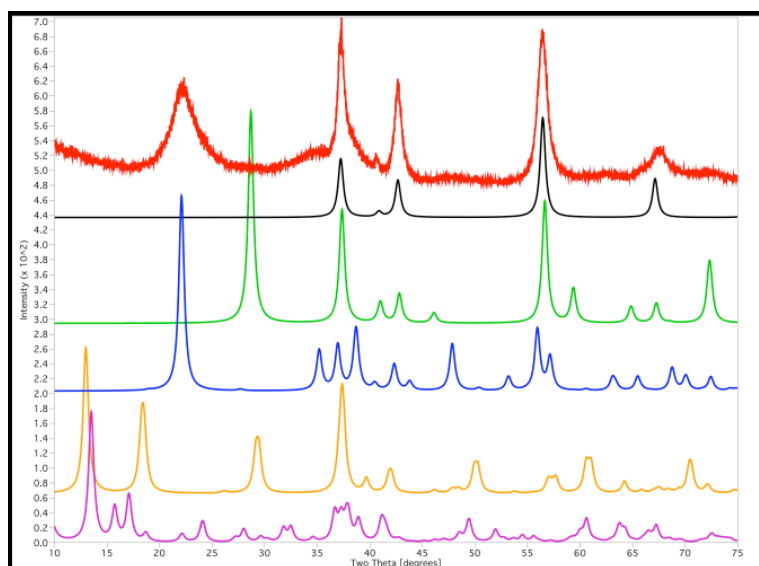


**Figure 6.1:** A comparison the simulated XRD patterns of various  $\text{MnO}_2$  phases to an experimental EMD (IBA 30) XRD pattern [red], 2x3 tunnel structure (modelled in section 6.4.2) [pink], 2x2 tunnel structure (modelled in section 6.4.1) [orange], ramsdellite [14] [blue], pyrolucite [15] [green], and  $\epsilon\text{-MnO}_2$  [16] [black].

There has long been a debate as to whether EMD is a homogeneous intergrowth or merely a very fine grain heterogeneous mixture of various  $\text{MnO}_2$  polymorphs. To investigate this, various combinations of pyrolucite, ramsdellite, and  $\epsilon\text{-MnO}_2$  phases were mixed, using the MIX function in CrystalDiffract [13], and the resulting XRD patterns examined. Binary mixtures of pyrolucite and ramsdellite gave relatively poor fits to experimental EMD diffraction patterns. Figure 6.2 shows the fit of a mixture containing 45% w/w pyrolucite and 55% w/w ramsdellite to experimental data. These percentages were thought to best represent the possible composition of EMD, as they were derived from the literature [17], where it was observed that about 30% of Mn atoms were found in pyrolucite layers in EMD. The poor fits indicate that EMD is more likely to be an intergrowth, rather than a mixture of discrete ramsdellite and pyrolucite phases.

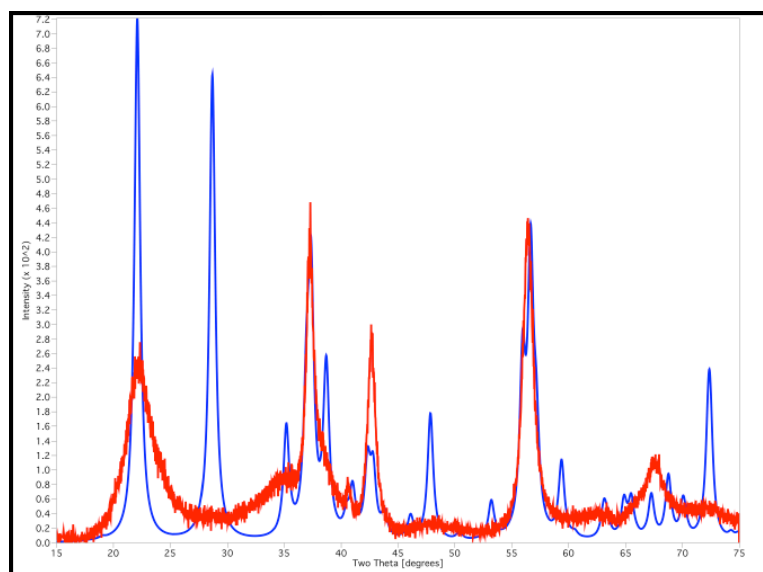


**Figure 6.2:** A comparison of the experimental EMD (IBA 30) XRD pattern [red], and a simulated mixture of 45% pyrolucite and 55% ramsdellite [blue].

Mixtures of ramsdellite and  $\epsilon$ - $\text{MnO}_2$  that contained high levels of  $\epsilon$ - $\text{MnO}_2$  fitted the experimental EMD diffraction data quite well, although the broadness of the experimental peaks are not reproduced and the presence of additional peaks are still an issue. Due to the nature of ramsdellite, however, it is unlikely that ramsdellite would be present in its pure form; it is far more likely that it would be present in a defective form, possibly containing both De Wolff and micro-twinning defects [17]. This hypothesis has some support from the literature, as an analysis carried out *via* Rietveld refinement found that EMD was a mixture of  $\gamma$ - $\text{MnO}_2$  and  $\epsilon$ - $\text{MnO}_2$  [18]. Figure 6.3 shows the fit of a mixture of 60%  $\epsilon$ - $\text{MnO}_2$  and 40% ramsdellite to experimental data, these percentages were chosen as they correspond to this Rietveld refinement [18].

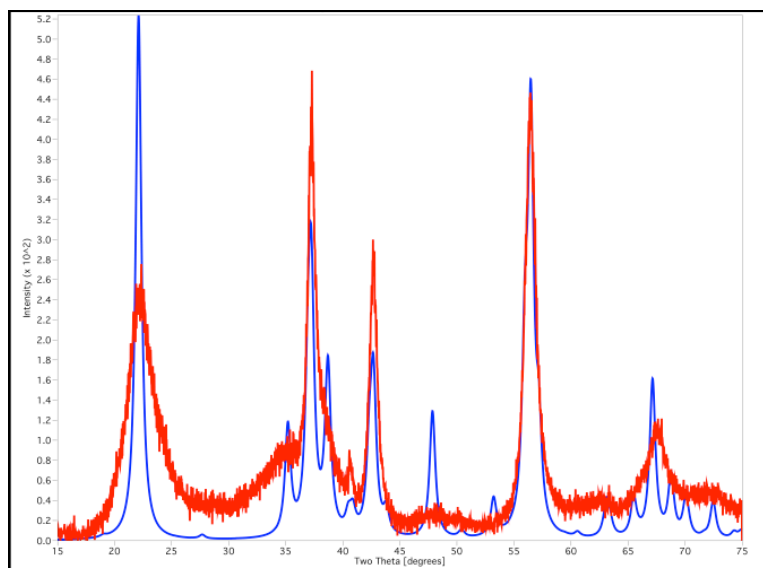


**Figure 6.3:** A comparison of the experimental EMD (IBA 30) XRD pattern [red], and a simulated mixture of 40% ramsdellite and 60%  $\epsilon$ -MnO<sub>2</sub> [blue].

Mixtures of all three phases produced patterns with relatively poor fits to experimental data, see Figure 6.4; this is mainly due to the peak at  $\sim 28^\circ$  2 $\theta$ , which is produced by pyrolucite. This was also the case in the binary mixture of pyrolucite and ramsdellite, which suggests that pyrolucite is not present as a discrete phase in EMD.

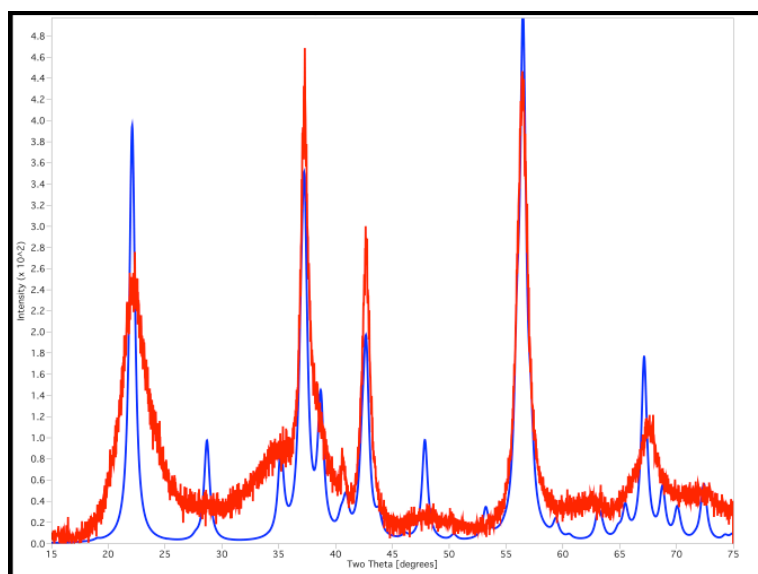


**Figure 6.4:** A comparison of the experimental EMD (IBA 30) XRD pattern [red], and a simulated mixture of 7% pyrolucite, 30% ramsdellite and 63%  $\epsilon$ -MnO<sub>2</sub> [blue].

After examination of these simulated XRD patterns, it seems unlikely that EMD is simply a fine grain heterogeneous mixture of pyrolucite, ramsdellite and  $\epsilon$ -MnO<sub>2</sub>. However a mixture of a ramsdellite phase that contains De Wolff and micro-twinning defects, with  $\epsilon$ -MnO<sub>2</sub> may be a possible explanation of the typical EMD XRD pattern. The work presented in this section is not new to the field, but it clearly shows that the EMD structure is far more complex than a simple mixture of MnO<sub>2</sub> phases.

### 6.3 Modelling the Crystal Structure of EMD

In order to model the crystal structure of EMD, calculations must be performed on model systems large enough to adequately represent the structural features of EMD. Since EMD is thought to contain a large number of defects, some of which are described as extended in the literature [17], the size of the model systems tends to be quite large. Unfortunately this excludes using quantum mechanics to model EMD structures, as the computational time for such calculations on these large model systems would be unreasonably large. With this in mind, this study used a force field method with a suitable potential model to investigate the structure of EMD.

Another issue that must be addressed when attempting to model EMD is the random nature of the structure. The EMD structure is thought to be based on the  $\gamma$ -MnO<sub>2</sub> structure, which has been described as a disordered, random intergrowth of ramsdellite and pyrolucite: this random nature adds to the complexity of modelling the structure of EMD. Fortunately, Chabre and Pannetier [17] reported that both random and ordered structures (albeit with structures that were not allowed to optimise) gave similar results, therefore because of the difficulties associated with modelling structures with random disordered ions, the structures produced in this study were fully ordered and non-random, which dramatically simplified the modelling process.

### 6.3.1 Theory

A classical force field approach was employed to describe the atomic interactions in manganese dioxide. The Born model was used, which involves partitioning the lattice energy into Coulombic point charge interactions and non-Coulombic interaction terms; the latter consists of short-range repulsion and medium range attractive dispersion forces. Temperature effects were not considered. Parameterization of the force field was achieved using a least squares approach. Experimental values of the unit cell parameters and atomic positions for ramsdellite [14] and pyrolucite [15] from the literature were used in the fitting process. The computational package *GULP* [12] was employed in computing the minimum energy structures and to assist in the fitting stage.

The non-Coulombic interactions were modelled using a Morse potential, which takes the form of Equation 6.1:

$$E(r) = D_e \left( 1 - e^{-\alpha(r_0 - r)^2} \right) \quad \text{Equation 6.1}$$

with the customisable parameters  $D_e$ ,  $\alpha$ , and  $r_0$  defining the energy contribution  $E$  for a particular pair of atoms at separation  $r$ , where  $D_e$  (in eV) is related to bond strength,  $\alpha$  (in  $\text{\AA}^{-1}$ ) is related to the curvature at the potential minimum, and  $r_0$  (in  $\text{\AA}$ ) is the equilibrium interatomic separation.

A geometry dependent charge model was employed to compute the electrostatic contribution to the lattice energy, as implemented in the *GULP* package [12]. The method used was the charge equilibration scheme of Goddard and Rappé [19], with a modification that evaluates the analytical derivatives more efficiently [12]. Using this approach, atomic charges are assigned by solving coupled equations involving the electronegativity and the Coulombic interaction between charge sites. Evaluation of the Coulombic interaction is split into two parts; the short-range interactions (within 15  $\text{\AA}$ ) are calculated by integration over two Slater  $s$  orbitals, and the long-range (beyond 15  $\text{\AA}$ ) interactions are taken to be the classical Coulomb potential. The latter are evaluated using the Ewald summation technique [20].

### 6.3.2 Potential Fitting

The initial stage of this work was aimed at accurately modelling the crystal structures of pyrolucite and ramsdellite. This was accomplished by employing existing model parameters as a starting point for the fitting process; namely existing manganese dioxide potentials that did not use the more accurate variable charge scheme [21, 22], and adapting previously published potentials for rutile [23, 24] and anatase [25]. The best result was derived from the rutile variable charge model of Swamy et al [23], with the final interatomic parameters given in Table 6.1.

**Table 6.1:** The fitted parameters for the Morse potentials in the variable charge model developed that best reproduced the structures of pyrolucite and ramsdellite.

	$D_e$ (eV)	$\alpha$ ( $\text{\AA}^{-1}$ )	$r_0$ ( $\text{\AA}$ )
Mn – O	1.09069	3.98071	1.78017
Mn – Mn	0.005645	1.69722	4.14158
O – O	0.041159	1.16724	3.69663

The quality of the derived potentials was judged by how well they reproduce the crystal structures of pyrolucite and ramsdellite (Figure 6.5, Figure 6.6 and Table 6.2). Note that an attempt was made to modify all potential parameters from their original form, since some were originally intended for non-manganese dioxide systems. In the case of the two manganese dioxide models, no better result than the original values could be found, even though a variable charge model was added. In Table 6.3, we present the best results that were obtained in this study for each of the derived potential models. The high quality of our variable charge model is evident from the fact that all calculated values differ from the experimental values by less than 2%; this is the only model for which such a result was obtained. In addition, the reason for the close match of the Woodley et al [21] and Sayle et al [24] results is the high degree of similarity between the point charges used for the atomic species.

**Table 6.2:** Comparison between experimental and calculated lattice parameters for pyrolucite [15] and ramsdellite [14].

	Pyrolucite			Ramsdellite		
	a (Å)	b (Å)	c (Å)	a (Å)	b (Å)	c (Å)
Calculated	4.3744	4.3744	2.8910	9.1997	4.4945	2.8979
Experimental (Å)	4.3983	4.3983	2.8730	9.3329	4.4533	2.8482
Difference (%)	-0.54	-0.54	0.63	-1.32	0.92	1.74

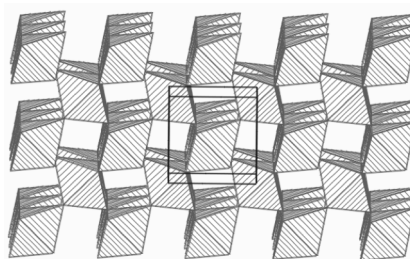


**Figure 6.5:** Simulated pyrolucite lattice viewed along the *c* axis.

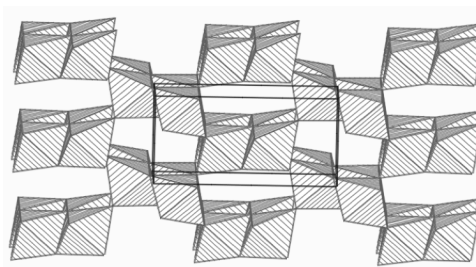


**Figure 6.6:** Simulated ramsdellite lattice viewed along the *c* axis.

**Table 6.3:** The percentage errors between the calculated and the experimental lattice parameters of pyrolucite [15] and ramsdellite [14] for the fitted potential models derived from the literature.

Original Publication	Pyrolucite			Ramsdellite		
	a	b	c	a	b	c
Swamy et al [23]	-0.54	-0.54	0.63	-1.32	0.92	1.74
Woodley et al [21]	-2.54	-2.54	2.77	-2.11	7.08	4.53
Woodley et al [22]	-2.28	-2.28	-1.41	-4.82	5.92	0.25
Sayle et al [24]	-2.25	-2.25	-1.43	-4.83	5.91	0.25
Bush et al [25]	-3.46	-3.46	3.39	-1.74	1.18	3.77

Dr Sean Fleming at Curtin University assisted in the potential fitting of the variable charge model.

## 6.4 Testing Potentials

Coordinates of various  $\text{MnO}_2$  polymorphs were taken from the ICSD database [26]. These structures were then imported into *GDIS* [10]. All atoms other than manganese and oxygen, were then removed from the crystal structure, and the structure optimized by *GULP* [12] using the derived potentials and the changes in structure observed. Since the counter ions in the experimental structures were removed, all the manganese ions are in the +4 oxidation state. The polymorphs modeled were:

- 2x2 tunnel structures (hollandite, corondite and cryptomelane)
- 2x3 tunnel structure (romanechite)
- 3x3 tunnel structure (todorokite)
- Spinel structure ( $\text{LiMn}_2\text{O}_4$ )

### 6.4.1 2x2 Tunnels Structures

The hollandite, coronadite and cryptomelane structures (Figures 1.6 – 1.8) have very similar structures, the only difference being the cations that charge balance the  $\text{Mn}^{3+}$  in the structure. Thus once the guest cations are removed (Figure 6.7), we would expect all three manganese dioxide frameworks to converge to the same result.

Table 6.4 shows that this is not the case.

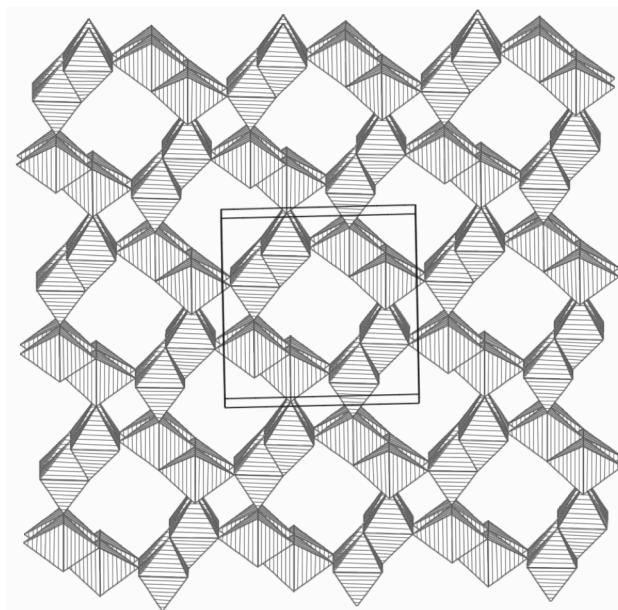


**Figure 6.7:** Simulated 2x2 tunnel structure viewed along the *b* axis.

**Table 6.4:** Comparison between experimental and calculated lattice parameters of hollandite, coronadite, and cryptomelane.

<b>Hollandite</b>	<b>- Parameters</b>			
$\text{Ba}_x(\text{Mn}^{4+}, \text{Mn}^{3+})_8\text{O}_{16}$	<b>a (Å)</b>	<b>b (Å)</b>	<b>c (Å)</b>	<b><math>\beta</math> (°)</b>
Experimental [27]	10.0060	2.8660	9.7460	91.17
Calculated	9.6906	2.8977	9.5709	90.28
Difference (%)	-3.15	1.11	-1.80	-0.98
<b>Coronadite</b>	<b>-</b>			
$\text{Pb}_x(\text{Mn}^{4+}, \text{Mn}^{3+})_8\text{O}_{16}$				
Experimental [28]	9.9380	2.8678	9.8340	90.39
Calculated	9.6332	2.8978	9.6295	90.01
Difference (%)	-3.07	1.05	-2.08	-0.42
<b>Cryptomelane</b>	<b>-</b>			
$\text{K}_x(\text{Mn}^{4+}, \text{Mn}^{3+})_8\text{O}_{16}$				
Experimental [29]	9.9560	2.8705	9.7060	90.95
Calculated	9.6935	2.8977	9.5676	90.29
Difference (%)	-2.64	0.95	-1.43	-0.73

In fact two different structures are obtained, Hollandite and Cryptomelane remain monoclinic, but Coronadite converges to a tetragonal structure. In agreement with the rules of Kitaigorodsky [30], the lower symmetry structure is more stable; however, the difference,  $2.148 \times 10^{-4}$  eV/mol, is very small. This would certainly suggest that the monoclinic and tetragonal structures would both be expected to form, and may explain why these structures have been reported in both tetragonal and monoclinic settings, although reports of the former may be due to the limited accuracy of the X-ray machines of the time.

In all three cases, the *a* and *c* parameters shrink appreciably on removal of the counter-ions, whilst the *b* parameter lengthens. This demonstrates that the large

counter-ions expand the dimensions of the channels but act to contract the cell axis along the length of the channels.

### 6.4.2 2x3 Tunnel Structures

**Table 6.5:** Comparison between initial and final lattice parameters of romanechite.

Romanechite - BaMn <sub>9</sub> O <sub>16</sub> (OH) <sub>4</sub>	Parameters			
	a (Å)	b (Å)	c (Å)	β (°)
Experimental [31]	9.5600	2.8800	13.8500	92.50
Calculated	9.5197	2.8958	13.1523	95.03
Difference (%)	-0.42	0.55	-5.04	2.73

Table 6.5 shows that the derived interatomic potentials also satisfactorily model the 2x3 tunnel structure of romanechite, Figure 6.8 show the simulated structure of romanechite with its counter ions removed. Again the cross section of the channels shrinks upon removal of the counter-ions, whilst the axis parallel to the channels expands.

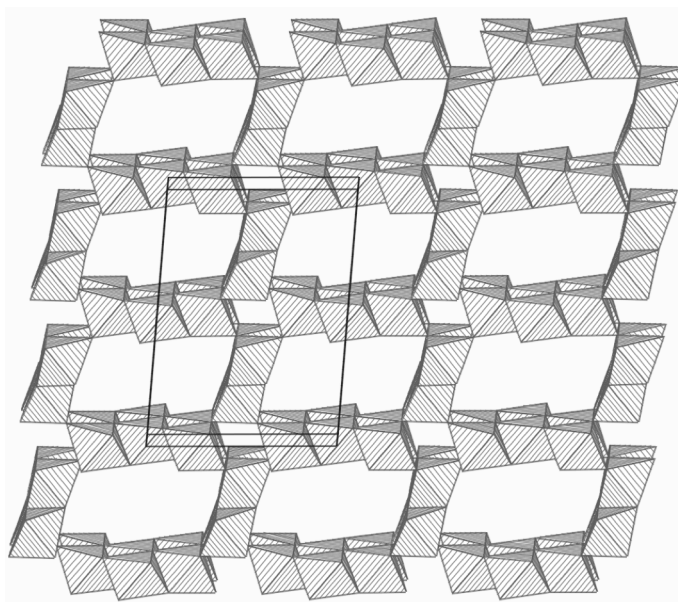


**Figure 6.8:** Simulated 2x3 tunnel structure viewed along the *b* axis.

### 6.4.3 3x3 Tunnel Structures

Efforts to model the tunnel structure of todorokite were unsuccessful as the tunnels always collapsed. This was not an entirely unexpected result. Todorokite is known to convert from the tunnel to the layer configuration under certain conditions [32], thus when the species contained within the tunnels are removed, it is highly probable that the tunnel structure will collapse.

### 6.4.4 Spinel Structures

For the sake of completeness and to assess the quality of our potentials, the spinel polymorph on  $\text{MnO}_2$  was modelled by removing the Li ions from a  $\text{LiMn}_2\text{O}_4$  structure characterised by Cho, and co-workers [33]. This Li free structure was then optimised and compared to the spinel  $\text{MnO}_2$  polymorph characterised by Mosbah and co-workers [34]. The results of this optimisation are shown in Table 6.6.

**Table 6.6:** Comparison between initial and final lattice parameters of spinel structures  $\text{LiMn}_2\text{O}_4$  and  $\lambda\text{-MnO}_2$ .

Spinel - $\text{LiMn}_2\text{O}_4 / \lambda\text{-MnO}_2$	Parameters		
	a (Å)	b (Å)	c (Å)
$\text{LiMn}_2\text{O}_4$ Experimental [33]	8.2363	8.2363	8.2363
$\lambda\text{-MnO}_2$ Experimental [34]	8.0290	8.0290	8.0290
Calculated	8.1172	8.1172	8.1172
$\lambda\text{-MnO}_2$ Difference (%)	1.10	1.10	1.10
$\text{LiMn}_2\text{O}_4$ Difference (%)	-1.45	-1.45	-1.45

Although spinel  $\text{MnO}_2$  structures such as  $\text{LiMn}_2\text{O}_4$  (Figure 1.5) have little relevance to the structure of EMD as they are based on a cubic close packed oxygen substructure, they provide a good test for the quality of the potentials, as the cell parameters for the pure  $\text{MnO}_2$  polymorph are available. The results (Table 6.6 and Figure 6.9) show the high quality of the potentials as the lattice parameter matches to within 1.1%.

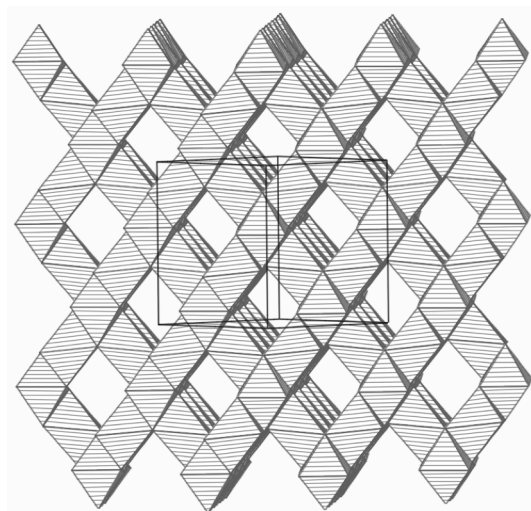


**Figure 6.9:** Simulated spinel structure viewed along  $ab$ .

#### 6.4.5 Stability of Polymorphs

The calculated stabilities of the polymorphs are listed in Table 6.7 and clearly show that pyrolucite is the most stable polymorph, in agreement with experimental results [35]. Ramsdellite is the next most stable polymorph and these two polymorphs are substantially more stable than the rest. As expected, the stability of the tunnel structures decreases as the tunnel size increases. The most surprising result is that the spinel-based structure is the least stable. The stability of several other possible  $\text{MnO}_2$  structures were also investigated; fully twinned pyrolucite (Tw-Pr)<sup>\*</sup> [16, 17]; fully twinned ramsdellite (Tw-R)<sup>†</sup> [16, 17]; and an ordered form of  $\epsilon$ - $\text{MnO}_2$  ( $\epsilon'_{[\text{Heuer}]}\text{-MnO}_2$ ) [36]. These results show that the stabilities of  $\text{MnO}_2$  polymorphs are quite similar, which may explain why intergrowths of different polymorphs are common in  $\text{MnO}_2$ . The stability of the fully twinned structures suggests that twinning is indeed likely in  $\text{MnO}_2$ , in fact the Tw-R structure is more stable than the tunnel structures. Of particular interest is the stability of the  $\epsilon'_{[\text{Heuer}]}\text{-MnO}_2$  structure,

<sup>\*</sup> The fully twinned pyrolucite (Tw-Pr) structure was derived from  $\alpha$ - $\text{PbO}_2$  structure.

<sup>†</sup> The fully twinned ramsdellite (Tw-R) structure was derived from a double  $\alpha$ - $\text{PbO}_2$  structure.

which shows that cation ordering in the  $\epsilon$ -MnO<sub>2</sub> structure can produce stable MnO<sub>2</sub> structures.

**Table 6.7: Calculated stabilities of various MnO<sub>2</sub> polymorphs.**

Structure	Stability (eV/mol)
Pyrolucite	-7.072
$\epsilon'$ <sub>[Heuer]</sub> -MnO <sub>2</sub>	-6.970
Tw-Pr	-6.969
Ramsdellite	-6.914
Tw-R	-6.833
Hollandite	-6.680
Coronadite	-6.680
Cryptomelane	-6.680
Romanechite	-6.526
Spinel	-6.524

A comparison of the relative stabilities calculated by this study and those calculated by Balachandran and co-workers [5], using a quantum mechanical description via Density Functional Theory (DFT) is presented in Table 6.8. Although the potentials produce energies around 5-10 times higher, the good correlation between our interatomic potential results and these DFT results, gives further evidence of the high quality of the potential model derived in this project. DFT is considered to be a more accurate method of calculating stabilities than interatomic potential methods, however DFT is time consuming and computationally expensive. Our interatomic potential method is less time consuming and computationally expensive, yet in this case at least, it still delivers results comparable to DFT calculations.

**Table 6.8:** A comparison of the relative stabilities calculated by this study (Qeq) and those calculated by Balachandran and co-workers [5], using DFT.

Structure	Relative Stabilities (eV/mol)	
	Interatomic Potential	DFT
Pyrolucite	0.000	0.000
$\epsilon'_{[\text{Heuer}]}-\text{MnO}_2$	0.102	0.016
Ramsdellite	0.158	0.022
Tw-Pr	0.103	0.037

#### 6.4.6 Conclusions Drawn from Potential Testing

The potentials for manganese dioxide derived in this study are of high quality as they correctly predict the lattice constants of pyrolucite, ramsdellite and  $\lambda$ -MnO<sub>2</sub> to within 2% of the experimental values. It is noteworthy that  $\lambda$ -MnO<sub>2</sub> was not included in the fitting set. The potentials have also been found to model the idealised structures of the polymorphs containing tunnels and suggest that tunnels larger than 2x3 are not stable without the presence of additional species within them. The calculated stabilities follow expected trends and the spinel-based structure is found to be the least stable polymorph.

## 6.5 References

1. Paglia, G., A.L. Rohl, G.E. Buckley, and J.D. Gale, *Determination of the structure of  $\gamma$ -alumina from interatomic potential and first-principles calculations: The requirement of significant numbers of nonspinel positions to achieve an accurate structural model*. Phys. Rev. B: Condens. Matter Mater. Phys., 2005. **71**(22): p. 224115-1-16.
2. Hill, J.-R., C.M. Freeman, and M.H. Rossouw, *Understanding gamma-MnO<sub>2</sub> by molecular modeling*. J. Solid State Chem., 2004. **177**: p. 165-175.
3. Balachandran, D., *First Principles Study of Structure, Defects and Proton Insertion in MnO<sub>2</sub>*, in *Department of Materials Science and Engineering*, 2001.
4. Balachandran, D., D. Morgan, and G. Ceder, *First Principles Study of H-insertion in MnO<sub>2</sub>*. J. Solid State Chem., 2002. **166**: p. 93-103.
5. Balachandran, D., D. Morgan, G. Ceder, and A. van de Walle, *First-principles study of the structure of stoichiometric and Mn-deficient MnO<sub>2</sub>*. J. Solid State Chem., 2003. **173**: p. 462-475.
6. Morgan, D., D. Balachandran, G. Ceder, and A. van de Walle. *A Drastic Influence of Point Defects on Phase Stability in MnO<sub>2</sub>*. in *Mat. Res. Symp. Proc.* 2003. Materials Research Society.
7. Maphanga, R.R., S.C. Parker, and P.E. Ngoepe, *Atomistic simulation of the surface structure of electrolytic manganese dioxide*. Surf. Sci., 2009. **603**(21): p. 3184-3190.
8. Sayle, T.X.T., C.R.A. Catlow, R.R. Maphanga, P. Ngoepe, and D. Sayle, *Generating MnO<sub>2</sub> nanoparticles using simulated amorphization and recrystallization*. J. Am. Chem. Soc., 2005. **127**(37): p. 12828-12837.

9. Sayle, T.X.T., R.R. Maphanga, P. Ngoepe, and D. Sayle, *Evolving microstructure in MnO<sub>2</sub> using amorphisation and recrystallisation*. J. Cryst. Growth, 2006. **294**(1): p. 118-129.
10. Fleming, S. and A. Rohl, *GDIS: A visualization program for molecular and periodic systems*. Z. Kristallogr., 2005. **220**: p. 580-584.
11. Palmer, D. and M. Conley, *CrystalMaker for Mac OS X*, 2004.
12. Gale, J.D. and A.L. Rohl, *The General Utility Lattice Program (GULP)*. Mol. Simul., 2003. **29**(5): p. 291-341.
13. Palmer, D., *CrystalDiffra for Mac OS X*, 2005.
14. Fong, C., B.J. Kennedy, and M.M. Elcombe, *A powder neutron diffraction study of lambda and gamma manganese dioxide and of LiMn<sub>2</sub>O<sub>4</sub>*. Z. Kristallogr., 1994. **209**(12): p. 941-945.
15. Baur, W.H., *Rutile-type compounds. V, Refinements of MnO<sub>2</sub> and MgF<sub>2</sub>*. Acta Crystallogr., 1976. **B32**: p. 2200-2204.
16. Chichagov, A.V., A.B. Belonozhko, A.L. Lopatin, T.N. Dokina, O.L. Samokhvalova, T.V. Ushakovskaya, and Z.V. Shilova, *Information-Calculating System on the Crystal Structure Data of Minerals (MINCRYST)*. Kristallografiya, 1990. **35**(3): p. 610-616.
17. Chabre, Y. and J. Pannetier, *Structural and Electrochemical Properties of the Proton / gamma MnO<sub>2</sub> System*. Prog. Solid State Chem., 1995. **23**: p. 1-130.
18. Simon, D.E., T.N. Andersen, and C.D. Elliott, *A Rietveld Refinement Model of EMD Powder Patterns*. ITE Lett. Batteries, New Technol. Med., 2000. **1**(3): p. 10-19.
19. Rappe, A.K. and W.A.I. Goddard, *Charge equilibration for molecular dynamics simulations*. J. Phys. Chem., 1991. **95**: p. 3358.

20. Ewald, P.P., *Ann. Phys*, 1921. **64**: p. 253.
21. Woodley, S.M., C.R.A. Catlow, P. Piszora, K. Stempin, and E. Wolska, *Computer modeling study of lithium ion distribution in quaternary Li-Mn-Fe-O spinels*. *J. Solid State Chem.*, 2000. **153**: p. 310.
22. Woodley, S.M., P.D. Battle, J.D. Gale, and C.R.A. Catlow, *The prediction of inorganic crystal structures using a genetic algorithm and energy minimisation*. *Phys. Chem. Chem. Phys.*, 1999. **1**: p. 2535.
23. Swamy, V., J.D. Gale, and L.S. Dubrovinsky, *Atomistic simulation of the crystal structure and bulk moduli of TiO<sub>2</sub> polymorph*. *J. Phys. Chem. Solids*, 2001. **62**.
24. Sayle, D.C., C.R.A. Catlow, M.A. Perrin, and P. Nortier, *Computer simulation study of the defect chemistry of rutile TiO<sub>2</sub>*. *J. Phys. Chem. Solids*, 1995(56): p. 799.
25. Bush, T.S., J.D. Gale, C.R.A. Catlow, and P.D. Battle, *Self-consistent interatomic potential for the simulation of binary and ternary oxides*. *J. Mater. Chem.*, 1994. **4**: p. 831.
26. *Inorganic Crystal Structure Database (ICSD)*. 1999.
27. Miura, H., *The crystal structure hollandite*. *Mineral. J.*, 1986. **13**: p. 119-129.
28. Post, J.E. and D.L. Bish, *Rietveld refinement of the coronadite structure*. *Am. Mineral.*, 1989. **74**(7-8): p. 913-917.
29. Post, J.E., R.B. Von Dreele, and P.R. Buseck, *Symmetry and cation displacement in hollandites: structure refinements of hollandite, crypomelane and priderite*. *Acta Crystallogr.*, 1982. **B38**: p. 1056-1065.
30. Kitaigorodsky, A.I., *Molecular Crystals and Molecules* 1973, New York: Academic Press.

31. Wadsley, A.D., *The crystal structure of psilomelane*. Acta Crystallogr., 1953. **6**: p. 433.
32. Williams, R.P., *Characterisation and Production of High Performance Electrolytic Manganese Dioxide for use in Primary Alkaline Cells.*, in *Department of Chemistry*, 1995, The University of Newcastle: Newcastle, Australia.
33. Cho, N.W., S. Chang, and H.P. Sung, *Synthesis and crystal structure refinement of Li (Mn-d) Ti(d) O4*. RIST Yongu Nonmun, 1997. **11**: p. 622.
34. Mosbah, A., A. Verbaere, and M. Tournoux, *Lithium manganate ( $Li_xMnO_2$ ) phases intercalated in the spinel type*. Mater. Res. Bull., 1983. **18**(11): p. 1375-1381.
35. Pannetier, J., *A comprehensive structural model of EMD and CMD based on De Wolff disorder and microtwinning*. Prog. Batteries Battery Mater., 1992. **11**: p. 51-55.
36. Heuer, A.H., A.Q. He, P.J. Hughes, and F.H. Feddrix, *Microstructure of Electrolytic MnO<sub>2</sub>: A Transmission Electron Microscopy Study of Bulk Material*. ITE Lett. Batteries, New Technol. Med., 2000. **1**(6): p. 76-80.

*Every reasonable effort has been made to acknowledge the owners of copyright material. I would be pleased to hear from any copyright owner who has been omitted or incorrectly acknowledged.*

## 7 MODELLING THE CRYSTAL STRUCTURE OF EMD – Part II: Modelling Defects in EMD, and Determination of a Structural Model

### 7.1 Foundation Work For This Project

As a precursor to the structural modelling component of this project, Dr Sean Fleming used the potential model derived in Chapter 6 and the DIFFaX code [1] to reproduce, and then extend the work of Chabre and Pannetier [2], and to investigate the crystal structure of EMD. Fleming used the potential model to calculate the formation energies of both De Wolff and micro-twinning defects. The results of these calculations (see Table 7.1) showed that the occurrence of a De Wolff defect is more favourable when based on the ramsdellite lattice i.e. attaching a strained pyrolucite lattice to a pre-existing ramsdellite lattice is slightly more energetically favourable than the reverse case. This is consistent with literature descriptions of the structure of EMD, which describe EMD as a ramsdellite matrix containing pyrolucite layers. The results of the micro-twinning calculations, strongly indicated that twinning on both the (021) and (061) planes should occur, which is in agreement with Pannetier [3]. In addition to this, these unpublished results suggest that a single twin is more likely to occur than a single De Wolff defect. It should be noted however, that this is for an isolated defect and therefore not necessarily an indicator for a greater degree of twinning within EMD.

**Table 7.1:** The energy cost, per unit area, for the formation of particular defects in the EMD crystal structure.

Defect Type	Formation Energy (J/m <sup>2</sup> )
De Wolff defect (ramsdellite reference)	0.1644
De Wolff defect (pyrolucite reference)	0.1991
Microtwinning on the (021) plane	0.0608
Microtwinning on the (061) plane	0.0750

The work described above was used as a foundation for the investigation of the crystal structure of EMD undertaken as part of this PhD thesis and reported in the following sections.

## 7.2 Modelling De Wolff Defects

Using our potential model, De Wolff defects were modelled using two methods, the “Slab Method”, and the “Layer Method”.

The Slab Method involved creating ramsdellite and pyrolucite surfaces along the (020) and (200) lattice planes respectively; these slabs were then allowed to dock with each other, and the resulting structures converted to a 3D supercells, which were then optimised and diffraction patterns simulated using these minimized structures. The concentration and segregation of De Wolff defects in the modelled structures were varied by changing the size of the ramsdellite and pyrolucite slabs used in the calculations. The previous calculations on De Wolff defects showed that it is energetically more favourable to attach a strained pyrolucite slab to a pre-existing ramsdellite slab, therefore the pyrolucite slabs were always docked to a base ramsdellite slab. The minimum thickness of a pyrolucite layer using this method was two unit cells or four octahedra. This was to ensure that the docking slabs are commensurate with one another. This limited the flexibility of this method, as defects that consist of pyrolucite layers less than four octahedra thick could not be modelled. In spite of this limitation the model provided valuable insights into the nature and occurrence of De Wolff defects in EMD.

The Layer Method involved applying our potential model to methods used by Hill and co-workers [4]. In order to model De Wolff defects, Hill *et al.* used a layer model that was previously employed by Schilling and Dahn [5]. In this model four different layers exist, A, B, C, and D, although layers B and D may have to be shifted by  $\frac{1}{2}$  in the *c*-direction (denoted by B' and D') in order to construct pyrolucite layers. In this layer model ramsdellite can be built via the sequence ...ABCDABCD... and pyrolucite via ...B'DB'DB'DB'D... Various concentrations and segregations of De Wolff defects can also be constructed using combinations of the above layers. Hill *et al.*, then optimised the structures created using the augmented consistent valence force field (CVFF) of Vessal. A stacking program was developed “in-house” at Curtin University to build various structures from these layers. These structures were then optimised using our potential model and diffraction patterns simulated.

### 7.2.1 The Slab Method

Simulated diffraction patterns of structures with various percentages of pyrolucite yield results that correspond well to those reported in the literature [2, 5]. As the percentage of pyrolucite within a ramsdellite structure increases, the following observations can be made:

- The  $110_{\text{rams}}$  peak moves to higher  $2\theta$  values, is reduced in intensity, and is significantly broadened.
- Several peaks appear in the region of the  $110_{\text{pyro}}$  peak, as the percentage of pyrolucite increases; these peaks coalesce and increase in intensity to form the  $110_{\text{pyro}}$  peak. Although it is not completely clear from these diffraction patterns, the  $110_{\text{rams}}$  peak seems to split/broaden and move to higher  $2\theta$  values. This peak then coalesces with the  $120_{\text{rams}}$ , which remains virtually stationary; and the  $130_{\text{rams}}$  peak which is shifted to lower  $2\theta$  values.
- The  $101_{\text{pyro}}$  peak becomes more prominent.
- The  $221_{\text{rams}}$  peak moves to slightly higher  $2\theta$  values to become the  $211_{\text{pyro}}$  peak.
- The  $240_{\text{rams}}$  peak moves to higher  $2\theta$  values to become the  $220_{\text{pyro}}$  peak.

These results are similar to the simulations performed by Chabre and Pannetier [2], although they did not include the effects of lattice relaxation, and confirmed their argument that diffraction lines with  $k/2+1=\text{even}$ , such as the 120 peak, are not affected by De Wolff defects and that lines with  $k=\text{odd}$  are significantly shifted and broadened. There are some differences with the simulations performed here with the simulated diffraction patterns showing that some lines with  $k/2+1$  even exhibit slight shifting and broadening. This is likely to be a result of the optimisation performed in this study. Figure 7.1 shows the effect of increasing of the amount of pyrolucite in the structure.

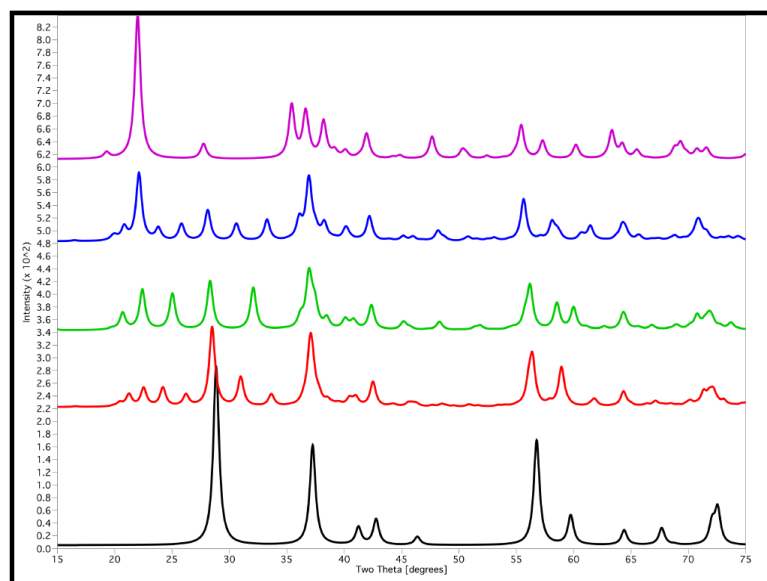


**Figure 7.1:** Simulated XRD patterns of various De Wolff structures using the slab method, showing the effect of increasing the percent of pyrolucite within the crystal structure. 100% pyrolucite [black], 67% pyrolucite [red], 50% pyrolucite [green], 33% pyrolucite [blue], 0% pyrolucite (ramsdellite)[pink].

To examine how the concentration of De Wolff defects within EMD affects its diffraction pattern, the thickness of the pyrolucite and ramsdellite layers involved in the defects was varied: thin layers result in a high defect concentration, while thick layers result in a low defect concentration. This can then be related to the segregation of the defects, which can be simply described as the degree of alternation between pyrolucite and ramsdellite layers. Therefore thin layers result in low levels of segregation ( $s < 0.5$ ), as the layers alternate more frequently and the occurrence of De Wolff defects (ramsdellite/pyrolucite interfaces) increases, thick layers result in high levels of segregation ( $s > 0.5$ ) which implies that ramsdellite and pyrolucite tend to occur as separate phases within the structure, that is the layers alternate less frequently, and the occurrence of De Wolff defects decreases. It should be noted that a simple model like this produces fully ordered defect structures, which may limit its accuracy when compared with experimental patterns, as the possibility of random arrangements of defects are not considered. Although random arrangements are neglected, the model is still suitable for determining general trends in the simulated patterns. Figure 7.2-Figure 7.4 show the effect of the concentration of De Wolff defects on the simulated XRD patterns of structures containing 33.33%,

50%, and 66.67% pyrolucite respectively. Decreasing the concentration of De Wolff defects (increasing the segregation) within a structure results in a reduction in size of the line shifts observed; increasing the segregation also results in features from both pyrolucite and ramsdellite XRD patterns becoming more dominant in the simulated XRD pattern. These findings are not unexpected, as when segregation increases the structure moves to become a mixture of discrete phases, rather than an intergrowth. The clearest example of this is Figure 7.2 which shows the characteristic peaks of both ramsdellite and pyrolucite become more defined as the segregation of the De Wolff defects increases.

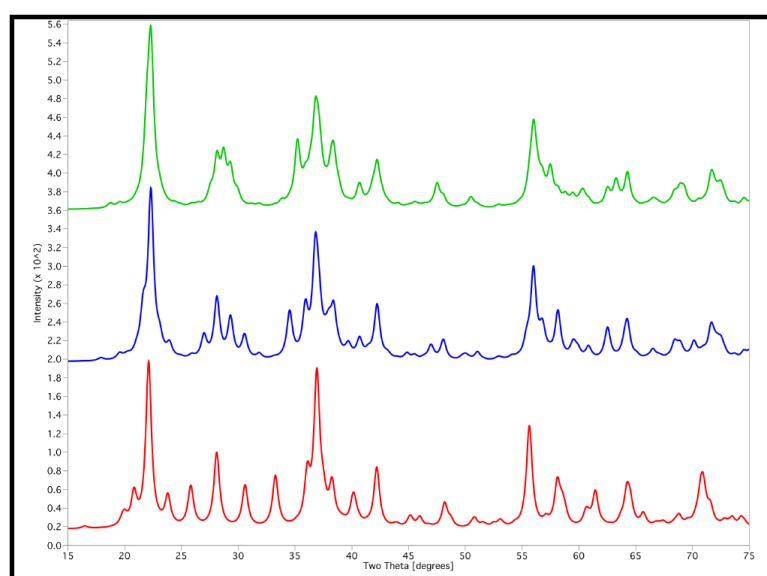


**Figure 7.2:** Simulated XRD patterns of De Wolff structures containing 33.33% pyrolucite, at low [red], medium [blue], and high [green] levels of segregation.

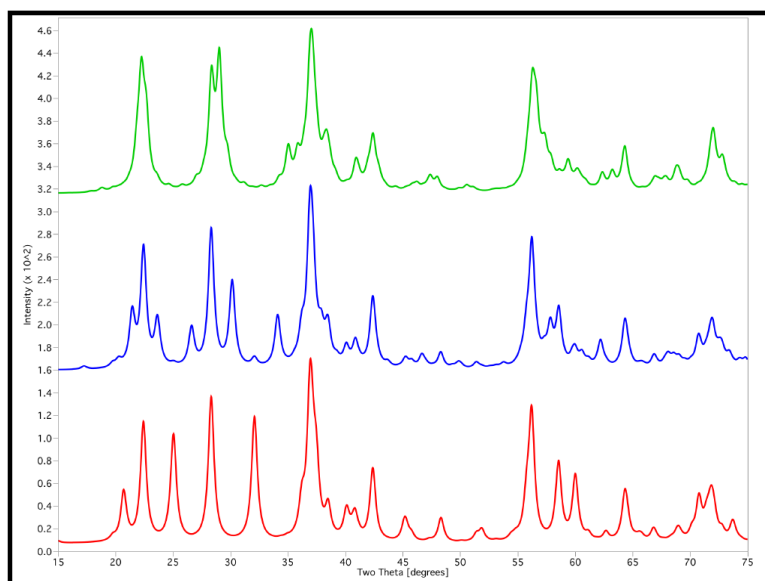


**Figure 7.3:** Simulated XRD patterns of De Wolff structures containing 50% pyrolycrite, at low [red], medium [blue], and high [green] levels of segregation.

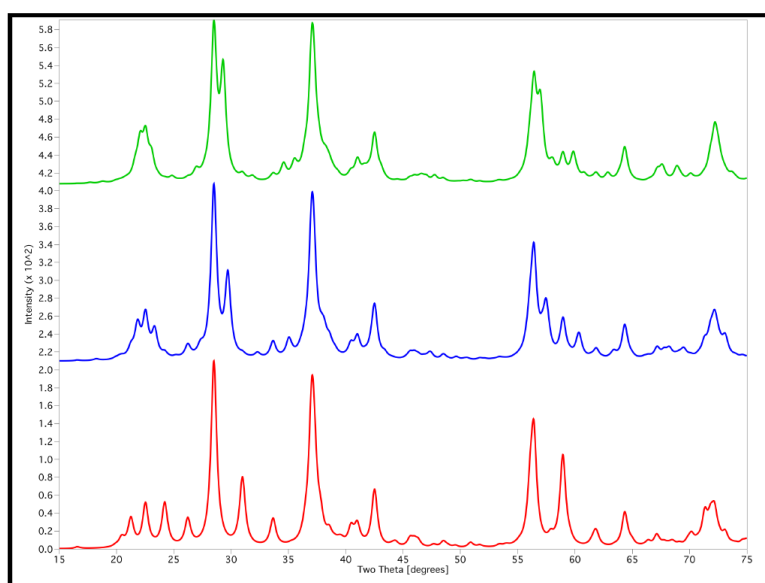


**Figure 7.4:** Simulated XRD patterns of De Wolff structures containing 66.67% pyrolycrite, at low [red], medium [blue], and high [green] levels of segregation.

### 7.2.1.1 Stabilities of De Wolff Structures Produced via the Slab Method

The stability of De Wolff structures produced by the slab method increases as the amount of pyrolycrite increases. This was expected as pyrolycrite is known to be the

most stable  $\text{MnO}_2$  polymorph, therefore the presence of De Wolff defects within the ramsdellite lattice should indeed stabilize the structure. Figure 7.5 shows there is a linear relationship between the stabilities of De Wolff structures relative to pure pyrolucite and the percent pyrolucite present in the structure and that the degree of segregation has only a slight effect on the stabilities. Figure 7.5 also shows  $kT$  at 298 K. This not only gives an idea of what configurations are accessible but is also used as a point of reference in the following Figures.

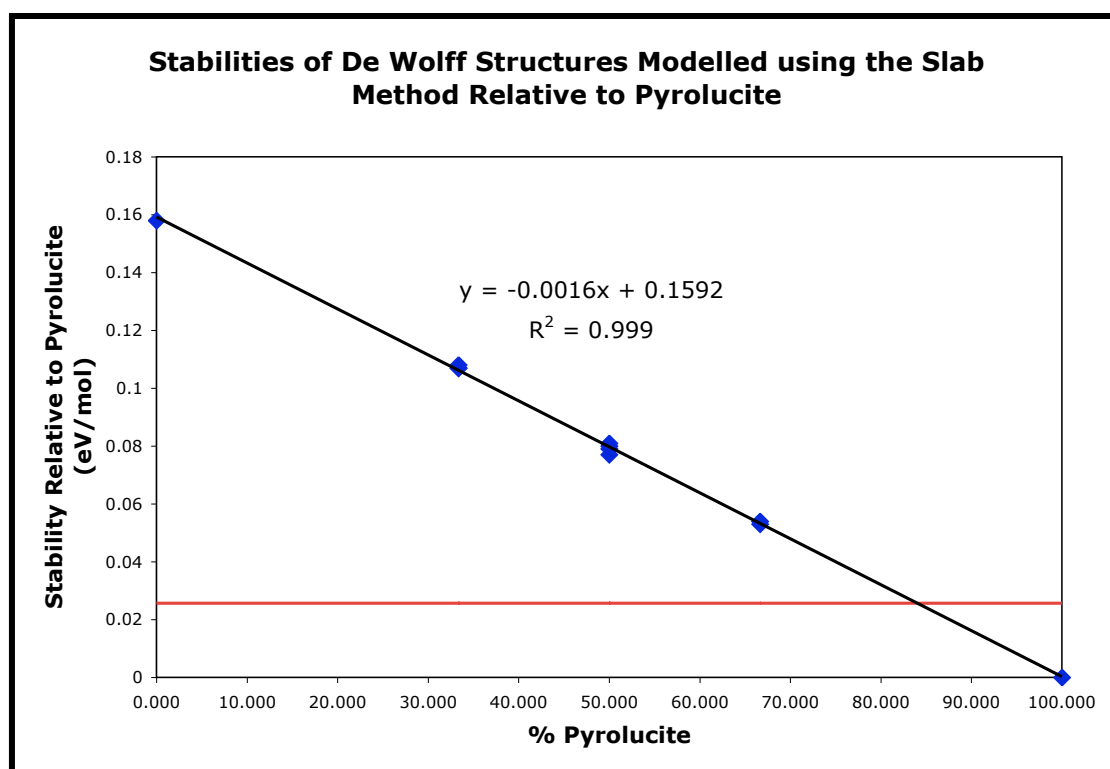


**Figure 7.5:** Stabilities of De Wolff structures modelled using the slab method relative to pure pyrolucite, and  $kT$  at 298K [red].

### 7.2.1.2 Conclusions Drawn by Modelling De Wolff Defects via the Slab Method

Several conclusions can be drawn by comparing the simulated XRD patterns produced by the slab method to experimental EMD XRD patterns. It appears that structures containing ~33% pyrolucite with low segregations give the best fit to experimental data (see Figure 7.6). This suggests that the EMD structure contains low levels of pyrolucite that are well dispersed in thin layers throughout the crystal

structure. This finding is consistent with that of Chabre and Pannetier, who found that EMD samples tended to have  $P_r$  values of approximately 0.45, which corresponds to about 30% of manganese atoms being situated in pyrolucite layers [2].

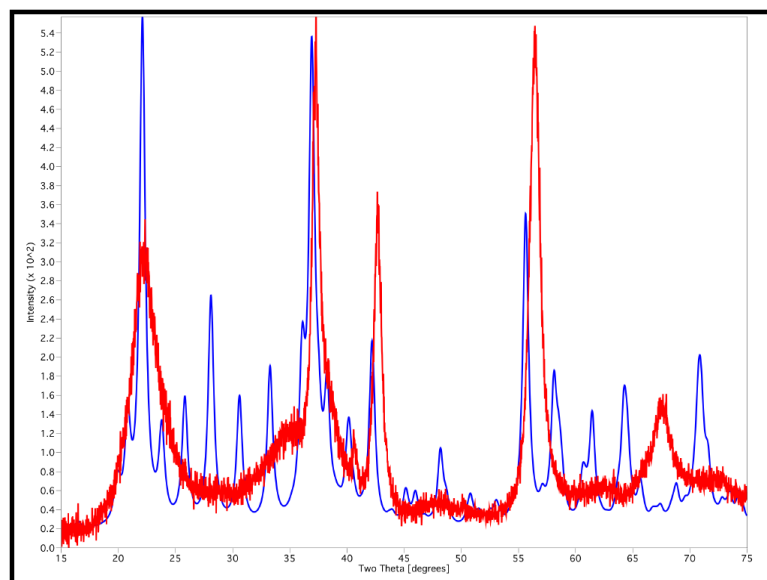


**Figure 7.6:** A comparison of an experimental EMD (IBA 30) XRD pattern [red], and a simulated XRD pattern of a De Wolff structure containing ~33% pyrolucite at low levels of segregation, using the slab method [blue].

Although there are many similarities between the simulated XRD pattern of a De Wolff structure containing ~33% pyrolucite at low levels of segregation and the experimental EMD XRD data, the simulated XRD pattern does not adequately explain all the features present in the experimental EMD pattern, suggesting that other defects may be present in the EMD crystal structure. Of particular interest are the additional peaks located in the region of 25 - 35° 2 $\theta$ , and the absence of the 061<sub>EMD</sub> peak in the simulated pattern. The additional peaks may be an artefact of the ordered nature of this model, or indicate that EMD actually contains less than 33.33% pyrolucite, as these peaks are located in the region of the 110<sub>pyro</sub> peak. The absence of the 061<sub>EMD</sub> peak is likely to be a result of this model neglecting the effects of twinning.

### 7.2.2 The Layer Method

The first step in applying our potential model to the layer method described in Hill *et al.* [4], is to compare the simulated XRD patterns of structures optimised with the potentials used by Hill *et al.* to structures optimised with our potential model. As expected our potentials performed well with Figure 7.7 showing that the difference between the simulated XRD patterns using the two potential models is slight, with the major differences occurring at higher  $2\theta$  values, where our model tends to give peak positions that are slightly higher than those predicted by the potential model employed by Hill *et al.* This result not only confirms that our potential model can be applied to the layer model used by Hill *et al.*, it also reinforces the high quality of our potential model for modelling  $\text{MnO}_2$  structures.

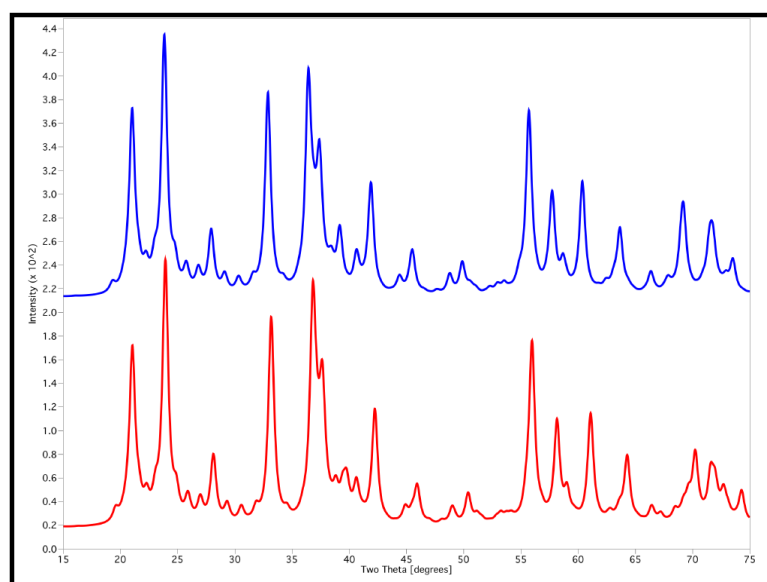


**Figure 7.7:** Simulated XRD patterns of a De Wolff structure containing 33.33% pyrolucite modelled with the layer method using the Hill *et al.*, potential model [blue] and our potential model [red].

The results obtained when using the layer method to model De Wolff defects are reproduced in Figure 7.8 and shows similar general trends to those observed when the slab method is used, and to those predicted by Chabre and Pannetier [2]. However the structures investigated using the layer method do show some differences in their simulated XRD patterns; these are listed below:

- At percentage pyrolucite values of  $\sim 33\%$ , the  $110_{\text{rams}}$  peak appears to split, leaving a strong peak at  $\sim 20.9^\circ 2\theta$ , and the  $130_{\text{rams}}$  peak has a higher than expected intensity. According to Chabre and Pannetier this maybe an artefact of using an ordered model, and can be explained by an unequal distribution of cations at  $x=0$  and  $x=1/2$  within the structure.
- The peak shifts were generally greater than those observed when the slab method was used to model these defects. This was especially evident in the shifts associated with the  $110_{\text{rams}}$  peaks, which shows a greater shift to higher  $2\theta$  values, as well as a greater reduction in intensity as the percentage of pyrolucite increases. This can be explained in terms of defect concentration, as these structures generally have thinner pyrolucite layers, thus the segregation of the defects is reduced and therefore the defect concentration is increased. This results in increases in peak shifts and broadening.

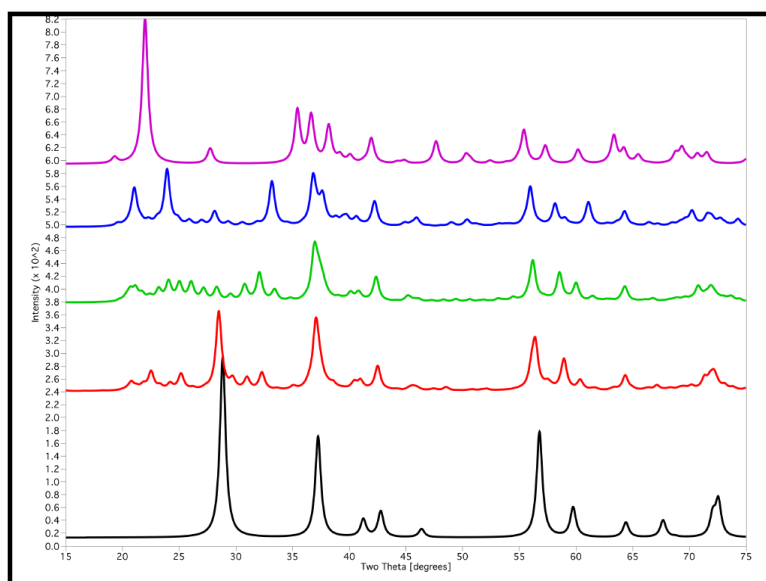


**Figure 7.8:** Simulated XRD patterns of various De Wolff structures using the layer method, showing the effect of increasing the percent of pyrolucite within the crystal structure. 100% pyrolucite [black], 67% pyrolucite [red], 50% pyrolucite [green], 33% pyrolucite [blue], 0% pyrolucite (ramsdellite) [pink].

The main benefit of using the layer method is the flexibility that the model offers, which means that a wider array of De Wolff structures can be investigated.

#### **7.2.2.1 Stabilities of De Wolff Structures Produced via the Layer Method**

The stabilities of De Wolff structures calculated by the layer method gave very similar results to the slab method. As expected, the stability of these structures increased in a linear fashion as the percent pyrolucite in the structures increased, this is illustrated in Figure 7.9. The figure also shows that the line of best fit of the layer method is very similar to that of the slab method suggesting that these two methods give the same energetics. These results, as was the case for the slab method, also show that the degree of segregation of the De Wolff defects has little affect on the stabilities of the structures; this suggests that it is the amount of pyrolucite in the structure, not its distribution that determines the stabilities of De Wolff structures. However, it should be noted that the segregation does affect the crystal structure, as shown by changes in the simulated XRD patterns, and therefore would be expected to affect the electrochemical properties of EMD.

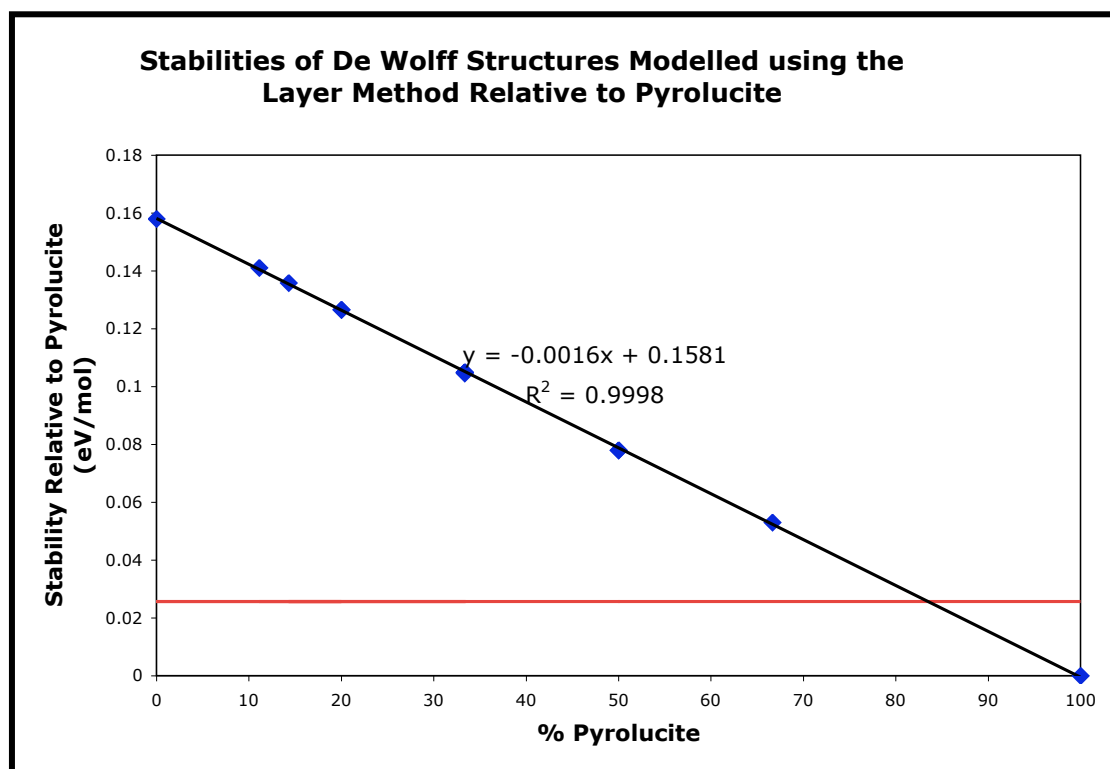


**Figure 7.9:** Stabilities of De Wolff structures modelled using the layer method relative to pure pyrolocite, and  $kT$  at 298K [red].

### 7.2.2.2 Conclusions Drawn by Modeling De Wolff Defects via the Layer Method

Similarly to the results of the slab method, the results of modelling De Wolff structures using the layer model provide further evidence that the EMD structure contains low levels of pyrolocite that are well dispersed in thin layers throughout the crystal structure. However, the results of the layer method suggest that EMD may only contain ~15% pyrolocite, as the simulated XRD patterns of these De Wolff structure give the best fits to experimental EMD patterns; this is illustrated in Figure 7.10. Although this result is in disagreement with those of Chabre and Pannetier [2], the result is in agreement with models put forward by Heuer [6] and Bowden [7]. However, a degree of caution should be taken with this result as De Wolff structures containing 10 – 20% pyrolocite all produced very similar simulated XRD patterns.

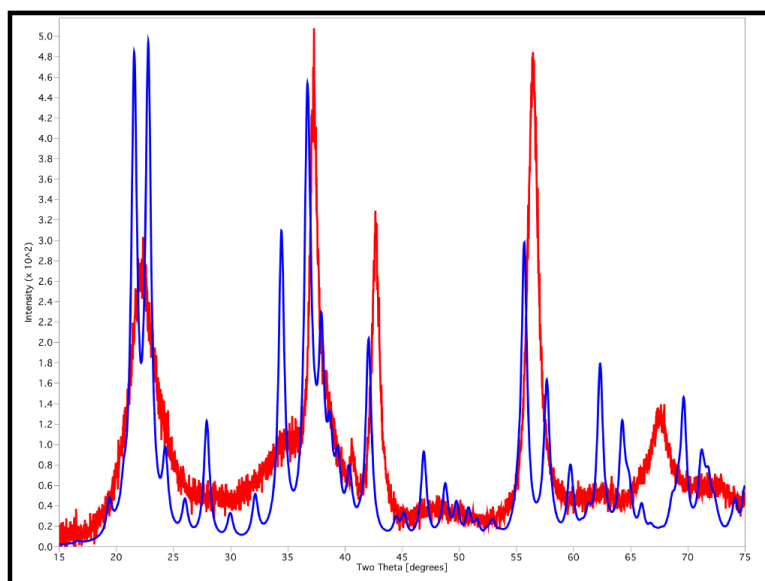


**Figure 7.10:** A comparison of an experimental EMD (IBA 30) XRD pattern [red], and a simulated XRD pattern of a De Wolff structure containing ~15% pyrolucite at low levels of segregation, using the layer method [blue].

Like the slab method, modelling De Wolff defects using the layer method does not adequately explain all the features present in the experimental EMD pattern, suggesting that other defects may be present in the EMD crystal structure. Once again the  $061_{\text{EMD}}$  is poorly represented in the simulated XRD pattern, suggesting that twinning may play an important role in the structure of EMD. However, the intensity of additional peaks in the  $25 - 35^\circ 2\theta$  region have been significantly reduced in the above simulated XRD pattern, suggesting that the above model may be a more suitable model than the one proposed by the slab method.

### 7.3 Modelling Micro-twinning

A simple approach was taken to construct the twin models. Micro-twinning does not affect the anionic lattice of ramsdellite, but is rather a redistribution of  $\text{Mn}^{4+}$  ions within the octahedral voids of the anionic lattice. Therefore instead of performing reflections to generate the twin planes, simple translations of selected rows of Mn atoms within the lattice were used to achieve the same goal. Construction of a twin using this method involved creating a surface (depth periodicity preserved and bond cleaving allowed) of the appropriate twin plane, and once the surface had been

created, the Mn atoms within the structure were rearranged by translating selected rows of Mn by positive or negative shifting vectors. The rows were shifted by a factor of  $\pm n.1/4b$ , where  $n$  is the appropriate integer and  $b$  is the  $b$  lattice parameter. If this is done correctly, the result is a characteristic “knee-shaped” twin. The surface is then converted to a 3D lattice and the structure minimised. This method will be referred to as the cation translation method.

The concentration of twinning within the structure can be controlled via two methods; firstly by varying the depth of the surface created; and secondly by varying the number of twin planes incorporated into the modelled structure, *i.e.* the number of times the shifting vector switches from positive to negative or vice versa. The percentage of twinning (Tw%) was calculated using Equation 7.2.

$$\text{Tw\%} = ([\text{Number of Twin Planes}]/[\text{Number Mn Rows}]) \times 100 \quad \text{Equation 7.2}$$

### 7.3.1 Micro-twinning on the 021 Lattice Plane

Investigations into twinning on the 021 lattice plane using the cation translation techniques yielded results similar to those of Chabre and Pannetier [2]. Figure 7.11 shows the effect of micro-twinning on the 021 lattice plane on the XRD pattern of ramsdellite. Increasing the concentration of twinning (Tw%) on the 021 plane resulted in:

- A clear merging of the 130, 021, and 111 peaks.
- A shift of the 110 peak to lower  $2\theta$  values, and a reduction in intensity. Some asymmetric broadening of this peak is also evident.
- The 121 peak shifts to lower  $2\theta$  values and merges with the 200 and 140 peaks.
- The 131 peak seems to be split and its intensity is severely reduced.
- The 221 and 240 peaks merge, and are shifted to slightly higher  $2\theta$  values as Tw% increases.
- An apparent converging of peaks at  $\sim 65.72^\circ 2\theta$ , to form a new peak, it is unclear what peaks are involved in this convergence, although the peak is located in the region of the 002 and 061 peaks.

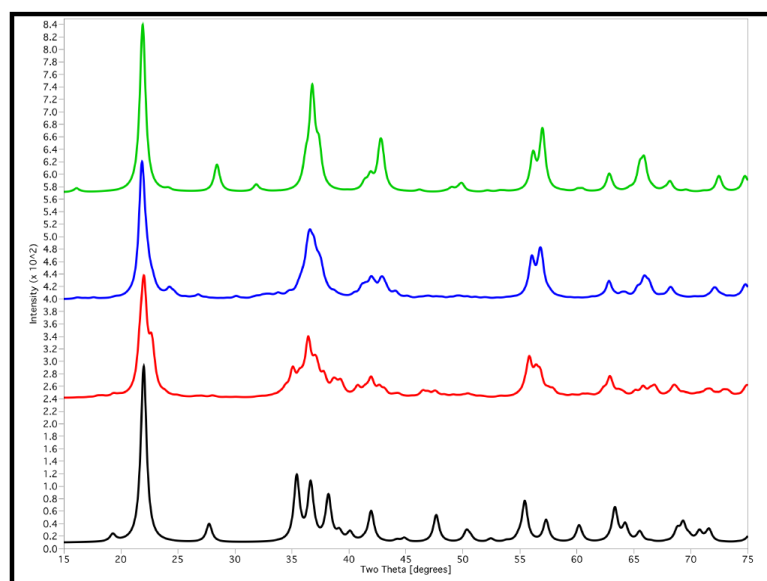


**Figure 7.11:** The effect of micro-twinning [021] on the simulated XRD patterns of ramsdellite structures: un-twinned ramsdellite [Black]; low level twinning (15%) [Red]; mid level twinning (56%) [Blue]; high level twinning (100%) [Green].

As the degree of twinning increases, the simulated XRD pattern moves closer to that of experimental EMD patterns, with a highly twinned ramsdellite structure producing a simulated pattern with 5 major peaks at  $\sim 21.91^\circ$ ,  $36.78^\circ$ ,  $42.89^\circ$ ,  $56.97^\circ$ , and  $65.85^\circ$   $2\theta$ . Figure 7.12 shows that a simulated XRD pattern of highly twinned ramsdellite ( $\text{Tw}\% = 100\%$ ) corresponds well to the diffraction pattern of EMD (Note: that at  $\text{Tw}\%$  values of less than 100%, the sharp peak located at  $\sim 28.42^\circ$   $2\theta$ , is not seen). The main difference between these patterns is the  $061_{\text{EMD}}$  peak. In the highly twinned pattern, this peak is either absent or located at  $2\theta$  values  $\sim 1.8^\circ$   $2\theta$  lower than that of the  $061_{\text{EMD}}$  peak, suggesting that twinning on the 061 lattice plane may play a role in determining the position of this peak. Although simulated XRD patterns of highly twinned ramsdellite closely resemble that of the EMD diffraction pattern, it does not adequately explain the features present in experimental patterns. Other than the differences mentioned previously in this paragraph, the highly twinned structures fail to accurately represent the so-called undulating background of experimental XRD patterns, the best example of this is the  $31 - 36^\circ$   $2\theta$  region of the patterns. The experimental EMD shows a broad diffuse shoulder peak, while the simulated highly twinned patterns have no corresponding features in this region.

This coupled with the absence of the EMD 200 peak ( $\sim 40.68^\circ 2\theta$ ) in the simulated pattern, show that EMD is not merely a ramsdellite structure with a high degree of twinning.

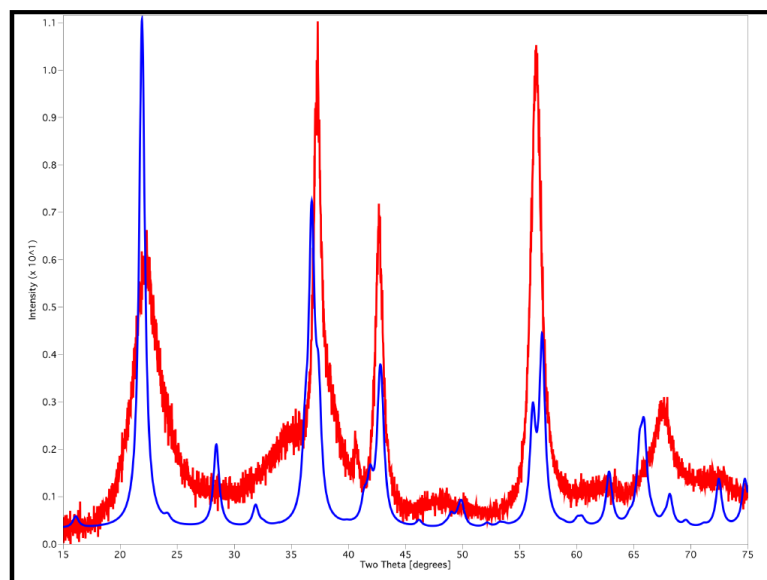


**Figure 7.12:** A comparison of the experimental EMD XRD pattern [Red] and a simulated XRD pattern of a highly twinned [021] (100%) ramsdellite crystal structure [Blue]

Chabre and Pannetier [2] believe that highly twinned structures are an explanation for the XRD patterns of so-called  $\epsilon$ - $\text{MnO}_2$  samples. This implies that  $\epsilon$ - $\text{MnO}_2$  is actually based on the orthorhombic ramsdellite structure, rather than the hexagonal space group specified in literature. Our research shows that the simulated diffraction patterns of highly twinned ramsdellite and  $\epsilon$ - $\text{MnO}_2$  structures compared quite well as illustrated in Figure 7.13. The main differences in the patterns, are the strong peak located at  $21.91^\circ 2\theta$ , in the highly twinned structure, the position of the peak located at  $65.85^\circ 2\theta$  which is  $\sim 1.29^\circ 2\theta$  lower than the closest corresponding  $\epsilon$ - $\text{MnO}_2$  peak and absence of the 002  $\epsilon$ - $\text{MnO}_2$  peak in the XRD pattern of highly twinned ramsdellite. The peak at  $21.91^\circ 2\theta$ , may explain the broad diffuse peak at similar  $2\theta$  values that is usually observed in experimental  $\epsilon$ - $\text{MnO}_2$  patterns, the location of the peak at  $\sim 65.85^\circ 2\theta$  and the absence of the 002  $\epsilon$ - $\text{MnO}_2$  peak, are less easily explained, as Chabre and Pannetier did not investigate twinning on the 061 lattice plane, and our simulations do not take into account any De Wolff defects present in

the structure. These results show that Chabre and Pannetiers' hypothesis is indeed plausible, as the XRD patterns produced are similar to that of highly disordered EMD. Although without a definitive experimental  $\epsilon$ -MnO<sub>2</sub> XRD pattern to compare these simulated patterns to, a full assessment is not possible.

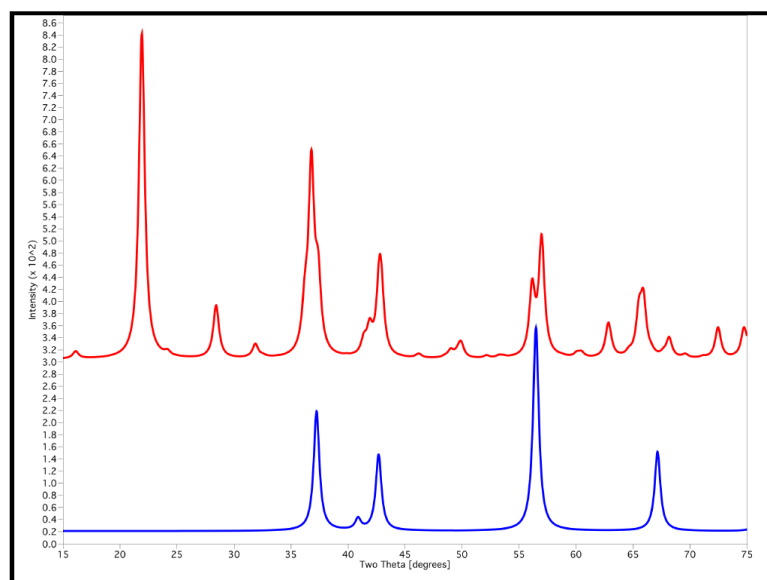


**Figure 7.13:** A comparison of the simulated XRD patterns of highly twinned (100%) ramsdellite crystal structure [Red] and  $\epsilon$ -MnO<sub>2</sub> [Blue].

### 7.3.1.1 Stabilities of 021 Twins

The stability of structures twinned on the 021 plane, was observed to decrease as the Tw% increased. This was expected, as the strain (due to shortening of Mn<sup>4+</sup> - Mn<sup>4+</sup> distances along the twin plane [2]) and the degree of disorder within the structure are known to increase with increased Tw%, and this should reduce the stability of the structure. Figure 7.14 show the stabilities of various 021 twin structures relative to pure ramsdellite. Unlike the stabilities of De Wolff structures, the relationship between Tw% and stability is non-linear and best described by a quadratic function. Comparison of these relative stabilities to the Boltzmann constant at 298 K, indicate that twinned structures with Tw% greater than ~19% are unique structures, not a result of structural changes due to thermal energy. However, caution should be used when applying this idealized model to real EMD materials, as this model does not take point defects such as Ruetschi defects into account, which have been shown by

Morgan and co-workers to significantly stabilise twinned ramsdellite structures [8-10]. Unfortunately the effect of point defects combined with planar defects cannot be easily modelled. However, as these defects are known to have little effect on the structural characteristics of EMD [2, 4, 11, 12], excluding point defects from this study will have minimal effects on the simulated XRD patterns created for comparison to experimental EMD patterns. This is confirmed by the results of Hill and co-workers [4].

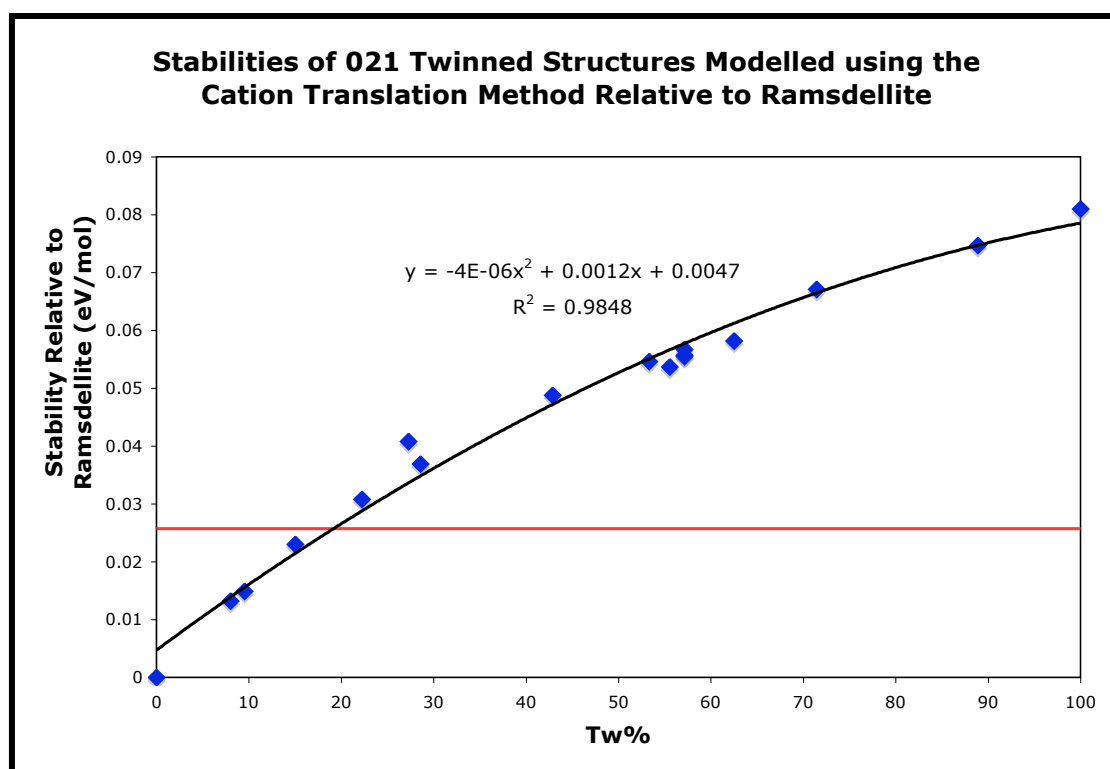


**Figure 7.14:** Stabilities of 021 twinned structures modelled using the cation translation method relative to pure ramsdellite, the Boltzmann constant ( $k$ ) at 298K [Red].

### 7.3.2 Micro-twinning on the 061 Lattice Plane

Modelling twinning on the 061 lattice plane using the cation translation method was not as successful as it was on the 021 plane. Unfortunately many 061 twin structures did not fully optimise, and although these minimised structure all had gradient normals of less than 0.1, these results should be treated with a degree of caution. These problems with optimisation are likely to be a result of the shorter  $\text{Mn}^{4+} - \text{Mn}^{4+}$

distances that are related to the occurrence of twin planes [2]. This suggests that our potential model may overestimate  $\text{Mn}^{4+} - \text{Mn}^{4+}$  repulsion; this is not unexpected as overlapping d-orbitals will provide a bonding contribution to the electrostatic repulsion. This effect can only be modelled using quantum mechanics, which is computationally expensive.

Figure 7.15 shows the effect of twinning on the 061 lattice plane on the simulated XRD pattern of ramsdellite. Unlike the results of twinning on the 021 lattice plane, the simulated XRD patterns of 061 twinned structures showed very few discernable trends. Increases in the concentration of twinning (Tw%) on the 061 lattice plane generally resulted in:

- Shifts of the 110 peak to lower  $2\theta$  values, although these shifts do not seem to be proportional to the degree of twinning, which may be an artefact of our potential model failing to completely minimize these structures. This peak also showed a degree of broadening, particularly in simulated patterns containing low levels of twinning, where the peak was observed to split. This broadening also resulted in an increase in the asymmetric character of the 110 peak.
- The merging of the 221 and 240 peaks. The position of this peak also fluctuates, however, there does not seem to be any correlation between peak position and Tw%, which again is a possible artefact of the failure of these structures to fully optimise.
- A merging of several peaks at  $\sim 65.38^\circ$   $2\theta$ , to form a broad peak. This new peak seems to be a result of the 002, 061, 151, and 112 merging.
- Unlike twinning of the 021 lattice plane, there were no trends apparent in the region of  $32$  to  $45^\circ$   $2\theta$ , although there is evidence of several peaks shifting and merging.
- The 131 peak is split and its intensity severely reduced.

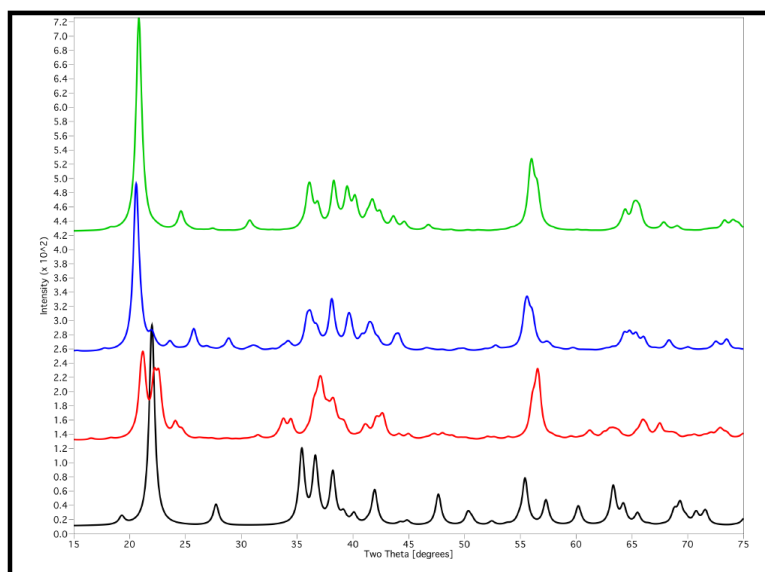


**Figure 7.15:** The effect of micro-twinning [061] on the simulated XRD patterns of ramsdellite structures: un-twinned ramsdellite [Black]; low level twinning (13%) [Red]; mid level twinning (50%) [Blue]; high level twinning (87%) [Green].

To the author's knowledge, this is the first time that the effects of twinning on the 061 lattice planes have been modelled, as a literature search for comparative data yielded no reference material. Examination of the simulated XRD patterns shows that 061 twinning may be partly responsible for some of the features present in the EMD XRD pattern, in particular; the positioning and asymmetric broadening of the  $110_{\text{EMD}}$  peak, and the shape and position of the  $221_{\text{EMD}}$  and  $061_{\text{EMD}}$  peaks. However, there are differences between the simulated and experimental XRD patterns in the region of  $32$  to  $45^\circ 2\theta$  (especially at high  $\text{Tw}\%$  values), indicating that the presence of twinning on the 061 lattice plane alone does not fully explain the XRD pattern of EMD, suggesting that other defects contribute to the structural features of EMD. As expected, medium to high levels of twinning on the 061 plane resulted in the merging of several peaks to produce a broad peak at  $\sim 65.6^\circ 2\theta$ , however this is  $\sim 1.9^\circ 2\theta$  lower than the corresponding experimental peak ( $061_{\text{EMD}}$ ). This underestimation is likely to be a result of our potential model overestimating  $\text{Mn}^{4+}$  -  $\text{Mn}^{4+}$  repulsion. However, the incorporation of other defects, such as De Wolff defects into the simulated structure may also play a role in the positioning of this peak. The simulated XRD patterns of 061 twin structures that contained low levels

of twinning (Tw% ~13%) show the best fits to experimental data, and this is illustrated in Figure 7.16.

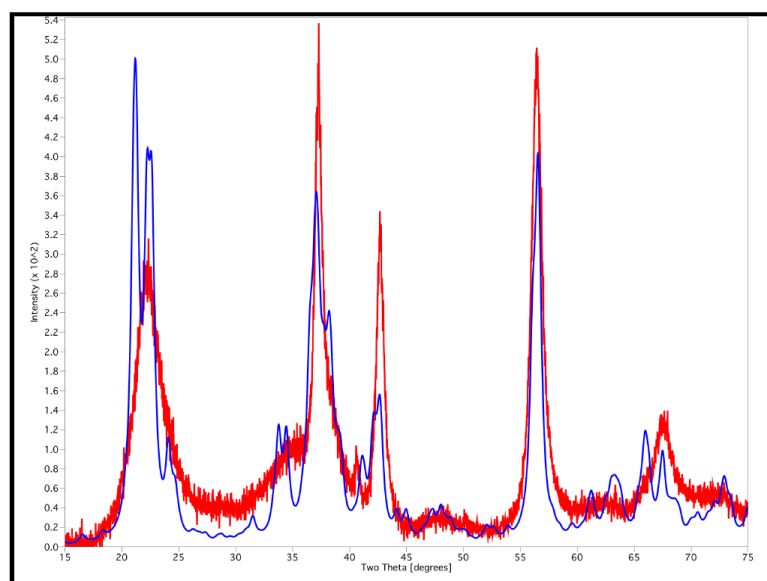


**Figure 7.16:** A comparison of the experimental EMD XRD pattern [Red] and a simulated XRD pattern of a twinned [061] (13%) ramsdellite crystal structure [Blue]

This result may be deceiving, however, as it does not consider the effects that De Wolff defects and twinning on the 021 lattice plane will have on the simulated XRD patterns. In reality, the Tw% is probably significantly higher, as generally EMD samples produce XRD patterns that have a single broad 061<sub>EMD</sub> peak, not the doublet which is present in the Tw% ~13% simulated XRD pattern. The results of this study suggest that structures that contain medium to high levels of twinning will produce a single broad peak in this region, although its position is generally underestimated by our potential model. Figure 7.17 shows a comparison of the simulated XRD pattern of a highly 061 twinned structure (Tw% ~87%) to an experimental EMD. Clearly the highly twinned structure produces a pattern with a poorer fit than the structure that contained low levels of twinning. However, assuming that the trends observed as a result of De Wolff defects and 021 twinning remain the same after these defects have been combined: the addition of De Wolff defects to this structure would broaden and shift the peak at 20.82° 2θ to higher 2θ values, the intensity of this peak would also decrease; and the addition of twinning on the 021 plane to this structure would result in the merging of the peaks in the region of 32 to 45° 2θ, into two broad peaks

located at  $\sim 37.3$  and  $42.7^\circ 2\theta$ . These alterations to the simulated XRD would significantly improve the fit of the highly 061 twinned structure to the experimental EMD XRD pattern.

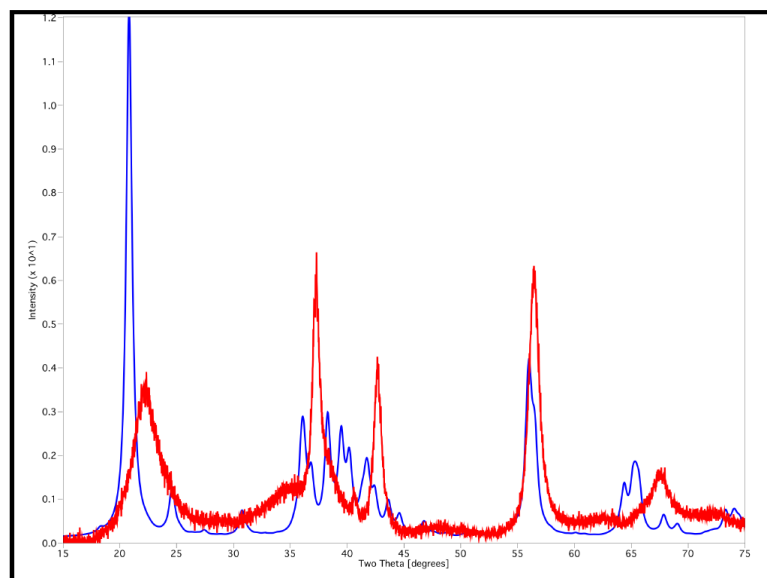


**Figure 7.17:** A comparison of the experimental EMD XRD pattern [Red] and a simulated XRD pattern of a highly twinned [061] (Tw%  $\sim 87\%$ ) ramsdellite crystal structure [Blue]

### 7.3.2.1 Stabilities of 061 Twins

The stabilities of 061 twin structures showed similar trends to the stabilities of 021 twins. Figure 7.18 shows the stabilities of various 061 twin structures relative to pure ramsdellite, and, like the stabilities of 021 twin structures, the stability of 061 twin structures decreased as the Tw% increased, and the relationship between stability and Tw% was also non-linear. This relationship was again best described by the quadratic function, shown in Figure 7.18. These results indicate that 061 twins are far less stable than 021 twins. This was to be expected as twinning on the 061 lattice planes produce “knee-shaped” kinks in the ramsdellite structure at a more acute angle ( $60^\circ$ ) than 021 twins ( $120^\circ$ ). As a result, the 061 structures would be expected to be more strained, with shorter  $\text{Mn}^{4+} - \text{Mn}^{4+}$  distances and therefore be less stable. Comparison of these relative stabilities to the Boltzmann constant at 298 K, indicate that twinned structures with Tw% greater than  $\sim 6\%$  are unique

structures, not a result of structural changes due to thermal energy. Although as previously mentioned in section 7.3.1.1, caution must be exercised when interpreting these results as this idealized model does not take the stabilizing effects of point defects such as Ruetschi defects into account.

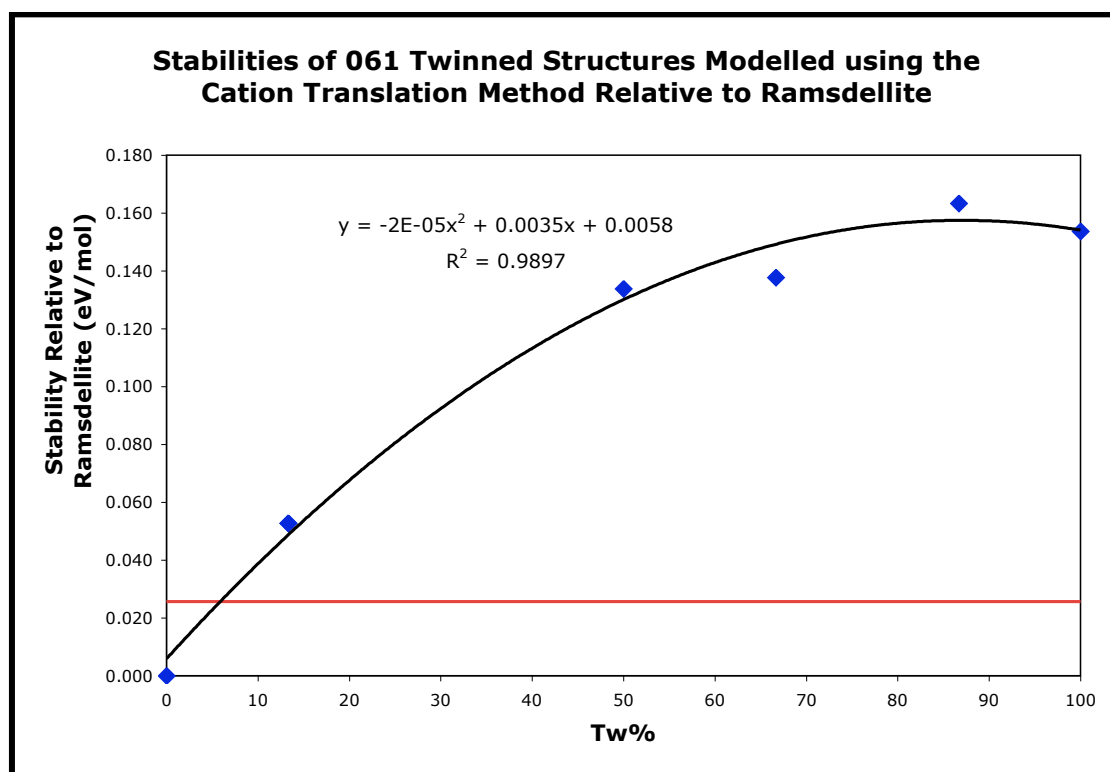


**Figure 7.18:** Stabilities of 061 twinned structures modelled using the cation translation method relative to pure ramsdellite, the Boltzmann constant ( $k$ ) at 298K [Red].

### 7.3.3 Conclusions Drawn by Modelling Microtwinning via the Cation Translation Method

The results obtained by using the cation translation method to model the effect of twinning on the 021 and 061 lattice planes suggest that twinning is indeed partly responsible for some of the features present in the EMD XRD pattern. In fact, twinning seems to have an impact on the position and shape of every major EMD peak, with the exception of the 200 peak. However, as a “stand alone” defect it does not adequately describe all of the features that are present in the EMD XRD, particularly the undulating background and the 200 peak. As expected, twinning on

the 061 lattice plane had more effect on the 061<sub>EMD</sub> peak than twinning on the 021 plane, and less of an effect on the 021<sub>EMD</sub> and 121<sub>EMD</sub> peaks. These results also suggest that twinning is prevalent within EMD, which is consistent with literature [2, 4, 7], although it would seem from the simulated XRD patterns that high levels of twinning (%Tw >70%) are more likely to occur on the 021 plane, as low level twinning on the 061 twin plane gives fairly good fits to experimental data.

#### 7.4 Combining Defects

The results from the previous sections show that separately De Wolff defects and micro-twinning cannot account for all of the features present in the experimental EMD XRD pattern. Similar conclusions were drawn by Schilling and Dahn [5] and Hill and co-workers [4]. De Wolff defects and micro-twinning have both been reported to occur in EMD; this, coupled with the high defect concentration of this material, means that it is highly unlikely that these defects will occur completely separately within the EMD crystal structure. Therefore, the next step in investigating the structure of EMD using molecular modelling is to model structures containing both these defect types.

Only structures that contained De Wolff defects and twinning on the 021 lattice plane were modelled. To produce combined defect structures, De Wolff structures were constructed using the layer method described in section 7.3. The 021 lattice plane was then redefined according to the cell parameters of the De Wolff structure and the cation translation method (described in section 7.4) was used to produce twinning within the structure. These structures were then optimised, and the XRD patterns simulated. Due to the complex nature of constructing these structures, a limited number of structures were investigated, in accordance with literature [2, 4, 7] and our modelling results; the %pyrolucite in these structures was kept at ~15% or ~33%; and the %Tw was kept relatively high at ~70 – 90%, although for the sake of completeness a few structures that contained low levels of twinning were modelled (%Tw ~15 – 30%).

The results presented in Figure 7.19 show that the best fit to experimental XRD data is obtained from a combined defect structure that contains ~15% pyrolucite and a

high level of twinning (%Tw ~75%). It is also reasonable to assume that the quality of this fit would further improve if twinning on the 061 lattice was incorporated into the combined defect structure. This result is consistent with those of Bowden and co-workers [7], who postulated that EMD contained approximately 15% pyrolucite and a high level of twinning, but is inconsistent with the results of Hill and co-workers [4] who postulated that EMD contained approximately 33% pyrolucite, and 80% twinning, which in turn are similar to the results of Chabre and Pannetier [2]. However, Chabre and Pannetier's model for the structure of EMD is known to break down when predicting the defect concentrations of highly disordered EMD materials such as the samples investigated in this project [2]. SPECS analysis of EMD samples also tends to support the results obtained by both this project and Bowden [7, 13].

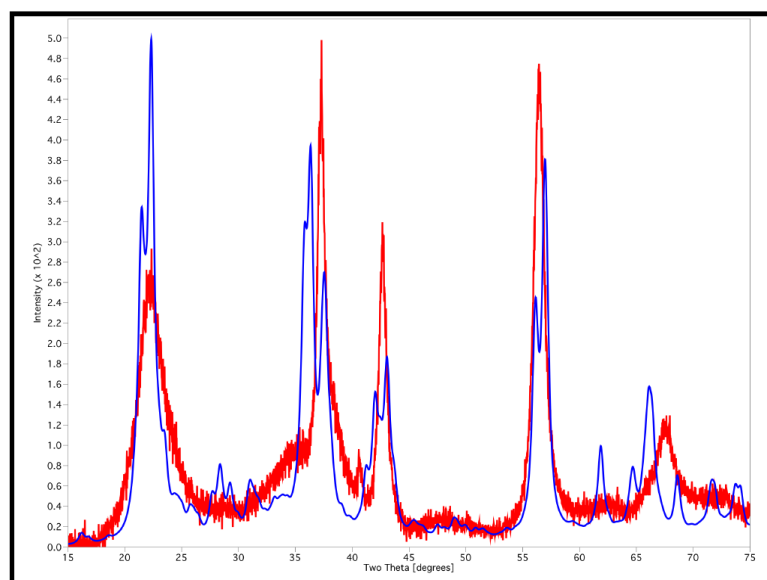


**Figure 7.19:** A comparison of the experimental EMD XRD pattern [Red] and a simulated XRD pattern of a combined defect structure (%pyrolucite ~15%, %Tw ~ 75%) [Blue].

### 7.5 $\epsilon$ -MnO<sub>2</sub>

As described in section 1.3.1.4, the  $\epsilon$ -MnO<sub>2</sub> structure is based on a defective NiAs type structure, with Mn<sup>4+</sup> randomly distributed over 50% of the available octahedral sites. The structure of  $\epsilon$ -MnO<sub>2</sub> was modelled using the potential model employed in this project; lattice parameters and atomic coordinates were taken from the MINCRYST database [14]. Disorder in the structure was simulated using a mean field model [15]. These structural parameters were used as they represent a synthetic form of akhtenskite ( $\epsilon$ -MnO<sub>2</sub>) that produced a simulated XRD pattern that was found to fit well to our experimental EMD XRD patterns.

Unfortunately, our variable charge model could not successfully optimise the structure of  $\epsilon$ -MnO<sub>2</sub>. The attempted optimisation of  $\epsilon$ -MnO<sub>2</sub> yielded  $a$  and  $b$  lattice parameters that were only reduced by 0.53%, however the  $c$  axis was greatly expanded by 12.22%. This is likely to be a result of the presence of Mn atoms in face-sharing octahedral positions, although it may also be an artefact of using a charge equilibration method in conjunction with mean field calculations. To test this hypothesis, the  $\epsilon$ -MnO<sub>2</sub> structure was modelled using fixed charges. These charges were derived from previously optimised MnO<sub>2</sub> structures (Table 7.2).

**Table 7.2:** The Charges of Mn and O used to model  $\epsilon$ -MnO<sub>2</sub> via a fixed charge method.

Atom	Charge (eV)
Mn	0.9226
O	-0.4613

The fixed charge optimisation of  $\epsilon$ -MnO<sub>2</sub> was effective and yielded  $a$  and  $b$  lattice parameters that were reduced by 3.16% and the  $c$  axis was expanded by 8.95%. This result suggests that our potential model does not cope well with the presence of face-sharing octahedra within MnO<sub>2</sub> structures, which results in shortened Mn<sup>4+</sup> - Mn<sup>4+</sup> distances. As mentioned previously our interatomic potentials almost certainly will overestimate the Mn<sup>4+</sup>—Mn<sup>4+</sup> repulsion, as the presence of overlapping d-orbitals will provide a bonding contribution in opposition to the electrostatic

repulsion. Therefore quantum mechanics must be used to model this phenomenon. However, even if this is the case, face-sharing octahedra will generally be less stable than edge and corner-sharing octahedra, as Pauling's rules state that face-sharing octahedra, occupied by high valency cations are unfavourable due to electrostatic forces [2]. To this author's knowledge,  $\epsilon$ -MnO<sub>2</sub> is the only MnO<sub>2</sub> polymorph whose structure may contain face-sharing octahedra, therefore  $\epsilon$ -MnO<sub>2</sub> can be uniquely classified by this structural trait. This also implies that some face-sharing octahedra may occur in EMD [16]. These results also suggest that face-sharing octahedra are not prevalent in the  $\epsilon$ -MnO<sub>2</sub> crystal structure, as their presence is likely to result in  $\epsilon$ -MnO<sub>2</sub> with an expanded *c* axis, which experimental data shows is not the case. Several authors have suggested cation/vacancy ordering within the  $\epsilon$ -MnO<sub>2</sub> crystal structure, and that because of Coulombic repulsion, there may be an avoidance of Mn<sup>4+</sup> cations at the centre of face-sharing octahedra [6, 17]. This is consistent with the findings of this study.

Experimental XRD patterns of  $\epsilon$ -MnO<sub>2</sub> are said to have a broad diffuse peak at  $\sim 21.10^\circ 2\theta$ , which is thought to be a result of the Mn<sup>4+</sup> distribution not being totally random. To test this, five  $\epsilon$ -MnO<sub>2</sub> super-cells were created, each originally containing 128 Mn atoms and 128 O atoms. Half of the Mn atoms were then randomly removed by hand, to simulate a random 50% occupancy of the available octahedral sites. The XRD patterns of these supercells were then simulated and averaged, and the resulting diffraction pattern (shown in Figure 7.20) gave similar results to those of Chabre and Pannetier, who observed a diffuse step in the background, although our results show that the less than perfect disorder due to the use of a periodic supercell results in multiple peaks in the lower  $2\theta$  regions. This suggests that ordering the cations within  $\epsilon$ -MnO<sub>2</sub> could indeed result in a diffuse peak at  $\sim 22^\circ 2\theta$ .

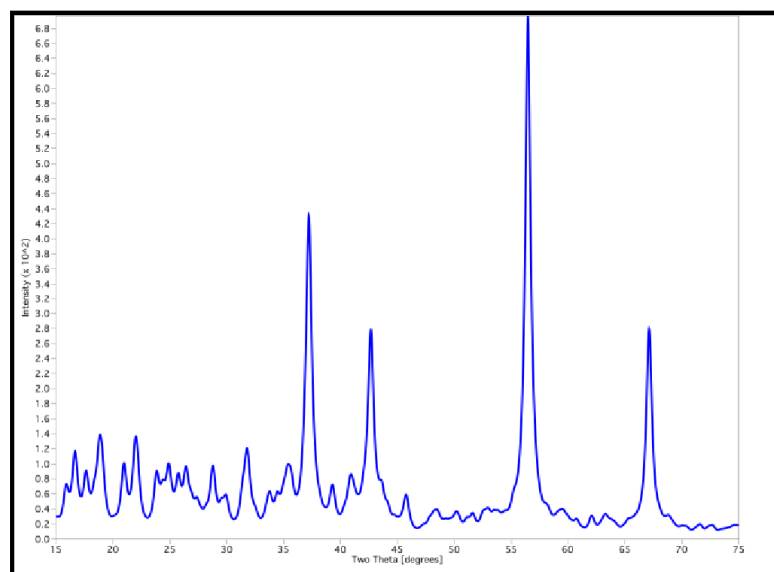


**Figure 7.20:** The averaged simulated XRD pattern of  $\epsilon$ -MnO<sub>2</sub> that has less than perfect disorder.

### 7.5.1 Cation/Vacancy Ordering in $\epsilon$ -MnO<sub>2</sub>

As mentioned above, several authors believe that cation/vacancy ordering is present in the  $\epsilon$ -MnO<sub>2</sub> structure and that it may explain features of the EMD XRD pattern. In order to test this hypothesis, several ordered supercells of  $\epsilon$ -MnO<sub>2</sub> were created, their structures optimised and their XRD patterns calculated.

The removal of edge sharing cations from the  $\epsilon$ -MnO<sub>2</sub> crystal structure results in a layer type structure (See Figure 7.21). This is reasonable, as MnO<sub>2</sub> is known to occur as layer structures such as birnessite. The simulated XRD patterns of both relaxed and un-relaxed structures produced similar peaks to the XRD pattern simulated from the literature  $\epsilon$ -MnO<sub>2</sub> structure (see Figure 7.21). The most notable difference is the strong peak located at  $\sim 20.42^\circ$   $2\theta$ . This result supports De Wolff's hypothesis [18] that the broad peak at  $\sim 22^\circ$   $2\theta$  may be a result of the avoidance of face sharing octahedra and cation/vacancy ordering. However this result contradicts structural calculations performed by Chabre and Pannetier [2], who observed a diffuse step, not a peak at  $\sim 20^\circ$   $2\theta$  in their simulated XRD pattern, a likely explanation for this is that they examined disordered  $\epsilon$ -MnO<sub>2</sub> with no face-sharing

octahedra, not a fully ordered  $\epsilon$ -MnO<sub>2</sub> structure such as the one produced by this study.

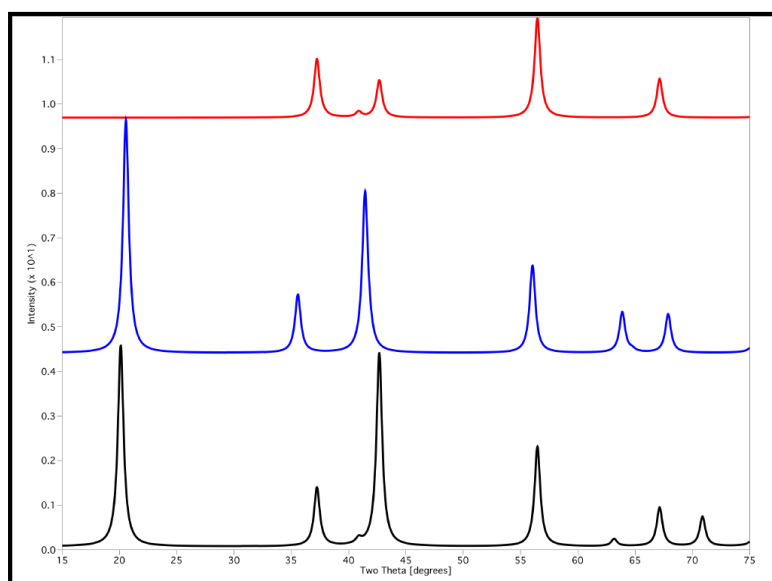


**Figure 7.21:** The simulated XRD patterns of  $\epsilon$ -MnO<sub>2</sub> with the edge sharing cation removed; Unrelaxed structure [black]; Relaxed structure [blue]; and the simulated XRD pattern of  $\epsilon$ -MnO<sub>2</sub> [red].

Foss *et al.* [19], observed  $\epsilon$ -MnO<sub>2</sub> that exhibited orthorhombic ordering while investigating MnO<sub>2</sub> grown on  $\alpha$ -Al<sub>2</sub>O<sub>3</sub> substrates. The unit cell of this phase of  $\epsilon$ -MnO<sub>2</sub> was found to be orthorhombic of space group  $Pmnn$  (No. 58), with lattice parameters of  $a = 2.75$ ,  $b = 4.76$ , and  $c = 4.302$  Å (Note: This unit cell definition was derived from cation ordering observed in  $\epsilon$ -MnO<sub>2</sub> with its original hexagonal setting). Figure 7.22 shows the crystal structure of this phase in its hexagonal setting [19]. The unrelaxed structure produced a simulated XRD pattern that was reminiscent of pyrolucite, once optimised the structure produced a simulated XRD that was almost an exact match to that of pyrolucite (see Figure 7.23). These calculations show that the ordered  $\epsilon$ -MnO<sub>2</sub> observed by Foss *et al.*, [19] is actually a strained pyrolucite structure, which is not stable in absence of the hexagonal  $\alpha$ -Al<sub>2</sub>O<sub>3</sub> substrates. This finding is significant as pyrolucite is a base structure for many structural models of EMD.

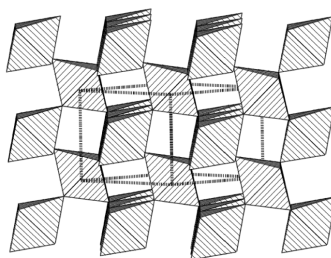


**Figure 7.22:** The optimised crystal structure of the ordered  $\epsilon$ -MnO<sub>2</sub> in its hexagonal setting as described by Foss and co-workers, viewed along  $ab$  [19].

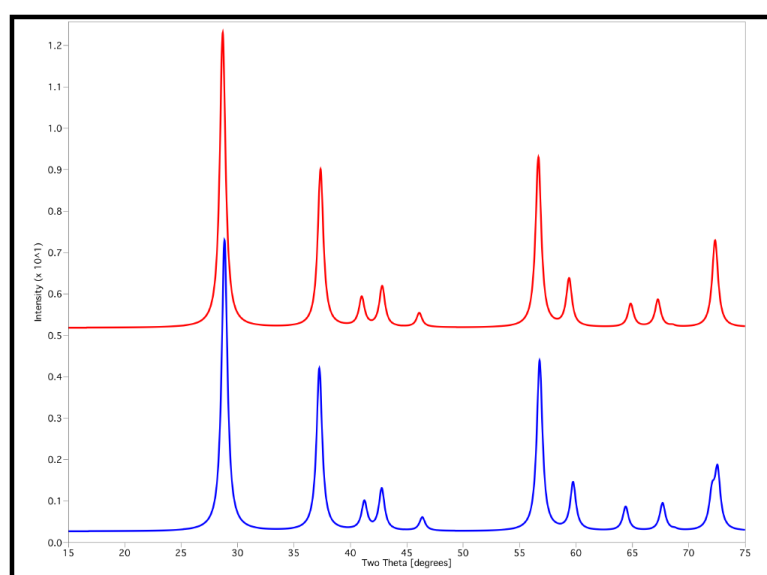


**Figure 7.23:** A comparison of the simulated XRD pattern of the optimised ordered  $\epsilon$ -MnO<sub>2</sub> in its hexagonal setting as described by Foss and co-workers [blue] [19], and the simulated XRD pattern of pyrolucite [red] [20].

Professor Nae-Lih Wu has conducted research on the  $\epsilon$ -MnO<sub>2</sub> crystal structure. He suggested that many MnO<sub>2</sub> polymorphs can be created by cation/vacancy ordering within the  $\epsilon$ -MnO<sub>2</sub> structure, and  $\epsilon$ -MnO<sub>2</sub> may be considered as an intergrowth of different MnO<sub>2</sub> structures [21]. Figure 7.24 shows an optimised “ramsdellite-like” structure that was produced in this study via cation ordering in the  $\epsilon$ -MnO<sub>2</sub> structure. Figure 7.25 shows that the simulated XRD pattern of this structure is almost an exact match to that of ramsdellite. This may indicate that cation/vacancy ordering within  $\epsilon$ -MnO<sub>2</sub> plays a non-trivial role in the crystal structure of EMD.

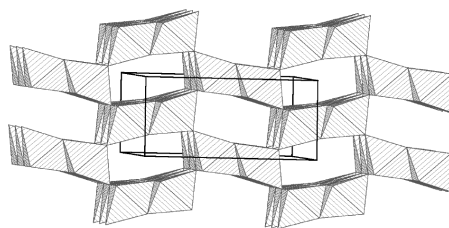


**Figure 7.24:** An optimised “ramsdellite-like” crystal structure that was produced via cation ordering in the  $\epsilon$ -MnO<sub>2</sub> structure, viewed along the  $b$  axis.

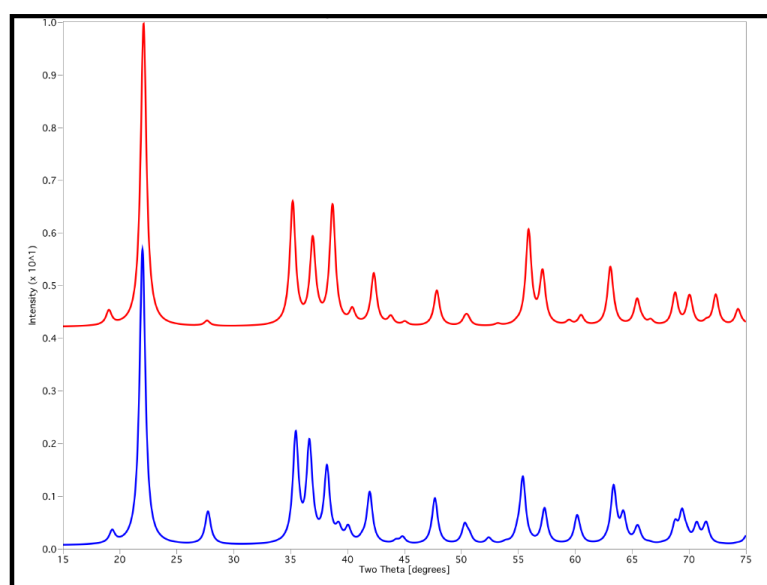


**Figure 7.25:** A comparison of the simulated XRD pattern of an optimised “ramsdellite-like” crystal structure that was produced via cation ordering in the  $\epsilon$ -MnO<sub>2</sub> structure [blue], and a simulated XRD pattern of ramsdellite [red] [22].

Heuer *et al.*[6] suggested a fully ordered  $\epsilon$ -MnO<sub>2</sub> structure as a result of their TEM studies of EMD; the optimised structure is shown in Figure 7.26. This structure is similar to ramsdellite, with the main difference arising from the structure containing alternating 2x1 and 1x1 tunnels. This results in a structure containing a series of “De Wolff-like” defects. Figure 7.27 shows the simulated XRD pattern of this structure, and the XRD pattern is similar to that of a ramsdellite structure containing De Wolff defects (Pr= 33%), which is unsurprising considering the structural similarities. This type of ordering also produced several peaks in the 19.8°- 24.6° 2 $\theta$  region, which

further strengthens De Wolff's hypothesis, and shows that ordering within  $\epsilon$ -MnO<sub>2</sub> can produce structures containing “De Wolff-like” defects.

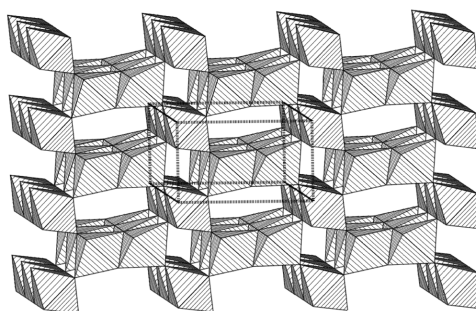


**Figure 7.26:** The optimised crystal structure of the ordered  $\epsilon$ -MnO<sub>2</sub> phase described by Heuer and co-workers [6], viewed along the *b* axis.

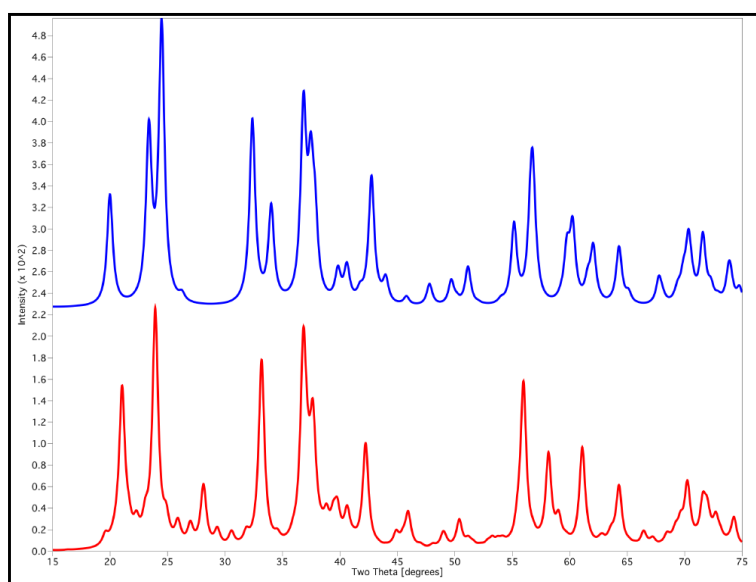


**Figure 7.27:** A comparison of the simulated XRD patterns of the ordered  $\epsilon$ -MnO<sub>2</sub> phase described by Heuer and co-workers [6] [blue] and a ramsdellite structure containing 33% pyrolucite [red].

The cations within the  $\epsilon$ -MnO<sub>2</sub> crystal structure can also be ordered in such a way as to produce a lattice that is representative of a ramsdellite lattice containing a single octahedral pyrolucite chain (see Figure 7.28). This is in fact the “true” definition of a De Wolff defect. In the context of this project, this is a major achievement, as until this point the minimum thickness of a De Wolff defect modelled was two pyrolucite

octahedra. The resulting structure contains ~15% pyrolucite. Figure 7.29 shows a comparison of the simulated XRD patterns of both this structure and a De Wolff structure produced via the layer method that contains similar levels of pyrolucite. The similarity of the patterns suggest that there is little structural difference between De Wolff structures containing single octahedral pyrolucite defects and those De Wolff defects that contain two pyrolucite octahedra, although the thickness of the pyrolucite layer may have a more significant effect on electrochemistry.

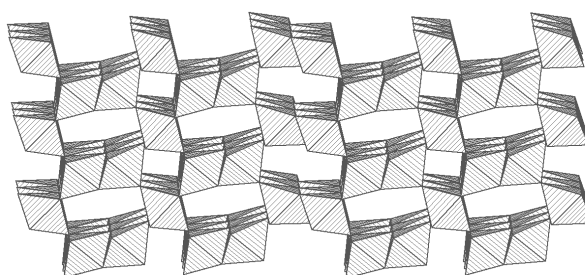


**Figure 7.28:** The optimised crystal structure of the ordered  $\epsilon$ -MnO<sub>2</sub> phase that is representative of a ramsdellite structure, which contains single chain pyrolucite defects.

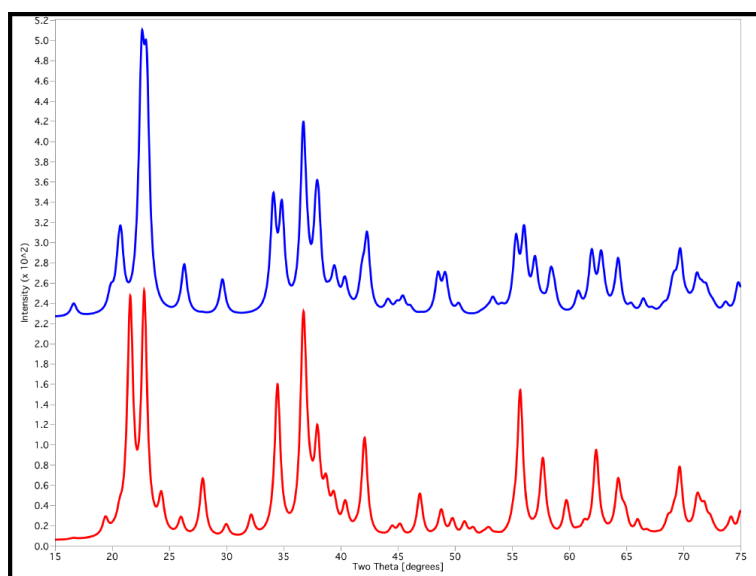


**Figure 7.29:** A comparison of the simulated XRD patterns of the ordered  $\epsilon$ -MnO<sub>2</sub> phase that is representative of a ramsdellite structure, which contains single chain pyrolucite defects, and a De Wolff structure produced via the layer method that contains similar levels of pyrolucite.

Producing structures via this cation/vacancy ordering technique allows a great deal of flexibility when attempting to model structures that may be present in EMD. A good example of this is shown in Figure 7.30, which shows the optimised crystal structure of a 1x3 MnO<sub>2</sub> tunnel structure within a typical ramsdellite lattice. This tunnel structure has significance as it has been reported by Turner and Buseck [23] to be present in nsutite ( $\gamma$ -MnO<sub>2</sub>) and therefore is likely to be present in EMD. Other such tunnel structures of differing sizes have also been reported by several authors to be present in EMD. The use of this method to model these structures allows us to investigate the possible effects of these structures on the EMD XRD pattern. Figure 7.31 shows a comparison of the simulated XRD pattern of the optimised 1x3 MnO<sub>2</sub> tunnel structure and the XRD pattern of IBA 30, which indicates that there are structural similarities between EMD and the 1x3 tunnel structures, suggesting that 1x3 tunnels may indeed be present in EMD. The presence of these larger tunnels presumably affects the efficiency of proton diffusion [23].

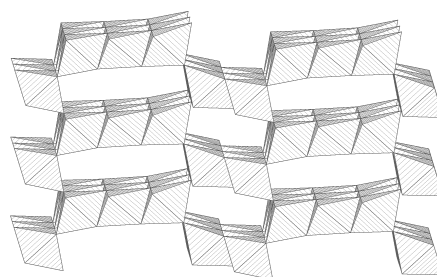


**Figure 7.30:** The optimised crystal structure of a 1x3 MnO<sub>2</sub> tunnel structure within a typical ramsdellite lattice.

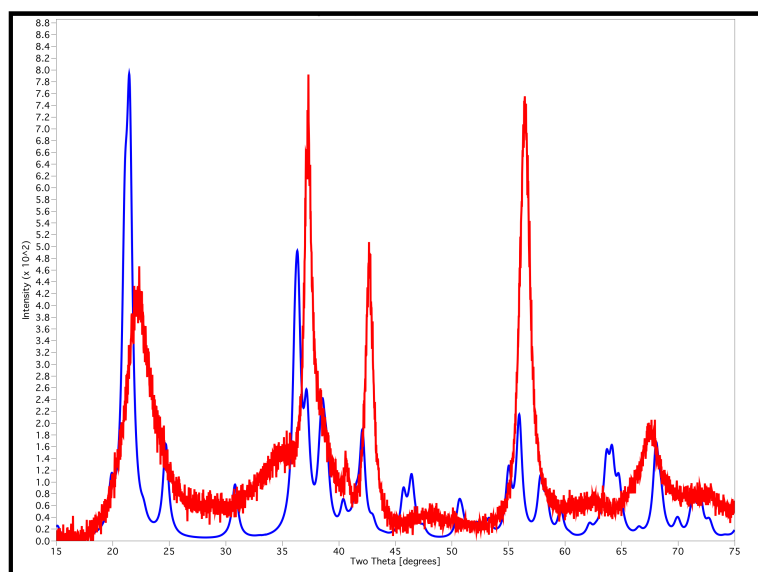


**Figure 7.31:** A comparison of the simulated XRD pattern of the optimised 1x3 MnO<sub>2</sub> tunnel structure and the XRD pattern of IBA 30.

All of the above simulated XRD patterns could have been simulated using unrelaxed super cells of the  $\epsilon$ -MnO<sub>2</sub> structure with differing cation decorations, however, this does not take into account interatomic interactions within these structures, and therefore these structures were optimised to better reflect the actual structures.

With the above knowledge in hand, it may be theoretically possible to explain the structure of EMD solely in terms of  $\epsilon$ -MnO<sub>2</sub> and cation/vacancy ordering. As pyrolucite, ramsdellite and  $\epsilon$ -MnO<sub>2</sub> share similar HCP anionic lattices, it is essentially their differing cationic decorations that give them their unique structures and symmetry. This modelling work has shown that it is possible for cation/vacancy ordering in  $\epsilon$ -MnO<sub>2</sub>, to produce pyrolucite, ramsdellite, and several other MnO<sub>2</sub> structures within the  $\epsilon$ -MnO<sub>2</sub> crystal lattice. Therefore it would be reasonable to assume that De Wolff defects and microtwinning as described in EMD literature could also occur as a result of cation/vacancy ordering. EMD could then be described as an  $\epsilon$ -MnO<sub>2</sub> lattice, which contains cation/vacancy ordering in the form of pyrolucite, ramsdellite, and other yet to be characterised MnO<sub>2</sub> structures, which may result in the presence of De Wolff defects, micro-twinning and/or other defects within these ordered domains. This would result in different symmetries within the same structure i.e. a hexagonal parent-symmetry from the  $\epsilon$ -MnO<sub>2</sub> and an

orthorhombic sub-symmetry from the ordered domains. This would explain why EMD XRD patterns can be indexed using both hexagonal and orthorhombic unit cells, with neither adequately explaining the peaks present. As the structure becomes more ordered, the hexagonal symmetry is lost and symmetry becomes predominately orthorhombic.

## **7.6 Determination of a structural model for EMD**

Determination of a suitable structural model for EMD is a difficult task, because of its random nature, extremely complex structure, high defect concentration and very small crystallite size. The above factors make accurate characterisation of EMD via XRD almost impossible. XRD analysis gives us a basic idea of what the crystal structure of EMD may be, but the broad peaks do not allow for detailed analysis. This, coupled with several different MnO<sub>2</sub> structures that may be present in EMD producing similar XRD patterns, leads to further ambiguity within the technique. However, the use of molecular modelling, complementary characterisation techniques, and previous structural literature allows us to make important conclusions about the possible components of EMD. We have shown in this chapter that there is evidence for two probable EMD structural models:

1. A mixed-phase model.
2. A single-phase model.

### **7.6.1 A Mixed-Phase Model**

In the mixed-phase model EMD can be thought of as a mixture of all the MnO<sub>2</sub> phases and defect structures that are known or thought to be components in the EMD crystal structure. This model assumes that each of these components is a separate “phase” and that their effect on the EMD XRD pattern is additive. The component phases expected to be used in this model are listed below:

- Ramsdellite.
- Pyrolucite.
- $\epsilon$ -MnO<sub>2</sub>, both totally disordered and ordered structures.
- De Wolff defect structures of various concentrations and segregations.

- Twinned ramsdellite structures, on both the 021 and 061 lattice planes at various concentrations.

The model creates a fit to experimental data by a step-by-step process of trial and error. Firstly the XRD patterns of the component phases are compared to the experimental EMD pattern using *CrystalDiffract* [24] and component phases that are obvious mismatches are removed from the component phase pool. The remaining component phases are then combined using the *CrystalDiffract* [24] Mix function, and the percentage of each component phase is then manipulated until a high quality match to the experimental pattern is achieved. At present this manipulation is done by hand and the patterns matched by eye, however it should be possible to develop a program that could automate this process. Figure 7.32 shows the experimental XRD pattern of IBA 30, and a simulated XRD pattern created using the mixed-phase model.

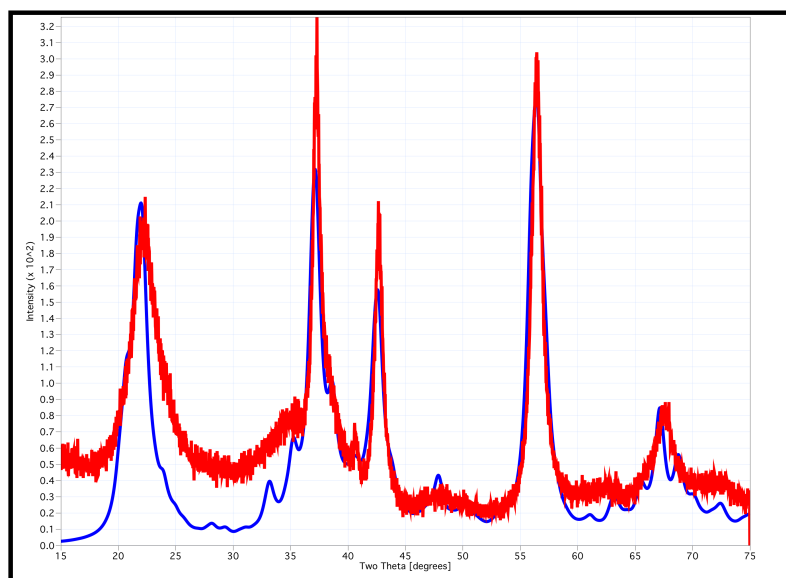


**Figure 7.32:** A Mixed phase model containing,  $\epsilon$ -MnO<sub>2</sub> (46%), ordered  $\epsilon$ -MnO<sub>2</sub> (2%), 021 twinned ramsdellite (25%), 061 twinned ramsdellite (20%), and ramsdellite containing De Wolff defects <33% pyrolucite> (7%) [blue], and the XRD pattern of IBA 30.

The main problem with this model is that it is not very robust, as many different combinations of phases can result in good matches to experimental patterns, therefore components of the model must be chosen very carefully.

### 7.6.2 A Single-Phase Model

This model is based on the  $\epsilon$ -MnO<sub>2</sub> structure, although it challenges the usual conventions in that this model uses totally disordered  $\epsilon$ -MnO<sub>2</sub> as a base structure to which order is added through the manipulation of cations and vacancies throughout the structure, resulting in a very flexible model.

This model would start by creating a suitable large supercell of  $\epsilon$ -MnO<sub>2</sub>. The cationic lattice of this supercell would be manipulated and then optimised to match experimental XRD. From this unit cell the amount of pyrolucite (De Wolff defects), ramsdellite, and twinning could be calculated, and the presence of any other ordered  $\epsilon$ -MnO<sub>2</sub> tunnel structures could be investigated. The challenge associated with this model is that a big supercell would be required, which in turn would mean that there would be literally trillions of possible cation positions. In a similar modelling study that used a supercell containing 160 atoms (96 anions and 64 cations) to model  $\gamma$ -alumina, Paglia *et al.* [25] examined a total of ~1.47 billion configurations. Unfortunately due to time constraints such a study for EMD was unable to be undertaken.

## 7.7 Conclusions

From this molecular modelling study of the structure of EMD, it can be concluded that the atomistic potential modelling of EMD generally gives reasonable structures which are comparable to those calculated using the more time consuming and computationally expensive DFT methods. In addition, allowing the defective structures to relax produced some broader and slightly shifted peaks than the results of Chabre and Pannetier, which is more consistent with the EMD XRD. However the weakness of this method its inability to accurately model face sharing octahedra, but as the face sharing octahedra are uncommon in MnO<sub>2</sub> structures this is not believed to be significant.

The modelling results of this study show that De Wolff defects, and both [021] and [061] twinning, are energetically possible within the EMD structure. It was shown that De Wolff defects, both [021] and [061] twinning, and cation ordering of  $\epsilon$ -MnO<sub>2</sub> all seem to contribute to the structure and subsequent XRD patterns of EMD.

The modelling showed that De Wolff defects contribute to the XRD pattern of EMD but do not fully explain all the features present in the patterns. The data suggest that EMD samples that exhibit XRD patterns similar to that of IBA 30, contain approximately 15 - 30% pyrolucite distributed in thin layers as De Wolff defects.

Micro-twinning on both the 021 and 061 planes were also shown to contribute to the XRD pattern of EMD, in fact twinning seems to impact the position and shape of every major EMD peak, with the exception of the 200 peak. However, as a stand-alone defect, twinning does not adequately describe the features present in the XRD pattern. The modelling results suggest that twinning is prevalent in EMD, with the structure containing high levels of twinning (%Tw >70%) on the 021 plane, and lower levels on the 061 plane.

When structures containing both De Wolff defects and 021 twins were modelled, the best fits to experimental EMD patterns were obtained by modelling structures containing ~15% pyrolucite, as De Wolff defects and a high level of twinning (%Tw ~75%).

However the most interesting results of this study were perhaps those obtained by modelling cation/vacancy ordering within the  $\epsilon$ -MnO<sub>2</sub> crystal structure. It was found that it would be a reasonable assumption that De Wolff defects, and micro-twinning could occur as a result of cation/vacancy ordering within the  $\epsilon$ -MnO<sub>2</sub> lattice. And that strictly speaking the difference between cation ordering, De Wolff defects and twinning is mainly semantics as they both produce similar structures that give similar results. This cation/vacancy may be the missing structural component that has been mentioned in the literature [4].

In fact the most promising EMD structural model proposed by this study is the single-phase model, which challenges conventional thinking, and uses the  $\epsilon$ -MnO<sub>2</sub> structure as its starting point structure. Expansion of this model would make for interesting future work in this field, and will be discussed further in Chapter 8.

## 7.8 References

1. Treacy, M.M.J., J.M. Newsam, and M.W. Deem, *A General Recursion Method for Calculating Diffracted Intensities from Crystals Containing Planar Faults*. Proc. R. Soc. Lond. A, 1991. **433**(1889): p. 499-520.
2. Chabre, Y. and J. Pannetier, *Structural and Electrochemical Properties of the Proton / gamma MnO<sub>2</sub> System*. Prog. Solid State Chem., 1995. **23**: p. 1-130.
3. Pannetier, J., *A comprehensive structural model of EMD and CMD based on De Wolff disorder and microtwinning*. Prog. Batteries Battery Mater., 1992. **11**: p. 51-55.
4. Hill, J.-R., C.M. Freeman, and M.H. Rossouw, *Understanding gamma-MnO<sub>2</sub> by molecular modeling*. J. Solid State Chem., 2004. **177**: p. 165-175.
5. Schilling, O. and J.R. Dahn, *Fits of the gamma-MnO<sub>2</sub> Structure Model to Disordered Manganese Dioxides*. J. Appl. Cryst., 1998(31): p. 396-406.
6. Heuer, A.H., A.Q. He, P.J. Hughes, and F.H. Feddrix, *Microstructure of Electrolytic MnO<sub>2</sub>: A Transmission Electron Microscopy Study of Bulk Material*. ITE Lett. Batteries, New Technol. Med., 2000. **1**(6): p. 76-80.
7. Bowden, W., R. Sirotna, and S. Hackney, *Manganese Dioxide for Alkaline Zinc Batteries: A single-phase model*. ITE Lett. Batteries, New Technol. Med., 2003. **4**(1): p. 26-37.
8. Morgan, D., D. Balachandran, G. Ceder, and A. van de Walle. *A Drastic Influence of Point Defects on Phase Stability in MnO<sub>2</sub>*. in *Mat. Res. Symp. Proc.* 2003. Materials Research Society.
9. Balachandran, D., D. Morgan, G. Ceder, and A. van de Walle, *First-principles study of the structure of stoichiometric and Mn-deficient MnO<sub>2</sub>*. J. Solid State Chem., 2003. **173**: p. 462-475.

10. Balachandran, D., *First Principles Study of Structure, Defects and Proton Insertion in MnO<sub>2</sub>*, in *Department of Materials Science and Engineering*, 2001.
11. Donne, S.W., *Alkaline manganese dioxide electrochemistry*. ITE Lett. Batteries, New Technol. Med., 2000. **1**: p. 915-925.
12. Ripert, M., C. Poinسیون, Y. Chabre, and J. Pannetier, *Structural study of proton electrochemical intercalation in manganese dioxide*. Phase Transitions, 1991. **32**: p. 205-209.
13. Bowden, W., R. Sirotina, and S. Hackney, *Manganese Dioxide for Alkaline Zinc Batteries: Why Electrolytic MnO<sub>2</sub>*. ITE Lett. Batteries, New Technol. Med., 2000. **1**(6): p. 53-64.
14. Chichagov, A.V., A.B. Belonozhko, A.L. Lopatin, T.N. Dokina, O.L. Samokhvalova, T.V. Ushakovskaya, and Z.V. Shilova, *Information-Calculating System on the Crystal Structure Data of Minerals (MINCRYST)*. Kristallografiya, 1990. **35**(3): p. 610-616.
15. Gale, J.D. and A.L. Rohl, *The General Utility Lattice Program (GULP)*. Mol. Simul., 2003. **29**(5): p. 291-341.
16. Burns, R.G. and V.M. Burns. *Recent Structural Data for Manganese (IV) Oxides*. in *Manganese Dioxide Symposium*. 1980. Tokyo: The Electrochemical Society, Inc.
17. Simon, D.E., T.N. Andersen, and C.D. Elliott, *A Rietveld Refinement Model of EMD Powder Patterns*. ITE Lett. Batteries, New Technol. Med., 2000. **1**(3): p. 10-19.
18. De Wolff, P.M., J.W. Visser, R. Giovanoli, and R. Brüstch, *Epsilon Manganese Dioxide*. Chimia, 1978. **32**(7): p. 257-259.

19. Foss, S., O. Nilsen, A. Olsen, and J. Tafto, *Structure determination of MnO<sub>2</sub> films grown on single crystal alpha-Al<sub>2</sub>O<sub>3</sub> substrates*. *Philos. Mag.*, 2005. **85**(11): p. 2689-2705.
20. Baur, W.H., *Rutile-type compounds. V, Refinements of MnO<sub>2</sub> and MgF<sub>2</sub>*. *Acta Crystallogr.*, 1976. **B32**: p. 2200-2204.
21. Wu, N.-L., personal communication, 2006.
22. Fong, C., B.J. Kennedy, and M.M. Elcombe, *A powder neutron diffraction study of lamda and gamma manganese dioxide and of LiMn<sub>2</sub>O<sub>4</sub>*. *Z. Kristallogr.*, 1994. **209**(12): p. 941-945.
23. Turner, S. and P.R. Buseck, *Defects in nsutite (gamma-MnO<sub>2</sub>) and dry-cell efficiency*. *Nature*, 1983. **304**: p. 143-146.
24. Palmer, D., *CrystalDiffract for Mac OS X*, 2005.
25. Paglia, G., A.L. Rohl, G.E. Buckley, and J.D. Gale, *Determination of the structure of gamma-alumina from interatomic potential and first-principles calculations: The requirement of significant numbers of nonspinel positions to achieve an accurate structural model*. *Phys. Rev. B: Condens. Matter Mater. Phys.*, 2005. **71**(22): p. 224115-1-16.

*Every reasonable effort has been made to acknowledge the owners of copyright material. I would be pleased to hear from any copyright owner who has been omitted or incorrectly acknowledged.*

## **8 FUTURE WORK**

During the course of this project it became evident that there were some opportunities for improvement in research techniques and some interesting avenues and concepts that could not be explored due to time constraints. This chapter will briefly discuss these opportunities.

### **8.1 Future Experimental Work**

With the foundation provided by this project, it is suggested that in future the research would adopt a more holistic approach; *i.e.* a small scale deposition rig should be developed that could accurately analyse the EMD deposition processes, while producing enough EMD for both structure analysis, and battery testing. An extension of the experimental work of this project would focus on improving characterisation techniques, organic additives, and *in-situ* work. These are briefly described below.

#### **8.1.1 Characterisation Techniques**

Due to the very nature of EMD it became evident that the techniques employed during this project lacked the sensitivity required to fully characterise the EMD samples produced, although they did supply sufficient data to apply crystal growth theory to the EMD deposition process. The author believes that significant advances need to be made in the sensitivity of both long and short range structural characterisation techniques before the structure of EMD can be fully defined.

#### **8.1.2 Organic Additives**

An interesting finding of this project was that organic additives can have a significant impact on the structure of the EMD produced, and the author believes that this warrants further investigation. An organic process additive that offered a reduction in deposition costs through energy savings and/or improved quality of the EMD produced would be very attractive to EMD producers worldwide.

### 8.1.3 *In-situ* Work

The novel simultaneous *in-situ* SR-GIXRD and EIS studies in the project were ambitious to say the least; however the marriage of an appropriate characterisation and electro-chemical technique could provide valuable information regarding the EMD deposition process. Ideally the analyses would incorporate a suite of electro-chemical techniques combined with characterisation techniques that could provide structural information about both surface, bulk and intermediate structures of EMD during electro-deposition, which given the nature of EMD and the conditions it is deposited under is extremely challenging.

It is the author's opinion that perfecting these techniques would require a large amount of fundamental *ex-situ* research marrying the correct electrochemical and structure characterisation techniques before it could be converted to the challenging EMD *in-situ* deposition environment.

## 8.2 Future Modelling Work

Throughout the modelling it became clear that models for the structure of EMD can be viewed from many perspectives; it this author's opinion that the best model is a single phase model based on the  $\epsilon$ -MnO<sub>2</sub> structure, which appears to be the most flexible, as it can account for both long and short range order in the EMD structure.

As mentioned previously, this model would start by creating a large supercell of  $\epsilon$ -MnO<sub>2</sub>. A computer program would then manipulate and optimise the cationic lattice of this supercell (essentially introducing order to a random lattice structure) to form the various defect features of the EMD; these could then be matched to experimental EMD XRD patterns. Then using the cation positions in this supercell that yield the lowest lattice energies, the amount of pyrolucite (De Wolff defects), ramsdellite, and twinning could be calculated, and the presence of any other ordered  $\epsilon$ -MnO<sub>2</sub> tunnel structures could be investigated.

This kind of approach has been used to model  $\gamma$ -alumina by Paglia *et al.* where they utilised a supercell containing 160 atoms (96 anions and 64 cations) [1] and exhaustively examined all possible ~1.47 billion configurations. The proposed work

would differ to that of Paglia *et al.* in that it would require a significantly larger supercell to fully model the system and therefore be extremely computationally expensive (in a supercell of the appropriate size for this model there would be literally trillions of possible cation positions). Thus a method would need to be developed that properly sampled from the entire phase space.

### 8.3 References

1. Paglia, G., A.L. Rohl, G.E. Buckley, and J.D. Gale, *Determination of the structure of  $\gamma$ -alumina from interatomic potential and first-principles calculations: The requirement of significant numbers of nonspinel positions to achieve an accurate structural model*. Phys. Rev. B: Condens. Matter Mater. Phys., 2005. **71**(22): p. 224115-1-16.

*Every reasonable effort has been made to acknowledge the owners of copyright material. I would be pleased to hear from any copyright owner who has been omitted or incorrectly acknowledged.*

### **Appendix I - ELECTROCHEMICAL STUDIES OF EMD**

In order to fully understand how the properties of EMD are influenced by changes in the deposition conditions, we must first have an understanding of the EMD deposition mechanism and electrochemical processes at the electrode/electrolyte interface. Ideally this information could be found in a literature search, however as there is some debate over the EMD deposition mechanism and the processes that occur at the electrode/electrolyte interface, it was decided that a brief electrochemical study using a combination of electrochemical impedance spectroscopy (EIS) and cyclic voltammetry (CV) would be conducted to confirm the mechanisms and interface processes suggested in the literature.

As the electrochemical studies in this project were only brief and did not elucidate any new information regarding the deposition mechanism the results have been omitted from the main body of this work. For the sake of completeness, however, they have been documented in this Appendix.

### Electrochemical Impedance Spectroscopy (EIS)

The EIS experimental method for this study is described in section 2.3.5. The results of the EIS analysis showed that the dominant component of the electrode impedance is a Warberg diffusion process (see Figure 1). This result compares well to the findings of Paul and Cartwright [1]. As the rotation speed had very little effect on the Warberg diffusion component of the spectra it can be assumed that this diffusion component is related to diffusion through a solid rather than diffusion through solution, as was similarly concluded by Paul and Cartwright [1].

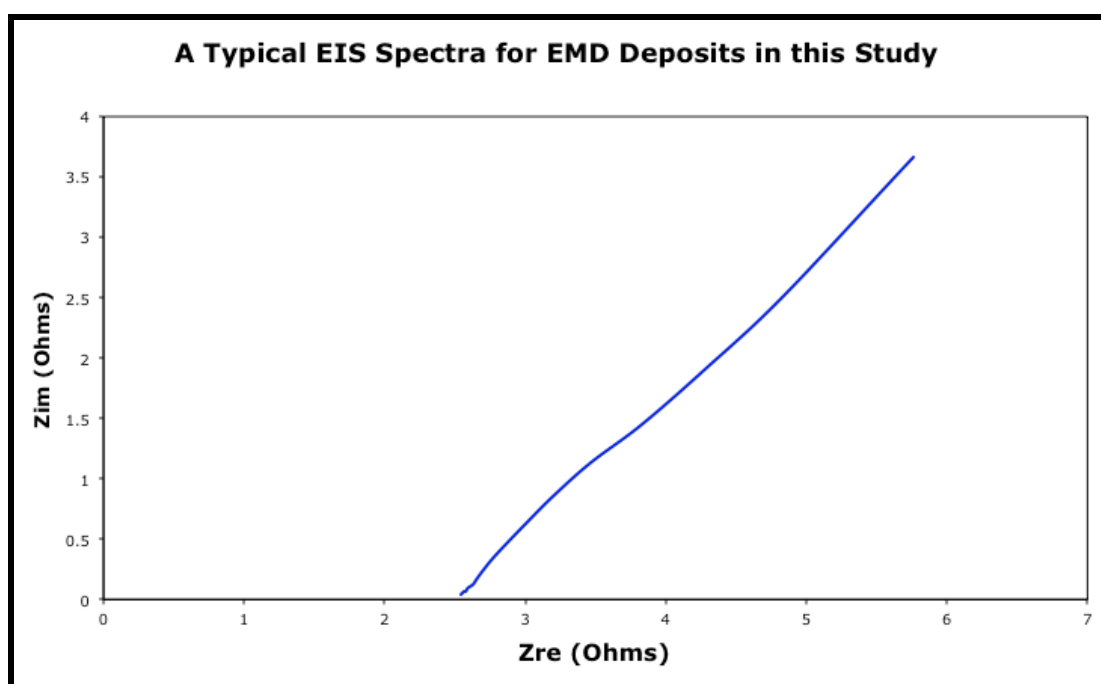


**Figure 1:** An example of the typical EIS plot obtained in this study.

### Cyclic Voltammetry (CV)

The CV experimental method for this study is described in section 2.3.4. The cyclic voltammetry scans performed in this study are shown in Figures 2-6. These results are generally consistent with literature reports [2-4]. However a brief investigation of these results concluded that far more extensive research than was allowed for in the scope of this project would be required to further decipher and rationalise discrepancies in current literature with regards to EMD deposition mechanisms. Therefore no further CV work or analysis was conducted.

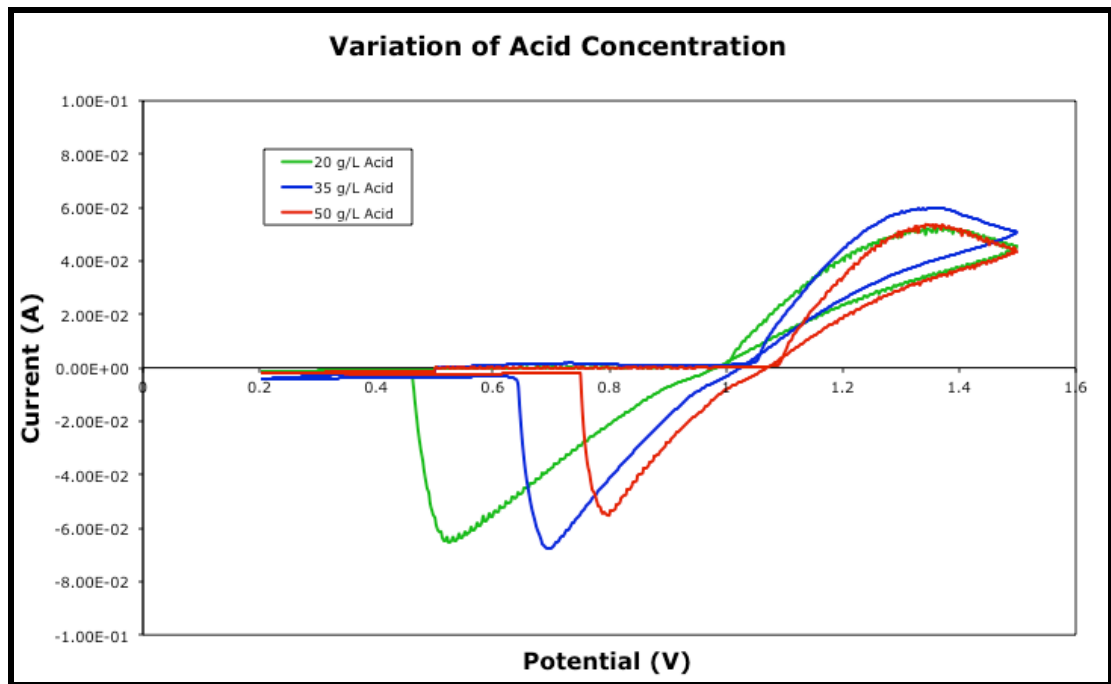


**Figure 2:** CV scans obtained at various acid concentrations from an electrolyte containing 60 g/L  $\text{Mn}^{2+}$  at 93 °C, and 20 g/L  $\text{H}_2\text{SO}_4$  [Green], 35 g/L  $\text{H}_2\text{SO}_4$  [Blue], and 50 g/L  $\text{H}_2\text{SO}_4$  [Red].

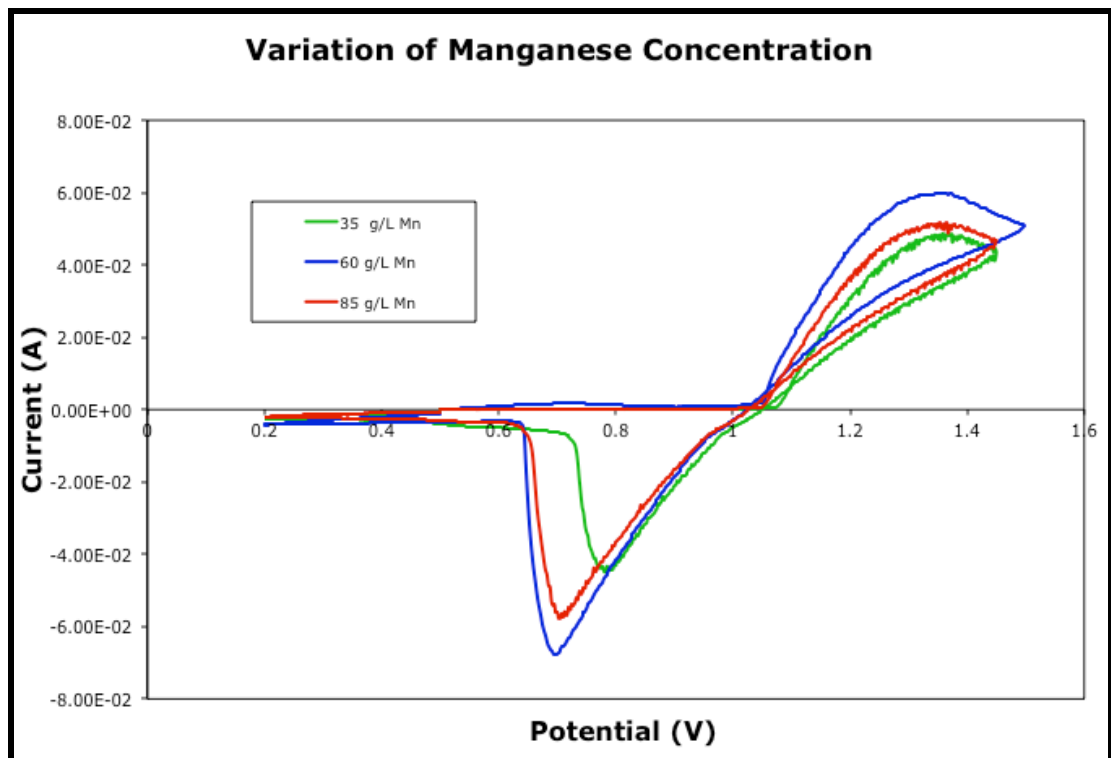


**Figure 3:** CV scans obtained at various manganese concentrations from an electrolyte containing 35 g/L  $\text{H}_2\text{SO}_4$  at 93 °C, and 35 g/L  $\text{Mn}^{2+}$  [Green], 60 g/L  $\text{Mn}^{2+}$  [Blue], and 80 g/L  $\text{Mn}^{2+}$  [Red].

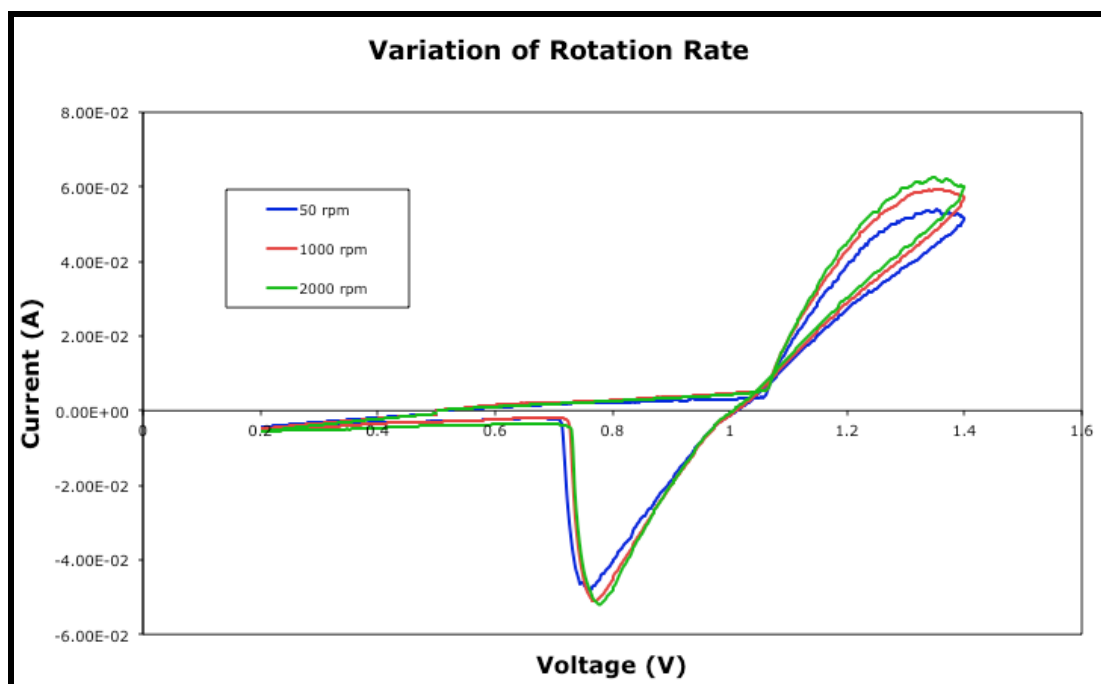


**Figure 4:** CV scans obtained at various rotation rates from an electrolyte containing 60 g/L  $\text{Mn}^{2+}$  and 35 g/L  $\text{H}_2\text{SO}_4$  at 93 °C, 50 rpm [Blue], 1000 rpm [Red], and 2000 rpm [Green].

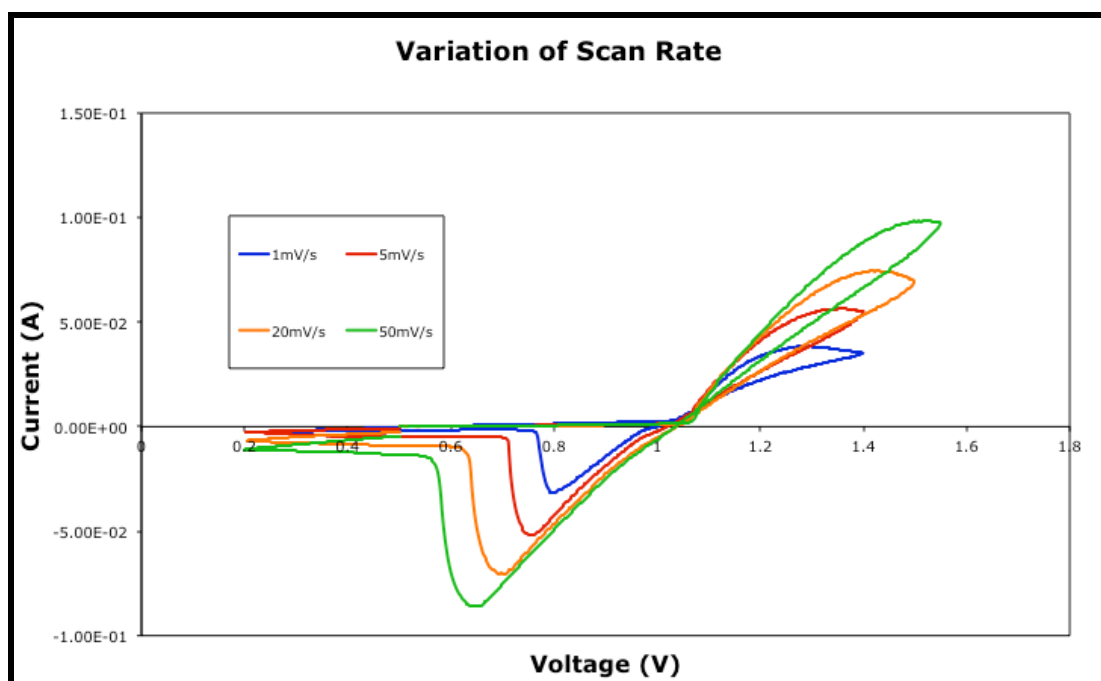


**Figure 5:** CV scans obtained at various scan rates from an electrolyte containing 60 g/L  $\text{Mn}^{2+}$  and 35 g/L  $\text{H}_2\text{SO}_4$  at 93 °C, 1 mV/s [Blue], 5 mV/s [Red], 20 mV/s [Orange] and 50 mV/s [Green].

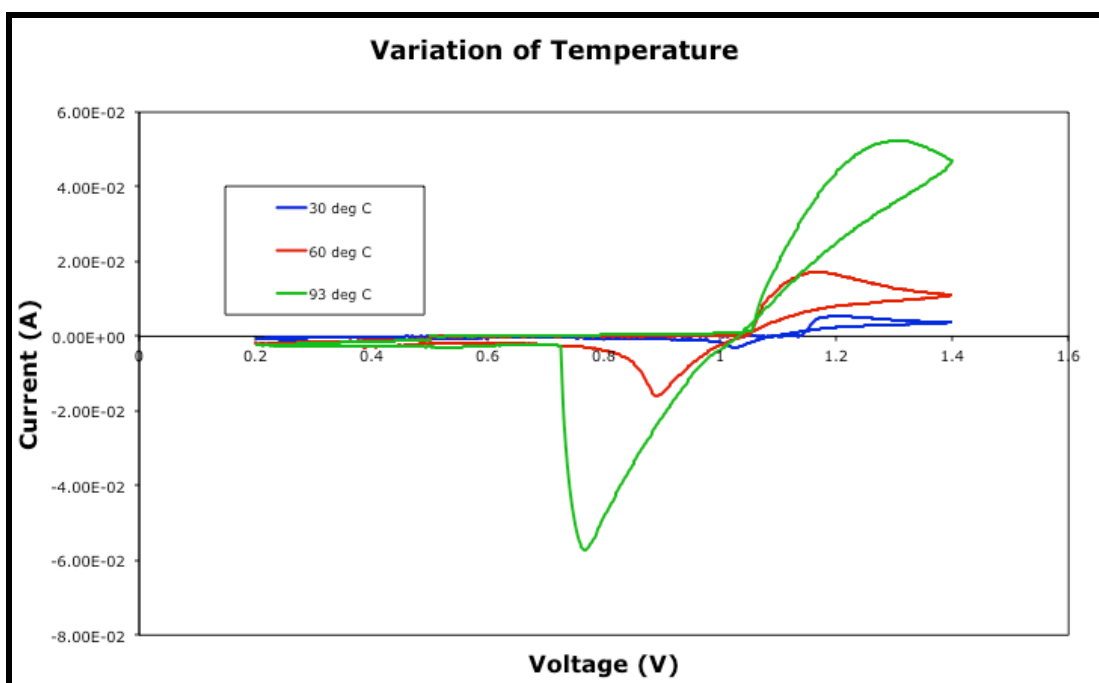


**Figure 6:** CV scans obtained at various temperatures from an electrolyte containing 60 g/L  $\text{Mn}^{2+}$  and 35 g/L  $\text{H}_2\text{SO}_4$  at 30 °C [Blue], 60 °C [Red], and 93 °C [Green].

## References

1. Paul, R.L. and A. Cartwright, *The Mechanism of the Deposition of Manganese Dioxide Part II. Electrode Impedance Studies*. J. Electroanal. Chem., 1986. **201**: p. 113-122.
2. Rodrigues, S., N. Munichandraiah, and A.K. Shukla, *A cyclic voltametric study of the kinetics and mechanism of electrodeposition of manganese dioxide*. J. Appl. Electrochem., 1998. **28**: p. 1235-1241.
3. Nijjer, S., J. Thonstad, and G.M. Haarberg, *Oxidation of manganese(II) and reduction of manganese dioxide in sulphuric acid*. Electrochim. Acta, 2000. **46**: p. 395-399.
4. Clarke, C.J., G.J. Browning, and S.W. Donne, *An RDE and RRDE study into the electrodeposition of manganese dioxide*. Electrochim. Acta, 2006. **51**(26): p. 5773-5784.

*Every reasonable effort has been made to acknowledge the owners of copyright material. I would be pleased to hear from any copyright owner who has been omitted or incorrectly acknowledged.*